

A New Three–Dimensional Vector Radiative Transfer Model and Applications to Saharan Dust Fields

Der Fakultät für Physik und Geowissenschaften

der Universität Leipzig

eingereichte

DISSERTATION

zur Erlangung des akademischen Grades

Doktor der Naturwissenschaften
(Dr. rer. nat)

vorgelegt

von **M.Sc. Vasileios Barlakas**

geboren in Thessaloniki / Griechenland

Leipzig, den 23.02.2016

1. Berichterstatter: Prof. Dr. Andreas Macke
2. Berichterstatter: Prof. Dr. Bernhard Mayer

Datum der Beschlussfassung: 04.07.2016

Bibliographic Description:

Barlakas, Vasileios

A New Three-Dimensional Vector Radiative Transfer Model and Applications to Saharan Dust Fields

University of Leipzig, Dissertation

108 p., 101 ref., 50 fig., 10 tab.

Abstract:

In this thesis a new three-dimensional (3D) vector radiative transfer model, the Solver for Polarized Atmospheric Radiative Transfer Applications (SPARTA) is introduced, validated against benchmark results, and applied to scientific problems. SPARTA employs the statistical forward Monte Carlo technique for efficient column-response pixel-based radiance calculations comprising polarization for 3D inhomogeneous cloudless and cloudy atmospheres. By means of SPARTA, two scientific issues in the field of radiative transfer are investigated. A sensitivity study has been conducted to illustrate the errors introduced by neglecting the effects of polarization in radiation simulations. Two atmospheric scenarios have been considered: a pure one-dimensional (1D) Rayleigh atmosphere and two-dimensional (2D) realistic inhomogeneous dust fields. In case of a purely molecular atmosphere, these errors strongly depend on molecular anisotropy, isotropic reflection, and more importantly, on single-scattering albedo and optical thickness (saturation occurs for τ close to 1). Overall errors in the reflected field range up to about 10.5 %. On the other hand, for rather high optical thickness, the bias induced by ignoring polarization for realistic inhomogeneous atmospheres is negligible (less than 1 %). In addition, solar radiative transfer simulations for LIDAR-measured fields of optical properties of Saharan dust have been performed in order to quantify the effects induced by neglecting the horizontal photon transport and internal inhomogeneities (3D radiative effects) in radiance simulations including polarization. Results are presented for two exemplary mineral dust fields constructed from LIDAR observations. For each case, three radiative calculations are investigated: a 1D calculation according to the plane-parallel (1D mode); an Independent Pixel Approximation (IPA mode); and the 2D mode. The differences in domain-averaged normalized radiances of reflection and transmission are insignificant between the 1D or IPA and 2D calculation modes. However, local differences were observed since extinction is hinge on horizontal spatial variability. In the areas with large spatial variability in optical thickness, the radiance fields of the 2D mode differ about $\pm 20\%$ for the first and second Stokes elements (I , Q) from the fields of the 1D mode. This work points to a brand-new field: the quantification of the sensitivity of polarization to 3D radiative effects.

Contents

1	Introduction	1
1.1	Mineral Dust Particles	1
1.2	Polarization in Remote Sensing	4
1.3	Challenges in Radiative Transfer Modelling	5
1.3.1	Errors Prompted by Neglecting Polarization	5
1.3.2	Radiative Effects	6
1.4	Objectives	7
1.5	Outline	7
2	Theoretical Background	8
2.1	Directions and Solid Angle	8
2.2	Radiometric Quantities	8
2.3	Polarization	10
2.3.1	Wave Formalism	10
2.3.2	The Stokes Parameters	12
2.4	Interactions of Electromagnetic Radiation and Single Particles	13
2.4.1	Amplitude Scattering Matrix	13
2.4.2	Transformation Phase Matrix	14
2.4.3	Single-Scattering Optical Properties	15
2.5	Interactions of Electromagnetic Radiation and Ensembles of Independent Particles	16
2.5.1	Single-Scattering Approximation	17
2.5.2	Ensembles of Particles	18
2.6	Normalized Scattering and Phase Matrices	18
2.7	Vector Radiative Transfer Equation	18
2.8	Numerical Methods to Solve the Radiative Transfer Equation	21
2.8.1	Adding-Doubling Method (A-DM)	21
2.8.2	Method of Successive Order of Scattering (MSOS)	22
2.8.3	Discrete Ordinate Method (DOM)	23
2.8.4	Spherical Harmonics Method (SHM)	23
2.8.5	Monte Carlo Method (MCM)	23
2.9	Existing Vector Radiative Transfer Models	24
3	SPARTA – Solver for Polarized Atmospheric Radiative Transfer Applications	26
3.1	Monte Carlo Random Sampling	26
3.2	SPARTA Description	27
3.2.1	Model Domain	27

3.2.2	Photon Initiation	27
3.2.3	Photon Tracing and Absorption	28
3.2.4	Anisotropic Scattering and Rotation of the Stokes Vector	29
3.2.5	Surface Reflection	33
3.2.6	Radiance Contribution and Local Estimate Method	35
3.2.7	SPARTA Efficiency	36
4	SPARTA Verification	38
4.1	Comparison Against Benchmark Results	38
4.1.1	Rayleigh Scattering Above a Lambertian Surface	38
4.1.2	Layered Cloud and Haze Atmospheres	39
4.1.3	Homogeneous Aerosol and Cloudy Atmospheres	49
4.2	Model Intercomparison Project	50
4.2.1	A4 - Spheroidal Aerosol Particles	54
4.2.2	A6 - Rayleigh Scattering Above an Ocean Surface	57
4.2.3	B2 - Rayleigh Scattering and Absorption for a Standard Atmosphere	57
4.2.4	B3 - Aerosol Profile and Standard Atmosphere	57
4.2.5	B4 - Standard Atmosphere with a Cloud Layer Above an Ocean Surface	60
5	Applications	65
5.1	Polarization Radiative Effects	65
5.1.1	Measurement Cases	65
5.1.2	Scattering Properties of Molecules and Aerosol Particles	67
5.1.3	Monte Carlo Simulations	69
5.2	Overall Radiative Effects	86
5.3	Errors Prompted by Neglecting Polarization in Radiance Computations	94
5.3.1	Molecular Atmosphere	94
5.3.2	Inhomogeneous Saharan Dust Fields	97
6	Summary, Conclusions, and Outlook	100
6.1	A New Radiative Transfer Solver	100
6.2	Implications from Neglecting Polarization	101
6.3	Quantification of Polarization Radiative Effects	102
6.4	Outlook	104
	Bibliography	106
	List of Symbols	117
	List of Abbreviations	121
	List of Figures	123
	List of Tables	126
	Acknowledgements	127

Curriculum Vitae**128**

1 Introduction

Non-spherical atmospheric particles have a significant impact on climate (Liou, 1986; Kaufman et al., 2002; IPCC, 2013). They scatter, absorb and change the polarization state of solar radiation depending on their shape, size, chemical composition and orientation. Even though this relationship is rather complex, its knowledge is an important condition for the interpretation of remote sensing measurements. Additionally, the comprehensive investigation of ground-based and airborne passive radiometric and polarization measurements require a vector radiative transfer model that accounts for multiple-scattering and polarization. Thus, the general objective of this work is the development of a new three-dimensional (3D) vector radiative transfer model to account for polarization effects due to multiple-scattering by non-spherical particles, i.e., coarse mode dust or ice particles.

This introduction, which is partly described in Barlakas et al. (2016), outlines the importance of non-spherical atmospheric mineral dust particles and the need to employ polarization in radiative transfer. The challenges in radiative transfer modeling, including errors prompted by neglecting polarization and domain heterogeneities in radiance simulations are described, followed by the major objectives of this work.

1.1 Mineral Dust Particles

Mineral dust comprises non-spherical soil particles suspended in the atmosphere. Its global emissions varies with location and season; estimates are in the range of 1000 and 3000 Tg yr⁻¹ (Tegen, 2003). Sea salt particles comprise another important aerosol particle type with similar flux rates (Andreae, 1995; Tegen, 2003). Figure 1.1 depicts the dominant aerosol types in the atmosphere (sulfate smoke, dust and sea salt particles) as analyzed by the Goddard Earth Observing System Model, Version 5 (GEOS-5). Note the huge dust plume and its transport from Western Africa towards the Caribbean. Anthropogenic activities, including extended land use and constructions, lead to an increase of anthropogenic mineral dust loads; about 30 % of the total mineral dust load is related to human activities (Ginoux et al., 2012). The majority of the dust sources are found in the Northern Hemisphere, with the Saharan desert being the largest mineral dust arsenal.

The atmospheric climate impact of anthropogenic mineral dust particles has not been reliably assessed, partly owing to incomplete understanding of their properties (IPCC, 2013). In addition, compared to other particles, dust particles are rather irregular in shape and structure clouding their understanding. As a consequence, according to the latest Intergovernmental Panel on Climate Change IPCC (2013), the radiative forcing (RF) linked to mineral dust

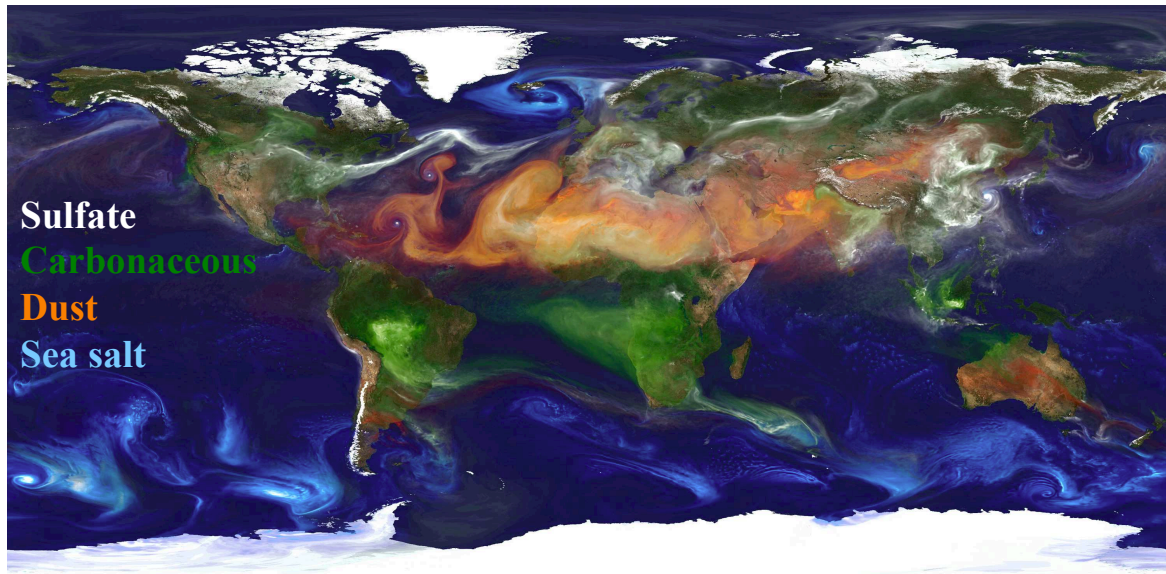


Figure 1.1: Portrait of global aerosols yielded by GEOS-5 (Goddard Earth Observing System Model, Version 5) at a 10 km resolution. Sulfate particles (white) resulting from volcano eruptions and fossil fuel emissions, carbonaceous/smoke (green) rises from fires, dust (orange/red) is lifted from the ground, and sea salt (blue) swirls inside cyclones. Image credit: William Putman, NASA/Goddard.

particles vary considerably ($-0.1 \pm 0.2 \text{ W m}^{-2}$, see Figure 1.2); even the sign of RF is not well determined (Haywood and Boucher, 2000).

Mineral dust particles have both a direct and indirect radiative effect. When they scatter and absorb solar radiation, the effect is direct. The indirect radiative effect is related to the ability of mineral dust particles to influence the cloud optical properties. Dust particles are considered effective ice nuclei (IN) leading to the formation of ice crystals (Cantrell and Heymsfield, 2005; Phillips et al., 2008; DeMott et al., 2010; Teller et al., 2012); they also form cloud condensation nuclei (CCN) producing cloud droplets (Levin et al., 1996; Zhang et al., 2007; Twohy et al., 2009). As a result, increasing the dust load in the atmosphere leads to an increase of CCN and IN, and therefore, influences the cloud albedo and changes the cloud lifetime, among others (IPCC, 2013). Note that when dust particles are uplifted to about 3 to 10 km height (i.e., owing to deep convection), they may be transported for thousands of kilometers before depositing (see Figure 1.1). Consequently, mineral dust affects atmospheric chemical processes (Tegen, 2003), ocean and terrestrial biogeochemistry (by supplying nutrients influencing the iron budget) that are far away from their source region (Hutchins and Bruland, 1998; Chadwick et al., 1999; Bristow et al., 2010). In addition, mineral dust particles also influence human health (respiratory problems) and visibility (Ginoux et al., 2012).

Both direct and indirect effects of atmospheric mineral dust particles are of immense importance, yet there is still low scientific understanding. Hence, in order to improve their scientific understanding a number of German research institutions launched a set of campaigns during the past years:

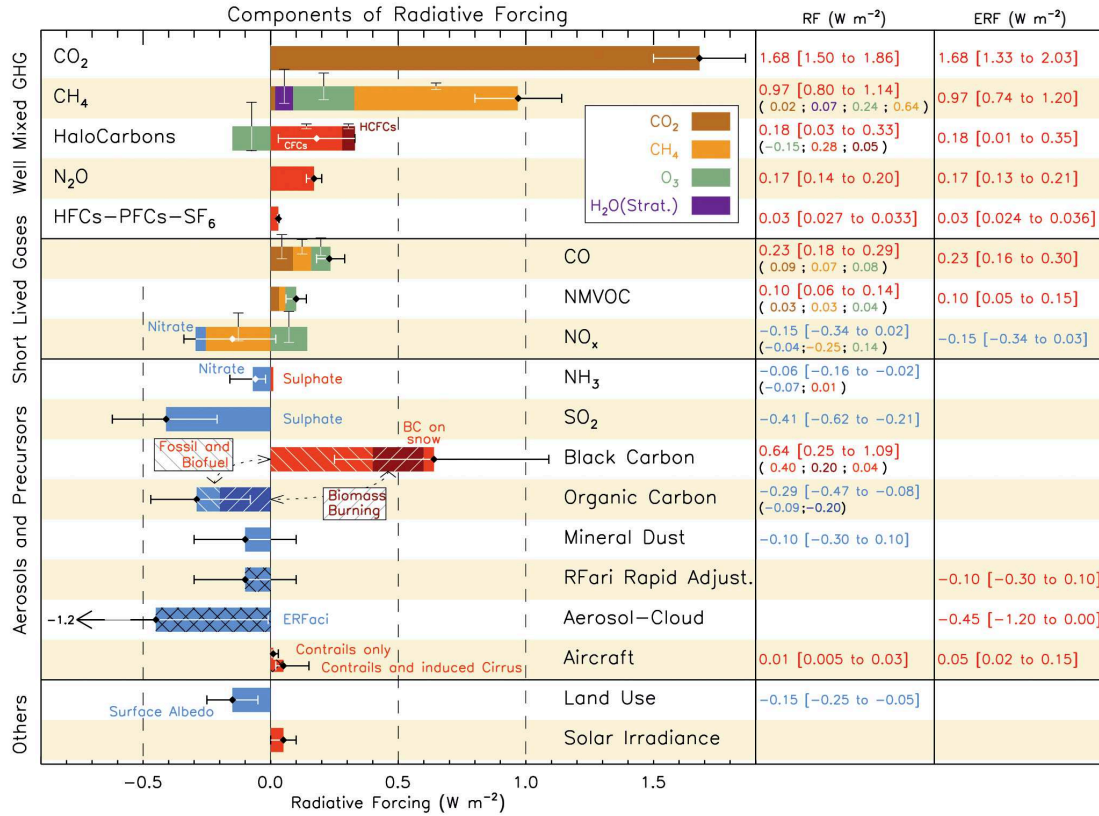


Figure 1.2: Radiative Forcing (RF) of climate change during the period 1750-2011 shown by emitted atmospheric components. Horizontal bars outline the overall uncertainty and the vertical bars are for the individual components. Values are RF except for the effective radiative forcing (ERF) due to aerosol cloud interactions. This figure is adopted from IPCC (2013); Technical summary.

- Saharan Mineral dUst experiMent (SAMUM) supported by the German Research Foundation (Deutsche Forschungsgemeinschaft, DFG), sub-experiments, namely SAMUM-1 (Morocco, 2006) and SAMUM-2 (Cape Verde, 2008). The aim of the SAMUM-1 was the investigation of the microphysical, chemical, optical, and radiative properties of the mineral dust particles in the area close to the major Saharan source region (Heintzenberg, 2009). SAMUM-2 focused on the characterization of Saharan dust after substantial long-range transport (Ansmann et al., 2011).
- Trans-Atlantic cruise of the research vessel METEOR from the Caribbean to the west coast of Africa (April-May 2013) (Kanitz et al., 2014), with a special emphasis on the characterization of mineral dust particles along their major transport route (see Figure 1.1). It was funded by the Leibniz Institute for Tropospheric Research (TROPOS) in Leipzig, Germany.
- Saharan Aerosol Long-range Transport and Aerosol-Cloud-Interaction Experiment (SALTRACE, <http://www.pa.op.dlr.de/saltrace>) aiming at the investigation of the long-range transport of Saharan mineral dust from the West coast of Africa towards the Caribbean (June-July 2013) (Chouza et al., 2015). It was funded by the Helmholtz

Association, the Deutsches Zentrum für Luft- und Raumfahrt (DLR), the Ludwig-Maximilians-Universität München (LMU), and TROPOS.

Ground-based, airborne in-situ, LIDAR (Light Detection And Ranging), and satellite remote sensing techniques, as well as modeling, have been employed to improve the characterization of aerosol particles. For example, the combination of LIDAR (depolarization and LIDAR ratios) and in-situ measurements (Ångström exponents) triggers a new approach to characterize the aerosol type (Ansmann et al., 2011). The non-spherical shape of mineral dust particles is introduced. Consequently, it enables the improvement and/or development of models; the updated modeling enhances the scientific understanding of the radiative effect linked to non-spherical mineral dust particles. Finally, the investigation of the dust long-range transport introduces significant differences in their optical properties (Ansmann et al., 2011; Kanitz et al., 2014).

For the purpose of this work, two LIDAR observations from SAMUM and METEOR campaigns were analyzed, offering the chance to simulate the radiative transfer in realistic mineral dust plumes. The profiles of extinction and scattering coefficients, single-scattering albedo, and scattering phase matrix of the inhomogeneous Saharan dust were constructed on the basis of the LIDAR measurements sharing the geometrical and optical properties of the dust plumes; these profiles are the input of a 3D radiative transfer model.

1.2 Polarization in Remote Sensing

To correctly interpret remote sensing data and derive the properties of aerosol particles, additional information is needed. Several studies pointed out that the use of polarization measurements is sensitive to particle microphysical properties (e.g., Hansen and Travis, 1974; Mishchenko and Travis, 1997; Boesche et al., 2006; Li et al., 2009). For instance, Li et al. (2009) illustrate that polarization helps constrain both the size distribution and the real part of the refractive index of the dust particles and outlines the higher sensitivity of polarization to the shape of the particle as compared to the radiance measurements (see Figure 1.3).

Nowadays, several remote sensing instruments employ polarization. For example, the Polarization and Directionality of the Earth's Reflectances (POLDER) instrument includes polarized information (Deschamps et al., 1994); it is a passive radiometer mounted on the satellite ADEOS I (Advanced Earth Observing Satellite 1) supporting multi-directional and polarized measurements. The Research Scanning Polarimeter (RPS) (Cairns et al., 1999, 2003), has been employed for ground-based and airborne measurements, the Multiangle SpectroPolarimetric Imager (MSPI) (Diner et al., 2013) was built to improve the POLDER instrument via increasing its resolution, and the CIMEL polarized sun/sky-photometer developed by CIMEL Electronique (Paris, France) CE318-DP (Li et al., 2014) was developed for polarization measurements.

Also, new retrieval algorithms that involve polarization have been produced (Chowdhary et al., 2004; Li et al., 2009).

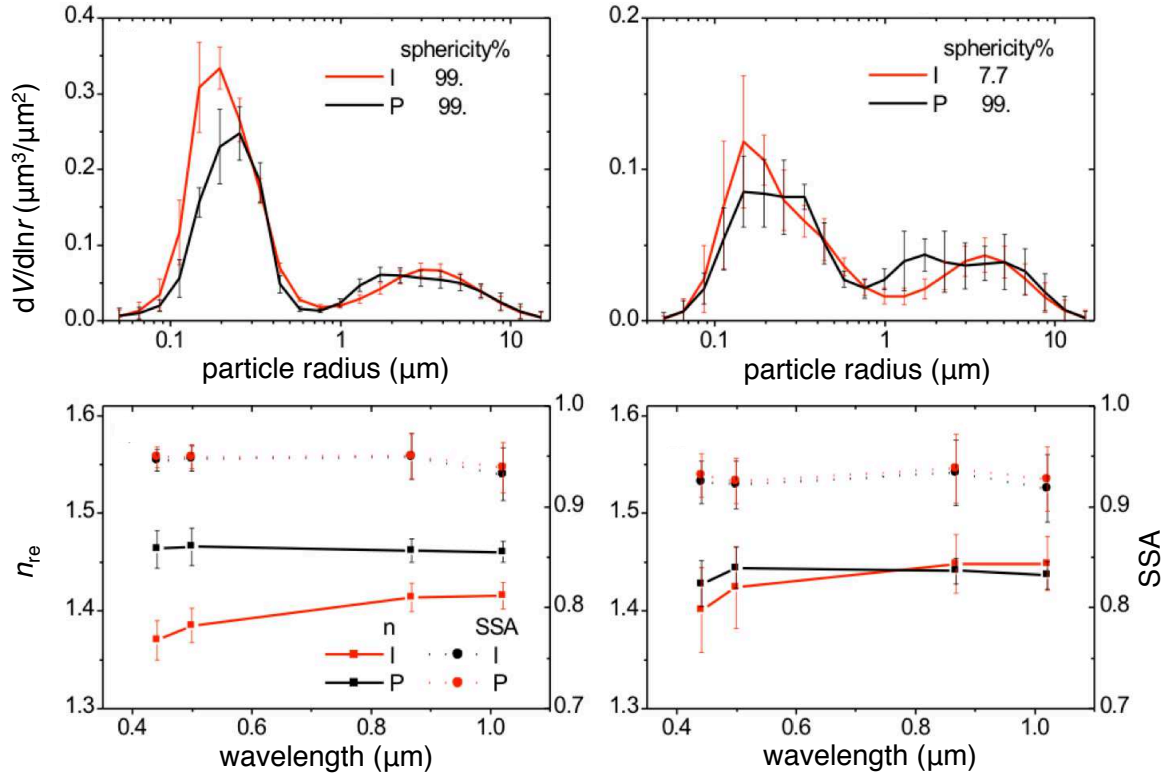


Figure 1.3: Retrieved dust properties ($dV/d\ln r$: particle size distribution, sphericity%: fraction of spherical aerosol component, n_{re} : real part of the refractive index, and SSA: single-scattering albedo) for two measurement scenarios, small particles (left panels) and coarse mode aerosol particles (right panels). Two AERONET inversion algorithms have been used: **a.** radiance-only (I) employing sky radiance and optical depth measurements and **b.** polarization (P) supplying degree of linear polarization measurements from the CIMEL Electronique CE318-DP. This figure is adopted from Li et al. (2009).

1.3 Challenges in Radiative Transfer Modelling

The investigation of ground-based and airborne passive radiance and polarization measurements requires radiative transfer models that account for multiple-scattering, absorption, and polarization. As a result, a growing number of one-dimensional (1D) and 3D vector models have been developed (Kokhanovsky et al., 2010; Emde et al., 2015) and the following two issues are discussed: errors by neglecting polarization and domain heterogeneities.

1.3.1 Errors Prompted by Neglecting Polarization

Albeit the increasing number of vector radiative transfer models, mostly scalar models are still employed for the analysis of the remote sensing data. However, ignoring the effects of polarization may lead to considerable errors in radiation simulations. Chandrasekhar (1960) was the first to report that in case of a pure molecular atmosphere the scalar radiative transfer approximation results in errors of about 10 %. A comprehensive investigation of the deviations between the vector and the scalar approaches for homogeneous Rayleigh scatter-

ing problems is linked to the work of Mishchenko et al. (1994) and Lacis et al. (1998). In agreement with former studies, errors up to 10 % were found resulting from low-orders of scattering. Limited research has been made for aerosol particles and realistic atmospheres (aerosol particles + molecules). Hansen (1971b) shows that for spherical cloud particles (with sizes of the order or greater than the wavelength of the incident electromagnetic radiation) the errors are in the order of 1 %. Kotchenova et al. (2006) investigated the errors in the reflected radiation for two atmospheric problems, a homogeneous layer including biomass burning smoke aerosol particles and including additional molecular scattering. The resulting errors are as large as 5.3 % for the pure aerosol and up to 4.3 % for the mixed scenario (depending on the wavelength).

1.3.2 Radiative Effects

A full 3D radiative transfer calculation in cloudy atmospheres is computationally expensive. Consequently, 1D radiative transfer models are employed to interpret remote sensing measurements. During the last decades, there has been an inconclusive debate about whether the 1D approximation is sufficient or the neglect of horizontal photon transport and the internal inhomogeneity of the field under investigation cause significant errors in radiance simulations (Benner and Evans, 2001; Di Giuseppe and Tompkins, 2003).

Várnai and Davies (1999) outline two approximations/effects induced by employing 1D models:

- "One-dimensional heterogeneity effect - 1D" denotes the errors caused by ignoring horizontal internal inhomogeneities (considering only vertical changes). Simulations are conducted for a homogeneous field by means of the domain-averaged optical properties, meaning the properties are averaged over the whole domain leading to the horizontally homogeneous 1D domain, omitting the horizontal variability of the domain. Alternative it is named "plane-parallel (PP) bias" (Cahalan et al., 1994a).
- "Horizontal transport effect" describes the errors induced by neglecting the horizontal photon transport between neighboring cells/pixels with different optical properties. It may further ignore interactions between neighboring clouds, leading to illuminating and shading effects (Di Giuseppe and Tompkins, 2003).

These two closely related physical processes, that are usually ignored in general circulation models (GCMs) (Di Giuseppe and Tompkins, 2003), are designated as the 3D radiative effects. A widely used simplification is the so-called Independent Pixel Approximation (IPA) (Cahalan et al., 1994b), whereby radiative transfer simulations are conducted pixel by pixel to approximate the full 3D radiative field. In this way, the horizontal inhomogeneity is taken into account, albeit the horizontal photon transport is still ignored. IPA has been extensively utilized in remote sensing (i.e., retrievals) and climate applications (Benner and Evans, 2001). Plenty former studies have focused on investigating the horizontal variability of the cloud (e.g., Cahalan et al., 1994b; Marshak et al., 1998) and smoothing effects (Davis et al., 1997).

Although there has been only limited research on the 3D radiative effects for dust fields (Torge et al., 2011), several studies have been carried out for inhomogeneous liquid water, mixed phase and ice clouds (e.g., Davis et al., 1997; Scheirer and Macke, 2001, 2003; Benner and Evans, 2001; Di Giuseppe and Tompkins, 2003; Cahalan et al., 2005). However, in these studies the issue under scrutiny was the radiative effects in the scalar radiative transfer scheme. In this work, the discussion centers on polarization effects. There is no compelling reason to claim that the scalar approximation is sufficient to describe the errors by disregarding horizontal internal inhomogeneities and horizontal photon transport in a microphysical domain. The goal of this work is to broaden such investigations by combining the 3D aspect with the vector radiative transfer scheme in order to quantify the sensitivity of polarization to such physical processes.

1.4 Objectives

Although several 1D and 3D vector models have been developed, the availability is usually restricted to the 1D codes (with only a few exceptions). Therefore, the Solver for Polarized Atmospheric Radiative Transfer Applications (SPARTA), participated in the model intercomparison project launched by the polarization working group of the International Radiation Commission (IRC) (Emde et al., 2015), has been developed in order to fill this gap. The model employs the forward Monte Carlo technique for efficient column-response pixel-based radiance calculations including polarization for 3D inhomogeneous cloudless and cloudy atmospheres. SPARTA is an open source, user-friendly model. It will help to compare and improve models (world-wide model assembly, model intercomparison). The major objective of this work is the application of SPARTA to scientific problems with a special emphasis on non-spherical mineral dust particles and polarization. Two scientific problems will be investigated:

- Errors prompted by neglecting polarization in radiance simulations for two atmospheric problems: a pure 1D Rayleigh atmosphere and 2D realistic dust fields.
- Polarization radiative effects due to the neglect of horizontal photon transport and the internal inhomogeneity in radiative transfer simulations for LIDAR-measured inhomogeneous Saharan dust fields performing 1D, IPA, and 2D calculations.

1.5 Outline

The fundamentals of radiative transfer theory used in the framework of this work are described in Chapter 2. In Chapters 3 and 4 the new three-dimensional (3D) vector radiative transfer model, SPARTA, is introduced and validated, respectively. In Chapter 5, SPARTA is employed to quantify polarization effects in the field of remote sensing with a special emphasis on polarization and non-spherical mineral dust particles. A conceptual conclusion of the thesis and an outlook are given in Chapter 6.

2 Theoretical Background

This chapter introduces the fundamentals of radiative transfer theory used in the framework of this work. The basic terminology of the radiometric quantities, the single-scattering and volumetric optical properties, plus the basic concepts of polarization are introduced. Furthermore, the vector radiative transfer equation and solution methods are reviewed. Finally, a list of the most commonly applied vector models is given. Definitions follow the textbooks of Stokes (1852), Chandrasekhar (1960), Hansen and Travis (1974), Seinfeld and Pandis (1998), Liou (2002), Mishchenko et al. (2002), and Wendisch and Yang (2012).

2.1 Directions and Solid Angle

To describe the transfer of radiation, the propagation direction of a pencil of radiation should be specified. The direction of propagation is specified by a unit vector, $\hat{\mathbf{k}}$, or by the couple (θ, ϕ) utilizing the zenith θ and azimuth ϕ angles.

The solid angle Ω is defined as the ratio of a spherical surface that an object covers as observed from the sphere's center. An infinitesimal solid angle, $d^2\Omega$, is given by:

$$d^2\Omega = \frac{d^2A}{r^2}, \quad (2.1)$$

where d^2A is the differential area element and r^2 the square of the radius. Note that the square of the differential operator refers to a 2D differential element. The solid angle is expressed in units of "steradians" (sr). For a sphere that is characterized by a surface area of $4\pi \cdot r^2$, its solid angle is 4π sr. The $d^2\Omega$ is expressed in spherical coordinates:

$$d^2\Omega = \sin\theta \, d\theta \, d\phi. \quad (2.2)$$

2.2 Radiometric Quantities

Consider a differential area element d^2A . The radiant energy E_{rad} in a time range $t + dt$ and in a wavelength (λ) range $\lambda + d\lambda$, that crosses through this area is indicated by the spectral radiant energy flux, Φ_λ :

$$\Phi_\lambda = \frac{d^2E_{\text{rad}}}{dt \, d\lambda}. \quad (2.3)$$

The $\Phi_\lambda(t)$ is measured in $\text{J s}^{-1} \text{nm}^{-1} = \text{W nm}^{-1}$. The normalized $\Phi_\lambda(t)$ over the differential area element d^2A denotes the spectral irradiance (spectral radiant energy flux density) given by:

$$F_\lambda = \frac{d^2\Phi_\lambda}{d^2A} = \frac{d^4E_{\text{rad}}}{d^2A dt d\lambda}. \quad (2.4)$$

F_λ in units of $\text{W m}^{-2} \text{nm}^{-1}$ defines the power of the electromagnetic (EM) radiation received per unit surface area from all directions of a half sphere (hemispheric). The spectral irradiance within a solid angle $d^2\Omega$, in a specific direction \hat{k} , describes the spectral radiance, $I_\lambda(\hat{k})$ (in units of $\text{W m}^{-2} \text{nm}^{-1} \text{sr}^{-1}$), which is defined by:

$$I_\lambda(\hat{k}) = \frac{d^4\Phi_\lambda}{\cos\theta d^2A d^2\Omega} = \frac{d^6E_{\text{rad}}}{dt d\lambda \cos\theta d^2A d^2\Omega}, \quad (2.5)$$

where θ is the angle between \hat{k} and the normal unit vector of the area element \hat{n} (angle of incidence, see Figure 2.1). In Eq. (2.5) the term $d^2A_\perp = d^2A \cdot \cos\theta$ (see Figure 2.1) indicates the propagation of the $\Phi_\lambda(t)$. It follows that the spectral irradiance can be obtained by a simple integration of the spectral radiance over the solid angle:

$$F_\lambda = \int \int_{2\pi} I_\lambda(\hat{k}) \cdot \cos\theta d^2\Omega = \int_0^{2\pi} \int_0^\pi I_\lambda(\theta, \phi) \cdot \cos\theta \cdot \sin\theta d\theta d\phi. \quad (2.6)$$

It is customary for atmospheric applications to differentiate between the upward irradiance F_λ^\uparrow and downward irradiance F_λ^\downarrow :

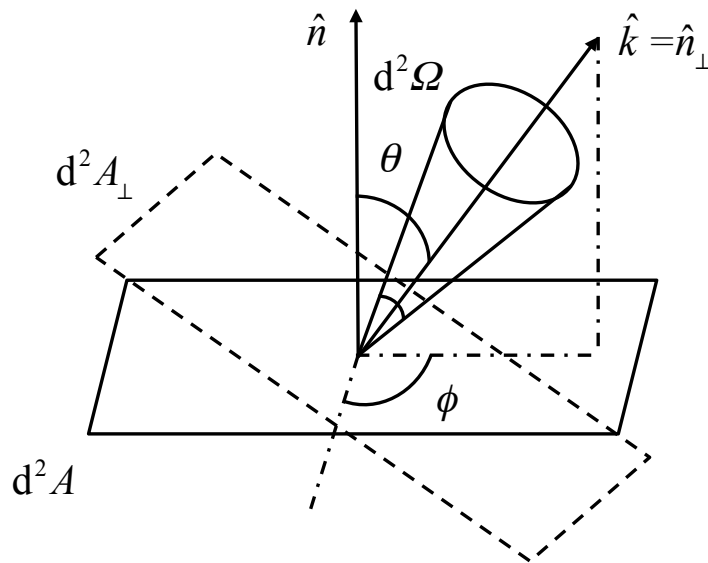


Figure 2.1: Illustration of the definition of radiances.

$$F_{\lambda}^{\uparrow} = \int_0^{2\pi} \int_0^{\pi/2} I_{\lambda}(\theta, \phi) \cdot \cos \theta \cdot \sin \theta \, d\theta \, d\phi \quad (2.7)$$

$$F_{\lambda}^{\downarrow} = - \int_0^{2\pi} \int_{\pi/2}^{\pi} I_{\lambda}(\theta, \phi) \cdot \cos \theta \cdot \sin \theta \, d\theta \, d\phi. \quad (2.8)$$

The downward F_{λ}^{\downarrow} is composed of two terms, the direct (coming directly from the sun, no scattering) and the diffuse (produced by multiple-scattering with molecules, aerosol particles, and surface reflection). The upward F_{λ}^{\uparrow} is related to diffuse radiation only.

At any altitude z above the surface, the dimensionless spectral albedo ρ_{λ} is defined as the ratio of F_{λ}^{\uparrow} and F_{λ}^{\downarrow} :

$$\rho_{\lambda}(z) = \frac{F_{\lambda}^{\uparrow}(z)}{F_{\lambda}^{\downarrow}(z)}. \quad (2.9)$$

ρ_{λ} describes the fraction of irradiance reflected by an object.

2.3 Polarization

2.3.1 Wave Formalism

Electromagnetic waves are characterized by specific polarization state. Starting from Maxwell's equations, the complex electric field vector, $\vec{\mathbf{E}}$ (in units of V m^{-1}), propagating along the z direction (in Cartesian coordinates) is described by:

$$\vec{\mathbf{E}} = \vec{\mathbf{E}}_0 \cdot \exp(i \cdot k \cdot z - i \cdot \omega_c \cdot t), \quad (2.10)$$

where $\vec{\mathbf{E}}_0$ denotes the complex electric amplitude vector (in units of V m^{-1}), $i = \sqrt{-1}$, $k = 2\pi \cdot \tilde{n}/\lambda$ is the wavenumber of the EM wave (for air or vacuum) with \tilde{n} representing the complex index of refraction, $\omega_c = 2\pi/\lambda$ is the circular frequency, and t is the time (in units of seconds). Figure 2.3 illustrates an EM wave travelling through a medium. The EM wave consists of the orthogonal **electric field vector** $\vec{\mathbf{E}}$ and the **magnetic field vector** $\vec{\mathbf{H}}$, each perpendicular to the direction of propagation. The power of the EM radiation in the direction of propagation is given by the time-averaged Poynting vector $\vec{\mathbf{F}}$, give by:

$$\langle \vec{\mathbf{F}} \rangle = \frac{1}{2} \text{Re} \left(\vec{\mathbf{E}} \times \vec{\mathbf{H}}^* \right). \quad (2.11)$$

The asterisk indicates for the complex conjugate value. The absolute value of the Poynting vector, $|\langle \vec{\mathbf{F}} \rangle| = F$, has the unit of irradiance (W m^{-2}).

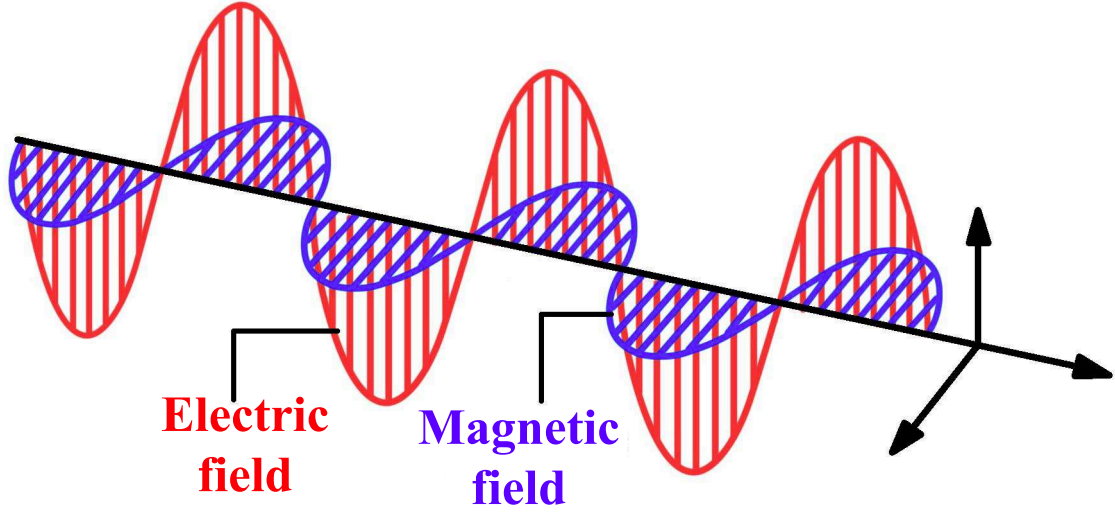


Figure 2.2: Electromagnetic wave illustration. The wave consists of the electric and magnetic field vectors. Figure is adopted from <http://newsciencephysics.blogspot.de/>.

The complex electric field vector consists of two orthogonal components parallel (subscript "||") and perpendicular (subscript "⊥") with respect to the reference plane including the direction of propagation:

$$\vec{\mathbf{E}} = E_{||} \cdot \hat{e}_{||} + E_{\perp} \cdot \hat{e}_{\perp}, \quad (2.12)$$

where $\hat{e}_{||}$ and \hat{e}_{\perp} are the base vectors parallel and perpendicular to the direction of propagation. From Eqs. (2.10) and (2.12), $\vec{\mathbf{E}}$ is given by:

$$\vec{\mathbf{E}} = \begin{pmatrix} E_{||} \\ E_{\perp} \end{pmatrix} \cdot \exp(i \cdot k \cdot z - i \cdot \omega_c \cdot t) = (E_{||} \cdot \hat{e}_{||} + E_{\perp} \cdot \hat{e}_{\perp}) \cdot \exp(i \cdot k \cdot z - i \cdot \omega_c \cdot t). \quad (2.13)$$

Since the remote sensing systems are not able to measure the complex EM field vector, but only the power of the EM wave (Poynting vector $\vec{\mathbf{F}}$), the real part of Eq. (2.13) should be considered:

$$|\langle \vec{\mathbf{E}} \rangle| = \begin{pmatrix} E_{0||} \cdot \cos(k \cdot z - \omega_c \cdot t + \zeta_{||}) \\ E_{0\perp} \cdot \cos(k \cdot z - \omega_c \cdot t + \zeta_{\perp}) \end{pmatrix}. \quad (2.14)$$

$E_{0||}$ and $E_{0\perp}$ are the amplitudes, and $\zeta_{||}$ and ζ_{\perp} are the phases of the electric field vector parallel and perpendicular to the reference plane. Polarization describes the orientation of the EM wave along its direction of propagation. Three characteristic polarization cases are given:

- Elliptical polarization, the tip of the EM wave vector follows an elliptical pattern in the reference plane. It occurs when $E_{0||} \neq E_{0\perp} \neq 0$ and the phase difference $\zeta_{\perp} - \zeta_{||} \neq 0$.

- Linear polarization, the tip of the EM wave vector follows a linear pattern in the reference plane. It occurs when $E_{0\parallel}$ or $E_{0\perp}$ is zero, or when $E_{0\parallel} = E_{0\perp}$ and $\zeta_{\perp} = \zeta_{\parallel}$.
- Circular polarization, the tip of the EM wave vector follows a circular pattern in the reference plane. It occurs when $E_{0\parallel} = E_{0\perp}$ and $\zeta_{\perp} - \zeta_{\parallel} = +90^\circ$ (clockwise rotation) or $\zeta_{\perp} - \zeta_{\parallel} = -90^\circ$ (counter clockwise rotation).

2.3.2 The Stokes Parameters

The conventional approach to consider polarization dates back to Stokes (1852), who discovered that the polarization behavior of the electromagnetic radiation can be represented by real observables. This resulted in the Stokes vector, defined by four components:

$$\vec{S} = \begin{pmatrix} F \\ Q \\ U \\ V \end{pmatrix}, \quad (2.15)$$

each of them carrying the units of irradiance (W m^{-2}) (Stokes, 1852). The Stokes vector represents both irradiance and polarization.

The Stokes vector is described by the components of a transverse electromagnetic field (e.g., Chandrasekhar, 1960):

$$F = \frac{1}{2} \sqrt{\frac{\epsilon}{\kappa}} \cdot (E_{\parallel} \cdot E_{\parallel}^* + E_{\perp} \cdot E_{\perp}^*), \quad (2.16)$$

$$Q = \frac{1}{2} \sqrt{\frac{\epsilon}{\kappa}} \cdot (E_{\parallel} \cdot E_{\parallel}^* - E_{\perp} \cdot E_{\perp}^*), \quad (2.17)$$

$$U = \frac{1}{2} \sqrt{\frac{\epsilon}{\kappa}} \cdot (E_{\parallel} \cdot E_{\perp}^* + E_{\perp} \cdot E_{\parallel}^*), \quad (2.18)$$

$$V = i \cdot \frac{1}{2} \sqrt{\frac{\epsilon}{\kappa}} \cdot (E_{\parallel} \cdot E_{\perp}^* - E_{\perp} \cdot E_{\parallel}^*). \quad (2.19)$$

Where E_{\parallel} and E_{\perp} are the two orthogonal electric field components parallel and perpendicular to the direction of propagation, ϵ is the electric permeability, κ is the magnetic permittivity, the asterisk represents the conjugate value. The first Stokes vector element, F , is the total irradiance, Q and U describe the linear and V the circular polarization. These parameters are defined using the local meridian plane as a plane of reference (Chandrasekhar, 1960) expressed by the propagation and vertical directions.

The dimensionless degree of polarization P is defined as:

$$P = \frac{\sqrt{Q^2 + U^2 + V^2}}{F} \leq 1. \quad (2.20)$$

For completely polarized EM radiation, $P = 1$, and for unpolarized EM radiation, $P = 0$. We may further define the degree of linear P_{lin} and circular polarization P_{cir} as

$$P_{\text{lin}} = \frac{\sqrt{Q^2 + U^2}}{F}, \quad (2.21)$$

$$P_{\text{cir}} = \frac{V}{F}. \quad (2.22)$$

2.4 Interactions of Electromagnetic Radiation and Single Particles

When an EM wave impinges on a single particle, plenty of distinct phenomena take place (e.g., scattering, absorption, thermal emission). The particle converts part of the energy of the EM wave into other forms of energy (e.g., heat); the remaining amount is redistributed in all directions. These phenomena are called absorption and scattering, respectively. Scattering may change the polarization state of the incident EM wave. Absorption may further cause thermal emission (radiation emission in all directions and frequencies), in case the absolute temperature of the particle is non-zero. The study of the single-scattering properties of particles is vital to interpret scattering and absorption processes and track changes in the polarization state of the incident EM wave.

An object with a refractive index different from the adjacent medium is employed to describe the scattering behavior of a single particle.

2.4.1 Amplitude Scattering Matrix

The geometric configuration for the scattering of an EM wave by a finite scattering object is illustrated in Figure 2.3. The reference plane defined by the incident and scattering directions is denoted as the scattering plane. The angle between the incident and the scattering directions is the scattering angle ϑ , and φ is the scattering azimuth angle relating the scattering plane to the reference direction. The incident electric field vector (subscript "inc"), may be decomposed into a parallel and a perpendicular components:

$$\vec{\mathbf{E}}_{\text{inc}} = E_{\parallel\text{inc}} \cdot \hat{\mathbf{e}}_{\parallel\text{inc}} + E_{\perp\text{inc}} \cdot \hat{\mathbf{e}}_{\perp\text{inc}}. \quad (2.23)$$

Then, the scattered electric field vector $\vec{\mathbf{E}}_{\text{sca}}$ (subscript "sca") at a distance r (observation position) is associated with the two components of the incident electric field ($E_{\parallel\text{inc}}$, $E_{\perp\text{inc}}$). Considering the far field approximation ($k \cdot r \gg 1$), the $\vec{\mathbf{E}}_{\text{sca}}$ is defined by:

$$\begin{pmatrix} E_{\parallel} \\ E_{\perp} \end{pmatrix}_{\text{sca}} = \frac{\exp[i \cdot k \cdot (r - z)]}{-i \cdot k \cdot r} \cdot \begin{pmatrix} A_{11} & A_{12} \\ A_{21} & A_{22} \end{pmatrix} \cdot \begin{pmatrix} E_{\parallel} \\ E_{\perp} \end{pmatrix}_{\text{inc}}. \quad (2.24)$$

The 2×2 matrix

$$\mathbf{IA} = \begin{pmatrix} A_{11} & A_{12} \\ A_{21} & A_{22} \end{pmatrix} \quad (2.25)$$

is the amplitude scattering matrix, describing the scattering and absorption processes. The scattering matrix elements A_{ij} ($i, j = 1, 2$), are the amplitude functions depending on the particle's shape, size, chemical composition, orientation and the λ of the incident EM field. In case of spherical particles, the number of elements is reduced to two ($A_{12} = A_{21} = 0$).

2.4.2 Transformation Phase Matrix

Considering the far field approximation ($k \cdot r \gg 1$), the scattered Stokes vector \vec{S}_{sca} is derived from the incident Stokes vector \vec{S}_{inc} , applying the following transformation:

$$\vec{S}_{\text{sca}} = \mathbf{Z} \cdot \vec{S}_{\text{inc}}. \quad (2.26)$$

Where \mathbf{Z} is the 4×4 transformation phase matrix. The phase matrix elements Z_{ij} ($i, j = 1, 4$), are expressed in terms of the amplitude scattering matrix. Albeit all the sixteen elements are non-zero, only nine independent relations among them exist; seven independent phase matrix elements exist (Mishchenko et al., 2002).

The transformation phase matrix is the link between the incident and the scattered Stokes vectors defined by their local meridional planes. Instead of \mathbf{Z} , the scattering phase matrix \mathbf{P} is often used:

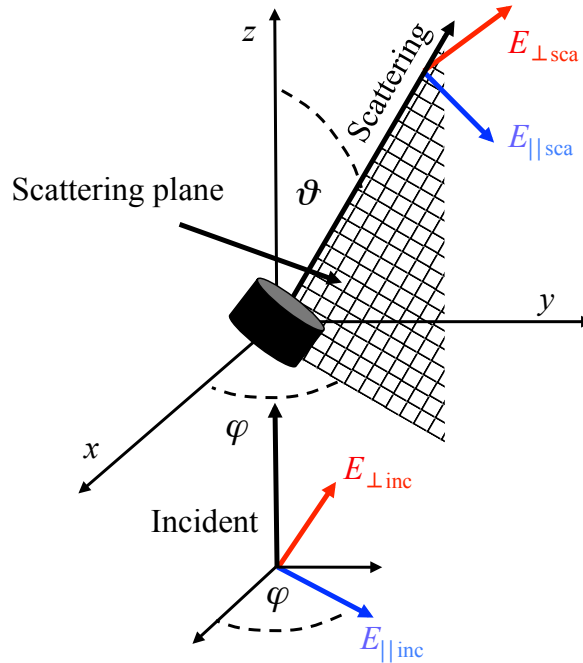


Figure 2.3: Illustration of scattering of an EM wave by an object.

$$\mathbf{P} = \begin{pmatrix} P_{11} & P_{12} & P_{13} & P_{14} \\ P_{21} & P_{22} & P_{23} & P_{24} \\ P_{31} & P_{32} & P_{33} & P_{34} \\ P_{41} & P_{42} & P_{43} & P_{44} \end{pmatrix}. \quad (2.27)$$

\mathbf{P} describes the single-scattering process of EM radiation by a particle with respect to a specific orientation. It is defined with respect to the scattering plane, defined by the incident and the scattering directions (see Figure 2.3). In case of forward scattering ($\vartheta = 0$):

$$\mathbf{P} = \mathbf{Z}. \quad (2.28)$$

More information about their relation is given in Subsection 3.2.4.

2.4.3 Single-Scattering Optical Properties

Single-scattering properties of particles in the atmosphere (gas molecules, cloud, and aerosol particles) that are crucial for radiative transfer theory are the extinction cross section C_{ext} , the single-scattering albedo $\tilde{\omega}$ and the scattering phase function \mathcal{P} . These parameters are derived from the mass/cross-section area, the spectral complex index of refraction \tilde{n} , the aerosol particle size distribution, as well as the shape, size, orientation and chemical composition.

The optical cross sections (in units of m^2), namely the extinction cross section C_{ext} , the scattering cross section C_{sca} , and the absorption cross section C_{abs} , describe how effective an individual particle interacts with EM radiation.

The radiant energy flux scattered by an individual particle, Φ_{sca} , is analogous to the incident flux density F_{inc} :

$$\Phi_{\text{sca}} = C_{\text{sca}} \cdot F_{\text{inc}}. \quad (2.29)$$

Likewise, in case of absorption radiant energy flux absorbed, Φ_{abs} , is defined:

$$\Phi_{\text{abs}} = C_{\text{abs}} \cdot F_{\text{inc}}. \quad (2.30)$$

The combination of scattering and absorption cross sections gives the extinction cross section, defining the attenuation of the F_{inc} due to scattering and absorption:

$$C_{\text{ext}} = C_{\text{sca}} + C_{\text{abs}}. \quad (2.31)$$

The ratio of C_{sca} to C_{ext} denotes the dimensionless particle single-scattering albedo $\tilde{\omega}$:

$$\tilde{\omega} = \frac{C_{\text{sca}}}{C_{\text{sca}} + C_{\text{abs}}}. \quad (2.32)$$

In other words, $\tilde{\omega}$ describes the fraction of incident radiation that is attenuated due to scattering over extinction. $\tilde{\omega}$ of 0 indicates non-scattering particles (extinction only due to absorption); conversely, $\tilde{\omega}$ of 1 implies non-absorbing particles (extinction only due to scattering).

In scalar radiative transfer theory, the phase function \mathcal{P} , which represents the relative angular distribution of the scattered radiation by a particle, is adequate to describe the scattering behavior. Let $\hat{\mathbf{k}}_{\text{inc}}(\theta_{\text{inc}}, \phi_{\text{inc}})$ be the incident direction, $\hat{\mathbf{k}}_{\text{sca}}(\theta_{\text{sca}}, \phi_{\text{sca}})$ the scattering direction, and $\mu = \cos \theta$. Then, \mathcal{P} is given by:

$$\int_0^{2\pi} \int_{-1}^1 \mathcal{P}(\mu_{\text{inc}}, \phi_{\text{inc}}; \mu_{\text{sca}}, \phi_{\text{sca}}) d\mu d\phi = 4\pi \text{ sr}. \quad (2.33)$$

The integral of the scattering phase function over the unit sphere is normalized to 4π . For randomly oriented particles, the scattering domain is characterized as macroscopically isotropic, meaning that there is no favored propagation direction. As a result, \mathcal{P} depends only on the scattering angle, ϑ , with respect to the incident direction, omitting any azimuthal angular dependence:

$$\vartheta = \arccos(\hat{\mathbf{k}}_{\text{inc}} \cdot \hat{\mathbf{k}}_{\text{sca}}). \quad (2.34)$$

ϑ ranges between 0 and π .

Other parameters applied in radiative transfer theory (for axially rotational symmetric scattering) are the asymmetry parameter g and the hemispheric backscatter ratio b . g is defined as:

$$g = \int_{4\pi} \mathcal{P}(\vartheta) \cdot \cos \vartheta d^2\Omega. \quad (2.35)$$

g ranges between -1 and $+1$. It is a measure for the preferred scattering direction, meaning that the more negative g is, the more radiation is scattered towards the back direction; conversely, the more positive g is, the more radiation is directed to the forward direction.

The hemispheric backscatter ratio or just backscatter ratio is the fraction of the scattered radiation directed towards the backward hemisphere. It is given by:

$$b = \frac{\int_{\pi/2}^{\pi} \mathcal{P}(\vartheta) \cdot \sin \vartheta d\theta}{\int_0^{\pi} \mathcal{P}(\vartheta) \cdot \sin \vartheta d\theta}. \quad (2.36)$$

2.5 Interactions of Electromagnetic Radiation and Ensembles of Independent Particles

Consider a population of particles (i.e., gas molecules, aerosol and cloud particles) contained in a sufficiently small volume element. The volumetric scattering properties are derived by the single-scattering properties assuming scattering by independent scatterers. The following approximations are considered:

- Individual particles are independent of each other with respect to their optical effects
- Scattering by independent particles is incoherent

2.5.1 Single-Scattering Approximation

Assume that the small volume element consists of N particles. N is sufficiently small, so that each particle is in the far-field zone of all other particles and multiple-scattering within the volume is negligible. In addition, the scattered EM radiation linked to the particles is incoherent. Consequently, the electric field scattered by the volume (at some large distance) is derived by the vector sum of the partial scattered field by the individual particles (Mishchenko et al., 2002):

$$\vec{\mathbf{E}}_{\text{sca}} = \sum_{j=1}^N \vec{\mathbf{E}}_{\text{sca},j} \quad (2.37)$$

Considering the far field approximation ($k \cdot r \gg 1$), the total volumetric amplitude scattering matrix is:

$$\mathbf{IA}(\hat{\mathbf{k}}, \hat{\mathbf{k}}_{\text{inc}}) = \sum_{j=1}^N \mathbf{IA}_j(\hat{\mathbf{k}}, \hat{\mathbf{k}}_{\text{inc}}) \quad (2.38)$$

The optical properties of the volume, namely the spectral volumetric extinction β_{ext} , scattering β_{sca} and absorption coefficients β_{abs} (in units of m^{-1}), are determined by:

$$\beta_{\text{ext}} = \sum_{j=1}^N (C_{\text{ext}})_j = N \langle C_{\text{ext}} \rangle, \quad (2.39)$$

$$\beta_{\text{sca}} = \sum_{j=1}^N (C_{\text{sca}})_j = N \langle C_{\text{sca}} \rangle, \quad (2.40)$$

$$\beta_{\text{abs}} = \sum_{j=1}^N (C_{\text{abs}})_j = N \langle C_{\text{abs}} \rangle. \quad (2.41)$$

Where $\langle C_{\text{ext}} \rangle$, $\langle C_{\text{sca}} \rangle$, and $\langle C_{\text{abs}} \rangle$ are the average extinction, scattering, and absorption cross sections per particle, respectively. The optical thickness τ of an optical medium is derived by integrating over β_{ext} between medium base z_{base} and medium top z_{top} :

$$\tau = \int_{z_{\text{base}}}^{z_{\text{top}}} \beta_{\text{ext}}(z') dz'. \quad (2.42)$$

In a similar manner the volumetric scattering and phase matrices are derived by:

$$\mathbf{P} = \sum_{j=1}^N \mathbf{P}_j = N \langle \mathbf{P} \rangle, \quad (2.43)$$

$$\mathbf{Z} = \sum_{j=1}^N \mathbf{Z}_j = N \langle \mathbf{Z} \rangle, \quad (2.44)$$

where $\langle \mathbf{P} \rangle$ and $\langle \mathbf{Z} \rangle$ are the average scattering and phase matrices per particle.

2.5.2 Ensembles of Particles

In practice, the volume element consists of particles with different sizes, refractive indices, and shapes. Thus, the volumetric scattering properties are derived by averaging the single-scattering properties over the distribution of particles. Eqs. (2.37) - (2.44) are replaced by the ensemble averages. For example, the ensemble averaged transformation phase matrix is given by:

$$\langle \mathbf{Z} \rangle = \sum_{j=1}^N n_j \cdot \langle \mathbf{Z}_j \rangle. \quad (2.45)$$

Where $\langle \mathbf{Z}_j \rangle$ is the individual phase matrix and n_j is the particle number density (weight).

2.6 Normalized Scattering and Phase Matrices

For practical reasons, instead of the regular scattering and phase matrices the normalized matrices are employed:

$$\tilde{\mathbf{P}} = \frac{4\pi}{\beta_{\text{sca}}} \mathbf{P} = \frac{4\pi}{\langle \beta_{\text{sca}} \rangle} \langle \mathbf{P} \rangle, \quad (2.46)$$

$$\tilde{\mathbf{Z}} = \frac{4\pi}{\beta_{\text{sca}}} \mathbf{Z} = \frac{4\pi}{\langle \beta_{\text{sca}} \rangle} \langle \mathbf{Z} \rangle, \quad (2.47)$$

The first element of the dimensionless normalized scattering matrix corresponds to the scattering phase function $\tilde{P}_{11} = \mathcal{P}$.

2.7 Vector Radiative Transfer Equation

When the scattering and absorbing media consist of a very large number of particles, multiple-scattering can no longer be neglected. The propagation of an EM wave through the atmosphere and its interaction with the atmospheric components (e.g., molecules, aerosol particles, and cloud particles) and/or the surface is described by the vector radiative transfer

equation. Considering the complexity of such media (atmosphere), this equation is usually simplified to macroscopically isotropic and mirror-symmetric scattering media. These media involve randomly oriented particles; each particle is mirror-symmetric or has a mirror-symmetric counterpart. In this case, the scattering matrix depends only on the scattering angle, ϑ , with respect to the incident direction, omitting any azimuthal angular dependence; there is no favored propagation direction or orientation of the scattering plane.

The integro-differential monochromatic vector radiative transfer equation for the Stokes vector of the EM wave ($\vec{\mathbf{S}}$) emergent from below a layer (see Figure 2.4), considering a plane-parallel atmosphere and macroscopically isotropic and symmetric media (randomly oriented particles), is given by (Liou, 2002):

$$\begin{aligned} \mu_{\text{det}} \frac{d\vec{\mathbf{S}}(\tau; \mu_{\text{det}}, \phi_{\text{det}})}{d\tau} = & -\vec{\mathbf{S}}(\tau; \mu_{\text{det}}, \phi_{\text{det}}) \\ & + \frac{\tilde{\omega}}{4\pi} \int_0^{2\pi} \int_{-1}^1 \tilde{\mathbf{Z}}(\mu_{\text{inc}}, \phi_{\text{inc}}; \mu_{\text{det}}, \phi_{\text{det}}) \cdot \vec{\mathbf{S}}(\tau; \mu_{\text{inc}}, \phi_{\text{inc}}) d\mu_{\text{inc}} d\phi_{\text{inc}} \\ & + \frac{\tilde{\omega}}{4\pi} \cdot \tilde{\mathbf{Z}}(-\mu_0, \phi_0; \mu_{\text{det}}, \phi_{\text{det}}) \cdot F_0 \cdot \begin{pmatrix} 1 \\ 0 \\ 0 \\ 0 \end{pmatrix} \cdot e^{-\tau/\mu_0} \\ & + (1 - \tilde{\omega}) \cdot B_\lambda(T) \cdot \begin{pmatrix} 1 \\ 0 \\ 0 \\ 0 \end{pmatrix}. \end{aligned} \quad (2.48)$$

Where μ is the cosine of the zenith angle θ . $(\mu_{\text{det}}, \phi_{\text{det}})$ stands for the viewing direction (detector direction, subscript "det"), $(\mu_{\text{inc}}, \phi_{\text{inc}})$ for the incident direction, and $(-\mu_0, \phi_0)$ is the downward solar direction. The equation consists of four self-explanatory terms:

$$\text{Loss by extinction} = -\vec{\mathbf{S}}(\tau; \mu_{\text{det}}, \phi_{\text{det}}). \quad (2.49)$$

This term denotes the extinction of $\vec{\mathbf{S}}$ of the EM wave due to attenuation (scattering and absorption by the atmospheric components) along the optical path towards the direction of the detector $(\mu_{\text{det}}, \phi_{\text{det}})$.

$$\text{Gain by multiple-scattering} = \frac{\tilde{\omega}}{4\pi} \int_0^{2\pi} \int_{-1}^1 \tilde{\mathbf{Z}}(\mu_{\text{inc}}, \phi_{\text{inc}}; \mu_{\text{det}}, \phi_{\text{det}}) \cdot \vec{\mathbf{S}}(\tau; \mu_{\text{inc}}, \phi_{\text{inc}}) d\mu_{\text{inc}} d\phi_{\text{inc}}. \quad (2.50)$$

This term represents the gain due to multiple-scattering of the diffuse $\vec{\mathbf{S}}$ from all the different initial directions $(\mu_{\text{inc}}, \phi_{\text{inc}})$ scattered into the direction of observation $(\mu_{\text{det}}, \phi_{\text{det}})$. $\tilde{\mathbf{Z}}$ is the normalized transformation phase matrix that describes the scattering procedure. This matrix will be explained in Subsection 3.2.4 for macroscopically isotropic and mirror-symmetric

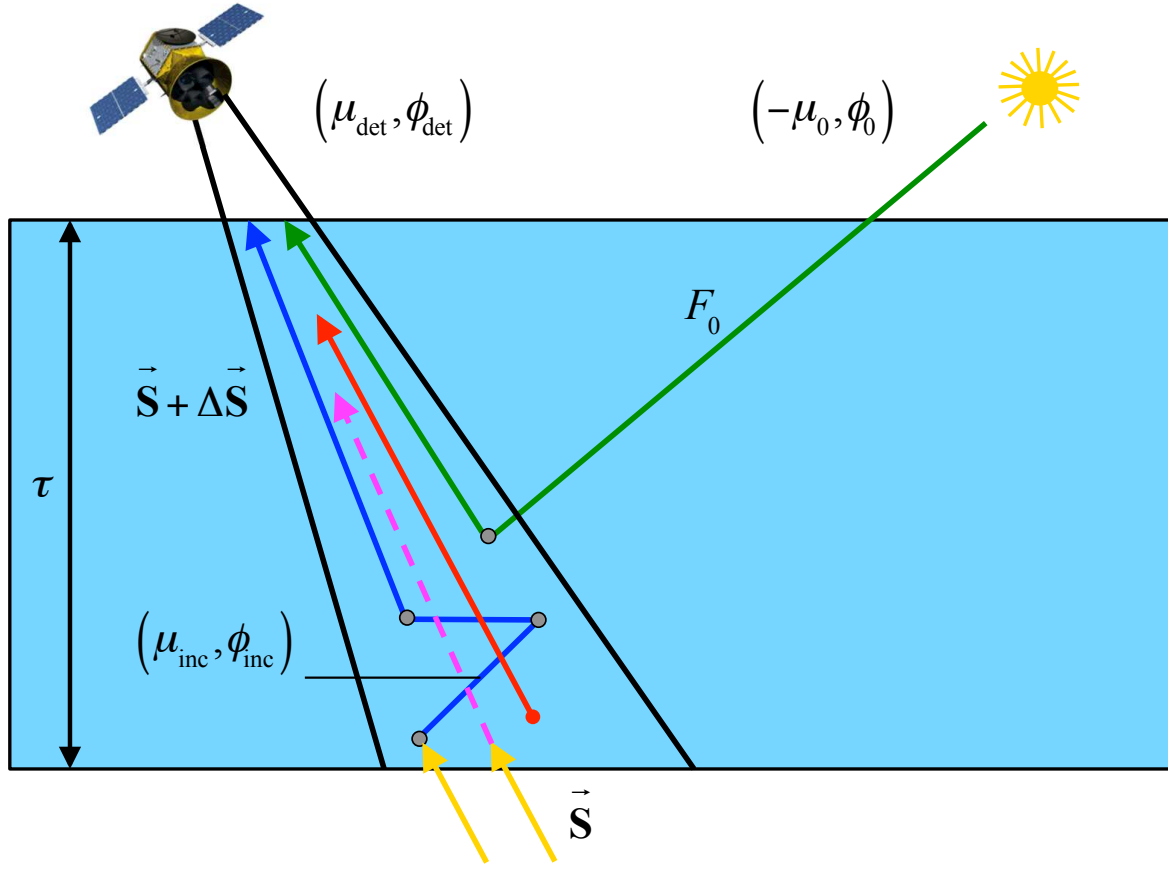


Figure 2.4: Transfer of diffuse Stokes vector of the EM wave, \vec{S} , emergent from below a layer: **Loss by extinction** owing to attenuation along the optical path towards $(\mu_{\text{det}}, \phi_{\text{det}})$; **gain by multiple-scattering** from all directions $(\mu_{\text{inc}}, \phi_{\text{inc}})$ to $(\mu_{\text{det}}, \phi_{\text{det}})$; **gain by single-scattering** of the incident unpolarized extraterrestrial quasi-monochromatic electromagnetic radiation (solar irradiance) from direction $(-\mu_0, \phi_0)$ to $(\mu_{\text{det}}, \phi_{\text{det}})$; and **gain by emission** within the layer directed into $(\mu_{\text{det}}, \phi_{\text{det}})$.

scattering media. Absorption is governed by the single-scattering albedo ω_0 and the division by 4π accounts for the normalization within the solid angle of 4π sr.

$$\text{Gain by single-scattering} = \frac{\tilde{\omega}}{4\pi} \cdot \tilde{\mathbf{Z}}(-\mu_0, \phi_0; \mu_{\text{det}}, \phi_{\text{det}}) \cdot F_0 \cdot \begin{pmatrix} 1 \\ 0 \\ 0 \\ 0 \end{pmatrix} \cdot e^{-\tau/\mu_0}. \quad (2.51)$$

The \vec{S} increases owing to single-scattering of the incident unpolarized extraterrestrial quasi-monochromatic electromagnetic radiation (solar irradiance) from the direction $(-\mu_0, \phi_0)$ to $(\mu_{\text{det}}, \phi_{\text{det}})$. Consequently, F_0 is attenuated exponentially along the photon path, according to the law of Bouguer–Beer.

$$\text{Gain by emission} = (1 - \tilde{\omega}) \cdot B_\lambda(T) \cdot \begin{pmatrix} 1 \\ 0 \\ 0 \\ 0 \end{pmatrix}. \quad (2.52)$$

This term denotes the thermal emission. The \vec{S} of the EM wave directed into $(\mu_{\text{det}}, \phi_{\text{det}})$ is enhanced by emission within the layer. It is driven by the law of Stefan–Boltzmann, referring to a perfect blackbody in thermodynamic equilibrium for which absorption and emission at every wavelength are identical. The amount of the diffuse \vec{S} absorbed is determined by $(1 - \tilde{\omega})$. Thermal emission is described by the unpolarized Planck blackbody matrix $B_\lambda(T) \cdot (1000)^T$ (superscript "T" represents the transpose vector). $B_\lambda(T)$ is the Planck's function, in units of $\text{W m}^{-2} \text{sr}^{-1} \mu\text{m}^{-1}$, given by:

$$B_\lambda(T) = \frac{2h \cdot c^2}{\lambda^5} \frac{1}{\exp[h \cdot c / (k_B \cdot \lambda \cdot T)] - 1}, \quad (2.53)$$

where $h = 6.6262 \times 10^{-34} \text{ J s}$ is the Planck's constant, $c = 2.997925 \times 10^8 \text{ m s}^{-1}$ is the velocity of light in vacuum, $k_B = 1.3806 \times 10^{-23} \text{ J deg}^{-1}$ is the Boltzmann constant, λ is the wavelength in m, and T is the absolute temperature given in K.

Note that the source term of thermal emission is neglected in the solar spectral region (0.2–5 μm), and, therefore, will not be considered in this work.

2.8 Numerical Methods to Solve the Radiative Transfer Equation

In order to solve the vector radiative transfer equation for complex scattering and absorbing atmospheric conditions several numerical methods have been developed. The comprehensive description of the methods employed to calculate the multiple-scattering of polarized light is beyond the scope of this work. However, we will briefly outline the elementary concept of the most common methods:

- Adding–Doubling Method (A–DM)
- Method of Successive Order of Scattering (MSOS)
- Discrete Ordinate Method (DOM)
- Spherical Harmonics Method (SHM)
- Monte Carlo Method (MCM)

For further information the reader is referred to the literature (e.g., Hovenier et al., 2004).

2.8.1 Adding–Doubling Method (A–DM)

The original idea of the adding method dates back to Stokes (1860). However, the adding method, in the framework it is known now, is linked to the work of van de Hulst (1980). In

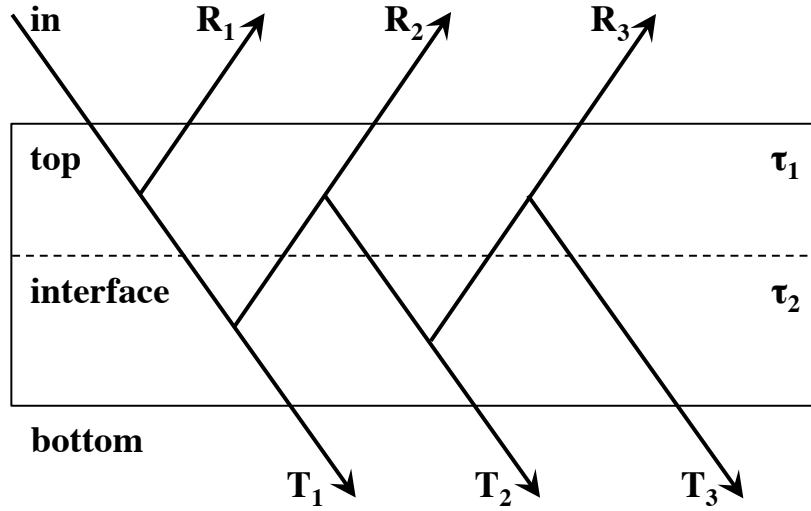


Figure 2.5: A schematic representation of the adding–doubling procedure. Configuration for radiation beam through two homogeneous, stacked layers of optical depths τ_1 and τ_2 and a black underlying surface. The overall reflected and transmitted radiation are symbolized by R and T , respectively.

addition, Hansen (1971a,b) further extended the method so that it can handle the polarization state of the EM radiation.

Following the comprehensive description by van de Hulst (1980), the radiative properties of a medium can be calculated assuming a plane–parallel atmosphere divided into stacks of thin layers with known properties (namely the reflection and transmission). The principle of this technique is illustrated in Figure 2.5. To put it more simply, imagine that there are two layers with optical depths of τ_1 and τ_2 , one of which overlies the other. When the reflection and transmission for both layers are well–defined and for thin initial layers the reflection and transmission is given in analytical form from the single–scattering approximation, the overall reflection and transmission can be determined by calculating successive reflections back and forth between the layers (Hansen and Travis, 1974; Wendisch and Yang, 2012). Particularly, if both layers are characterized by the same properties, the adding method is referred to as the doubling method.

2.8.2 Method of Successive Order of Scattering (MSOS)

The employment of the Method of Successive Order of Scattering (MSOS) involves an atmosphere divided into optically thin layers. It is an iterative method, where the multiple–scattering of each layer is treated as a series of single–scattering events. Basically, MSOS accounts the contribution from all orders of scattering to the total radiation (Hansen and Travis, 1974). The larger the number of the scattering events, the smaller its contribution to the total radiation (because of extinction). Moreover, the numerical integration for the diffuse radiation is carried out utilizing the decomposition in Fourier modes (Wendisch and Yang, 2012) and infinite modes should lead to convergence.

The main disadvantage of MSOS lies on its principle. While being a straightforward method,

it becomes inefficient for complex atmospheres with high optical thickness and rather weak absorption. In such cases, the number of orders needed to achieve convergence is excessively high and the computation time is increasing dramatically.

2.8.3 Discrete Ordinate Method (DOM)

The concept of the Discrete Ordinate Method (DOM) is traced back to the work of Schuster (1905) and Schwarzschild (1906) and their description of the two-stream technique. Later on, Wick (1943), followed by Chandrasekhar (1960), further extended the technique resulting in the method with n discrete ordinates.

DOM involves a Fourier decomposition of the radiative transfer equation and employs a Gaussian quadrature sum (using $2n$ discretized, namely the number of streams). As a consequence, the integro-differential form is discretized into standard differential equations of first order over τ by substituting the integrals over the direction cosines by a finite sum. By simulating the atmosphere as a stack of homogeneous layers a set of first order differential equations is derived with consistent optical properties (including the surface contribution) (Hovenier et al., 2004). The latter procedure is iterated in order to achieve convergence.

The primary advantage of the DOM is that the computational efforts are independent of the optical depth. However, the computation time increases with increasing vertical resolution. Another drawback is that the method itself relies heavily on mathematics and is difficult to program (Hansen and Travis, 1974). DOM is impractical for strongly peaked phase matrices, when high angular resolution is needed.

2.8.4 Spherical Harmonics Method (SHM)

Another efficient method to solve the vector radiative transfer equation, closely related to the DOM, is the Spherical Harmonic Method (SHM). According to the SHM, the radiance field is decomposed to a finite number of spherical harmonics (Hansen and Travis, 1974). In comparison to DOM, only the decomposition of the azimuth dependence is required and, therefore, the computation time does not increase for strongly peaked phase matrices. Knowing the close relation between DOM and SHM, benchmark calculations of both approaches may generate identical results (Zdunkowski et al., 2007).

For the scalar radiative transfer equation, SHM was first introduced by Davison and Sykes (1957) and Lenoble (1961). Later on, it was further extended to include polarization by Benassi et al. (1985) and Garcia and Siewert (1986). The latest contribution is linked to the work of Evans (1998), who developed the spherical harmonics discrete ordinate method (SHDOM) model, which is applicable to 3D media. Lately, polarization was included to SHDOM utilizing the generalized spherical harmonics method of Doicu et al. (2013).

2.8.5 Monte Carlo Method (MCM)

The statistical Monte Carlo technique was first developed in the 1940's by Metropolis and Ulam (1949). Thereafter, a rapidly growing literature on MCMs appeared

(Cashwell and Everett, 1959; Kattawar and Plass, 1967; Collins et al., 1972; Marchuk et al., 1980; Mayer, 2009). The MCM is based on probability theory and random sampling to produce numerical results.

The Monte Carlo technique is considered a flexible approach to simulate photon transport. Here, photons refer to imaginary discrete "packets" or "units" of the incident energy rather than the physical photons (quantum electrodynamics) (Mishchenko, 2009). In brief, the MCM goes as follows: a large number of photons are generated from a source (sun) and traced throughout their propagation in a scattering and absorbing medium (atmosphere) until a scattering event takes place. The nature of interaction is determined and the new direction of propagation is calculated using the scattering phase function as the probability density function for sampling. The photon is terminated when it is absorbed or exits the scattering media.

The main advantages of the MCM are:

- It is based on conceptually simple physics and is simple to program.
- It is time-dependent and can handle 3D problems with arbitrary geometry.
- It calculates both vector and scalar results at the same time.
- Detectors can be placed at any position and in any direction.

The weaknesses of MCM are:

- Since the calculation is statistical, results are always subject to statistical uncertainty, given by the inverse square root of the number of photons used for the simulations. Increasing the selected number of photons will ameliorate the errors.
- For scattering media with large optical depths, the method requires long computation times.

In this thesis, the method employed to solve the vector radiative transfer equation is the Monte Carlo technique. A comprehensive description of the MCM is found in Chapter 3.

2.9 Existing Vector Radiative Transfer Models

Several 1D and 3D radiative transfer models have been developed to simulate radiative transfer. In most cases, the 1D vector models are freely available for the scientific community, the same does not generally hold for 3D radiative transfer models. Table 2.1 lists the most commonly used vector radiative transfer models and tabulates their basic features. The methods employed to solve the radiative transfer equation, as well as their availability and references are included. Most of the models employ the DOM and can be used for 1D atmospheres (e.g., ARTS, IPOL, MVDOM, Pstar, SCIATRAN, VDISORT). Two models (DAK and PolRadTran) utilize the A-DM (limited to 1D applications). The SOSM, SHM and MCM can be used for both 1D and 3D atmospheres, with the latter one being the most flexible.

Table 2.1: Overview on the most commonly used vector radiative transfer models. Their methodology, geometry, availability and references are summarized. GPL stands for the GNU General Public License. Abbreviations: ARTS - Atmospheric Radiative Transfer Simulator, DAK - Doubling-Adding KNMI (Koninklijk Nederlands Meteorologisch Instituut), IPOL - Intensity and POLarization, MVDOM - Modified Vectorial Discrete Ordinates Method, MYSTIC - Monte-Carlo code for the phYSically correct Tracing of photons In Cloudy atmospheres, PolRadTran - Polarized Radiative Transfer, Pstar - Polarized radiance System for Transfer of Atmospheric Radiation, SCIATRAN - radiative transfer model for SCIAMACHY (SCanning Imaging Absorption SpectroMeter for Atmospheric CHartography), SOSVRT - Successive Order of Scattering Vector Radiative Transfer model, VDISORT - Vector DIScrete Ordinate Radiative Transfer model, 3DMCPOL - Three-dimensional polarized Monte Carlo atmospheric radiative model, 6SV1 - Second Simulation of a Satellite Signal in the Solar Spectrum, Vector, version 1.

Model	Method	Geometry	References	Availability
ARTS	1D DOM 3D MCM	1D/3D	Buehler et al. (2005)	GPL
DAK	A-DM	1D	Stammes et al. (1989)	no
IPOL	DOM	1D	Korkin et al. (2013) ftp://climate1.gsfc.nasa.gov/skorkin/IPOL/	yes
MVDOM	DOM	1D	Budak and Korkin (2008) Kokhanovsky et al. (2010)	yes
MYSTIC	MCM	1D/3D	Mayer (2009) Emde et al. (2010)	1D - GPL
PolRadTran	A-DM	1D	Evans and Stephens (1991)	yes
Pstar	DOM	1D	Ota et al. (2010)	yes
SCIATRAN	DOM	1D	Rozanov et al. (2005) Rozanov and Kokhanovsky (2006) Rozanov et al. (2014)	yes
SHDOM	SHM/DOM	1D/3D	Evans (1998)	yes
SOSVRT	SOS	1D	Min and Duan (2004) Duan et al. (2010)	yes
VDISORT	DOM	1D	Weng (1992a) Weng (1992b) Schulz et al. (1999)	yes
3DMCPOL	MCM	1D/3D	Cornet et al. (2010) Fauchez et al. (2014)	no
6SV1	SOS	1D	Kotchenova et al. (2006) http://6s.ltdri.org	yes

3 SPARTA – Solver for Polarized Atmospheric Radiative Transfer Applications

In this chapter, the basic concepts and definitions of a new three-dimensional vector radiative transfer model SPARTA (Solver for Polarized Atmospheric Radiative Transfer Applications) are introduced. The model employs the forward Monte Carlo technique for efficient column-response, pixel-based radiance calculations including polarization for 3D inhomogeneous cloudless and cloudy atmospheres. SPARTA is based on the scalar Monte Carlo model of the Leibniz Institute of Marine Sciences (now GEOMAR) at the UNiversity of Kiel (MC-UNIK, Macke et al. 1999), which participated in the international Intercomparison of 3D Radiation Codes (I3RC, Cahalan et al. 2005). In this thesis, MC-UNIK has been extended to account for polarization effects due to multiple-scattering by non-spherical particles, i.e., coarse mode dust or ice particles. The details of the implementation of polarization in MC-UNIK are also presented; the differences between MC-UNIK and SPARTA are outlined. Parts of this chapter, have been published in Barlakas et al. (2014) and Barlakas et al. (2016).

3.1 Monte Carlo Random Sampling

The Monte Carlo method is based on probability theory and random sampling to produce numerical results. Following the comprehensive description by Cashwell and Everett (1959), the fundamental principle of the Monte Carlo method involves sampling a random variable $\psi \in (\psi_1, \psi_2)$ from a well-defined probability density function (PDF) $p(\psi)$ utilizing uniformly distributed random numbers over the interval $(0, 1)$. Let $p(\psi) d\psi$ be the probability of ψ lying between ψ and $\psi + d\psi$, and $\psi_1 \leq \psi < \psi_2$, then, the PDF is a normalized density function satisfying the following normalization:

$$\int_{\psi_1}^{\psi_2} p(\psi) d\psi = 1. \quad (3.1)$$

In order to sample a variable ψ from a PDF $p(\psi)$, the cumulative probability density function, denoted as $G(\psi)$, is defined by:

$$G(\psi) = \frac{\int_{\psi_1}^{\psi} p(\psi') d\psi'}{\int_{\psi_1}^{\psi_2} p(\psi') d\psi'}. \quad (3.2)$$

Hence, ψ is sampled by drawing a uniformly distributed random number ξ ($0 \leq \xi < 1$) and inverting G :

$$\psi = G^{-1}(\xi). \quad (3.3)$$

3.2 SPARTA Description

3.2.1 Model Domain

SPARTA considers a 3D Cartesian domain, which is split into grid-boxes, defined by geometrical dimensions along x -, y -, and z -directions. A total volumetric extinction $\beta_{\text{ext}}^{\text{tot}}$ and scattering coefficient $\beta_{\text{sca}}^{\text{tot}}$ (see Eqs. 2.39 and 2.40), a total normalized scattering phase matrix $\tilde{\mathbf{P}}^{\text{tot}}(\vartheta)$ with the scattering angle ϑ , and a total single-scattering albedo $\tilde{\omega}^{\text{tot}}$ are allocated to each grid-box. The superscript "tot" indicates the combined optical properties of the different types of particles (e.g., molecules, aerosol, and cloud particles), which are contained in each grid-box. A 2D representation of the model domain is illustrated in Figure 3.1.

Directions are specified by means of the angles θ and ϕ (Hovenier et al., 2004; Mishchenko et al., 2002). The azimuth angle ϕ is counted clockwise when looking upwards (positive z -direction) and the zenith angle θ is the angle with respect to the upward normal direction (measured from the positive z -direction). As a consequence, the viewing zenith angle θ_{det} is measured from the upward normal, meaning it ranges between 0° and 90° for the reflected, and between 90° and 180° for the transmitted EM radiation.

Note that SPARTA can be used as a 1D radiative transfer model performing independent pixel by pixel simulations by simply fixing the x - and y - geometrical components of the photons to the initial values preventing the horizontal photon transport between the pixels; the horizontal inhomogeneity is considered. This scheme is denoted as IPA mode. In addition, the model can run in a 2D mode accounting for the variability in only one horizontal direction (x or y).

3.2.2 Photon Initiation

Simulations begin with a photon entering randomly at the top layer of the model domain. The initial incident direction (subscript "inc") is expressed in terms of the solar position with a direction derived from the directional cosines:

$$\hat{\mathbf{k}}_{\text{inc},0} = \begin{pmatrix} k_{\text{inc},0}^x \\ k_{\text{inc},0}^y \\ k_{\text{inc},0}^z \end{pmatrix} = \begin{pmatrix} \sin \theta_0 \cdot \cos \varphi_0 \\ \sin \theta_0 \cdot \sin \varphi_0 \\ -\cos \theta_0 \end{pmatrix}, \quad (3.4)$$

where θ_0 and φ_0 are the solar zenith and azimuth angles, respectively.

In the vector scheme, the incident quasi-monochromatic electromagnetic wave is considered unpolarized and characterized by a weight, the Stokes weight, whose value is set originally to unity:

$$\vec{\mathbf{S}}_{\text{inc},0} = \begin{pmatrix} 1 \\ 0 \\ 0 \\ 0 \end{pmatrix}. \quad (3.5)$$

3.2.3 Photon Tracing and Absorption

In the Monte Carlo technique the propagation of photons through a medium is traced until they either leave the model domain at the top of the atmosphere (TOA) or until they are absorbed. In case a photon reaches the edge of the domain, periodic boundary conditions are applied, meaning the photon re-enters the domain from the exact opposite side preserving its directional vector and conserving energy. Following Marchuk et al. (1980), the free path lengths of a photon are simulated by random number processes with attenuation described by

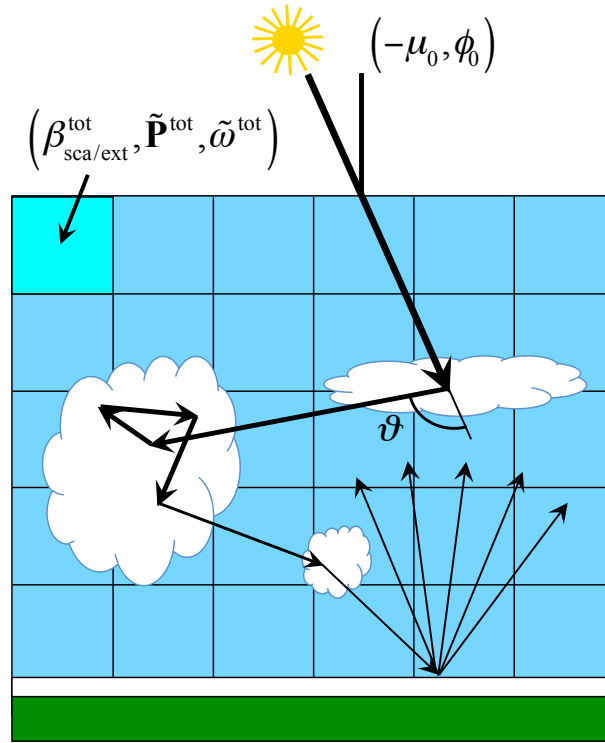


Figure 3.1: 2D representation of the scheme of the photon path within the 3D domain of the Monte Carlo radiative transfer model: $(-\mu_0, \phi_0)$ is the initial incident photon direction (downward solar direction) defined by the cosine of the solar zenith ($\mu_0 = \cos \theta_0$) and azimuth angles (ϕ_0), $\beta_{\text{sca/ext}}^{\text{tot}}$ stands for either the total volumetric scattering (subscript "sca") or extinction coefficient (subscript "ext"), $\tilde{\mathbf{P}}^{\text{tot}}$ for the total normalized scattering phase matrix, and $\tilde{\omega}^{\text{tot}}$ is the total single-scattering albedo. The superscript "tot" indicates the combined optical properties of the different types of particles which are contained in each grid-box.

the law of Bouguer–Beer. In the original MC-UNIK model, the later procedure is quantified by the probability density function:

$$p_{\text{ext}} = \exp \left(- \int_0^l \beta_{\text{ext}}^{\text{tot}} dl \right). \quad (3.6)$$

$\beta_{\text{ext}}^{\text{tot}}$ is the total volumetric extinction coefficient and dl is the path element of the photon path. At each scattering event, absorption is considered by reducing the original scalar weight by multiplication with the single-scattering albedo. In SPARTA, the free path length is determined by the total volumetric scattering coefficient ($\beta_{\text{sca}}^{\text{tot}}$) and the probability density function is given by:

$$p_{\text{sca}} = \exp \left(- \int_0^l \beta_{\text{sca}}^{\text{tot}} dl \right). \quad (3.7)$$

Absorption is taken into account by decreasing the initial Stokes weight by the estimated total absorption coefficient ($\beta_{\text{abs}}^{\text{tot}}$), along the photon path, with the Bouguer–Beer law:

$$p_{\text{abs}} = \exp \left(- \int_0^l \beta_{\text{abs}}^{\text{tot}} dl \right). \quad (3.8)$$

In particular, photons are traced from the starting point on one grid-box surface to the intersection with the nearest neighbor grid-box surface as illustrated in Figure 3.2, and as outlined by Macke et al. (1999). This procedure is repeated ϱ times until the cumulated optical thickness:

$$\tau_{\text{cum}} = \sum_{\varrho} \beta_{\text{sca}}^{\text{tot}} \cdot l_{\varrho}, \quad (3.9)$$

exceeds the randomly chosen (exponentially distributed) optical thickness τ_{rand} . l_{ϱ} denotes the step lengths within the individual grid-boxes. Subsequently, the photon steps backward by:

$$l_{\text{back}} = \frac{\tau_{\text{cum}} - \tau_{\text{rand}}}{\beta_{\text{sca}}^{\text{tot}}}, \quad (3.10)$$

to ensure that the total photon path exactly matches τ_{rand} .

3.2.4 Anisotropic Scattering and Rotation of the Stokes Vector

A major difference between the scalar and the vector approach involves amendments in the scattering description. In case of a scattering event the new propagation direction (scattering direction) needs to be calculated $\hat{\mathbf{k}}_{\text{sca}}(\theta_{\text{sca}}, \phi_{\text{sca}})$ from the previous direction and the scattering zenith and azimuth angles (Marchuk et al., 1980). For scalar radiative transfer theory, the scalar scattering phase function \mathcal{P} (see Eq. 2.33), is adequate to describe the scattering

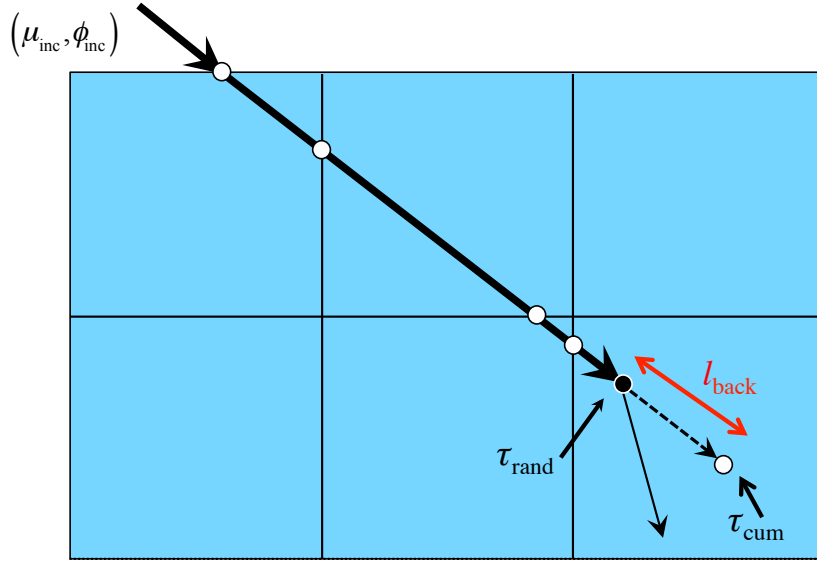


Figure 3.2: Illustration of photon tracing within a regular array of cloud boxes: (μ_{inc}, ϕ_{inc}) stands for the incident direction, τ_{rand} and τ_{cum} are the randomly chosen and the cumulated optical thickness, and l_{back} denotes the backward photon step.

process. It depends on the scattering angle (ϑ) with respect to the incident direction, omitting any azimuthal angular dependence. Polarization introduces an anisotropy of the scattering direction depending on the frame of reference. Consequently, the interaction between a photon and a particle is described by a 4×4 matrix, the normalized scattering phase matrix $\tilde{\mathbf{P}}$ (see Section 2.6). Considering an ensemble of randomly oriented particles that form a macroscopically isotropic and mirror-symmetric scattering medium, the number of scattering phase matrix elements is reduced to six (van de Hulst, 1981):

$$\tilde{\mathbf{P}}(\vartheta) = \begin{pmatrix} \tilde{P}_{11}(\vartheta) & \tilde{P}_{12}(\vartheta) & 0 & 0 \\ \tilde{P}_{12}(\vartheta) & \tilde{P}_{22}(\vartheta) & 0 & 0 \\ 0 & 0 & \tilde{P}_{33}(\vartheta) & \tilde{P}_{34}(\vartheta) \\ 0 & 0 & -\tilde{P}_{34}(\vartheta) & \tilde{P}_{44}(\vartheta) \end{pmatrix}, \quad (3.11)$$

As it was already mentioned, the scattering phase matrix is defined with respect to the scattering plane, defined by the incident and the scattering directions. Furthermore, it relates the Stokes vector elements linked to the two directions, specified with respect to their reference planes (Mishchenko et al., 2002). In order to derive the Stokes vector of the scattered EM wave $\vec{\mathbf{S}}_{sca}$ with respect to its plane of reference (plane containing the scattering and vertical directions, see Subsection 2.3.2), the incident Stokes vector (expressed in a plane defined by the incident and vertical directions) has to be transformed to the scattering plane so that the scattering phase matrix multiplication can be carried out (see Figure 3.3). The scattered Stokes vector is given by:

$$\vec{\mathbf{S}}_{sca} = \mathbf{R}(-\eta_2) \cdot \tilde{\mathbf{P}}(\vartheta) \cdot \mathbf{R}(\pi - \eta_1) \cdot \vec{\mathbf{S}}_{inc} = \tilde{\mathbf{Z}}(\theta_{inc}, \phi_{inc}; \theta_{sca}, \phi_{sca}) \cdot \vec{\mathbf{S}}_{inc}. \quad (3.12)$$

Here $\tilde{\mathbf{Z}}$ is the normalized transformation phase matrix that describes the scattering procedure, η_1 and η_2 are the rotation angles, and $\mathbf{R}(\eta)$ is the rotation matrix (see Figure 3.4):

$$\mathbf{R}(\eta) = \begin{pmatrix} 1 & 0 & 0 & 0 \\ 0 & \cos 2\eta & -\sin 2\eta & 0 \\ 0 & \sin 2\eta & \cos 2\eta & 0 \\ 0 & 0 & 0 & 1 \end{pmatrix}. \quad (3.13)$$

The rotation angles are computed from $\hat{\mathbf{k}}_{\text{inc}}$ and $\hat{\mathbf{k}}_{\text{sca}}$ using spherical trigonometry (Mishchenko et al., 2002):

$$\cos \eta_1 = \frac{\cos \theta_{\text{sca}} - \cos \theta_{\text{inc}} \cdot \cos \vartheta}{\sin \theta_{\text{inc}} \cdot \sin \vartheta}, \quad (3.14)$$

$$\cos \eta_2 = \frac{\cos \theta_{\text{inc}} - \cos \theta_{\text{sca}} \cdot \cos \vartheta}{\sin \theta_{\text{sca}} \cdot \sin \vartheta}. \quad (3.15)$$

The following relations are additionally used:

$$c = \cos 2\eta = 2 \cdot \cos^2 \eta - 1, \quad (3.16)$$

$$s = \sin 2\eta = \pm 2 \cdot \sqrt{(1 - \cos^2 \eta)} \cdot \cos \eta, \quad (3.17)$$

where η represents both η_1 or η_2 . The sign depends on the difference $(\phi_{\text{sca}} - \phi_{\text{inc}})$. When $0 \leq (\phi_{\text{sca}} - \phi_{\text{inc}}) \leq \pi$, the "+" sign is applied. When $0 \leq (\phi_{\text{inc}} - \phi_{\text{sca}}) \leq \pi$, the "-" sign should be used. Furthermore, one should take limits when the denominator of Eqs. (3.14) and (3.15)

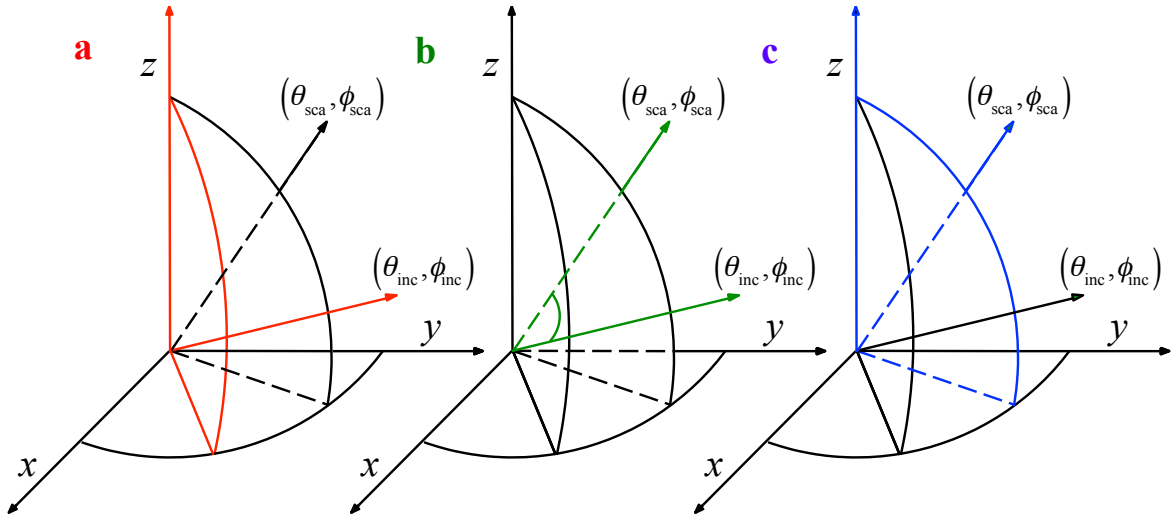


Figure 3.3: Illustration of the three different planes of reference under discussion: (a) Reference plane of the incident Stokes vector defined by the incident $(\theta_{\text{inc}}, \phi_{\text{inc}})$ and vertical directions (incident meridian plane), (b) Scattering plane defined by the incident $(\theta_{\text{inc}}, \phi_{\text{inc}})$ and scattering directions $(\theta_{\text{sca}}, \phi_{\text{sca}})$, and (c) Reference plane of the scattered Stokes vector defined by the scattering $(\theta_{\text{sca}}, \phi_{\text{sca}})$ and vertical directions (scattering meridian plane).

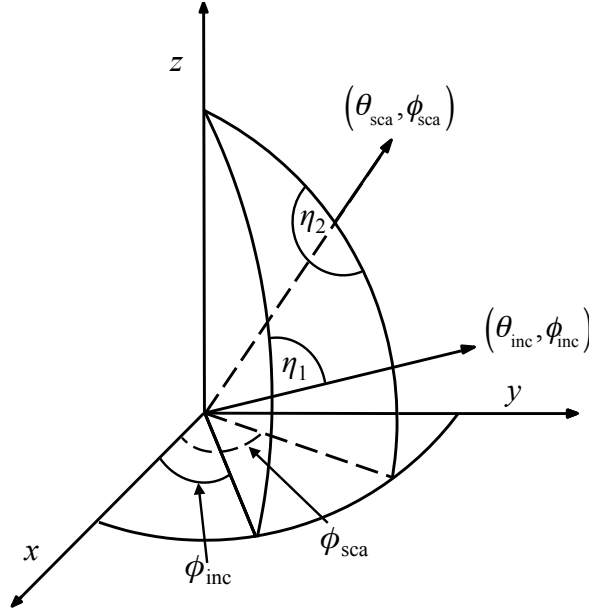


Figure 3.4: The geometry of anisotropic scattering: incident $(\theta_{\text{inc}}, \phi_{\text{inc}})$ and scattering $(\theta_{\text{sca}}, \phi_{\text{sca}})$ directions. η_1 and η_2 are the rotation angles, and ϕ_{inc} and ϕ_{sca} are the azimuth angles of the incident and scattering directions, respectively.

vanishes. Performing the matrix multiplication in the definition of the transformation phase matrix and taking into account Eqs. (3.13) - (3.17) (omitting the scalar products between the parameters) leads to the following analytical form:

$$\tilde{\mathbf{Z}}(\theta_{\text{inc}}, \phi_{\text{inc}}; \theta_{\text{sca}}, \phi_{\text{sca}}) = \begin{pmatrix} \tilde{P}_{11}(\vartheta) & c_1 \tilde{P}_{12}(\vartheta) & s_1 \tilde{P}_{12}(\vartheta) & 0 \\ c_2 \tilde{P}_{12}(\vartheta) & c_1 c_2 \tilde{P}_{22}(\vartheta) - s_1 s_2 \tilde{P}_{33}(\vartheta) & s_1 c_2 \tilde{P}_{22}(\vartheta) + c_1 s_2 \tilde{P}_{33}(\vartheta) & s_2 \tilde{P}_{34}(\vartheta) \\ -s_2 \tilde{P}_{12}(\vartheta) & -c_1 s_2 \tilde{P}_{22}(\vartheta) - s_1 c_2 \tilde{P}_{33}(\vartheta) & -s_1 s_2 \tilde{P}_{22}(\vartheta) + c_1 c_2 \tilde{P}_{33}(\vartheta) & c_2 \tilde{P}_{34}(\vartheta) \\ 0 & s_1 \tilde{P}_{34}(\vartheta) & -c_1 \tilde{P}_{34}(\vartheta) & \tilde{P}_{44}(\vartheta) \end{pmatrix}. \quad (3.18)$$

For polarization problems, the transformation phase matrix and not just the scattering phase function describes the volumetric scattering process and must be used as the probability density function to sample the new direction. Particularly, the PDF could be obtained from the Stokes vector of the scattered EM wave $\vec{\mathbf{S}}_{\text{sca}}$ (see Eq. 3.12). By integrating $\vec{\mathbf{S}}_{\text{sca}}$ over the solid angle (normalization), the cumulative joint probability density function of the scattering zenith and azimuth angles is derived:

$$G(\vartheta, \varphi) = \int_0^{2\pi} \int_0^\pi \vec{\mathbf{S}}_{\text{sca}} \cdot \sin \theta \, d\vartheta \, d\varphi. \quad (3.19)$$

Sampling the new direction from the physically correct cumulative PDF, $G(\vartheta, \varphi)$, is rather complicated and leads to numerical problems. Therefore, a randomly chosen angle (between 0 and 2π) is utilized to derive the scattering azimuth angle φ and the first normalized scattering matrix element ($\tilde{P}_{11} = \mathcal{P}$, as in the scalar approach), that is given in discrete steps (with

scattering angles ϑ_i), is used to obtain the scattering angle ϑ according to the precalculated cumulative probability density function:

$$G_{i-1} < \xi < G_i \text{ with } G_i = \sum_{j=1}^i \tilde{P}_{11}(\vartheta_j) \cdot \Delta\Omega(\vartheta_j), \quad (3.20)$$

where $\Delta\Omega(\vartheta_j)$ is the solid angle interval corresponding to a finite scattering angle interval $(\vartheta_{i,\min}, \vartheta_{i,\max})$ with center angle ϑ_i , and ξ stands for a random number uniformly distributed between 0 and 1. The exact scattering angle is then interpolated by:

$$\vartheta = \vartheta_{i,\min} + t \cdot \vartheta_{i,\max}, \quad (3.21)$$

with,

$$t = \frac{\xi - G_{i-1}}{G_i - G_{i-1}}. \quad (3.22)$$

The following correction should be applied:

$$\vec{S}_{\text{sca}} = \tilde{P}_{11}^{-1} \cdot \tilde{\mathbf{Z}} \cdot \vec{S}_{\text{inc}}. \quad (3.23)$$

Whenever a scattering event takes place, ϑ is sampled from the phase function, replacing the normalized transformation phase matrix $\tilde{\mathbf{Z}}$ with the reduced matrix $\tilde{P}_{11}^{-1} \cdot \tilde{\mathbf{Z}}$. This approach is called importance sampling method (Collins et al., 1972; Marchuk et al., 1980; Emde et al., 2010).

Once the scattering zenith and azimuth angles (ϑ, φ) are known, the new propagation direction (scattering direction), $\hat{\mathbf{k}}_{\text{sca}}(\theta_{\text{sca}}, \phi_{\text{sca}})$, is calculated from $\hat{\mathbf{k}}_{\text{inc}}(\theta_{\text{inc}}, \phi_{\text{inc}})$ (or $\hat{\mathbf{k}}_{\text{inc},0}$ in case of the first scattering event) using the following formulas (Marchuk et al., 1980):

$$k_{\text{sca}}^x = k_{\text{inc}}^x \cdot \cos \vartheta - (k_{\text{inc}}^y \cdot \sin \varphi + k_{\text{inc}}^x \cdot k_{\text{inc}}^z \cdot \cos \varphi) \cdot \sqrt{\frac{1 - \cos^2 \vartheta}{1 - (k_{\text{inc}}^z)^2}}, \quad (3.24)$$

$$k_{\text{sca}}^y = k_{\text{inc}}^y \cdot \cos \vartheta + (k_{\text{inc}}^x \cdot \sin \varphi - k_{\text{inc}}^y \cdot k_{\text{inc}}^z \cdot \cos \varphi) \cdot \sqrt{\frac{1 - \cos^2 \vartheta}{1 - (k_{\text{inc}}^z)^2}}, \quad (3.25)$$

$$k_{\text{sca}}^z = k_{\text{inc}}^z \cdot \cos \vartheta + (1 - (k_{\text{inc}}^z)^2) \cdot \cos \varphi \cdot \sqrt{\frac{1 - \cos^2 \vartheta}{1 - (k_{\text{inc}}^z)^2}}. \quad (3.26)$$

3.2.5 Surface Reflection

In scalar radiative transfer theory, the surface contribution is given by the surface Bidirectional Reflection Distribution Function (BRDF), explaining the way the incoming irradiance from one direction $(\theta_{\text{inc}}, \phi_{\text{inc}})$ is reflected by a surface into the direction of reflection (subscript "refl") $(\theta_{\text{refl}}, \phi_{\text{refl}})$. The BRDF is given by the ratio of the reflected radiance over the incoming irradiance (Marshak and Davis, 2005):

$$\text{BRDF}(\theta_{\text{inc}}, \phi_{\text{inc}}; \theta_{\text{refl}}, \phi_{\text{refl}}) = \frac{dI(\theta_{\text{refl}}, \phi_{\text{refl}})}{dF(\theta_{\text{inc}}, \phi_{\text{inc}})}. \quad (3.27)$$

In the vector scheme, the BRDF is replaced by the bidirectional polarized reflectance matrix, describing polarization due to surface reflection.

SPARTA considers either isotropic reflection (Lambertian surface) or anisotropic ocean reflection as outlined by Mishchenko and Travis (1997). Lambertian reflection represents a surface, which reflects isotropically and completely depolarizes the incident radiation. The angular distribution of the reflected radiation is uniform and independent of the incident direction and state of polarization. Considering a surface albedo of α_L , the corresponding reflection matrix is given by:

$$\mathbf{IR}_L = \begin{pmatrix} \alpha_L & 0 & 0 & 0 \\ 0 & 0 & 0 & 0 \\ 0 & 0 & 0 & 0 \\ 0 & 0 & 0 & 0 \end{pmatrix}. \quad (3.28)$$

To consider anisotropic and polarizing ocean reflection, the code by Mishchenko and Travis (1997) has been implemented into SPARTA. It calculates the reflection matrix for rough water surfaces ($\mathbf{IR}_{\text{ocean}}$) utilizing the Fresnel formulas. Considering the downward incident $\hat{\mathbf{k}}_{\text{inc}}(\theta_{\text{inc}}, \phi_{\text{inc}})$ and reflection directions $\hat{\mathbf{k}}_{\text{refl}}(\theta_{\text{refl}}, \phi_{\text{refl}})$ and $\mu = \cos \theta$, the $\mathbf{IR}_{\text{ocean}}$ is expressed as follows:

$$\mathbf{IR}_{\text{ocean}}(\mu_{\text{refl}}, \mu_{\text{inc}}, \phi_{\text{refl}} - \phi_{\text{inc}}) = \frac{|\vec{\mathbf{k}}_d|^4}{4\mu_{\text{refl}} \cdot \mu_{\text{inc}} \cdot |\hat{\mathbf{k}}_{\text{refl}} \times \hat{\mathbf{k}}_{\text{inc}}|^4 \cdot (k_d^z)^2 \cdot 2s^2} \cdot \exp(-W) \cdot \mathbf{M}_{\text{refl}}, \quad (3.29)$$

where,

$$\vec{\mathbf{k}}_d = k_d^x \cdot \hat{e}_x + k_d^y \cdot \hat{e}_y + k_d^z \cdot \hat{e}_z, \quad (3.30)$$

denotes the surface normal vector for specular reflection of $\hat{\mathbf{k}}_{\text{inc}}$ to $\hat{\mathbf{k}}_{\text{refl}}$. s^2 denotes the mean square surface slope of the waves (Cox and Munk, 1954):

$$2s^2 = 0.003 + 0.00512 \cdot w, \quad (3.31)$$

depending on the near-surface wind velocity w (in units of m s^{-1}). In Eq. (3.29) the term $\exp(-W)$ represents the Gaussian distribution of the surface slope. W is given by:

$$W = \frac{(k_d^x)^2 + (k_d^y)^2}{2(k_d^z)^2 \cdot s^2}. \quad (3.32)$$

\mathbf{M}_{refl} is a 4×4 matrix based on the Fresnel formulas and the geometrical configuration. The Fresnel formulas describe the reflection and refraction (transmission) of the EM wave when travelling between media of different refractive indices, i.e., \tilde{n}_1 and \tilde{n}_2 (Wendisch and Yang, 2012). For example, the Fresnel coefficients for reflection of an EM wave polarized perpendicular and parallel to the plane of reflection are given by:

$$r_{\perp} = \frac{\tilde{n}_1 \cdot \cos \Theta_1 - \tilde{n}_2 \cdot \cos \Theta_2}{\tilde{n}_1 \cdot \cos \Theta_1 + \tilde{n}_2 \cdot \cos \Theta_2}, \quad (3.33)$$

$$r_{\parallel} = \frac{\tilde{n}_2 \cdot \cos \Theta_1 - \tilde{n}_1 \cdot \cos \Theta_2}{\tilde{n}_2 \cdot \cos \Theta_1 + \tilde{n}_1 \cdot \cos \Theta_2}, \quad (3.34)$$

where Θ_1 and Θ_2 are the incident and refracted angles with respect to the surface normal, respectively. For further information about the Fresnel formulas and how to derive the \mathbf{M}_{refl} elements the reader is referred to the literature (Mishchenko and Travis, 1997). Finally, shadowing effects are implemented into the SPARTA code. Following Tsang and Li (2001), in order to take the shadowing effects due to waves into account, the \mathbf{IR} is multiplied by a bidirectional shadowing function $S(\mu_{\text{refl}}, \mu_{\text{inc}})$:

$$S(\mu_{\text{refl}}, \mu_{\text{inc}}) = \frac{1}{1 + \Lambda(\mu_{\text{refl}}) + \Lambda(\mu_{\text{inc}})}, \quad (3.35)$$

where

$$\Lambda(\mu_{\text{refl}}) = \frac{1}{2} \left[\sqrt{\frac{2(1 - \mu_{\text{refl}}^2)}{\pi}} \cdot \frac{s}{\mu_{\text{refl}}} \cdot \exp\left(-\frac{\mu_{\text{refl}}^2}{2s^2 \cdot (1 - \mu_{\text{refl}}^2)}\right) - \text{erfc}\left(\frac{\mu_{\text{refl}}}{s \cdot \sqrt{2(1 - \mu_{\text{refl}}^2)}}\right) \right]. \quad (3.36)$$

erfc denotes the complementary error function.

3.2.6 Radiance Contribution and Local Estimate Method

In order to efficiently obtain accurate radiance calculations, reducing the noise for strongly peaked phase matrices, the Local Estimate Method (LEM) has been applied (Collins et al., 1972; Marchuk et al., 1980; Marshak and Davis, 2005). It accounts for the probability that the photon is scattered into the direction of the sensor at each scattering process, always considering the attenuation τ along the photon path according to the law of Bouguer–Beer. A 2D representation of the scheme of the Local Estimate Method is found in Figure 3.5.

Thus, the simulated Stokes vector (carrying the units of radiance; resulting from each pixel) is given by:

$$\vec{\mathbf{S}} = \frac{1}{N_{\text{ph}}} \cdot \sum_{N_{\text{ph}}} \sum_M \frac{\tilde{\mathbf{Z}}(\theta_{\text{inc}}, \phi_{\text{inc}}; \theta_{\text{det}}, \phi_{\text{det}})}{4\pi} \cdot \frac{\exp(-\tau)}{\cos(\theta_{\text{det}})}, \quad (3.37)$$

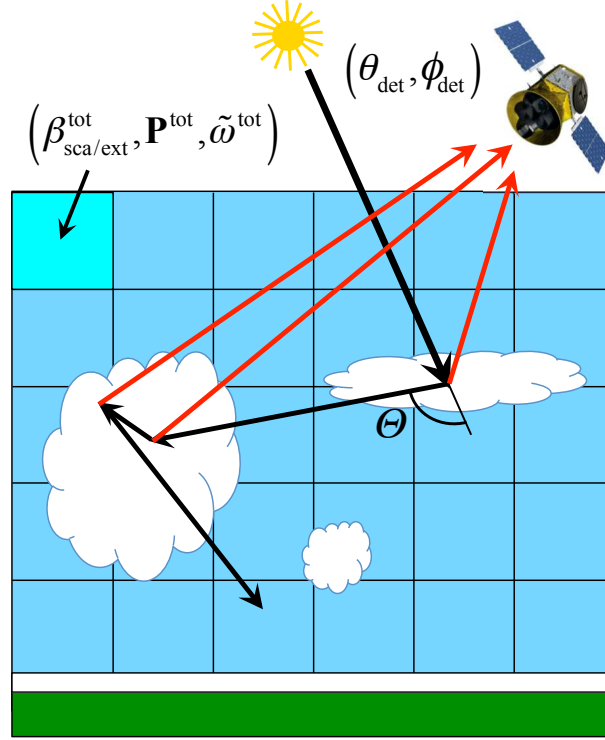


Figure 3.5: 2D representation of the scheme of the Local Estimate Method (see Figure 3.1): The red lines illustrate the contribution of each scattering event considering the extinction, integrated over all the grid-boxes on the way towards the direction of observation $(\theta_{\text{det}}, \phi_{\text{det}})$.

$\tilde{\mathbf{Z}}/4\pi$ represents the scattering probability density. Dividing by $\cos(\theta_{\text{det}})$ accounts for the slant area in the radiance definition. Consequently, the contribution should be summed over all the scattering events M and the number of photons N_{ph} , and normalized over N_{ph} .

Finally, the following normalized radiance is obtained:

$$\text{Normalized Radiance} = \frac{\pi \cdot \tilde{\mathbf{S}}}{\mu_0 \cdot F_0 \cdot (1000)^T}. \quad (3.38)$$

The normalized radiance holds for both the reflectivity and transmissivity (depending on the viewing direction). $F_0 \cdot (1000)^T$ is the incident unpolarized extraterrestrial quasi-monochromatic electromagnetic radiation (solar irradiance) with μ_0 being the cosine of the solar zenith angle.

3.2.7 SPARTA Efficiency

SPARTA is written in Fortran 90 and its performance has been tested on an Intel Core i7 processor with 2.6 GHz. The computation time (Central Processing Unit, CPU) is mostly dependent on the grid resolution of the model domain, the solar and viewing directions, the phase matrix, and more importantly, on the optical thickness. Three realistic atmospheric scenarios were considered. Simulations were performed for 1D standard atmospheres

Table 3.1: Computation times for 10 individual simulations. Rayleigh scattering at $\lambda = 325$ nm wavelength, Rayleigh scattering at $\lambda = 350$ nm, and mixed atmosphere (Rayleigh + spheroids) at $\lambda = 350$ nm, for one viewing direction. The errors correspond to standard deviation.

Settings	Rayleigh (325 nm)	Rayleigh (350 nm)	Mixed (350 nm)
10^4 photons	0.104 s (0.224 %)	0.098 s (0.209 %)	1.393 s (0.821 %)
10^5 photons	0.618 s (0.110 %)	0.550 s (0.106 %)	1.897 s (0.488 %)

(Anderson et al., 1986) at 325 nm and 350 nm wavelengths above a black non-scattering surface. The model domain consists of 30 equidistant layers and is lifted to 30 km height. The Rayleigh optical thickness is approximately 0.96 at 325 nm wavelength and 0.62 at 350 nm wavelength. In case of aerosol scattering, prolate spheroidal particles with an optical thickness of 0.2 were added (Gasteiger et al., 2011). The corresponding CPU times for the diffuse upward radiation at TOA are listed in Table 3.1.

4 SPARTA Verification

Benchmark results are available from plenty of sources including Coulson et al. (1960); Garcia and Siewert (1986, 1989); Mishchenko (1991); Wauben and Hovenier (1992); de Haan et al. (1987); Natraj et al. (2009); Kokhanovsky et al. (2010) among others. The performance of SPARTA has been tested for various atmospheric conditions, involving randomly oriented prolate spheroids (Wauben and Hovenier, 1992), as well as Rayleigh atmospheres and aerosol layers (Kokhanovsky et al., 2010) with a black non-scattering surface. The ability of SPARTA to correctly describe effects due to isotropic surface reflection was checked by comparison to exact results from numerical solutions of the vector radiative transfer equation (Natraj et al., 2009) and tabulated values from de Haan et al. (1987). In addition, SPARTA participated in the model intercomparison project that the polarization working group of the International Radiation Commission (IRC) launched (Emde et al., 2015). This chapter addresses our attempts to validate SPARTA and quantify its accuracy. Results and Figures presented in this chapter were published in Barlakas et al. (2014, 2016) and Emde et al. (2015).

4.1 Comparison Against Benchmark Results

4.1.1 Rayleigh Scattering Above a Lambertian Surface

For a single Rayleigh layer above Lambertian surfaces, SPARTA was validated against data from Natraj et al. (2009). These data have been computed utilizing a more accurate approach to the representation of the X and Y functions introduced in Chandrasekhar (1960) and Coulson et al. (1960). The values of the Stokes vector involve a set of different optical thicknesses (0.02 - 1.0), surface albedos (0 - 0.8), solar zenith angles θ_0 and viewing zenith angles θ_{det} (0° - 88.85°), and relative azimuth angles (azimuth angle between sun direction and viewing direction), $\phi = \phi_{\text{det}} - \phi_0$, (0° - 180°). In this work, the solar azimuth angle is set to zero and, therefore, $\phi = \phi_{\text{det}}$.

Four test cases were defined with special emphasis on surface reflection, starting from an optically thin atmosphere ($\tau = 0.02$) to thicker cases ($\tau = 1$). A concise description of the test cases is given in Table 4.1, where $\mu_0 = \cos \theta_0$ is the cosine of the solar zenith angle, $\mu_{\text{det}} = \cos \theta_{\text{det}}$ is the cosine of the zenith angle of the detector, ϕ is the relative azimuth angle, α_L is the surface albedo, and TOA and BOA (Bottom Of the Atmosphere) refer to the output altitudes.

Simulations were conducted for homogeneous, plane-parallel, Rayleigh layers, molecular absorption was not considered. The number of photons used for all test cases was 10^8 . Results

Table 4.1: Test cases for comparison between SPARTA and the tabulated values by Natraj et al. (2009) for pure molecular scattering. τ is the optical thickness, μ_0 is the cosine of the solar zenith angle, μ_{det} is the cosine of the zenith angle of the detector, ϕ is the relative azimuth angle, α_L is the surface albedo, and TOA and BOA refer to the output altitude, top of the atmosphere and bottom of the atmosphere respectively. Principal plane: fixed azimuth angle but varying zenith angles. Almucantar plane: fixed zenith angle but varying azimuth angles.

Case	τ	μ_0	μ_{det}	ϕ	α_L	Altitude
1	0.02	0.92	0.4	almucantar	0.00, 0.25, 0.80	TOA
2	0.10	0.80	principal	90	0.00, 0.25, 0.80	TOA & BOA
3	0.50	0.80	principal	90	0.00, 0.25, 0.80	TOA & BOA
4	1.00	1.00	principal	0	0.00, 0.25, 0.80	TOA & BOA

were obtained by 10 individual Monte Carlo simulations. The Rayleigh scattering phase matrix is given without the depolarization factor (see blue line in Figure 4.1) by:

$$\tilde{\mathbf{P}}(\vartheta) = \frac{3}{4} \begin{pmatrix} 1 + \cos^2 \vartheta & \cos^2 \vartheta - 1 & 0 & 0 \\ \cos^2 \vartheta - 1 & 1 + \cos^2 \vartheta & 0 & 0 \\ 0 & 0 & 2 \cos \vartheta & 0 \\ 0 & 0 & 0 & 2 \cos \vartheta \end{pmatrix}. \quad (4.1)$$

In Figure 4.2 results for Case 1 are presented, which is a test for appropriate surface reflection. The three left panels correspond to the Stokes vector for the diffuse upward radiation at the TOA. The three right panels depict the relative differences in percent of SPARTA results for the Stokes vector as related to the benchmark results. Note that the fourth Stokes parameter is zero for molecular scattering, and it disappears at ϕ of 0° and 180° . The absolute value of the relative differences is less than 0.05 % for I , and up to 0.08 % for Q and U . The comparison for the Case 1 confirms that the Lambertian surface has been implemented correctly. The results for the test Cases 2-4 are illustrated in Figures 4.3 to 4.8. They compare the Stokes parameters for the diffuse radiation for both the BOA and the TOA for two solar zenith angles (0° and 36.87°), and two ϕ (0° and 90°) in the principal plane. The relative differences are less than $\pm 0.15\%$ for I , and less than $\pm 0.18\%$ and $\pm 0.05\%$ for Q and U for all test cases.

4.1.2 Layered Cloud and Haze Atmospheres

De Haan et al. (1987) report benchmark results using the adding and doubling approach, where a set of two scattering problems has been investigated. The first scattering case considers a homogeneous plane-parallel atmosphere with a layer of water-haze droplets, optical thickness of 1, above a black surface. They selected the haze droplets introduced in Deirmendjian (1969), whose scattering phase matrix expansion coefficients have been provided by de Rooij and van der Stap (1984), also used by Brown and Xie (2012). The second case includes an inhomogeneous atmosphere with an optical thickness of 0.6, which is composed of two homogeneous layers and a Lambertian surface albedo of 0.1. The upper layer consists of molecules only (no absorption) with an optical thickness of 0.1. The lower

one consists of a mixture of haze droplets and molecules with an optical thickness of 0.4 and 0.1, respectively.

To consider Rayleigh scattering, the full scattering phase matrix representation has been used, see Eq. (4.2) and Hansen and Travis (1974); Emde et al. (2010), whereby a depolarization factor (δ) of 0.0279 was selected, that corresponds to air molecules (Chandrasekhar, 1960). The phase matrix elements for both particles are shown in Figure 4.1.

$$\tilde{\mathbf{P}}(\vartheta) = \frac{3}{3 + \Delta} \begin{pmatrix} 1 + \Delta \cdot \cos^2 \vartheta & -\Delta \cdot \sin^2 \vartheta & 0 & 0 \\ -\Delta \cdot \sin^2 \vartheta & \Delta \cdot (1 + \cos^2 \vartheta) & 0 & 0 \\ 0 & 0 & 2\Delta \cdot \cos \vartheta & 0 \\ 0 & 0 & 0 & (3\Delta - 1) \cdot \cos \vartheta \end{pmatrix}, \quad (4.2)$$

where

$$\Delta = \frac{1 - \delta}{1 + \delta}. \quad (4.3)$$

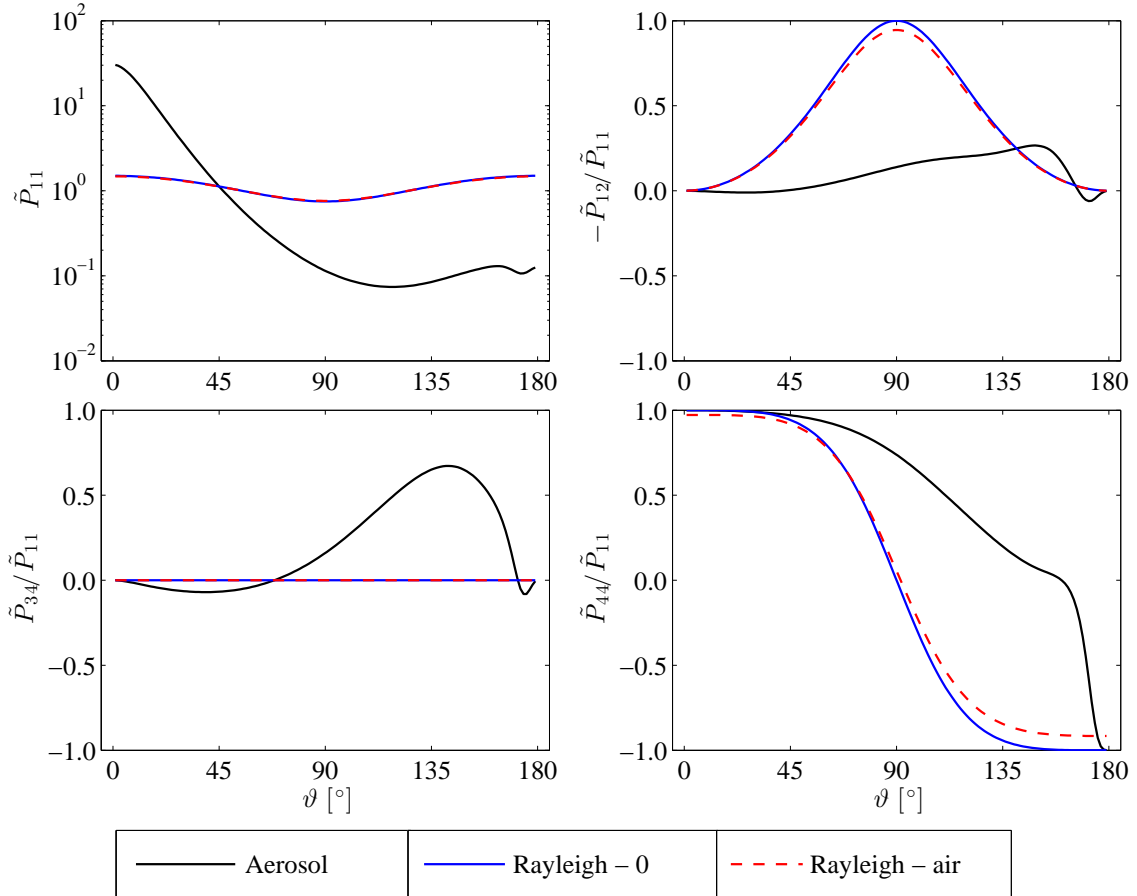


Figure 4.1: Scattering phase matrix elements for the aerosol case and for two different molecular scattering cases. For the first Rayleigh scattering case, the depolarization factor was set to zero and for the second, the number 0.0279 was adopted, which represents air.

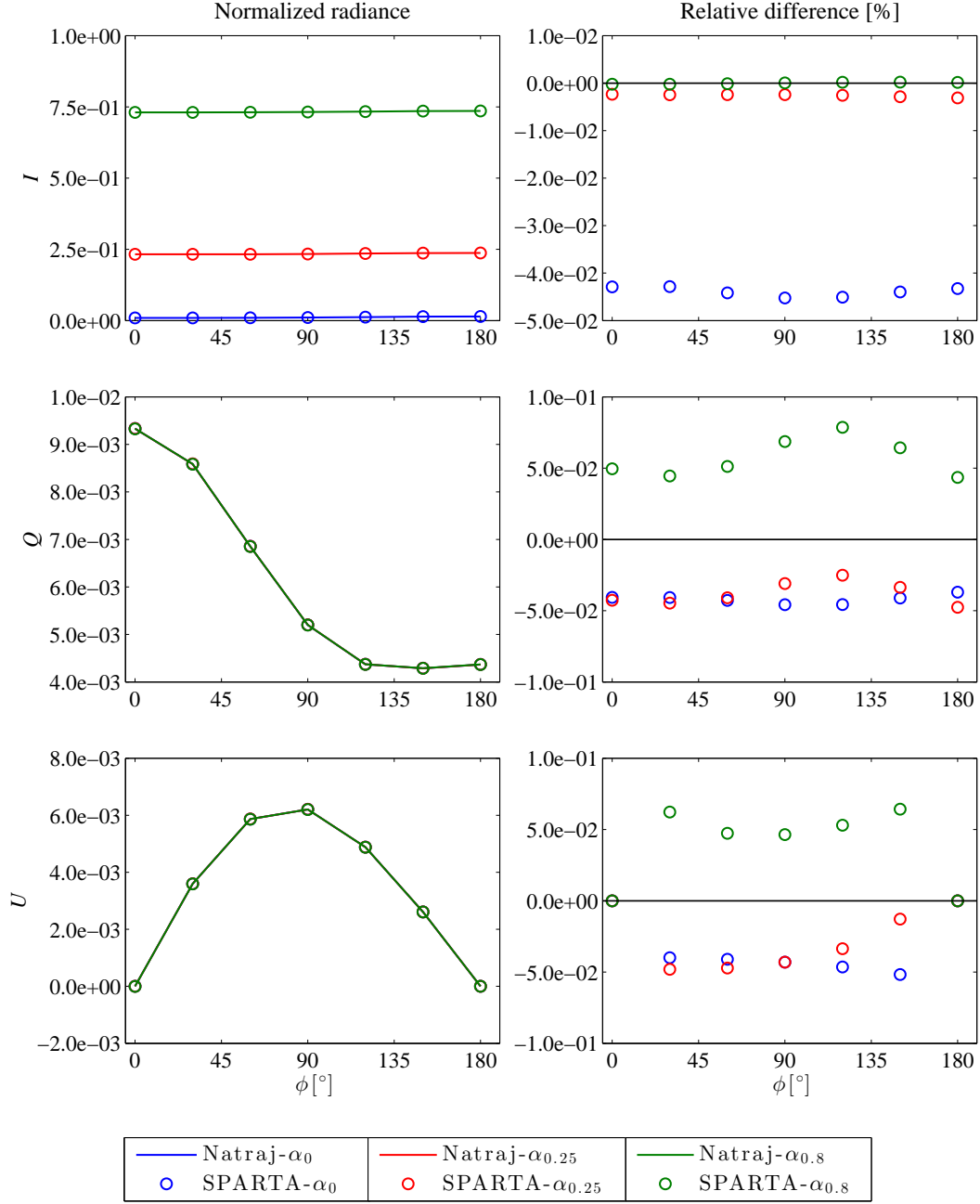


Figure 4.2: Comparison between SPARTA and the tabulated values by Natraj et al. (2009) for Case 1, test for surface reflection ($\alpha_L = 0, 0.25, 0.8$). Optically thin atmosphere ($\tau = 0.02$), $\mu_0 = 0.92$, and $\phi = 90^\circ$. Left: Stokes vector at the TOA (line - Natraj, circles - SPARTA). Right: Relative differences in percent of SPARTA as correlated to the benchmark results.

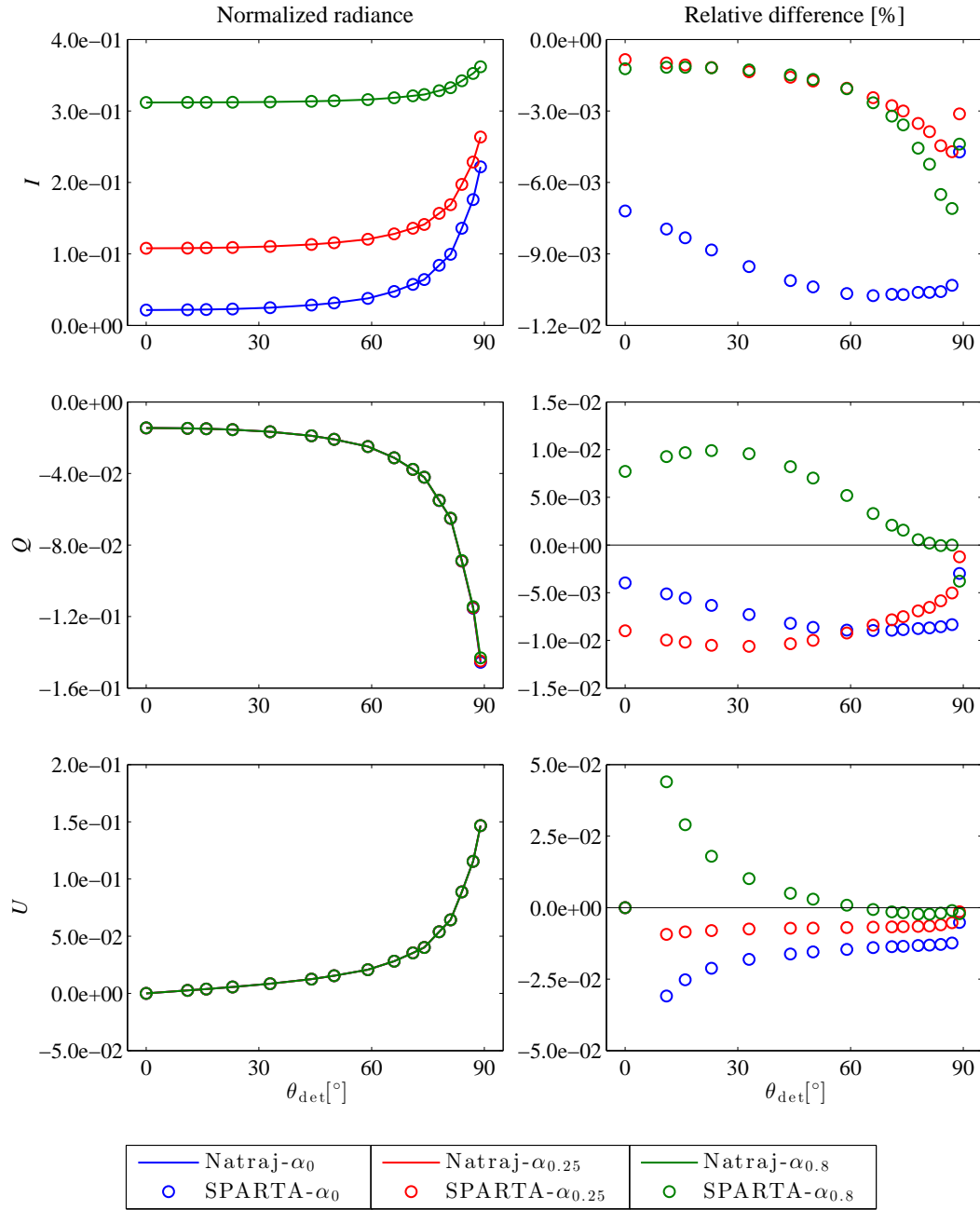


Figure 4.3: Comparison between SPARTA and the tabulated values by Natraj et al. (2009) for Case 2, for $\tau = 0.1$, $\mu_0 = 0.8$, $\phi = 90^\circ$, and $\alpha_L = 0, 0.25, 0.8$. Left: Stokes vector at the TOA (line - Natraj, circles - SPARTA). Right: Relative differences in percent of SPARTA as correlated to the benchmark results.

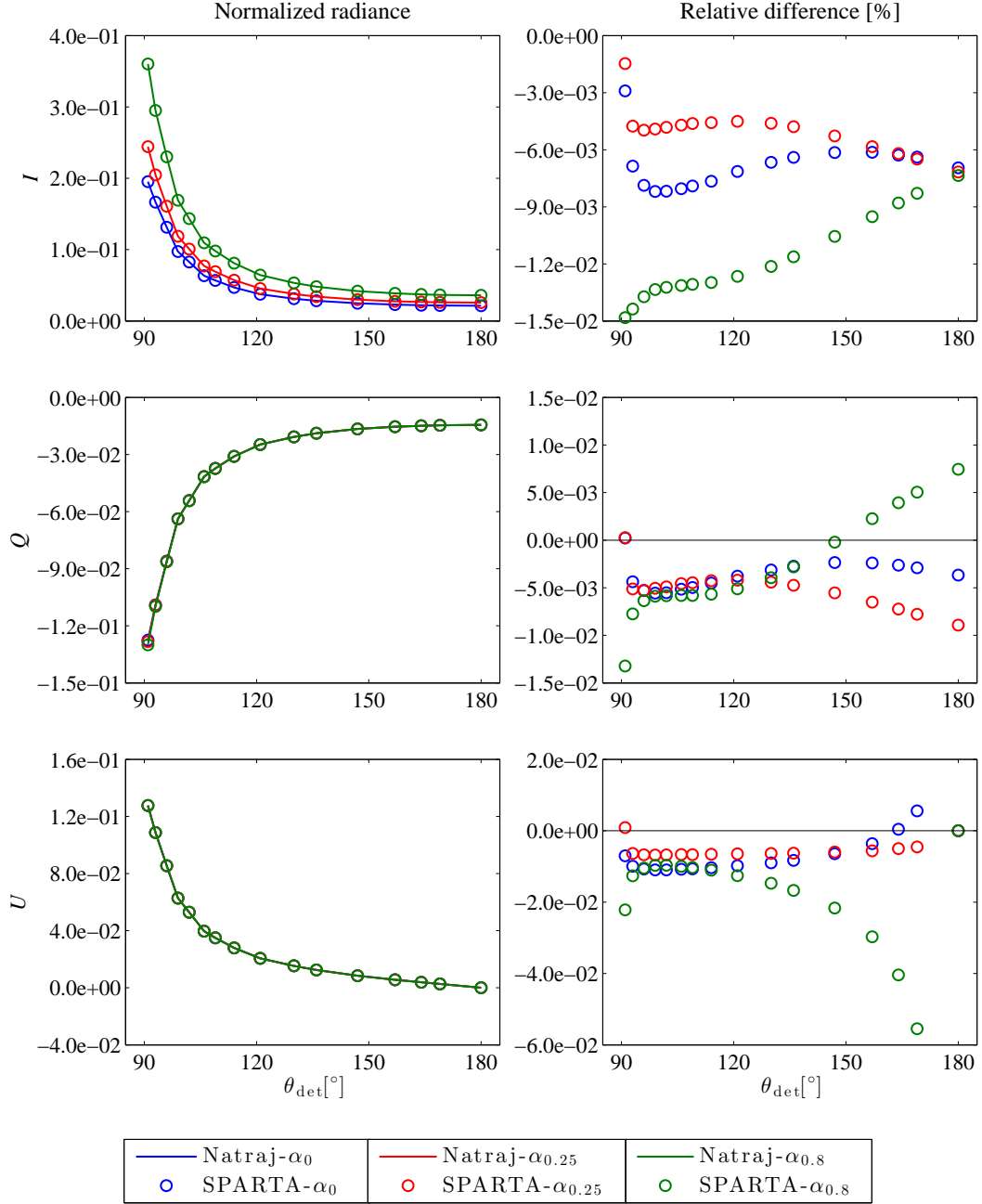


Figure 4.4: The same as in Figure 4.3, but for the Stokes vector at the BOA.

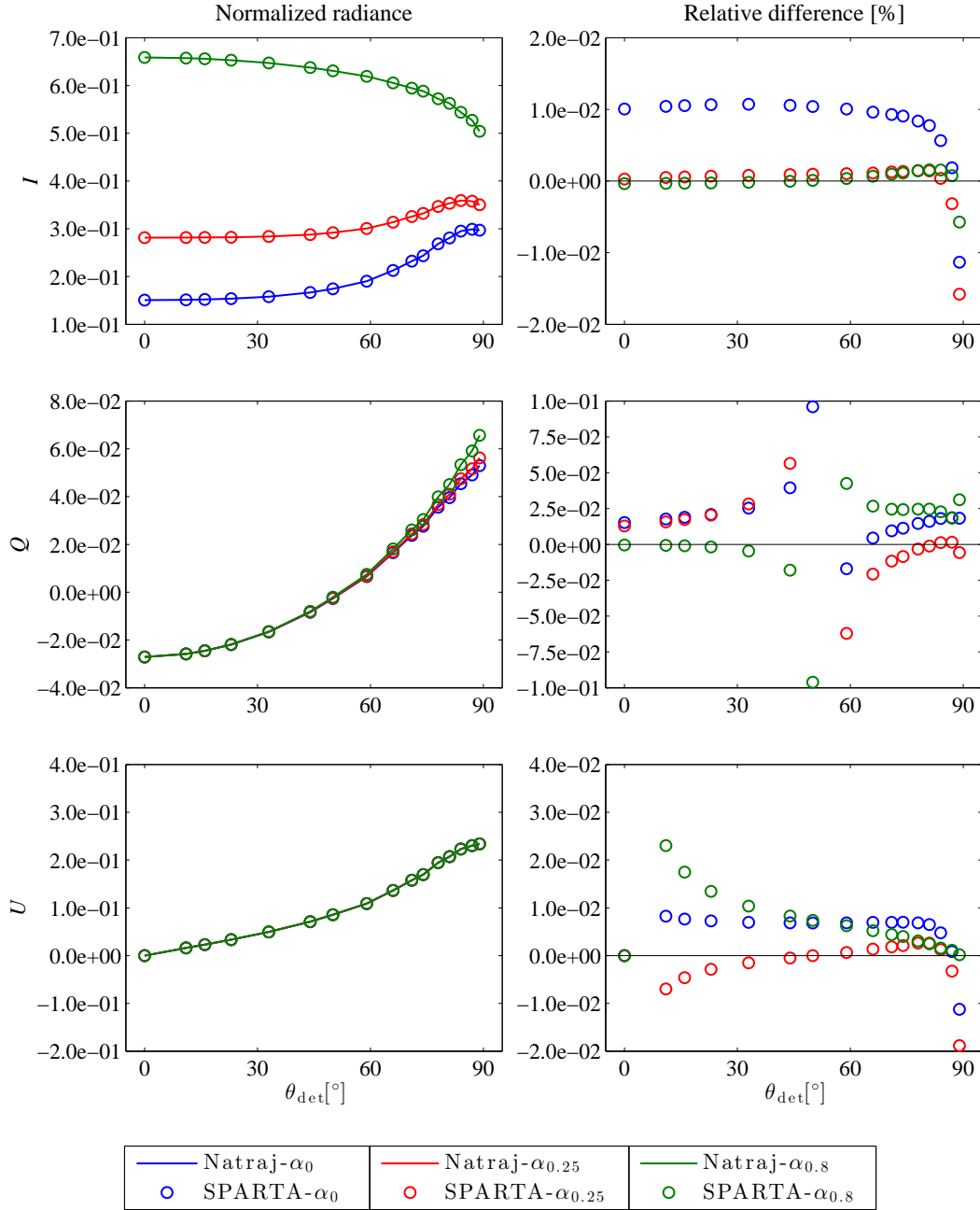


Figure 4.5: Comparison between SPARTA and the tabulated values by Natraj et al. (2009) for Case 3, for $\tau = 0.5$, $\mu_0 = 0.8$, and $\phi = 90^\circ$. Left: Stokes vector at the TOA (line - Natraj, circles - SPARTA). Right: Relative differences in percent of SPARTA as correlated to the benchmark results.

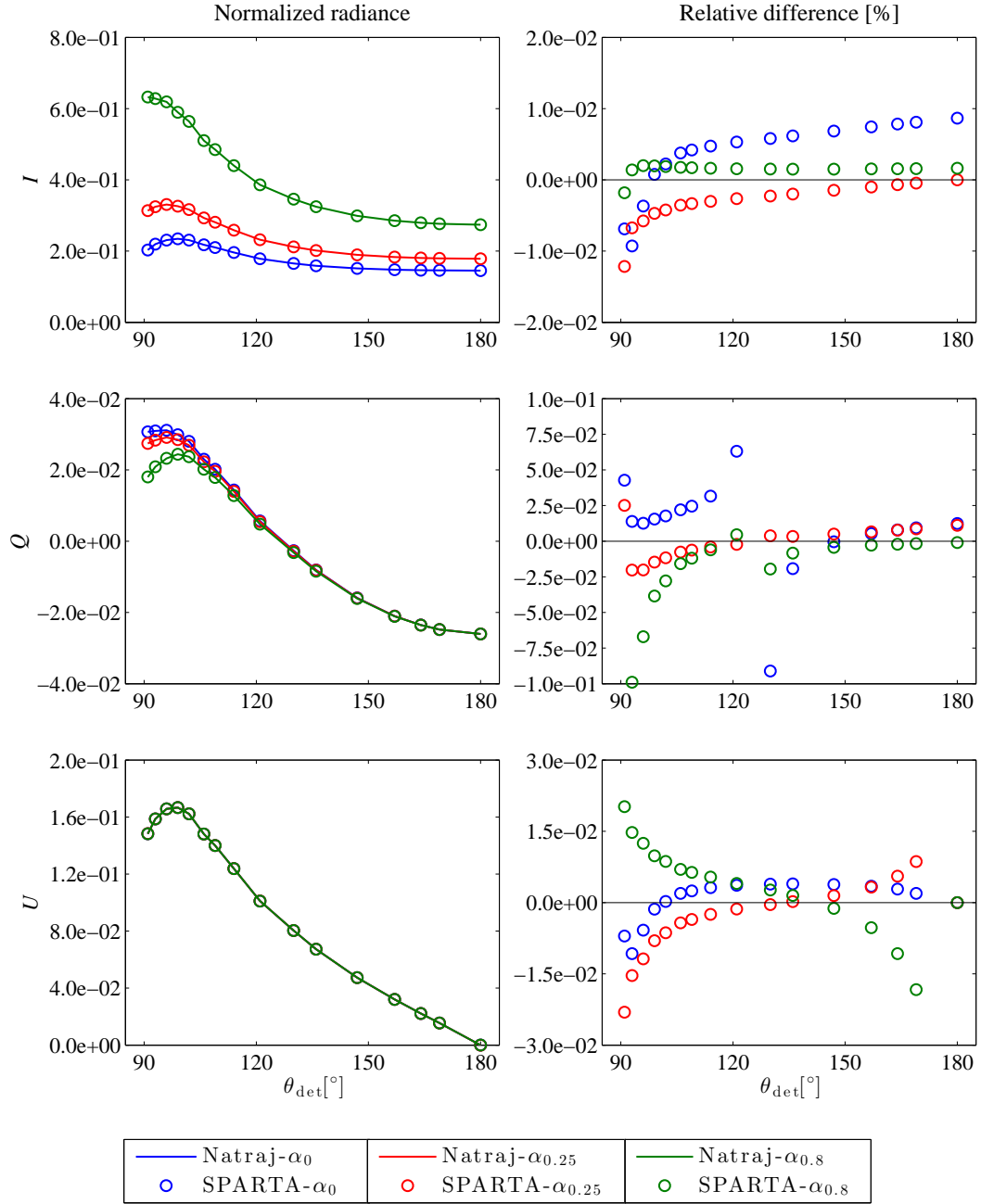


Figure 4.6: The same as in Figure 4.5, but for the Stokes vector at the BOA.

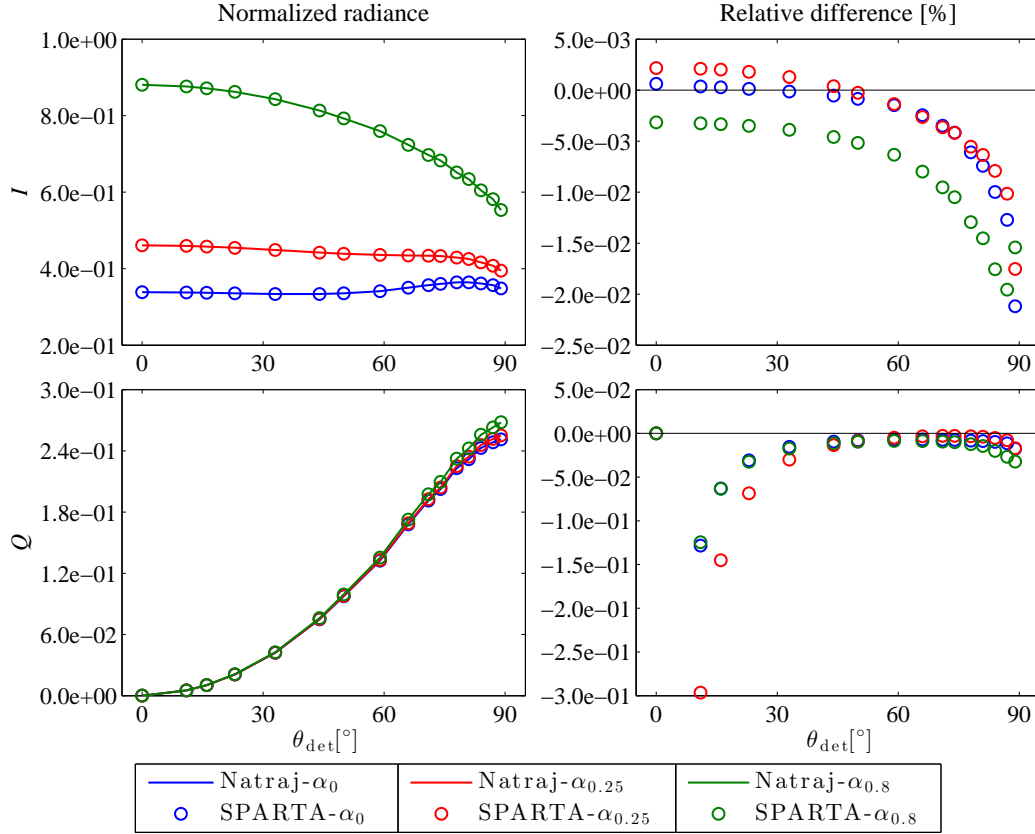


Figure 4.7: Comparison between SPARTA and the tabulated values by Natraj et al. (2009) for Case 4, for $\tau = 0.5$, $\mu_0 = 1$, and $\phi = 0^\circ$. Left: Stokes vector at the TOA (line - Natraj, circles - SPARTA). Right: Relative differences in percent of SPARTA as correlated to the benchmark results.

The results of the comparison between the tabulated values by de Haan et al. (1987) and those calculated by SPARTA is compiled in Tables 4.2 - 4.5. They show the Stokes parameters for the reflected diffuse radiation at the TOA. The errors correspond to two standard deviations (2σ), resulting from 10 individual simulations.

The relative differences of SPARTA for all the components of the Stokes vector as compared to the tabulated values have also been computed. Values of the Stokes components close to zero are left out as they can artificially boost large relative differences. For the homogeneous case, the relative differences are less than $\pm 0.096\%$ for the first Stokes element, less than $\pm 0.39\%$ for Q , and up to $\pm 0.45\%$ for U . The relative differences for the inhomogeneous scattering case are less than $\pm 0.056\%$ for the first Stokes element, $\pm 0.64\%$ for the second Stokes element, and $\pm 0.008\%$ for the third element. For V , the absolute values of the relative differences for both the homogeneous and inhomogeneous cases are $\pm 2.71\%$ and $\pm 1.55\%$, respectively (values of V below 0.00005 were ignored). This is due to the fact that the Monte Carlo method results are always subject to statistical uncertainty. The smaller the value of the Stokes vector the larger the notable Monte Carlo noise. In order to ameliorate such noise and precisely determine V , more than 10^{10} photons should be used for the simulations (increasing computation time) or variance reduction techniques should be

Table 4.2: Comparison between SPARTA and the benchmark results by de Haan et al. (1987). Stokes vector for a homogeneous layer of water–haze droplets in the reflected diffuse radiation at the TOA. The cosine of the solar zenith angle is 0.5 and the cosines of the three viewing directions are $\mu_{\text{det}} = 0.1, 0.5, 1.0$. The viewing zenith angles ϕ_{det} are 0° and 30° . No ground reflection. The errors correspond to two standard deviations (2σ).

$\mu_0 = 0.5$	$\mu_{\text{det}} = 0.1$		$\mu_{\text{det}} = 0.5$		$\mu_{\text{det}} = 1.0$	
$\phi_{\text{det}} = 0^\circ$	de Haan	SPARTA	de Haan	SPARTA	de Haan	SPARTA
I	1.10269	1.10331 ± 0.00070	0.31943	0.31953 ± 0.00010	0.03303	0.03303 ± 0.00003
Q	0.00460	0.00461 ± 0.00001	−0.00288	$−0.00288 \pm 0.00000$	−0.00298	$−0.00298 \pm 0.00000$
U	0.00000	0.00000 ± 0.00001	0.00000	0.00000 ± 0.00000	0.00000	0.00000 ± 0.00000
V	0.00000	0.00000 ± 0.00000	0.00000	0.00000 ± 0.00000	0.00000	0.00000 ± 0.00000
$\phi_{\text{det}} = 30^\circ$	de Haan	SPARTA	de Haan	SPARTA	de Haan	SPARTA
I	0.66414	0.66438 ± 0.00067	0.25209	0.25215 ± 0.00019	0.03303	0.03304 ± 0.00003
Q	0.00030	0.00030 ± 0.00001	−0.00144	$−0.00144 \pm 0.00000$	−0.00149	$−0.00149 \pm 0.00000$
U	−0.00277	$−0.00276 \pm 0.00002$	−0.00414	$−0.00414 \pm 0.00001$	−0.00258	$−0.00258 \pm 0.00000$
V	0.00004	0.00004 ± 0.00000	0.00002	0.00002 ± 0.00000	0.00000	0.00000 ± 0.00000

Table 4.3: As in Table 4.2 but the cosine of the solar zenith angle is 0.1.

$\mu_0 = 0.1$	$\mu_{\text{det}} = 0.1$		$\mu_{\text{det}} = 0.5$		$\mu_{\text{det}} = 1.0$	
$\phi_{\text{det}} = 0^\circ$	de Haan	SPARTA	de Haan	SPARTA	de Haan	SPARTA
I	2.93214	2.93314 ± 0.00057	0.22054	0.22075 ± 0.00005	0.00929	0.00929 ± 0.00000
Q	0.00990	0.00987 ± 0.00000	0.00098	0.00098 ± 0.00000	−0.00082	$−0.00082 \pm 0.00000$
U	0.00000	0.00000 ± 0.00000	0.00000	0.00000 ± 0.00000	0.00000	0.00000 ± 0.00000
V	0.00000	0.00000 ± 0.00000	0.00000	0.00000 ± 0.00000	0.00000	0.00000 ± 0.00000
$\phi_{\text{det}} = 30^\circ$	de Haan	SPARTA	de Haan	SPARTA	de Haan	SPARTA
I	0.76910	0.76969 ± 0.00015	0.13283	0.13293 ± 0.00003	0.00929	0.00929 ± 0.00001
Q	−0.00376	$−0.00376 \pm 0.00001$	0.00022	0.00022 ± 0.00000	−0.00041	$−0.00041 \pm 0.00000$
U	0.00314	0.00313 ± 0.00000	−0.00053	$−0.00052 \pm 0.00000$	−0.00071	$−0.00071 \pm 0.00000$
V	0.00001	0.00001 ± 0.00000	0.00001	0.00001 ± 0.00000	0.00000	0.00000 ± 0.00000

Table 4.4: Comparison between SPARTA and the benchmark results by de Haan et al. (1987). Stokes vector for an inhomogeneous atmosphere of molecules and water–haze droplets in the reflected diffuse radiation at the TOA above a Lambertian surface with an albedo of 0.1. The cosine of the solar zenith angle is 0.5 and the cosines of the three viewing directions are $\mu_{\text{det}} = 0.1, 0.5$, and 1.0. The viewing zenith angles ϕ_{det} are 0° and 30° . The errors correspond to two standard deviations (2σ).

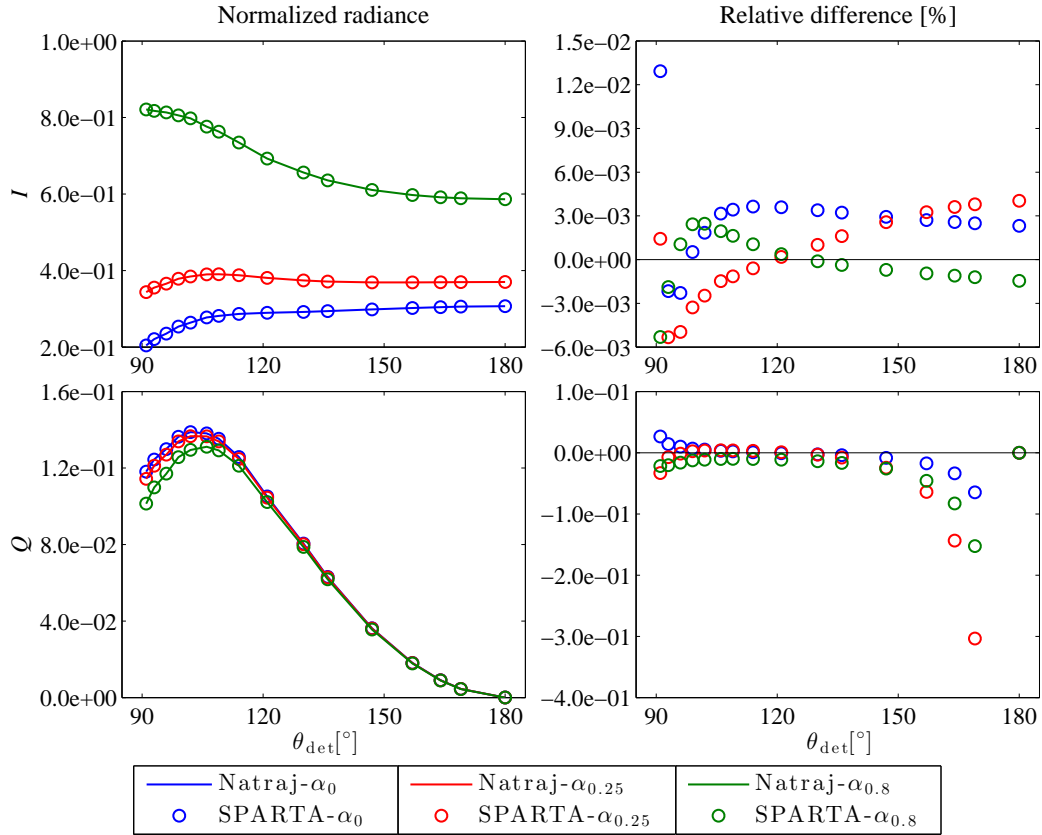
$\mu_0 = 0.5$	$\mu_{\text{det}} = 0.1$		$\mu_{\text{det}} = 0.5$		$\mu_{\text{det}} = 1.0$	
$\phi_{\text{det}} = 0^\circ$	de Haan	SPARTA	de Haan	SPARTA	de Haan	SPARTA
I	0.53295	0.53321 ± 0.00017	0.20843	0.20851 ± 0.00006	0.09368	0.09370 ± 0.00003
Q	−0.02834	$−0.02835 \pm 0.00004$	−0.03630	$−0.03630 \pm 0.00002$	−0.02416	$−0.02416 \pm 0.00001$
U	0.00000	0.00001 ± 0.00004	0.00000	0.00000 ± 0.00001	0.00000	0.00000 ± 0.00000
V	0.00000	0.00000 ± 0.00000	0.00000	0.00000 ± 0.00000	0.00000	0.00000 ± 0.00000
$\phi_{\text{det}} = 30^\circ$	de Haan	SPARTA	de Haan	SPARTA	de Haan	SPARTA
I	0.41814	0.41823 ± 0.00016	0.18497	0.18501 ± 0.00007	0.09368	0.09369 ± 0.00002
Q	−0.00006	$−0.00006 \pm 0.00004$	−0.01965	$−0.01965 \pm 0.00002$	−0.01208	$−0.01208 \pm 0.00001$
U	−0.07311	$−0.07311 \pm 0.00004$	−0.04140	$−0.04140 \pm 0.00002$	−0.02092	$−0.02092 \pm 0.00001$
V	0.00011	0.00011 ± 0.00000	0.00004	0.00004 ± 0.00000	0.00000	0.00000 ± 0.00000

Table 4.5: As in Table 4.4 but the cosine of the solar zenith angle is 0.1.

$\mu_0 = 0.1$	$\mu_{\text{det}} = 0.1$		$\mu_{\text{det}} = 0.5$		$\mu_{\text{det}} = 1.0$	
$\phi_{\text{det}} = 0^\circ$	de Haan	SPARTA	de Haan	SPARTA	de Haan	SPARTA
I	0.52277	0.52297 ± 0.00007	0.10659	0.10665 ± 0.00002	0.02601	0.02601 ± 0.00000
Q	0.01151	0.01150 ± 0.00002	-0.00519	-0.00519 ± 0.00001	-0.01498	-0.01498 ± 0.00000
U	0.00000	0.00000 ± 0.00001	0.00000	0.00000 ± 0.00000	0.00000	0.00000 ± 0.00000
V	0.00000	0.00000 ± 0.00000	0.00000	0.00000 ± 0.00000	0.00000	0.00000 ± 0.00000
$\phi_{\text{det}} = 30^\circ$	de Haan	SPARTA	de Haan	SPARTA	de Haan	SPARTA
I	0.27630	0.27639 ± 0.00006	0.08363	0.08366 ± 0.00002	0.02601	0.02601 ± 0.00001
Q	0.03437	0.03438 ± 0.00002	0.00384	0.00384 ± 0.00001	-0.00749	-0.00749 ± 0.00000
U	-0.01604	-0.01605 ± 0.00001	-0.01449	-0.01449 ± 0.00001	-0.01298	-0.01298 ± 0.00000
V	0.00003	0.00003 ± 0.00000	0.00002	0.00002 ± 0.00000	0.00000	0.00000 ± 0.00000

implemented (truncation techniques Rozanov and Lyapustin, 2010; Buras and Mayer, 2011). Variance reduction techniques may speed up simulations; however, they are not based on physics.

The comparisons demonstrated that SPARTA represents multiple-scattering and surface reflection with high accuracy and is capable of calculating polarization radiances for different atmospheric conditions.

**Figure 4.8:** The same as in Figure 4.7, but for the Stokes vector at the BOA.

4.1.3 Homogeneous Aerosol and Cloudy Atmospheres

Kokhanovsky et al. (2010) present the findings of the model intercomparison project comprising seven vector radiative transfer models, including the cases of Rayleigh, aerosol and cloudy atmospheres with a black non-scattering surface. The benchmark data have been generated using SCIATRAN (Rozanov et al., 2005; Rozanov and Kokhanovsky, 2006; Rozanov et al., 2014), which is a software package based on the DOM. Simulations were conducted for 1D non-absorbing (single-scattering albedo of 1), homogeneous, plane-parallel layers assuming a molecular and aerosol optical thickness of 0.3262, a cloud optical thickness of 5, and a black underlying surface (the surface albedo is 0).

In Barlakas et al. (2014), SPARTA was validated through Kokhanovsky et al. (2010) benchmark data for the first two cases (Rayleigh and aerosol layers). The results were obtained by individual Monte Carlo simulations. In this thesis, the accuracy of SPARTA is quantified for the last two cases (aerosol particles and cloud layers) because a comprehensive validation for molecular atmospheres was carried out in Subsection 4.1.1. For the aerosol particle layer, 10^8 , and for the cloudy case 10^9 photons were used. The aerosol and cloud particle scattering phase matrices were calculated employing Mie theory (Mie, 1908) at $\lambda = 412$ nm wavelength. The complex scattering phase matrices are shown in Figure 4.9.

In Figure 4.10, the Stokes vector for the aerosol case in the reflected (left panels) and transmitted (right panels) diffuse radiation, pertaining to a solar zenith angle of 60° , a relative azimuth angle (ϕ) of 0° , 90° , and 180° and different viewing zenith angles is presented. Note here that for ϕ of 0° and 180° the third and fourth Stokes elements are 0. In addition, a relative azimuth angle of 0° corresponds to the exact backscattering direction. The comparison for the cloud case linked to a ϕ of 90° is illustrated in Figure 4.11. For the aerosol atmosphere, there is an excellent agreement between SPARTA and the output from SCIATRAN for I , Q , U . However, for the last Stokes element, V , a slight noise is identified (for scattering angles close to 90° , Figure 4.10). Similar results are found in the comparison for the thick cloud layer. Particularly, the strongly peaked cloud scattering phase matrix (see Figure 4.9) increases the noise in radiance simulations for V (and even for U with increasing viewing zenith angle) (Figure 4.11). Nevertheless, there is no bias, and the strong forward scattering peak is correctly represented.

The relative differences of SPARTA for the first three components of the Stokes vector as compared to the benchmark results were also calculated. The last Stokes element was excluded since its very small values (less than 0.0001 for the aerosol and below 0.00006 for the cloud particles) lead to artificial large relative differences. In addition, where the values of the other components of the Stokes vector tend to zero are ignored. The comparison for both case studies for the reflected and transmitted radiation is shown in Table 4.6. Only the maximum relative differences in percent, over the entire spectrum of the viewing directions, are listed. SPARTA yields precise results for I , Q , U for the aerosol layer. The maximum relative differences are less than $\pm 0.43\%$ for I , $\pm 1.38\%$ for Q (or less than $\pm 0.82\%$ excluding the observation zenith angle of 89°), and $\pm 0.87\%$ for U , for the used number of photons 10^8 . For the cloud layer, these differences are less than $\pm 0.51\%$ for I , and $\pm 5.41\%$ for Q (or below $\pm 3.86\%$ excluding the observation zenith angles between 63° and 82° , where the values of

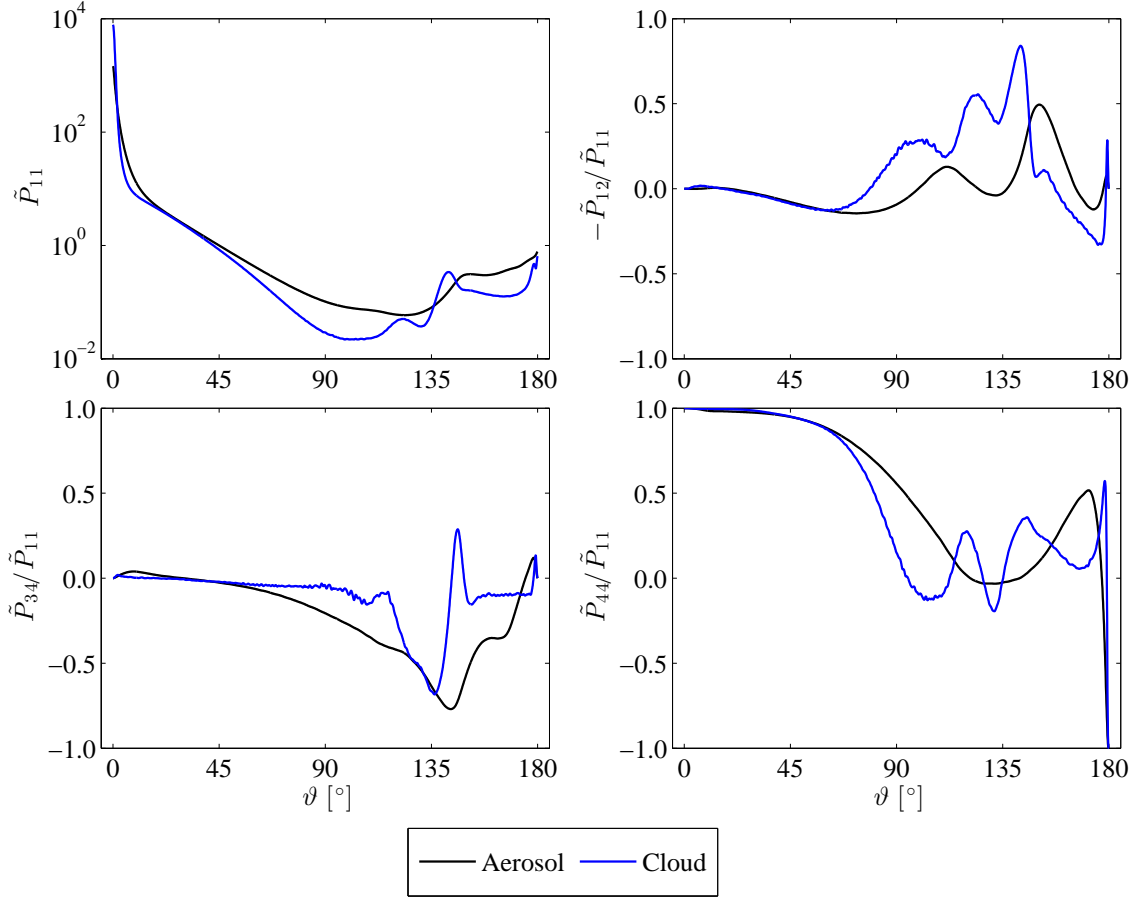


Figure 4.9: Scattering phase matrix elements for the aerosol and cloud cases.

Table 4.6: Comparison between SPARTA and SCIATRAN. Maximum relative differences in percent, over the whole spectrum of the viewing directions, for the first three Stokes components (I , Q , U) for the aerosol and cloud cases, for both the reflected (TOA) and transmitted (BOA) radiation.

Altitude	Aerosol			Cloud		
	I	Q	U	I	Q	U
TOA	± 0.43	± 1.38	± 0.87	± 0.24	± 5.41	± 3.59
BOA	± 0.32	± 0.82	± 0.46	± 0.51	± 3.86	± 5.19

Q are close to 0, see left panels in Figure 4.11), and $\pm 5.19\%$ for U . For U , and more importantly, for V the selected number of photons, 10^9 , were not sufficient to diminish the noise in MC simulations. For such strongly peaked scattering phase matrices, more than 10^{10} photons, should be employed (Kokhanovsky et al., 2010).

4.2 Model Intercomparison Project

SPARTA participated in the model intercomparison project that the International Polarized Radiative Transfer (IPRT) working group of the International Radiation Commission

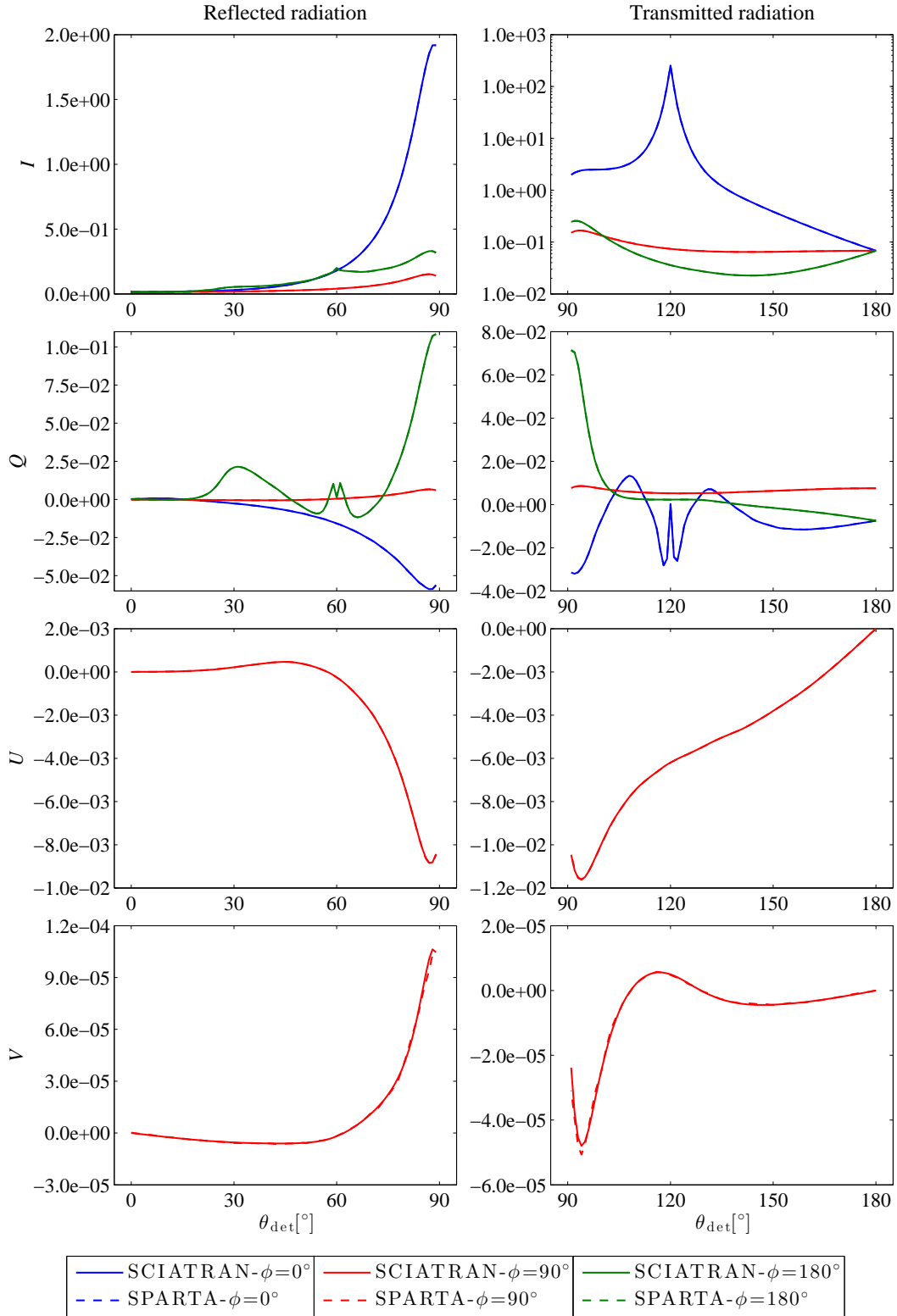


Figure 4.10: The Stokes vector for the aerosol layer in the reflected (left panels) and transmitted (right panels) radiation (straight lines - SCIATRAN, dashed lines - SPARTA). The solar zenith angle is 60° and the ϕ are 0°, 90°, and 180°.

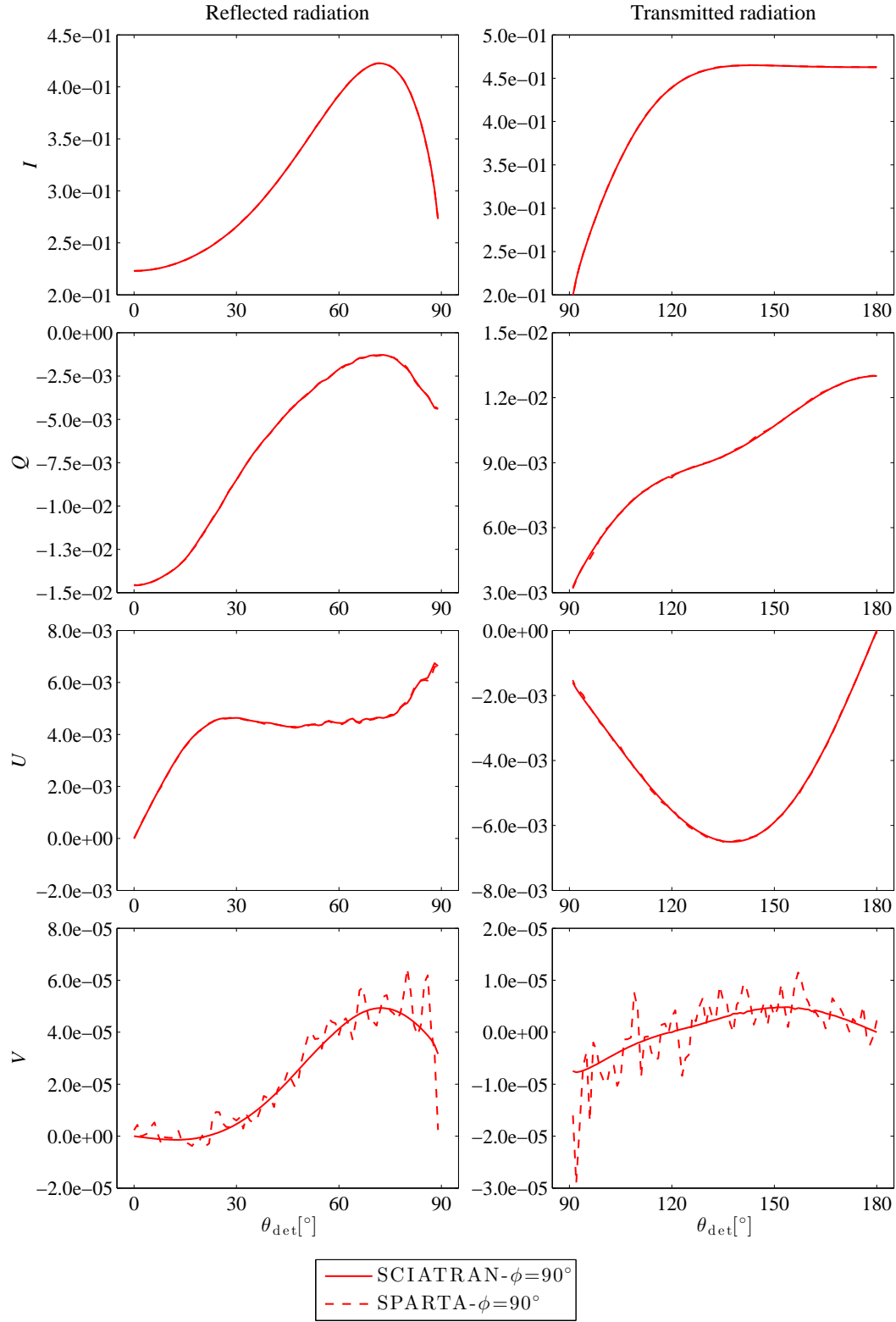


Figure 4.11: The same as in Figure 4.10, but for the cloud case.

launched (Emde et al., 2015). Six polarized radiative transfer models took part in this project, namely 3DMCPOL, IPOL, MYSTIC, Pstar, SHDOM, and SPARTA. Their basic features are listed in Section 2.9 (see Table 2.1); The aim of this project centers on providing benchmark results for a wide range of scenarios involving aerosol particles with realistic scattering phase matrices, polarizing ocean reflection and standard multi-layer atmospheres. Ten cases were considered:

A) Scenarios involving single-layers:

- A1 - Rayleigh scattering.
- A2 - Rayleigh scattering above a Lambertian surface.
- A3 - Spherical aerosol particles.
- A4 - Spheroidal aerosol particles.
- A5 - Liquid water cloud.
- A6 - Rayleigh scattering above an ocean surface.

B) Scenarios involving multi-layers:

- B1 - Rayleigh scattering for a standard atmosphere.
- B2 - Rayleigh scattering and absorption for a standard atmosphere.
- B3 - Aerosol profile and standard atmosphere.
- B4 - Standard atmosphere with a cloud layer above an ocean surface.

For further information about the test cases and the performance of the intercompared models the reader is referred to (Emde et al., 2015) and the IPRT webpage (<http://www.meteo.physik.uni-muenchen.de/~iprt/doku.php>).

The performance of SPARTA in this intercomparison was excellent, considering the noise of the Monte Carlo technique in radiance simulations. The major comparison is compiled in Tables 4.7 and 4.8 for the single-layer and multi-layer scenarios, respectively; tables are adopted from Emde et al. (2015). They tabulate the relative root mean square differences in percent between MYSTIC and SPARTA over the whole spectrum of the viewing directions (for the diffuse radiation for both the BOA and the TOA). For the scenarios involving single-layers, these differences are less than 0.2% for I and up to 2.9% for Q and U , dominated by case A5 due to the strong forward peak of the phase function of the water cloud droplets (see Figure 4.12) (less than 0.14% for I , 0.36% for Q , and 0.27% for U if A5 is excluded). Likewise, for the multi-layer cases, the corresponding differences are up to 0.3% for I , and up to 4.4% for Q and U , but excluding the most demanding case of cloud layer above ocean surface, namely B4, these differences are less than 0.08% for the first three Stokes elements. The number of photons selected for all the scenarios in this intercomparison was 10^8 ; results were obtained by individual Monte Carlo simulations.

In this work, the discussion will focus on atmospheric conditions not considered so far in this chapter, namely, spheroidal particles, ocean reflection, and standard atmospheres including

Table 4.7: Comparison between SPARTA and MYSTIC. Relative root mean square differences in percent for the single-layer scenarios. Columns $A5_{\text{part}}^{\text{pp}}$, $A5_{\text{part}}^{\text{al}}$ denote the relative root mean square differences excluding viewing angles between 0° and 10° (solar aureole); subscripts "pp" and "al" stand for the principal and almucantar planes. Abbreviation: n/a - not available.

SPARTA	A1	A2	A3	A4	$A5^{\text{pp}}$	$A5_{\text{part}}^{\text{pp}}$	$A5^{\text{al}}$	$A5_{\text{part}}^{\text{al}}$	A6
<i>I</i>	0.088	0.011	0.051	0.027	0.183	0.198	0.213	0.143	0.146
<i>Q</i>	0.367	0.055	0.120	0.041	2.256	1.725	2.050	2.011	0.152
<i>U</i>	0.275	0.042	0.084	0.060	n/a	n/a	2.928	2.881	0.231
<i>V</i>	n/a	n/a	0.639	2.607	n/a	n/a	67.027	64.972	n/a

Table 4.8: The same as in Table 4.7, but for the multi-layer scenarios. Columns $B3_{\text{part}}$, $B4_{\text{part}}$ denote the relative root mean square differences excluding viewing angles between 0° and 10° (solar aureole). Abbreviation: n/a - not available.

SPARTA	B1	B2	B3	$B3_{\text{part}}$	B4	$B4_{\text{part}}$
<i>I</i>	0.020	0.013	0.055	0.026	0.344	0.326
<i>Q</i>	0.030	0.029	0.071	0.045	3.710	2.699
<i>U</i>	0.023	0.023	0.064	0.036	4.368	2.856
<i>V</i>	n/a	n/a	1.982	1.439	182.181	88.770

molecular absorption (i.e., A4, A6, B2, B3, and B4). The scattering phase matrix elements for the three kind of particles (i.e., Rayleigh, spheroidal particles, water cloud droplets) considered in this section are found in Figure 4.12. In addition, the comparison will be restricted on the difference between SPARTA and MYSTIC. Note that for all cases normalized radiances are compared according to (not as in Eq. 3.38):

$$\text{Normalized Radiance} = \frac{\vec{S}}{F_0 \cdot (1000)^T}. \quad (4.4)$$

4.2.1 A4 - Spheroidal Aerosol Particles

The normalized Stokes vector in the reflected (upward at the TOA) and transmitted (downward at the BOA) radiation for a single-layer atmosphere containing randomly-oriented prolate spheroids has been calculated. No molecules were considered. The optical properties for the prolate spheroidal particles were derived at 350 nm wavelength as outlined by Gasteiger et al. (2011), utilizing the T-matrix (Mishchenko and Travis, 1997) and geometric optics (Yang et al., 2007) codes. The corresponding scattering phase matrix, described by Eq. (3.11), is illustrated by the black line in Figure 4.12. Computations involved an optical thickness of 0.2, a single-scattering albedo ($\tilde{\omega}$) of 0.787581, a solar position of ($\theta_0 = 40^\circ, \phi_0 = 0^\circ$), and a black non-scattering surface (surface albedo of 0); a set of different viewing zenith angles θ_{det} ($0^\circ - 80^\circ$ at BOA, and $100^\circ - 180^\circ$ at TOA with 5° increment), and relative azimuth angles ($0^\circ - 180^\circ$ with 5° increment) was selected. Note that MYSTIC follows the opposite convention for both the viewing zenith (with respect to the downward normal) and azimuth (anti-clockwise direction) angles as compared to SPARTA (see Sub-

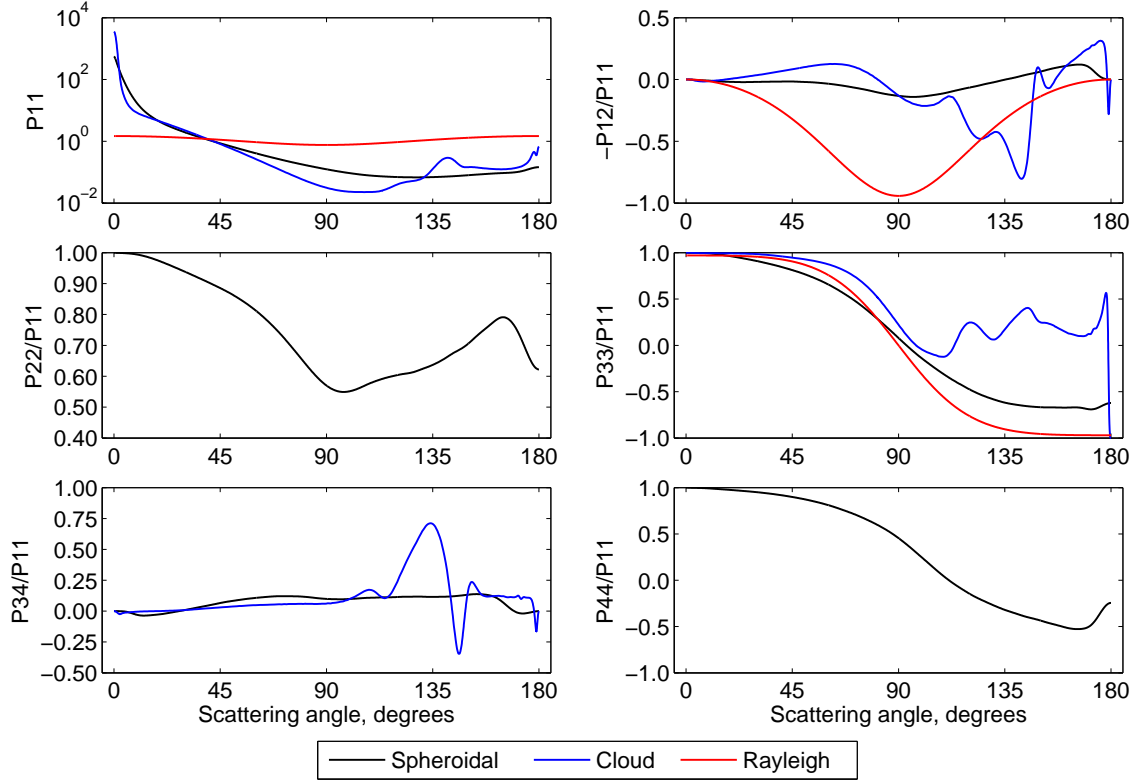


Figure 4.12: Phase matrix elements for the spheroidal aerosol particles, water cloud droplets (spherical), and molecular scattering (with a depolarization factor of 0.03) considered in cases A4, A6, B2, B3, and B4.

section 3.2.1), meaning the reflection and transmission definitions are reversed and the sign of the third and fourth Stokes components (U , V) are opposite.

In Figure 4.13, results are presented for three ϕ (0° , 45° , and 90°). The left panels show the normalized Stokes vector for the diffuse upward radiation at the TOA as a function of θ_{det} , and the right panels illustrate the absolute differences between SPARTA and MYSTIC. Note that for ϕ of 0° , U and V are zero.

The radiation field in the left plots illustrates the agreement between the models. The lines lie exactly on top of each other. For the last Stokes component, V , the curves could be slightly distinguished from one another. This can be explained by the very small values of circular polarization V (note the difference in magnitudes between the Stokes elements). Increasing the used number of photons will improve the accuracy in simulations. The right panels quantify the level of agreement between SPARTA and MYSTIC. For the first three Stokes components these differences are about three orders of magnitude less than the corresponding Stokes values. In particular, the relative root mean square differences are less than 0.06 % for the I , Q , and U and about 2.6 % for the last component V (see Table 4.7).

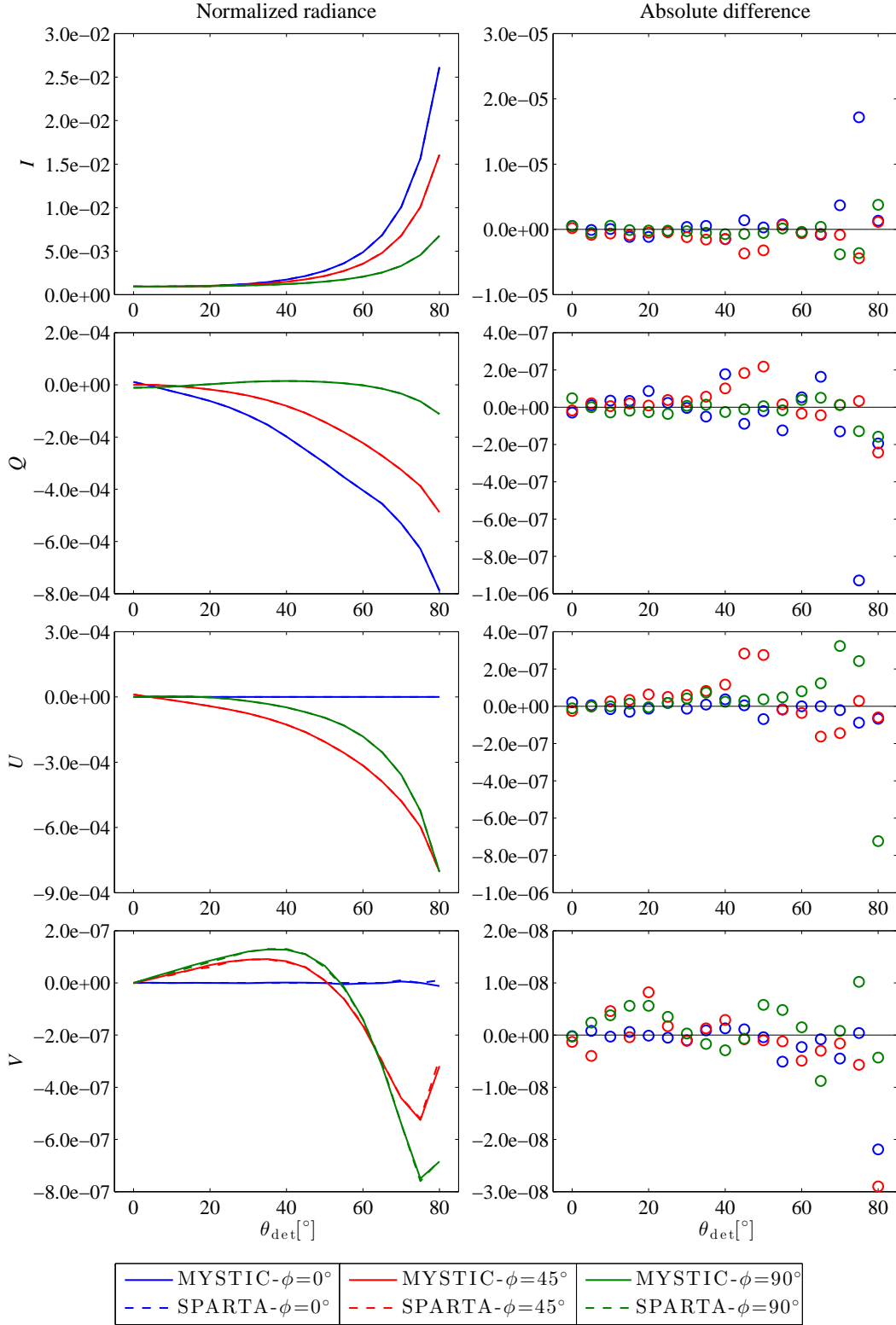


Figure 4.13: Comparison between SPARTA and MYSTIC for case A4: Spheroidal aerosol particles, $\tau = 0.2$, $\tilde{\omega} = 0.787581$, a solar position of ($\theta_0 = 40^\circ$, $\phi_0 = 0^\circ$), ϕ of 0° , 45° , and 90° , and $\alpha_L = 0$. Left: Normalized Stokes vector at the TOA (straight lines - MYSTIC, dashed lines - SPARTA). Right: Absolute differences between SPARTA and MYSTIC.

4.2.2 A6 - Rayleigh Scattering Above an Ocean Surface

To describe effects owing to anisotropic and polarizing ocean reflection, simulations were run for a single Rayleigh layer with an optical thickness of 0.1, pertaining to a solar position of $(\theta_0 = 45^\circ, \phi_0 = 0^\circ)$ above rough water surface. Towards this direction, the code by Mishchenko and Travis (1997) has been employed, calculating the reflection matrix for water surfaces utilizing the Fresnel formulas (see Subsection 3.2.5). The complex index of refraction in case of water is $\tilde{n} = 1.33 + 0 \cdot i$, and the near-surface wind speed was set to 2 m s^{-1} . The Rayleigh scattering phase matrix was interpreted in the analytical form, see Eq. (4.2), and a depolarization factor of 0.03 was used (red line in Figure 4.12). Molecular absorption was switched off.

The comparison between SPARTA and MYSTIC for the case of ocean reflection is depicted in Figure 4.14. It corresponds to the diffuse Stokes vector in the reflected radiation. Likewise the previous case (Figure 4.13), there is a very good agreement between the two models, their lines are coincident. Looking at the Table 4.7, the relative root mean square differences are less than 0.23 % for the Stokes vector (V is zero due to molecular scattering.) This case indicates that ocean reflection has been implemented correctly in SPARTA. Note that the phenomenon sunglint has been also reproduced by both models for a ϕ of 0° . This phenomenon occurs when the sun (here with a position of $(\theta_0 = 45^\circ, \phi_0 = 0^\circ)$) reflects off the ocean surface at the exact same angle at which the detector is observing the surface. However, the sunglint is not observed for a viewing angle of 45° , since water surface cannot be smooth, but rather rough.

4.2.3 B2 - Rayleigh Scattering and Absorption for a Standard Atmosphere

This scenario is a proper test for molecular absorption. The 1D fields of scattering and absorption coefficients have been generated at 325 nm wavelength for a US-standard model atmosphere (Anderson et al., 1986). The model atmosphere consists of 30 equidistant layers and is lifted to 30 km height. Only molecular scattering has been considered, whereby a depolarization factor of 0.03 has been selected, and the surface albedo was set to 0 (ideal absorbing surface). The solar position is $(\theta_0 = 60^\circ, \phi_0 = 0^\circ)$.

Figure 4.15 depicts the results for the Rayleigh multi-layer atmosphere underlying a black non-scattering surface for the transmitted radiation at the BOA. As for the cases of single-layer setups, an outstanding agreement between SPARTA and MYSTIC is noticed. By quantifying their accord, deviations of only up to 0.03 % for the first three Stokes elements were calculated (see Table 4.8). The bottom line is that molecular absorption is considered correctly in SPARTA.

4.2.4 B3 - Aerosol Profile and Standard Atmosphere

This case is the subsequent next step after the scenario B2, meaning in a standard Rayleigh atmosphere (with a depolarization factor of 0.03) including molecular absorption, with scattering and absorption coefficients calculated at 350 nm wavelength, a profile of aerosol par-

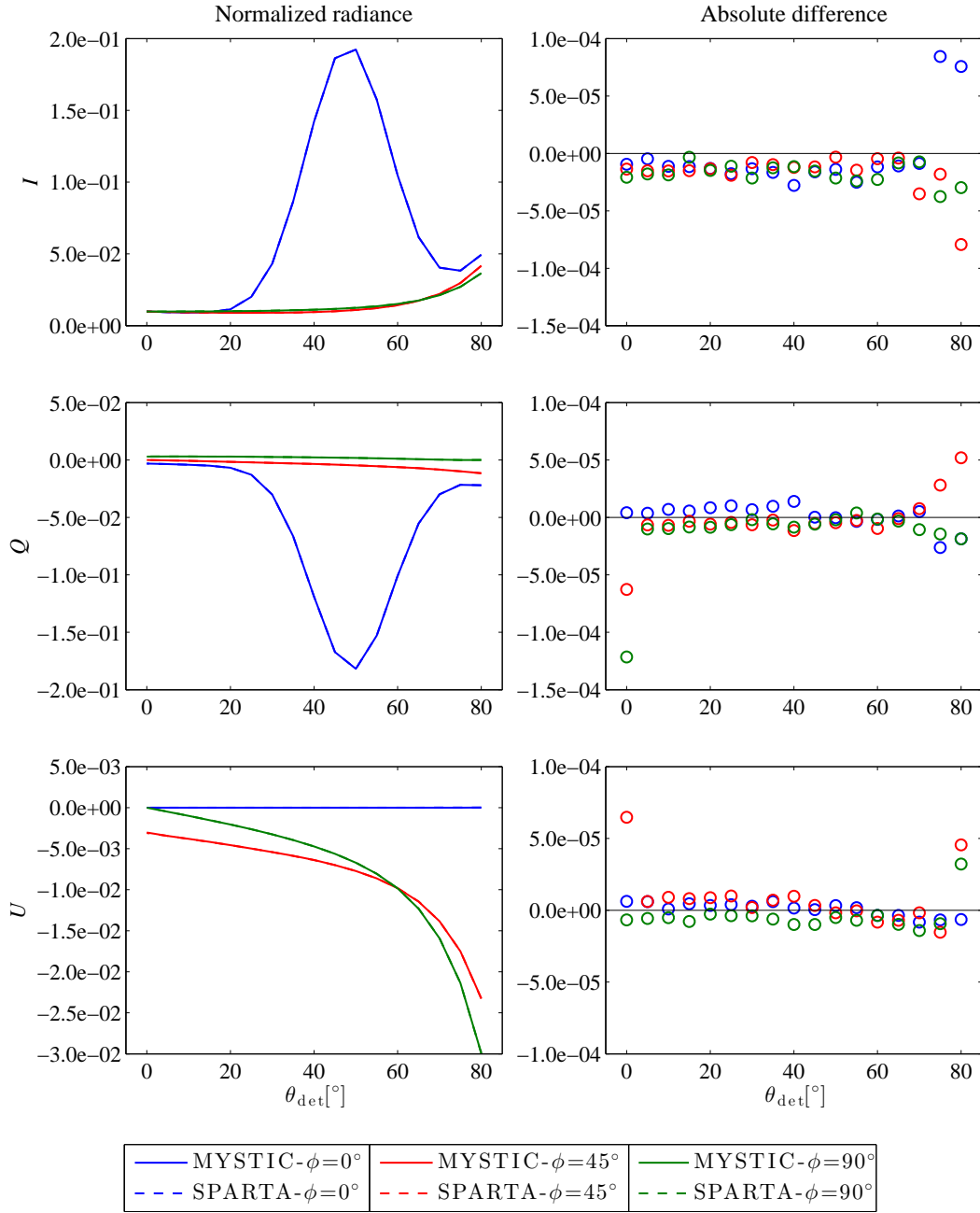


Figure 4.14: Comparison between SPARTA and MYSTIC for case A6: Rayleigh scattering above an ocean surface, $\tau = 0.1$, $\tilde{\omega} = 1$, a solar position of $(\theta_0 = 45^\circ, \phi_0 = 0^\circ)$, and ϕ of 0° , 45° , and 90° . Left: Normalized Stokes vector at the TOA (straight lines - MYSTIC, dashed lines - SPARTA). Right: Absolute differences between SPARTA and MYSTIC.

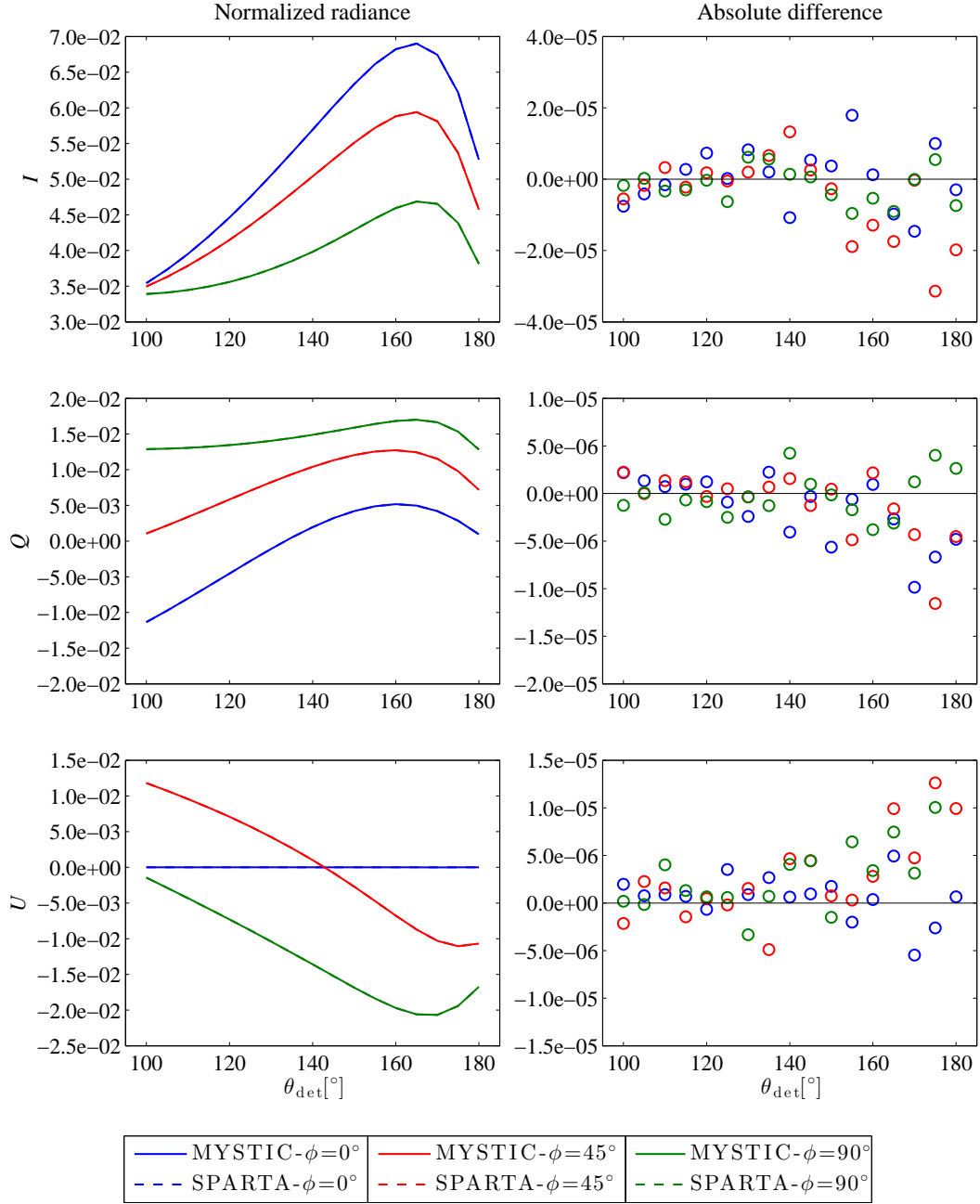


Figure 4.15: Comparison between SPARTA and MYSTIC for case B2: Rayleigh scattering and absorption for a standard atmosphere at 325 nm wavelength, a solar position of $(\theta_0 = 60^\circ, \phi_0 = 0^\circ)$, ϕ of 0° , 45° , and 90° , and $\alpha_L = 0$. Left: Normalized Stokes vector at the BOA (straight lines - MYSTIC, dashed lines - SPARTA). Right: Absolute differences between SPARTA and MYSTIC.

ticles has been added (Emde et al., 2015). The aerosol microphysical properties correspond to prolate spheroidal particles, adopted from Subsection 4.2.1.

Results are presented for the downward radiation field (transmission at the BOA) for a solar position of $(\theta_0 = 30^\circ, \phi_0 = 0^\circ)$, three ϕ (0° , 45° , and 90°), and a black underlying surface (see Figure 4.16). In the same way, there is an exceptional concurrence between the models, their outputs cannot be told apart.

Both models can represent the strong forward peak of the scattering phase function of the ensemble of spheroidal particles (see the black line in the P_{11} plot of Figure 4.12); it is illustrated in the I component of the Stokes vector. Table 4.8 outlines that the largest deviation between SPARTA and MYSTIC is 0.071 % for the first three Stokes components, or 0.045 % if the solar aureole is excluded (viewing directions between 0° and 10°). For V the differences are about 2 % (or 1.5 % without the solar aureole regime).

4.2.5 B4 - Standard Atmosphere with a Cloud Layer Above an Ocean Surface

The final and most complicated scenario, with high demands in computation power for the Monte Carlo models, involves a standard molecular atmosphere with a cloud layer underlying ocean reflection. For Rayleigh scattering, a depolarization factor of 0.03 was considered; molecular absorption was excluded. For ocean reflection, the same definitions and settings as in Subsection 4.2.2 were adopted, meaning refractive index of $\tilde{n} = 1.33 + 0 \cdot i$, representing water, and near-surface wind speed of 2 m s^{-1} . The cloud layer is characterized with an optical thickness of 5 and stretches between 2 and 3 km height. The cloud microphysical properties, representing water cloud droplets (spherical) with an effective radius of $10 \text{ }\mu\text{m}$, have been calculated utilizing Mie theory at 800 nm wavelength (libRadtran package Wiscombe, 1980; Mayer and Kylling, 2005). The resulting scattering phase matrix is depicted by the blue line in Figure 4.12.

Figures 4.17 and 4.18 illustrate the full Stokes vector for the diffuse radiation at the BOA and the TOA, respectively, considering a solar position of $(\theta_0 = 60^\circ, \phi_0 = 0^\circ)$, and relative azimuth angles of 0° , 45° , and 90° . Here, the largest deviations were observed. Starting from surface transmittance, left panels of Figure 4.17, SPARTA and MYSTIC agree very well for I , even for the strong forward peak of the phase function of the water cloud droplets. However, for the other Stokes components (Q , U , and V), we can clearly observe the Monte Carlo noise; especially for V . For this Stokes component, the MC noise in SPARTA is at the same magnitude or even larger than its actual values.

Despite this, no systematic error was found; it is clearly the statistical uncertainty of the MC technique. In the right panels, the differences between the models are shown. These differences are about two orders of magnitude less than the corresponding Stokes values for Q and U , but at the same magnitude for V . In the same direction are the findings for the normalized Stokes vector for the upward diffuse radiation at the TOA. Going back to Table 4.8, the relative root mean square differences are 0.34 % for the I , and in the range of 3-4 % for linear polarization (Q , U). These differences are slightly decreased, providing that the solar aureole is excluded (0.32 % for I , and between 2-3 % for Q and U).

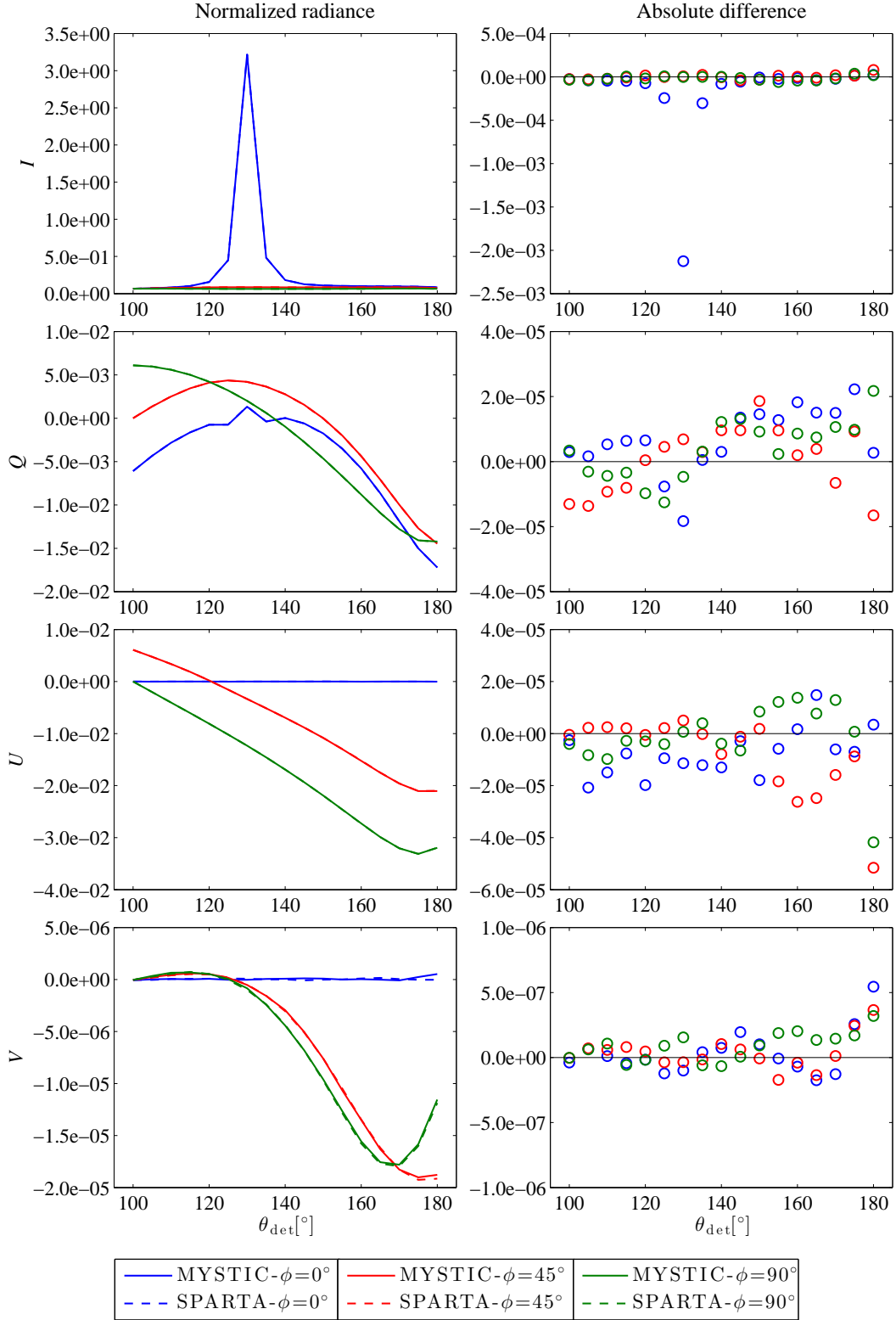


Figure 4.16: Comparison between SPARTA and MYSTIC for case B3: Aerosol profile of spheroidal particles and a standard atmosphere at 350 nm wavelength, a solar position of ($\theta_0 = 30^\circ, \phi_0 = 0^\circ$), ϕ of 0° , 45° , and 90° , and $\alpha_L = 0$. Left: Normalized Stokes vector at the BOA (straight lines - MYSTIC, dashed lines - SPARTA). Right: Absolute differences between SPARTA and MYSTIC.

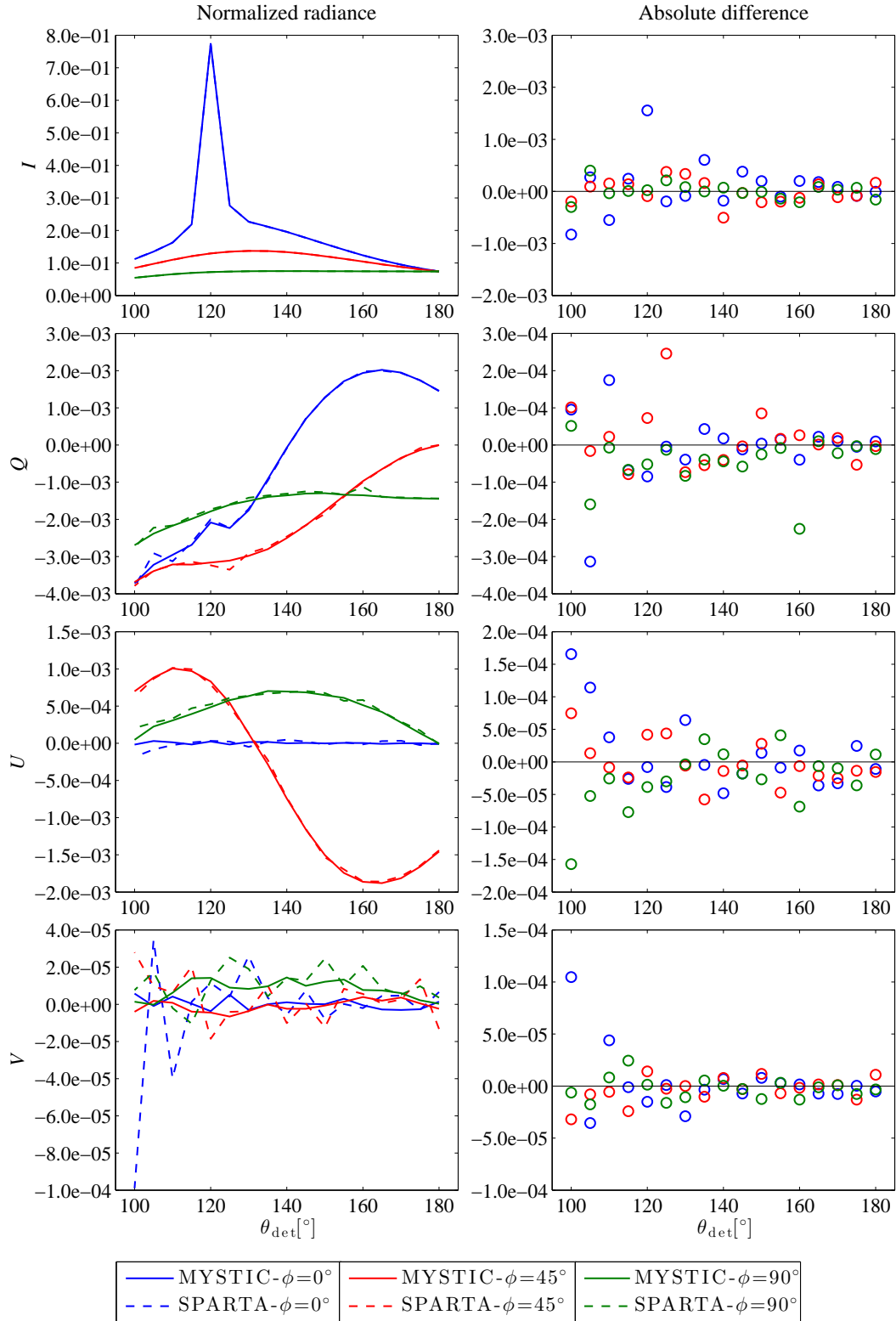


Figure 4.17: Comparison between SPARTA and MYSTIC for case B4: Standard atmosphere with a cloud layer above an ocean surface at 800 nm wavelength, a solar position of ($\theta_0 = 60^\circ$, $\phi_0 = 0^\circ$), and ϕ of 0° , 45° , and 90° . Left: Normalized Stokes vector at the BOA (straight lines - MYSTIC, dashed lines - SPARTA). Right: Absolute differences between SPARTA and MYSTIC.

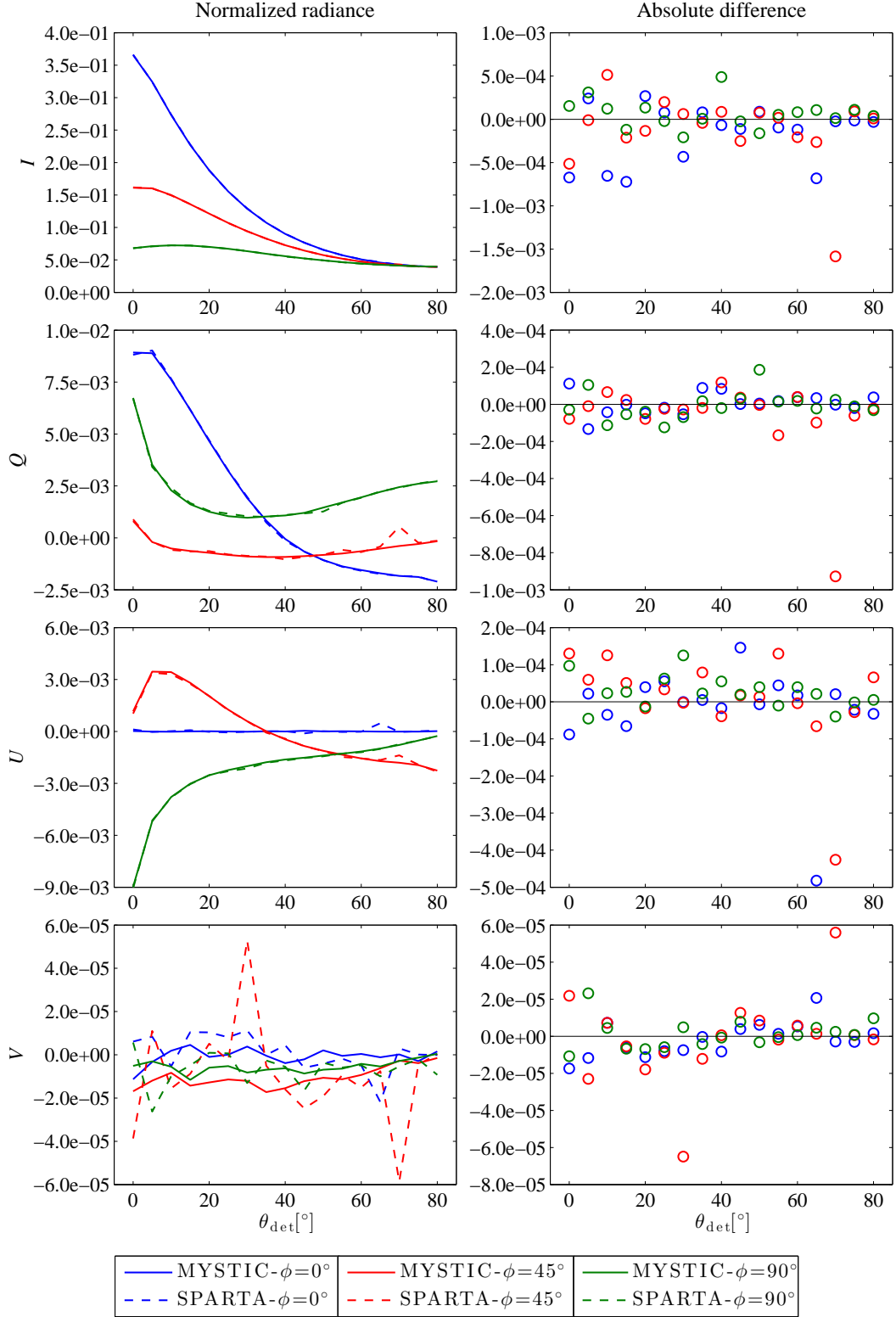


Figure 4.18: The same as in Figure 4.17, but for the Stokes vector at the TOA.

Recall that for all the cases of this intercomparison 10^8 photons were used; results were produced from individual simulations. For such demanding scenarios and particles with rather asymmetric phase matrix, more than 10^9 photons should be employed for the simulations (see the cloud case in Subsection 4.1.3).

5 Applications

While in Chapters 3 and 4 a new three-dimensional vector radiative transfer model is introduced and validated (respectively), in this chapter, this new tool is employed to quantify polarization effects in the field of remote sensing. Solar radiative transfer simulations for LIDAR-measured fields of optical properties of Saharan dust have been performed in order to quantify the polarization effects induced by neglecting the horizontal photon transport and internal inhomogeneities in radiance simulations. Results are presented for two LIDAR-based measurement cases. In addition, a sensitivity study has been carried out to illustrate the effects prompted by ignoring polarization in radiance simulations for a pure 1D Rayleigh atmosphere. The effects of polarization for a realistic 2D scenario are also discussed. Parts of this Chapter were published in Barlakas et al. (2016).

5.1 Polarization Radiative Effects

By means of SPARTA, polarization radiative effects for LIDAR-measured inhomogeneous Saharan dust fields are discussed, performing 2D, IPA and 1D reflectance and transmittance calculations at 532 nm wavelength.

5.1.1 Measurement Cases

Two case studies have been investigated. Case 1 is related to the measurements in the night from 3 to 4 June 2008, during the second phase of the SAMUM project (Heintzenberg, 2009; Ansmann et al., 2011; Tesche et al., 2011). Case 2 considered the nighttime measurements of 23 May 2013, from the trans-Atlantic cruise of the research vessel METEOR (Kanitz et al., 2014).

The LIDAR measurements of extinction coefficients at 532 nm wavelength for the two measurement cases are illustrated in Figure 5.1 and Figure 5.2. They correspond to the height-time LIDAR profile in terms of the 5 and 2.3 min averaged extinction coefficient in inverse Megameters (Mm^{-1}). The observations on 3-4 June 2008 record two distinct dust layers as outlined by Tesche et al. (2011). A thin dust layer between 1-2 km and an elevated thicker layer between 3-5 km separated by a transition layer (close to clean air, but not particle-free). The LIDAR measurements also indicate a pure Rayleigh atmosphere above 5 km and a marine boundary layer (MBL) that is lifted to about 1 km height. On 23 May 2013 the measured data indicate a well defined dust plume that stretched from 0.7 to 4.8 km height with maximum extinction coefficients of 340 Mm^{-1} . A MBL and a layer consisting of molecules only are documented below and above the dust layer. Further information about the latter test case can be found in Kanitz et al. (2014).

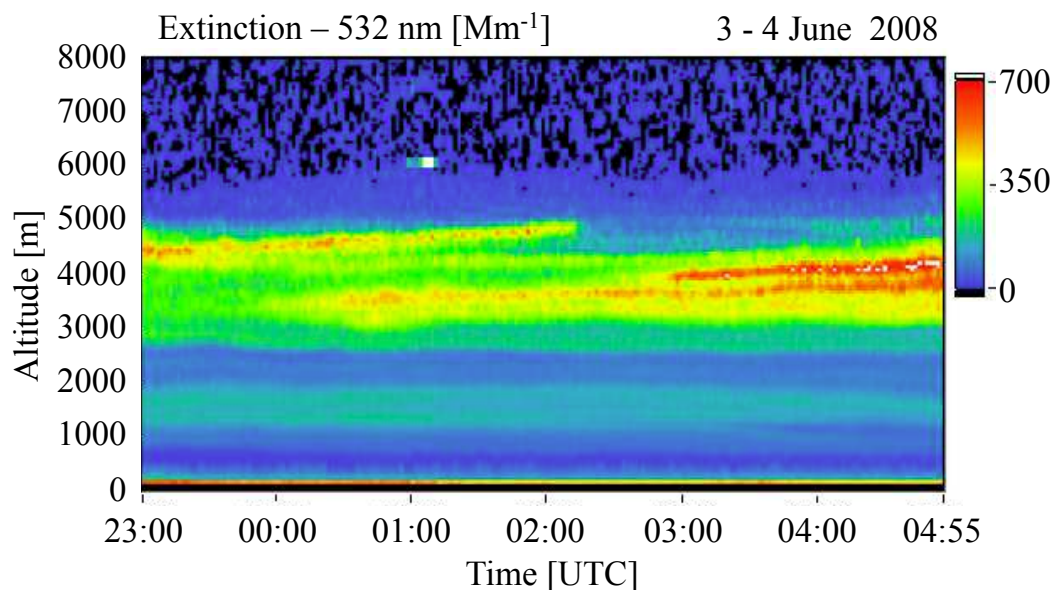


Figure 5.1: Height - time display of LIDAR measurements during the SAMUM-2 field experiment in terms of the 2.3 min-averaged extinction coefficient. Measurement example: Cape Verde, 3-4 June 2008. Courtesy of Holger Baars, TROPOS.

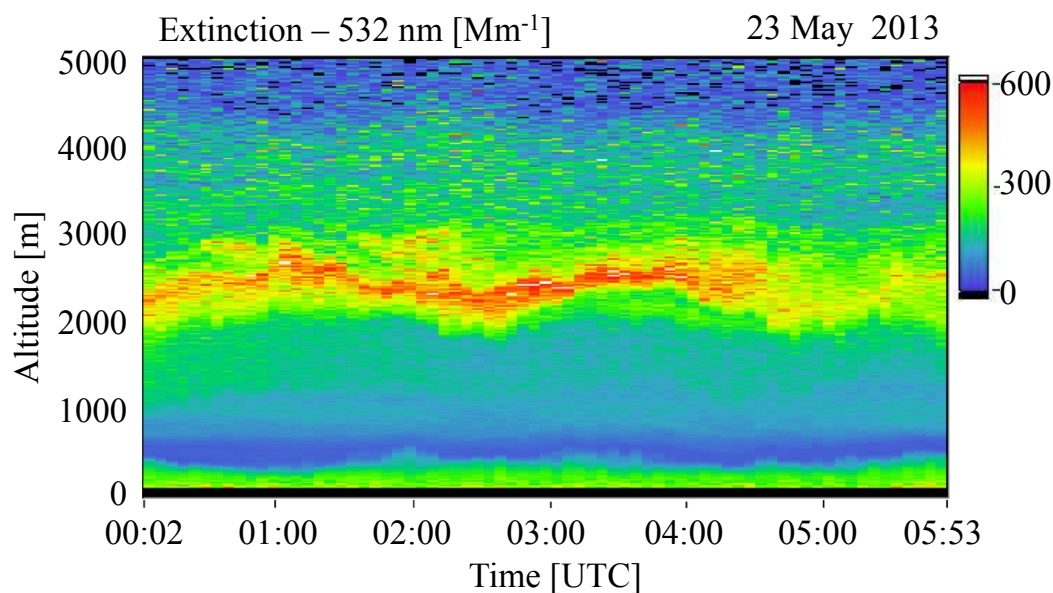


Figure 5.2: Height - time display of LIDAR measurements during the METEOR cruise in terms of the 5 min-averaged extinction coefficient. Measurement example: Cape Verde, 23 May 2013. Courtesy of Holger Baars, TROPOS.

5.1.2 Scattering Properties of Molecules and Aerosol Particles

The 2D fields of extinction and scattering coefficients, single-scattering albedo and scattering phase matrix of the inhomogeneous Saharan dust were constructed on the basis of the LIDAR measurements sharing the geometrical and optical properties of dust plumes. The height-time LIDAR aerosol extinction profiles (including molecular extinction) were converted into vertically integrated optical thickness (see Figure 5.3). The model domains were defined by $209 \times 1 \times 168$ pixels with a size of 0.96 km along the horizontal axis (overall ~ 201.2 km), for the SAMUM case, and $70 \times 1 \times 1321$ pixels with a size of 2.06 km along the horizontal axis (overall ~ 144.6 km), for the METEOR case. The vertical length of the entire grid is about 10 km for both scenarios, with a pixel size of 60 m and 7.5 m, respectively.

The scattering Rayleigh phase matrix was taken in the analytical form (see Eq. 4.2). The wavelength dependent depolarization factor ($\delta = 0.0842$ for $\lambda = 532$ nm) and the scattering coefficients were computed using the formulation given in Bodhaine et al. (1999). Molecular absorption was parameterized with the LOWTRAN band model (Pierluissi and Peng, 1985), as adopted from the SBDART code (Ricchiuzzi et al., 1998). For both scattering and absorption coefficients a tropical model atmosphere has been considered (Anderson et al., 1986). The volumetric scattering and absorption coefficient profiles are shown in Figure 5.4.

The aerosol microphysical properties of the MBL correlate with water soluble particles for dif-

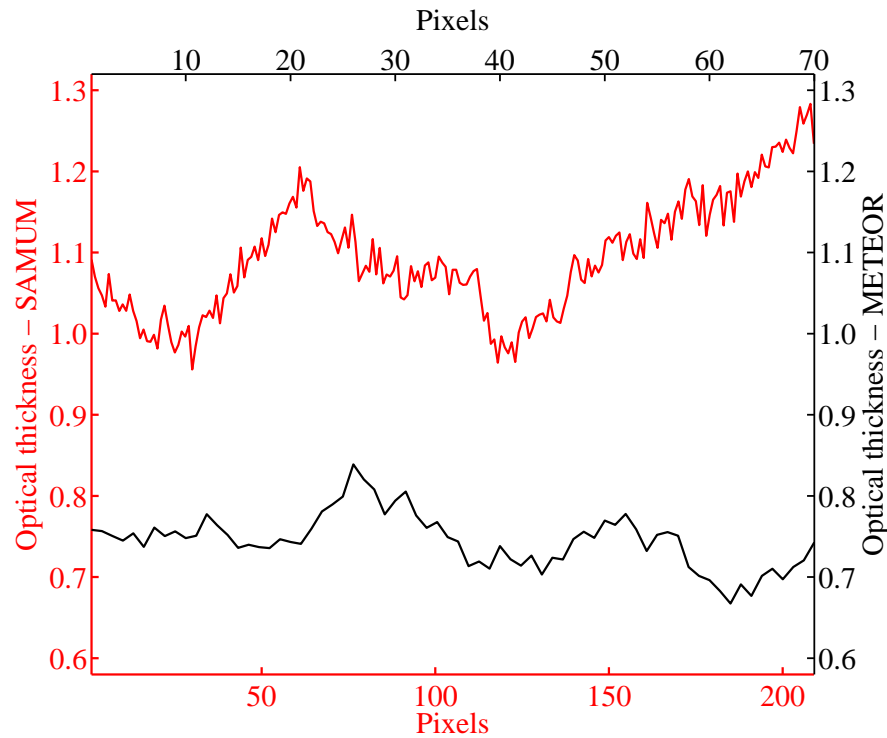


Figure 5.3: Optical thickness at 532 nm for the SAMUM measurement case (red line) and the METEOR measurement case (black line).

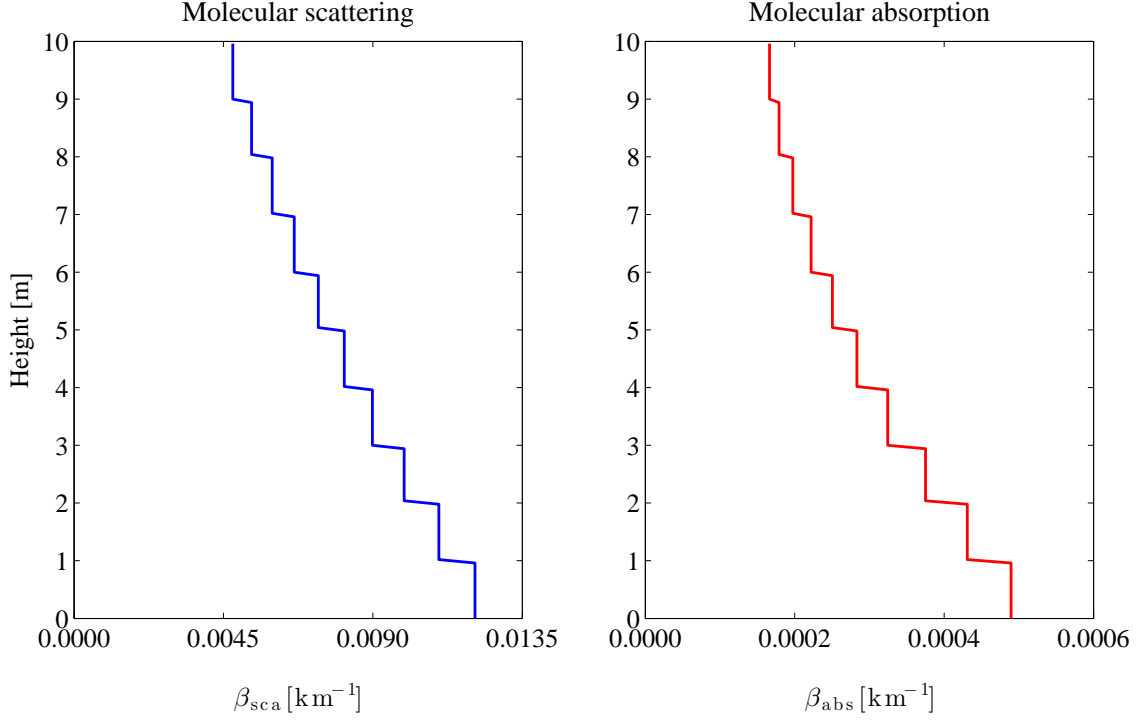


Figure 5.4: Scattering and absorption coefficient profiles at 532 nm for the Rayleigh atmosphere.

ferent relative humidity at 532 nm according to the sounding measurements (OPAC database Hess et al., 1998; Emde et al., 2010).

For the dust scattering properties, the scattering phase matrix data by Torge et al. (2011) were used. This study draws on research conducted on the measurements in the course of the SAMUM project (Otto et al., 2009; Kandler et al., 2009, 2011). The optical properties of non-spherical dust particles have been calculated utilizing the MIESCHKA code (Wauer et al., 2004), which is a T-matrix code, for rather small spheroids with a size parameter of up to 40. For larger irregular shaped particles (size parameter of up to 143), a ray-tracing code (Macke et al., 1997) anchored in the geometric optics method has been employed. Five particle size classes have been considered with an effective radius ranging from 0.166 μm to 13.804 μm . A detailed explanation of the methods used to model the scattering phase matrices of the mineral dust particles is given in Torge et al. (2011). Figure 5.5 illustrates the scattering phase matrix elements for the five particle size classes and the mean scattering phase matrix elements over all the size classes examined in this study.

The total scattering phase matrix $\tilde{\mathbf{P}}^{\text{tot}}(\vartheta)$ at each grid box is derived by averaging the Rayleigh scattering phase matrix, $\tilde{\mathbf{P}}_{\text{r}}(\vartheta)$, and the scattering phase matrix of dust particles, $\tilde{\mathbf{P}}_{\text{d}}(\vartheta)$, weighted over their characteristic volumetric scattering coefficients ($\beta_{\text{sca}}^{\text{r}}$ and $\beta_{\text{sca}}^{\text{d}}$ for the individual grid box):

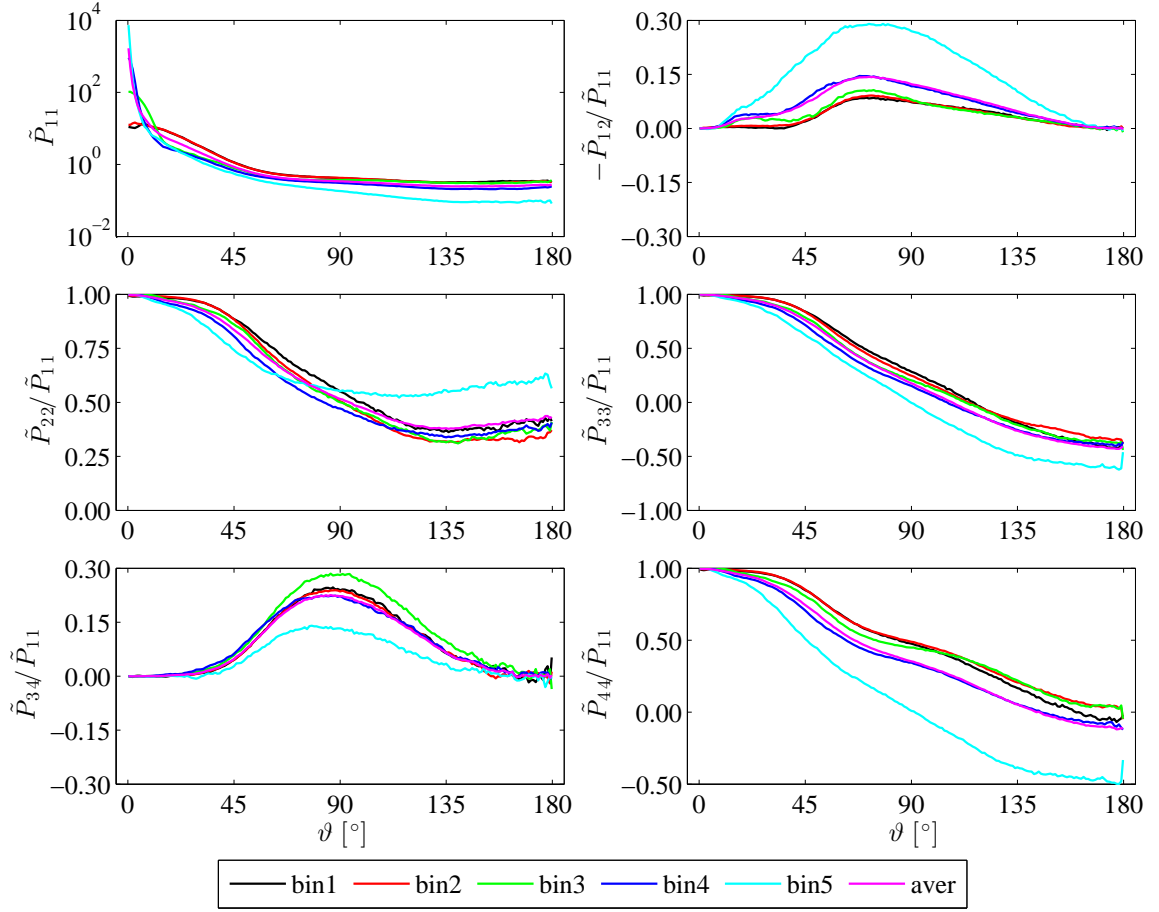


Figure 5.5: Scattering phase matrix elements for the five particle size classes and the mean scattering phase matrix elements over all the different size classes considered in this study. Particle size classes with effective radius 0.166 μm (bin1), 0.501 μm (bin2), 1.514 μm (bin3), 4.571 μm (bin4), and 13.804 μm (bin5).

$$\tilde{\mathbf{P}}^{\text{tot}}(\vartheta) = \frac{\beta_{\text{sca}}^{\text{r}} \cdot \tilde{\mathbf{P}}_{\text{r}}(\vartheta) + \beta_{\text{sca}}^{\text{d}} \cdot \tilde{\mathbf{P}}_{\text{d}}(\vartheta)}{\beta_{\text{sca}}^{\text{r}} + \beta_{\text{sca}}^{\text{d}}}, \quad (5.1)$$

Likewise, the total single-scattering albedo is given by the sum of the Rayleigh scattering coefficient and the scattering coefficient of the aerosol particles divided by the total volumetric extinction coefficient.

5.1.3 Monte Carlo Simulations

Polarized radiative transfer simulations using SPARTA were conducted for three different solar zenith angles (0° , 47° , and 70°), the same viewing directions for the reflected radiation at the TOA, and the supplementary angles (180° , 133° , and 110°) for the transmitted radiation at the BOA, and a relative azimuth angle of 0° above a Lambertian surface with albedo $\alpha_{\text{L}} = 0.05$, that corresponds to an ocean surface. Besides, the number of photons was 10^9

(10 individual simulations) so that the Monte Carlo noise, resulting from the strongly peaked dust phase matrices (Figure 5.5), is diminished.

2D - 1D Comparison

The domain-averaged normalized radiances of reflection and transmission have been calculated between the 2D and 1D modes, meaning the 2D results were averaged over the whole number of pixels and compared to the 1D counterpart. These differences are compiled in Table 5.1. Note that this comparison illustrates the total radiative effect (internal heterogeneity + horizontal photon transport).

The differences in the domain-averaged reflectivity and transmissivity are insignificant between the 2D and 1D modes. Quantitatively we see in Table 5.1 that these differences are limited to 0.316 % for I , and 1.277 % for Q in case of the SAMUM measurement scenario and up to 0.141 % for I , and 0.932 % for Q in case of the METEOR scenario. Therefore, the 2D normalized reflectance and transmittance fields were compared pixel by pixel with the 1D to locate and quantify the maximum differences to the domain average. The following figures

Table 5.1: Domain-averaged differences between the 2D and 1D modes for both the reflected (TOA) and transmitted (BOA) radiation.

TOA	SAMUM		METEOR	
$\theta_0 = 0^\circ$	I	Q	I	Q
$\theta_{\text{det}} = 0^\circ$	0.072	0.018	0.038	0.012
$\theta_{\text{det}} = 47^\circ$	0.074	0.005	0.058	0.030
$\theta_{\text{det}} = 70^\circ$	0.102	0.008	0.071	0.012
$\theta_0 = 47^\circ$	I	Q	I	Q
$\theta_{\text{det}} = 0^\circ$	0.052	0.006	0.016	0.019
$\theta_{\text{det}} = 47^\circ$	0.086	0.012	0.030	0.017
$\theta_{\text{det}} = 70^\circ$	0.089	0.004	0.059	0.037
$\theta_0 = 70^\circ$	I	Q	I	Q
$\theta_{\text{det}} = 0^\circ$	0.026	1.277	0.008	0.932
$\theta_{\text{det}} = 47^\circ$	0.055	0.006	0.027	0.027
$\theta_{\text{det}} = 70^\circ$	0.087	0.015	0.029	0.001
BOA	SAMUM		METEOR	
$\theta_0 = 0^\circ$	I	Q	I	Q
$\theta_{\text{det}} = 180^\circ$	0.122	0.014	0.079	0.048
$\theta_{\text{det}} = 133^\circ$	0.077	0.009	0.078	0.097
$\theta_{\text{det}} = 110^\circ$	0.451	0.665	0.045	0.043
$\theta_0 = 47^\circ$	I	Q	I	Q
$\theta_{\text{det}} = 180^\circ$	0.137	0.009	0.041	0.032
$\theta_{\text{det}} = 133^\circ$	0.284	0.514	0.141	0.033
$\theta_{\text{det}} = 110^\circ$	0.094	0.059	0.079	0.054
$\theta_0 = 70^\circ$	I	Q	I	Q
$\theta_{\text{det}} = 180^\circ$	0.316	0.302	0.127	0.244
$\theta_{\text{det}} = 133^\circ$	0.137	0.085	0.074	0.060
$\theta_{\text{det}} = 110^\circ$	0.150	0.034	0.060	0.019

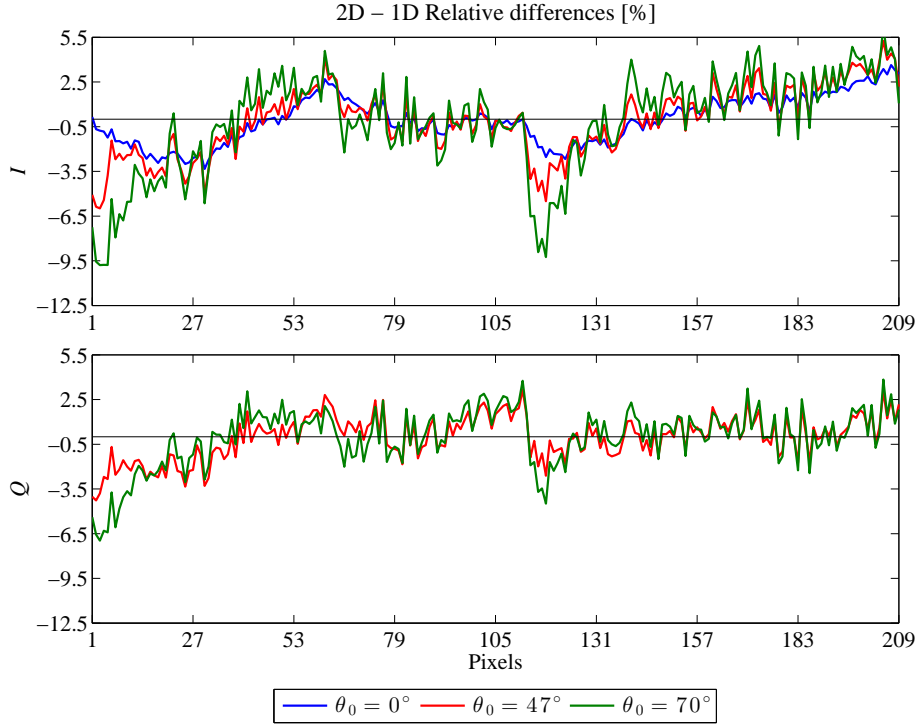


Figure 5.6: SPARTA simulated reflectance field including polarization for the SAMUM case: Relative differences in percent between 2D and 1D calculations for three solar zenith angles 0° , 47° , and 70° at a viewing zenith angle of 0° . Upper: first Stokes element. Lower: second Stokes element.

illustrate the relative differences (RD) in percent between the 2D calculations (horizontal + vertical photon transport) and the 1D calculations (only vertical photon transport), for the different sun positions (0° , 47° , and 70°) as a function of the pixel number. The upper plots depict the first Stokes component (I) and the lower plots the second component (Q).

Starting from the SAMUM measurement case, results are compiled in Figures 5.6 and 5.7 for the reflected radiation at the TOA ($\theta_{\text{det}} = 0^\circ$ and 47° , where the observed effects are largest). From Table 5.1, the domain-averaged reflectivity is almost identical for both the 1D and 2D calculations. However, at the regions with large spatial gradient in optical thickness, the radiance field of the 2D mode differs by about $\pm 9.8\%$ for I and $\pm 6.9\%$ for Q in case of $\theta_{\text{det}} = 0^\circ$ and $\pm 12.2\%$ for I and $\pm 8.1\%$ for Q for $\theta_{\text{det}} = 47^\circ$ from the fields of the 1D mode (see Figures 5.6 and 5.7). The combined radiative effect is more pronounced in I rather than in Q . Note in the lower plot of Figure 5.6 that the RD corresponding to a solar position of $\theta_0 = 0^\circ$ are excluded because for detector position of 0° the resulting values of linear polarization (Q) are too small to derive the relative difference between the 2D and 1D modes. In general, increasing the solar zenith angle, the RD, as well as the range, and average of RD are increasing because the photon path length is increasing and, therefore, the number of scattering events is increasing as well (see Table 5.2). In other words, an increase in the solar zenith angle gives the initial solar photon an increased horizontal component, leading to enhanced of the photon propagation within the atmosphere. As a result, the total radiative effect due to the neglected domain internal heterogeneities and horizontal photon

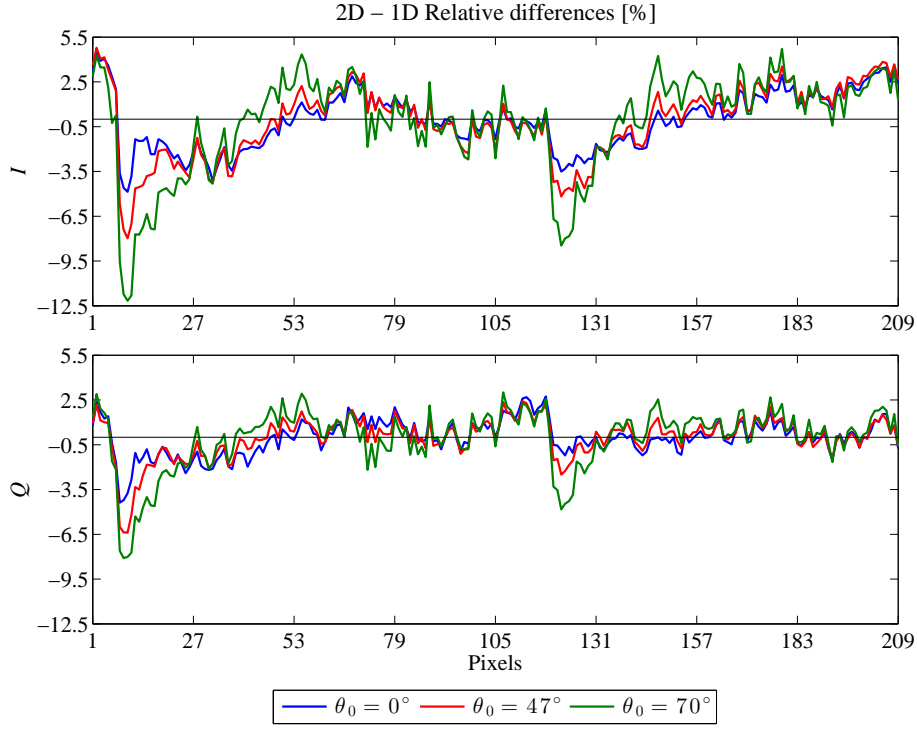


Figure 5.7: The same as in Figure 5.6 but for a viewing zenith angle of 47° .

transport is intensified.

In the same direction are the findings for the METEOR case (see Figures 5.8 and 5.9) for the first Stokes component I , but the resulting RD are much lower, less than $\pm 5.3\%$ (for $\theta_{\text{det}} = 0^\circ$ and 47°). For Q , no increase of RD with increase of the solar zenith angle were observed. RD range up to $\pm 3.1\%$. The smaller differences are explained by the lower variability that is resolved by the larger horizontal pixel size, and more importantly, by the lower gradient in optical thickness (see Figure 5.3). At a solar zenith angle of 0° and a viewing zenith angle of 0° , no RD were calculated for the second Stokes element, owing to its very small values (see Figure 5.8).

A closer look at Tables 5.2 and 5.3 indicates some exceptions. For example, for the SAMUM measurement scenario and a viewing zenith angle of 70° , the relative difference dependency on the solar position is not detected. RD range up to $\pm 9.9\%$ for I and $\pm 6.8\%$ for Q . For the METEOR scenario, although for observation zenith angles of 0° and 47° no trend was observed for Q , for 70° the RD dependency on the solar position holds.

For the transmitted radiation at the BOA, results are presented for observation zenith angles of 180° and 110° (see Figures 5.10 and 5.11), for the SAMUM measurement case. Table 5.1, shows that the differences between the 2D and 1D modes for the domain-averaged transmissivity are insignificant. On the other hand, in Figures 5.10 and 5.11 extreme values of the relative differences between the two modes (especially in Figures 5.11) are observed. These extreme values, denoted by the shaded areas in Figures 5.10 and 5.11, could be explained by the periodic boundary conditions employed in SPARTA. The major premise of this as-

Table 5.2: SAMUM measurement case analysis: Maximum, minimum, range, average of positive values, average of negative values, and average of the relative difference in percent between the 2D and 1D modes for both the reflected and transmitted radiation. Abbreviation: n/a - not available.

	<i>I</i>			<i>Q</i>		
Parameter	$\theta_0 = 0^\circ$	$\theta_0 = 47^\circ$	$\theta_0 = 70^\circ$	$\theta_0 = 0^\circ$	$\theta_0 = 47^\circ$	$\theta_0 = 70^\circ$
TOA	Viewing zenith angle of 0°					
maximum	3.6319	5.2585	6.2057	n/a	3.1451	3.8428
minimum	-3.3319	-5.9833	-9.7929	n/a	-4.2670	-6.9685
range	6.9638	11.2418	15.9986	n/a	7.4121	10.8113
average _{pos}	1.2877	1.7412	2.2464	n/a	1.0760	1.3291
average _{neg}	-1.2546	-1.8957	-2.8721	n/a	-1.2749	-1.6688
average	1.2712	1.8184	2.5592	n/a	1.1755	1.4990
TOA	Viewing zenith angle of 47°					
maximum	4.4363	4.7805	4.7117	2.7352	2.4152	3.0087
minimum	-4.8689	-7.9736	-12.1659	-4.3733	-6.3868	-8.0956
range	9.3051	12.7542	16.8776	7.1086	8.8020	11.1043
average _{pos}	1.4833	1.6953	1.8512	0.9153	0.8597	1.1160
average _{neg}	-1.6213	-2.2697	-3.2540	-0.8772	-1.0975	-1.8750
average	1.5523	1.9825	2.5526	0.8962	0.9786	1.4955
TOA	Viewing zenith angle of 70°					
maximum	2.7231	1.7930	3.5017	3.3459	2.3689	2.8512
minimum	-3.5628	-5.4313	-9.8750	-3.6939	-5.4196	-6.8169
range	6.2859	7.2243	13.3767	7.0398	7.7885	9.6681
average _{pos}	0.9896	0.7143	1.3402	0.7295	0.6974	1.0150
average _{neg}	-1.2759	-1.2763	-2.3029	-0.7897	-1.0025	-1.5618
average	1.1328	0.9953	1.8216	0.7596	0.8500	1.2884
BOA	Viewing zenith angle of 180°					
maximum	2.7658	4.6561	4.5058	2.4165	3.0667	4.9533
minimum	-3.8205	-6.2312	-10.8537	-2.8913	-7.2659	-9.5531
range	6.5863	10.8873	15.3595	5.3077	10.3326	14.5064
average _{pos}	0.9850	1.7541	1.7432	1.0240	1.0081	1.9122
average _{neg}	-1.1843	-2.0074	-2.7840	-1.1155	-1.4087	-2.4726
average	1.0847	1.8808	2.2636	1.0697	1.2084	2.1924
BOA	Viewing zenith angle of 133°					
maximum	7.9892	3.4031	5.9502	4.4302	8.3210	7.1574
minimum	-4.0986	-10.5837	-16.8177	-4.3908	-26.3171	-15.5440
range	12.0879	13.9868	22.7680	8.8210	34.6380	22.7015
average _{pos}	1.6292	1.4834	2.2521	1.0300	3.3412	2.9652
average _{neg}	-1.6598	-2.5882	-3.1336	-1.3753	-5.4702	-3.7747
average	1.6445	2.0358	2.6928	1.2026	4.4057	3.3700
BOA	Viewing zenith angle of 110°					
maximum	4.2000	5.3818	17.2405	5.5535	7.7826	14.0430
minimum	-2.5266	-8.7733	-49.3384	-7.1360	-19.5572	-18.5835
range	6.7266	14.1551	66.5790	12.6894	27.3398	32.6265
average _{pos}	1.1310	2.0860	7.7957	1.6180	3.6232	4.7148
average _{neg}	-0.8162	-2.4659	-13.0624	-2.1078	-5.1061	-5.4186
average	0.9736	2.2760	10.4290	1.8629	4.3647	5.0667

Table 5.3: The same as in Table 5.2 but for the METEOR measurement case.

	<i>I</i>			<i>Q</i>		
Parameter	$\theta_0 = 0^\circ$	$\theta_0 = 47^\circ$	$\theta_0 = 70^\circ$	$\theta_0 = 0^\circ$	$\theta_0 = 47^\circ$	$\theta_0 = 70^\circ$
TOA	Viewing zenith angle of 0°					
maximum	2.8370	4.2780	5.3460	n/a	3.1000	2.4940
minimum	-2.5610	-3.3180	-4.7640	n/a	-2.6000	-2.2290
range	5.3983	7.5963	10.1102	n/a	5.6999	4.7234
average _{pos}	0.7276	1.0548	1.5671	n/a	1.0514	0.8309
average _{neg}	-0.8565	-1.1279	-1.4623	n/a	-0.8462	-0.7836
average	0.7921	1.0914	1.5147	n/a	0.9488	0.8072
TOA	Viewing zenith angle of 47°					
maximum	3.5740	4.9560	5.3240	2.9140	3.0600	2.6250
minimum	-2.6640	-3.8830	-5.1810	-2.3540	-2.4700	-2.6170
range	6.2379	8.8389	10.5051	5.2681	5.5303	5.2421
average _{pos}	0.9756	1.3523	1.4663	1.0265	1.0075	0.7596
average _{neg}	-1.0621	-1.4770	-1.6661	-0.7935	-0.8566	-0.8902
average	1.0188	1.4146	1.5662	0.9100	0.9321	0.8249
TOA	Viewing zenith angle of 70°					
maximum	2.7340	3.2140	3.1910	1.8080	2.0290	1.6040
minimum	-2.5160	-3.0760	-3.9960	-1.3320	-1.7070	-1.9080
range	5.2501	6.2896	7.1869	3.1398	3.7361	3.5126
average _{pos}	1.0352	1.1145	1.3041	0.5579	0.6205	0.6316
average _{neg}	-0.9529	-1.0826	-1.1446	-0.5081	-0.5711	-0.7083
average	0.9940	1.0985	1.2244	0.5330	0.5958	0.6700
BOA	Viewing zenith angle of 180°					
maximum	4.3590	6.3886	5.7611	3.9915	3.4010	3.2048
minimum	-6.2415	-6.8113	-5.9359	-5.9845	-2.6790	-2.7292
range	10.6005	13.1999	11.6969	9.9760	6.0800	5.9340
average _{pos}	1.6628	1.7863	1.5253	1.4933	1.1238	0.9824
average _{neg}	-2.3841	-1.8846	-1.6864	-2.4339	-1.3027	-0.9952
average	2.0234	1.8355	1.6058	1.9636	1.2132	0.9888
BOA	Viewing zenith angle of 133°					
maximum	5.7854	2.5348	2.8670	2.9435	4.6008	2.4102
minimum	-5.0969	-4.5214	-3.1365	-3.0208	-7.4139	-3.7048
range	10.8823	7.0562	6.0035	5.9642	12.0147	6.1150
average _{pos}	1.8677	0.8783	1.0566	1.2898	1.9403	0.9464
average _{neg}	-1.7169	-1.3984	-1.0667	-1.2393	-2.2568	-1.1782
average	1.7923	1.1383	1.0617	1.2646	2.0985	1.0623
BOA	Viewing zenith angle of 110°					
maximum	3.9425	2.6291	7.3888	3.7854	2.8369	n/a
minimum	-3.2817	-4.3252	-13.0474	-3.0616	-3.9055	n/a
range	7.2242	6.9543	20.4362	6.8470	6.7425	n/a
average _{pos}	1.3741	0.9588	3.0487	1.2255	0.9470	n/a
average _{neg}	-1.2463	-1.1524	-3.9219	-1.1055	-1.0339	n/a
average	1.3102	1.0556	3.4853	1.1655	0.9904	n/a

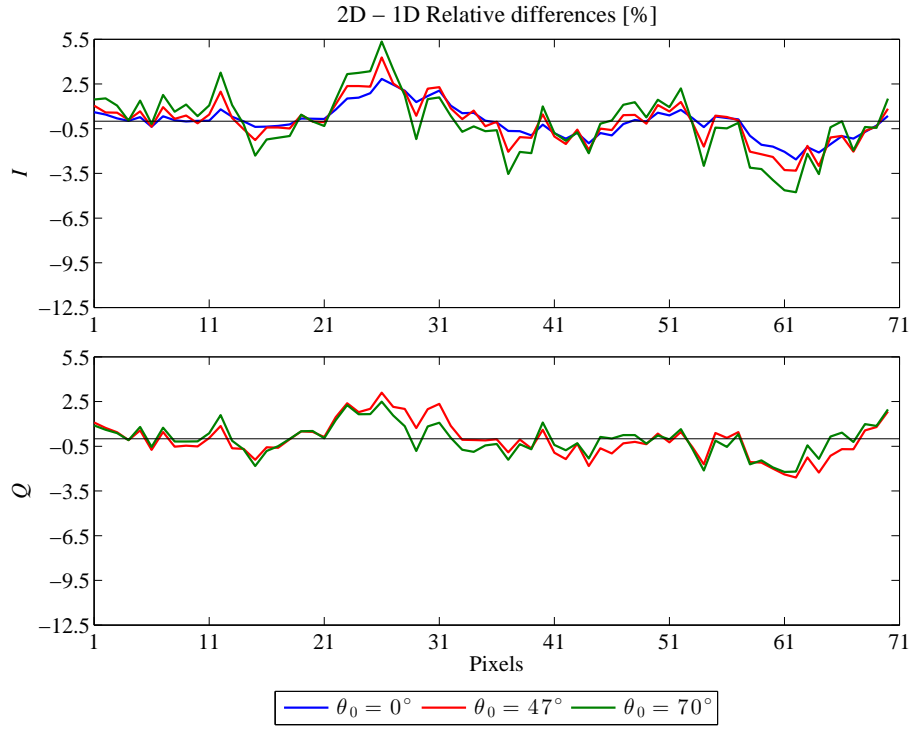


Figure 5.8: The same as in Figure 5.6 but for the METEOR measurement case.

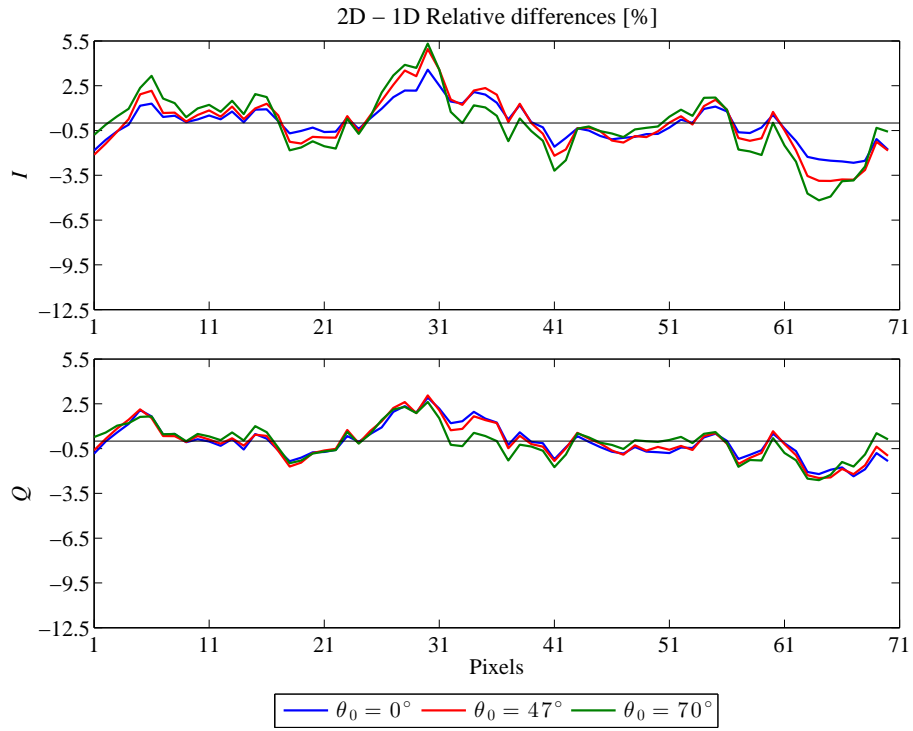


Figure 5.9: The same as in Figure 5.8 but for a viewing zenith angle of 47° .

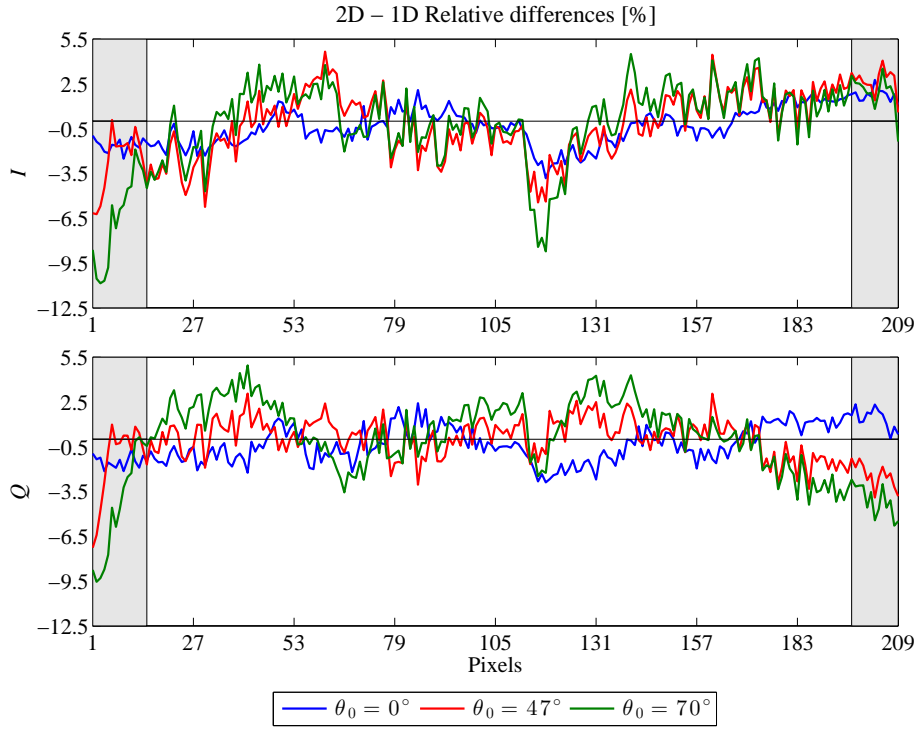


Figure 5.10: SPARTA simulated transmittance field including polarization for Case 1 (SAMUM) at 532nm: Relative differences in percent between 2D and 1D calculations for three different solar zenith angles 0° , 47° , and 70° at a viewing zenith angle of 180° . Upper: first Stokes element. Lower: second Stokes element. Shaded areas correspond to pixels influenced by an artificial strong gradient in optical thickness.

sumption is found in Figure 5.1, illustrating the basis on which the model domain was built, namely the height–time LIDAR aerosol extinction profile for the SAMUM measurement case. In the right edge of this domain the largest optical thickness is located. Consequently, the use of periodic boundary conditions employed in SPARTA may provide an artificial strong gradient, moving photons from the right region (location of maximum multiple–scattering process) of the domain to the left, leading to the largest differences between the 2D and 1D. For the pair of the first two Stokes elements (I, Q), these differences are: $(\pm 10.8\%, \pm 9.5\%)$ for $\theta_{\text{det}} = 180^\circ$ (where the horizontal photon transport is less pronounced as compared to the other viewing directions), $(\pm 16.8\%, \pm 26.3\%)$ for $\theta_{\text{det}} = 133^\circ$, and $(\pm 49.3\%, \pm 19.5\%)$ for Q for $\theta_{\text{det}} = 110^\circ$ (see Table 5.2). Nevertheless, excluding the shaded areas, the following RD are derived $(\pm 8.7\%, \pm 4.9\%)$ for $\theta_{\text{det}} = 180^\circ$, $(\pm 6.2\%, \pm 16.5\%)$ for $\theta_{\text{det}} = 133^\circ$, and $(\pm 21.4\%, \pm 18.2\%)$ for $\theta_{\text{det}} = 110^\circ$. Similar to the findings for the reflectivity, the same trends are noticed for the transmissivity, meaning, by increasing θ_0 the horizontal photon transport is increasing, and accordingly, the range, and average of RD are increasing (see Table 5.2); yet, the viewing zenith angle of 133° poses an exception, since the average of the maximum values of the relative differences is found for $\theta_0 = 47^\circ$. Note that the reflectance field in Figures 5.6 and 5.7 may also be “contaminated” by an artificial strong gradient in optical thickness.

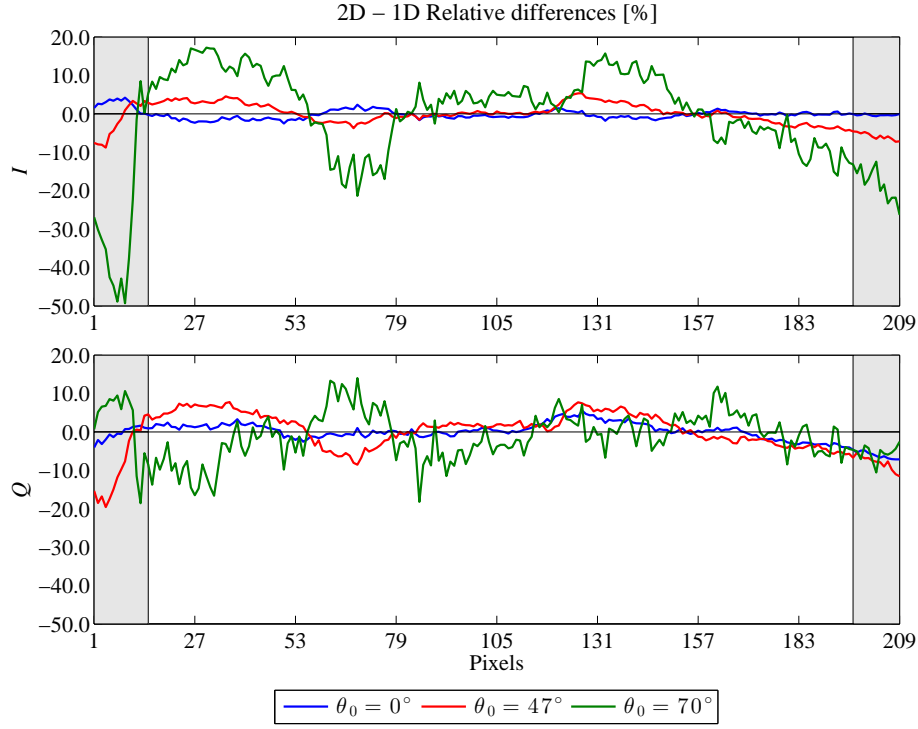


Figure 5.11: The same as in Figure 5.10 but for a viewing zenith angle of 110° .

Finally, Figures 5.12 and 5.13 outline the corresponding RD for the diffuse downward radiation at the BOA with respect to the METEOR measurement scenario (θ_0 of 180° and 110°). In this case, such extreme values of the RD were not observed. The largest gradient in optical thickness is found in the middle of the domain (see Figure 5.2), where the RD reach the maximum for I . The maximum differences for Q are found at the right side of the domain where a rather strong horizontal spatial gradient in optical thickness is more evident in Q rather than in I (see Figures 5.12 and 5.13). Specifically, the resulting total bias for (I, Q) is $(\pm 6.8\%, \pm 5.9\%)$ for $\theta_{\text{det}} = 180^\circ$, $(\pm 5.8\%, \pm 7.4\%)$ for $\theta_{\text{det}} = 133^\circ$, and $(\pm 13.1\%, \pm 3.9\%)$ for $\theta_{\text{det}} = 110^\circ$ (see Table 5.3). In addition, no results are presented for Q in case of $\theta_0 = 70^\circ$ and θ_{det} of 110° (no relative difference is computed for rather low values of the Stokes components). The usual trend of the relative difference dependency on the solar position is not detected. On the other hand, sometimes, an opposite trend is identified (i.e., for $\theta_{\text{det}} = 133^\circ$ for the first Stokes element, and $\theta_{\text{det}} = 180^\circ, 110^\circ$ in case of linear polarization). Accordingly, increasing the solar position, decreases the RD (and also the average of RD), indicating that the total radiative effect is not driven by the horizontal photon transport component. This is no surprise considering the lower horizontal spatial resolution of this scenario (2.06 km) as compared to the SAMUM scenario (0.96 km).

In conclusion, the total radiative effect is very sensitive to the viewing direction. Moreover, its two components do not have the same sign and the pattern introduced by the dependency on the solar zenith angle may be violated (e.g., in case of the reflectivity the maximum deviations are found for a detector zenith angle of 47°). The influence of the solar zenith angle can be seen for a fixed viewing direction and varying the sun position (see Figures 5.6

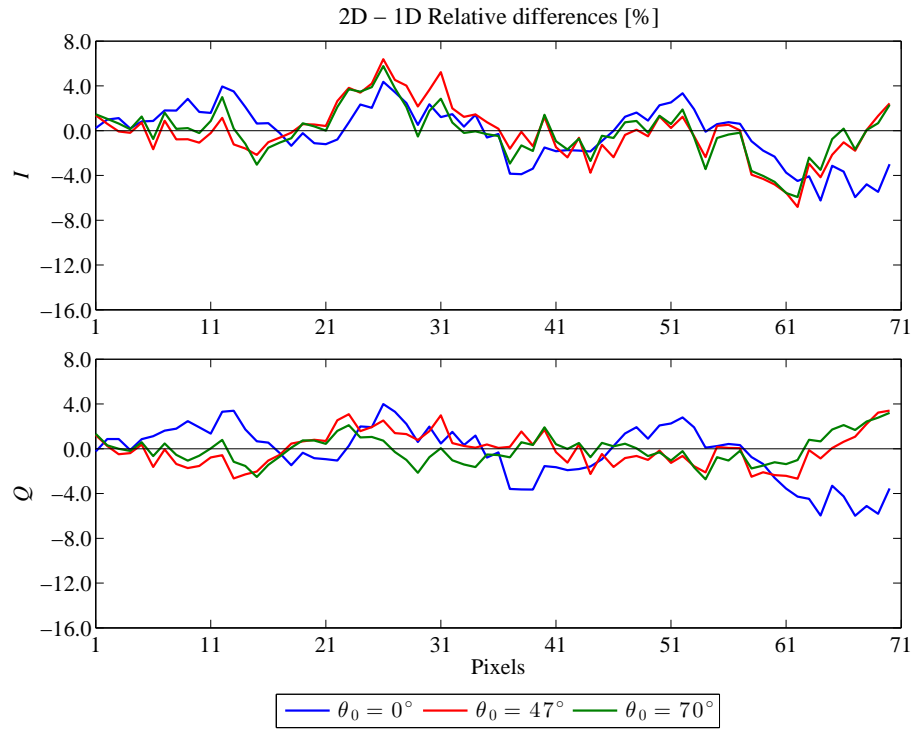


Figure 5.12: The same as in Figure 5.10 but for METEOR measurement case.

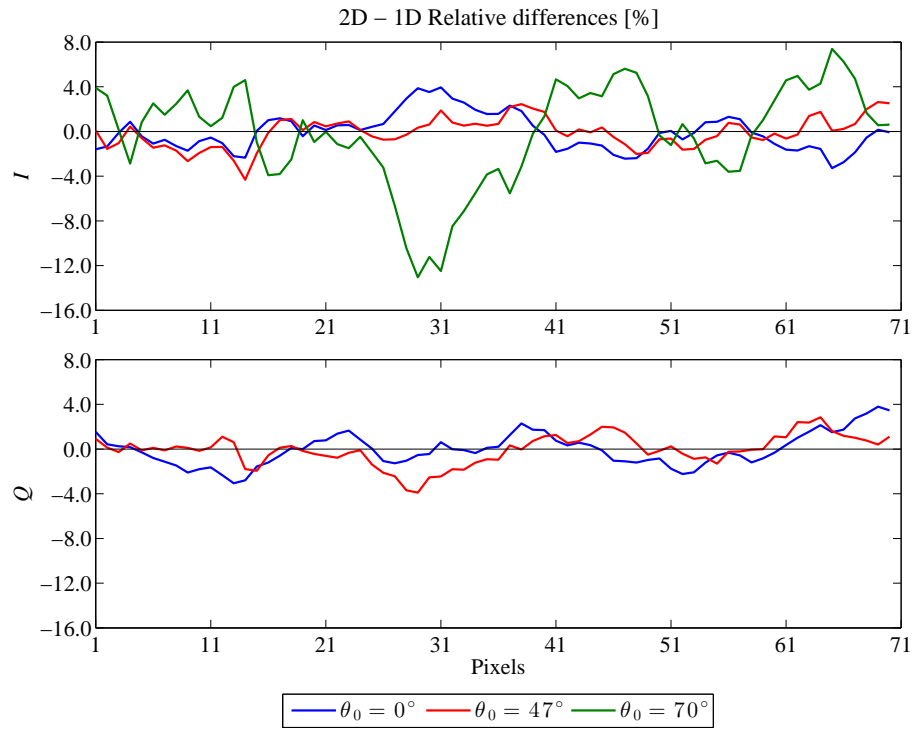


Figure 5.13: The same as in Figure 5.12 but for a viewing zenith angle of 110° .

and 5.8). In addition, the influence of the viewing geometry is better outlined when the solar position is set to zero and varying the detector position (see Tables 5.2 and 5.3).

For the METEOR case and sun overhead ($\theta_0 = 0^\circ$), the RD are more pronounced for the zenith transmitted radiation ($\theta_{\text{det}} = 180^\circ$) rather than in the nadir reflected radiation ($\theta_{\text{det}} = 0^\circ$). Considering the variability in optical thickness (see Figure 5.3), the radiances in the reflected field are smoothed since the photons go through the thick dust layer twice. Consequently, the resulting total bias is lower as compared to the bias yielded for the transmitted field. Increasing the solar zenith angle, the differences between the total bias found for the zenith transmitted and nadir reflected fields are reduced (are becoming comparable, see Tables 5.2 and 5.3), demonstrating that the optical thickness variability is represented better. For the SAMUM case, the artificial strong gradient poses far-reaching difficulties of interpretation. Furthermore, the differences found for the latter case are larger than in the METEOR one, owing to the largest gradient in τ , the artificial strong gradient in τ , and the vertical aerosol profile (see Figures 5.1 and 5.2). Last but not least, these errors are more dominant for the first Stokes element rather than for Q . The exception to this rule is found for a viewing zenith angle of 133° for both scenarios.

2D - IPA Comparison

The comparison between the full 2D inhomogeneous Saharan dust scheme and the 1D approximation introduces the combined radiative effect of horizontal inhomogeneity (HI) and horizontal photon transport (HPT). These two close-related physical processes are rather difficult to discriminate from each other. The subsequent step is to employ the Independent Pixel Approximation (e.g., Cahalan et al., 1994b; Davis et al., 1997; Benner and Evans, 2001) performing 1D radiative transfer computations for each pixel/column of the 2D domain. In IPA mode, the horizontal heterogeneity is conserved, although the horizontal photon transport is still ignored, and therefore, the latter effect can be quantified.

An illustration of 2D and IPA simulations for nadir reflectance (I Stokes component only since the value of Q is in the 4th decimal) and zenith transmittance (Q Stokes component only) radiance fields is shown in Figure 5.14. The straight lines denote the 2D mode, whereas, the dashed lines the IPA mode. The realistic 2D mode appears smoother as compared to IPA. As described above (2D - 1D comparison), there should be a correlation between the gradient in optical thickness and the magnitude of the radiative effects. However, such a correlation was not found. This may be no surprise considering the rather low optical thickness of our measurement cases (see Figure 5.3) and more importantly the very large horizontal pixel size (0.96 km for the SAMUM and 2.06 km for the METEOR measurement cases). Cahalan et al. (1994b) stated that, for rather small pixel sizes, IPA simulations lead to an increase of the errors prompted by neglecting the horizontal photon transport. However, increasing the horizontal pixel size results in a decrease of the horizontal transport effect and an increase of the 1D heterogeneity effect. The latter will be analyzed later on.

To quantify the magnitude of the effect introduced owing to IPA, the relative errors in percent between 2D and IPA simulations have been calculated as follows

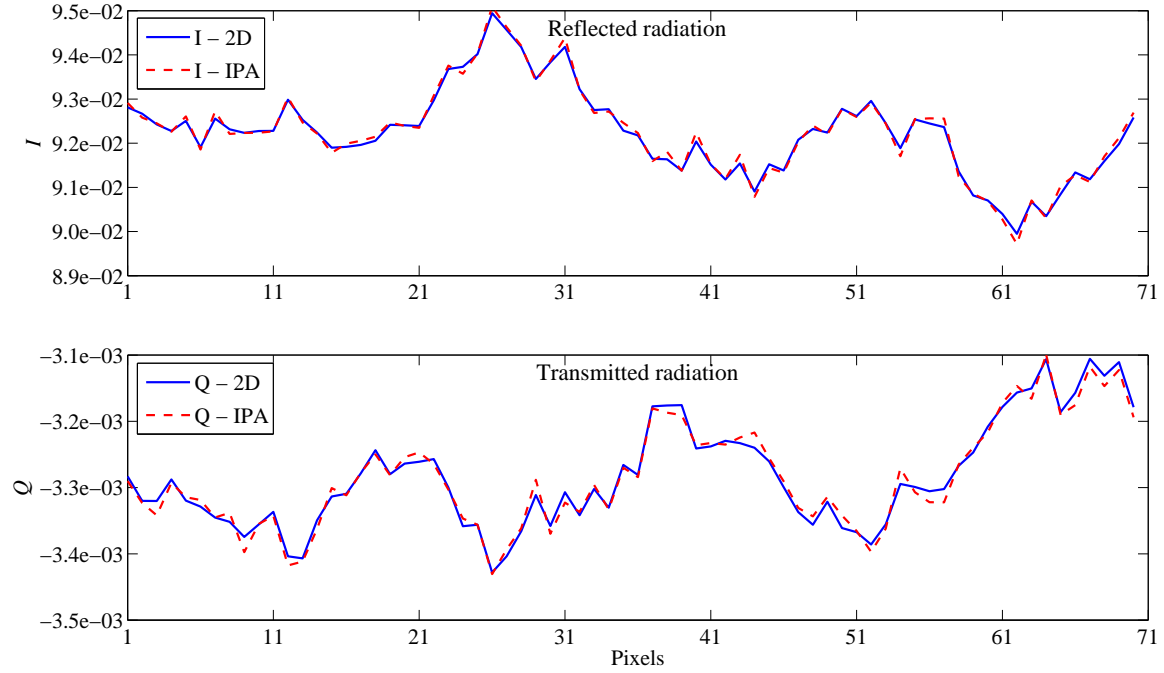


Figure 5.14: Comparison of 2D and IPA modes for sun overhead in case of nadir reflectivity ($\theta_{\text{det}} = 0^\circ$ - I Stokes component only) and zenith transmissivity ($\theta_{\text{det}} = 180^\circ$ - Q Stokes component only) as a function of the pixel number (METEOR). The straight lines denote the 2D mode, whereas, the dashed lines the IPA mode.

$$\text{RD}_{\text{IPA}} = \frac{2\text{D} - \text{IPA}}{2\text{D}} \cdot 100\% \quad (5.2)$$

The bias due to the IPA mode is listed in Tables 5.4 and 5.5 for the SAMUM and METEOR case, respectively.

For nadir (0°) and zenith (180°) observations, the IPA bias follows the same behavior for both measurement cases. In Figure 5.15 results are shown for the TOA nadir reflection for the SAMUM case and in Figure 5.16 for the surface zenith transmission for the METEOR case. For sun overhead (blue lines), there is a good agreement between the 2D and IPA simulations. The relative difference in percent between the two calculation schemes is less than 1 % and 2 % for the first and second Stokes components, respectively (for both measurement scenarios), indicating that the effect due to the neglect of horizontal photon transport is negligible. For larger solar zenith angles, the horizontal photon transport effect starts playing an important role and the IPA bias is getting larger, meaning that the $\text{RD}_{2\text{D}-\text{IPA}}$, as well as the range and average of $\text{RD}_{2\text{D}-\text{IPA}}$ are increasing. This can be explicated by the increased probability that a photon may hit the dust field from the side leading to illuminating and shading effects enhancing the radiative effect, in agreement with Cahalan et al. (1994a); Di Giuseppe and Tompkins (2003). The resulting bias for (I, Q) is $(\pm 9.2\%, \pm 6.9\%)$ for TOA and $(\pm 10.9\%, \pm 11.5\%)$ for BOA for the SAMUM case. The corresponding values for the METEOR case are $(\pm 2.5\%, \pm 1.5\%)$ for TOA and $(\pm 2.8\%, \pm 2.5\%)$ for BOA.

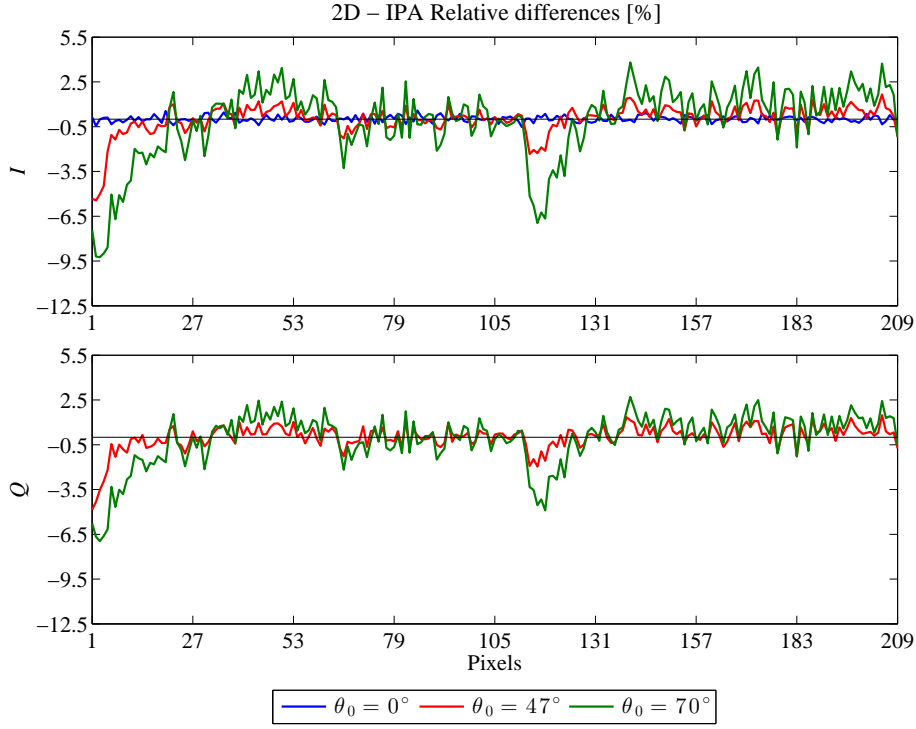


Figure 5.15: SPARTA simulated reflectance field including polarization for the SAMUM case: Relative differences in percent between 2D and IPA modes for three solar zenith angles 0° , 47° , and 70° at a viewing zenith angle of 0° . Upper: first Stokes element. Lower: second Stokes element.

A closer look at Tables 5.4 and 5.5 shows a higher sensitivity of the error to the viewing geometry; the same pattern is found (an increase in the viewing direction leads to an increase of the IPA bias). These dependencies of the solar and viewing directions on the radiative effects interfere with each other causing problems coming up with concrete conclusions. Nevertheless, Tables 5.4 and 5.5 indicate the following maximum absolute errors for (I, Q) ; the maximum errors are always found for $\theta_0 = 70^\circ$:

- SAMUM: **a.** $\theta_{\text{det}} = 47^\circ$ - (12 %, 8 %) and **b.** $\theta_{\text{det}} = 110^\circ$ - (64 %, 20 %) or (20 %, 13.6 %) if the areas with possible artificial gradient in τ are excluded.
- METEOR: **a.** $\theta_{\text{det}} = 70^\circ$ - (4.8 %, 3 %) and **b.** $\theta_{\text{det}} = 110^\circ$ - (9.4 %, n/a).

To summarize, in contrast to the findings of the 2D - 1D comparison, the errors induced by ignoring the HPT are larger for nadir reflection at the TOA as compared to zenith surface transmission. Increasing the solar zenith angle, the HPT is enhanced, and the divergence between the IPA bias found for the zenith transmitted and nadir reflected fields is decreasing (see Tables 5.4 and 5.5). The latter trend is a slightly weaker for the SAMUM case, considering the artificial gradient in optical thickness "contamination" (see Tables 5.4 and 5.5). Between the two measurement cases the bias is more pronounced in the SAMUM case, due to the smaller horizontal pixel size (Di Giuseppe and Tompkins, 2003), whereby the horizontal photon transport plays a major role for specific illumination and observation geometries.

These results are in line with those of Scheirer and Macke (2001), Benner and Evans (2001),

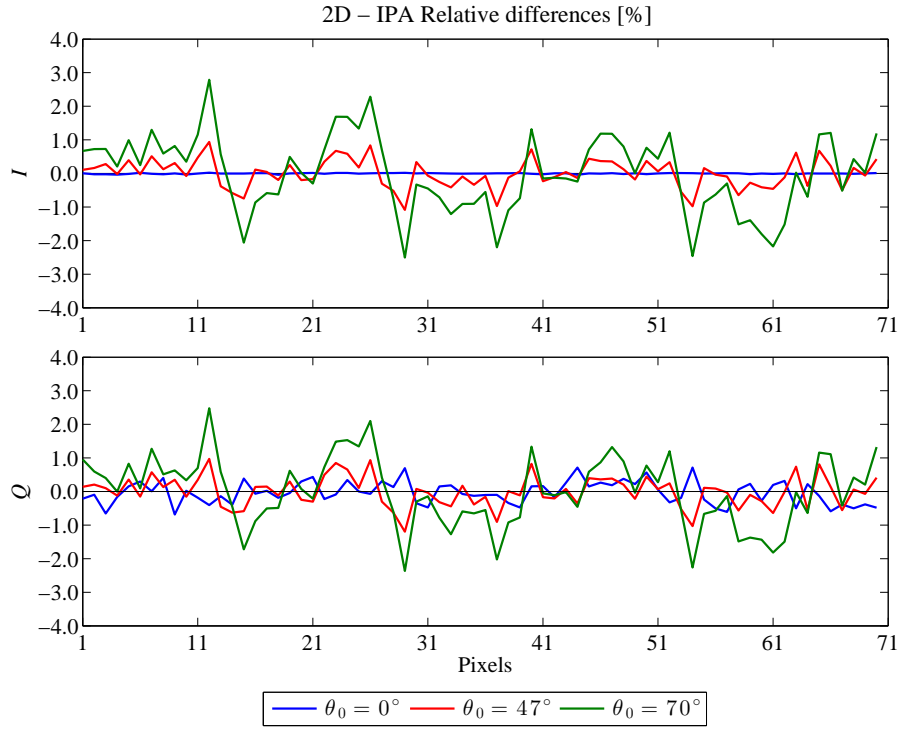


Figure 5.16: The same as in Figure 5.15 but for the METEOR case for a viewing zenith angle of 180° .

Di Giuseppe and Tompkins (2003), Cahalan et al. (2005), and Torge et al. (2011). These authors concluded that the radiative effects are dominant in areas with strong horizontal gradient in optical thickness.

IPA - 1D comparison

Driven by the different magnitude of the horizontal photon transport effect between the two measurement cases, the IPA versus 1D calculations (pixel by pixel) have been investigated,

$$RD_{\text{IPA-1D}} = \frac{\text{IPA} - \text{1D}}{\text{IPA}} \cdot 100\% \quad (5.3)$$

This comparison, renders information of the significance of the horizontal inhomogeneity effect (1D bias).

To begin with, the 1D bias in the reflected radiation for both LIDAR-measured scenarios follows a specific pattern: for zenith solar illumination ($\theta_0 = 0^\circ$ and $\theta_{\text{det}} = 0^\circ, 47^\circ, 70^\circ$) and nadir observation ($\theta_{\text{det}} = 0^\circ$ and $\theta_0 = 0^\circ, 47^\circ, 70^\circ$) the error owing to the optical heterogeneity for the first Stokes component is almost the same (SAMUM: $\pm 4.2\%$, METEOR: $\pm 3.3\%$). Such behavior is not evident for the 1D bias linked to the second Stokes component. An example for the METEOR case is depicted in Figure 5.17 (nadir observation, upper left plot); the lines lie nearly on top of each other. The 1D bias refers to the heterogeneity

Table 5.4: SAMUM measurement case analysis: Maximum, minimum, range, average of positive values, average of negative values, and average of the relative difference in percent between the 2D and IPA modes for both the reflected and transmitted radiation. Abbreviation: n/a - not available.

	<i>I</i>			<i>Q</i>		
Parameter	$\theta_0 = 0^\circ$	$\theta_0 = 47^\circ$	$\theta_0 = 70^\circ$	$\theta_0 = 0^\circ$	$\theta_0 = 47^\circ$	$\theta_0 = 70^\circ$
TOA	Viewing zenith angle of 0°					
maximum	0.5791	1.6546	3.7990	n/a	1.4790	2.6973
minimum	-0.5331	-5.4415	-9.2395	n/a	-4.8530	-6.9576
range	1.1121	7.0962	13.0385	n/a	6.3320	9.6550
average _{pos}	0.1870	0.5271	1.4619	n/a	0.4894	1.0166
average _{neg}	-0.1436	-0.8278	-2.3273	n/a	-0.6859	-1.6357
average	0.1653	0.6775	1.8946	n/a	0.5877	1.3262
TOA	Viewing zenith angle of 47°					
maximum	5.1213	5.0711	4.7819	3.1817	2.5608	3.4405
minimum	-3.2737	-6.6243	-12.0105	-3.7925	-6.4067	-8.0295
range	8.3950	11.6954	16.7925	6.9742	8.9674	11.4700
average _{pos}	1.0740	1.1454	1.6952	0.8115	0.8733	1.1944
average _{neg}	-0.8946	-1.1713	-2.7733	-0.9894	-1.0163	-1.8192
average	0.9843	1.1584	2.2343	0.9005	0.9448	1.5068
TOA	Viewing zenith angle of 70°					
maximum	4.3306	2.2140	3.6135	3.1714	2.3199	3.3028
minimum	-2.7844	-4.5256	-10.5478	-3.3553	-5.2532	-6.9167
range	7.1150	6.7396	14.1613	6.5267	7.5731	10.2194
average _{pos}	1.4344	0.7125	1.4065	0.9090	0.7711	1.0985
average _{neg}	-0.9924	-0.9833	-2.7783	-1.0312	-1.2067	-1.6258
average	1.2134	0.8479	2.0924	0.9701	0.9889	1.3622
BOA	Viewing zenith angle of 180°					
maximum	0.0620	1.8263	4.4533	1.7588	2.2085	4.5936
minimum	-0.0609	-6.8986	-10.9663	-1.3700	-8.6275	-11.5564
range	0.1229	8.7249	15.4196	3.1287	10.8360	16.1500
average _{pos}	0.0179	0.6196	1.6300	0.4113	0.7671	1.6824
average _{neg}	-0.0182	-0.8854	-2.4607	-0.4040	-1.1220	-2.6461
average	0.0181	0.7525	2.0454	0.4076	0.9446	2.1643
BOA	Viewing zenith angle of 133°					
maximum	8.0060	2.3972	6.0426	2.4965	6.3716	6.5520
minimum	-2.4303	-10.6704	-20.6141	-1.8850	-26.5657	-19.2391
range	10.4364	13.0676	26.6566	4.3815	32.9373	25.7911
average _{pos}	1.2604	0.7815	2.0603	0.5703	2.1466	2.2851
average _{neg}	-0.8919	-1.1472	-3.4650	-0.5326	-3.4561	-3.7250
average	1.0762	0.9643	2.7627	0.5514	2.8014	3.0050
BOA	Viewing zenith angle of 110°					
maximum	4.4480	3.2393	15.2663	2.8618	6.3672	10.6766
minimum	-2.5971	-11.8452	-64.3852	-5.7168	-24.0224	-20.1485
range	7.0450	15.0845	79.6515	8.5785	30.3896	30.8251
average _{pos}	1.1930	1.1669	6.2055	0.9198	2.5575	3.4879
average _{neg}	-0.7337	-1.7524	-12.8525	-1.1133	-4.1138	-4.2595
average	0.9633	1.4597	9.5290	1.0165	3.3357	3.8737

Table 5.5: The same as in Table 5.4 but for the METEOR measurement case.

	<i>I</i>			<i>Q</i>		
Parameter	$\theta_0 = 0^\circ$	$\theta_0 = 47^\circ$	$\theta_0 = 70^\circ$	$\theta_0 = 0^\circ$	$\theta_0 = 47^\circ$	$\theta_0 = 70^\circ$
TOA	Viewing zenith angle of 0°					
maximum	0.2567	0.9723	2.3822	n/a	0.5206	1.5478
minimum	-0.2268	-1.0661	-2.5289	n/a	-0.7147	-1.5389
range	0.4835	2.0384	4.9111	n/a	1.2353	3.0868
average _{pos}	0.0670	0.3520	0.9823	n/a	0.1795	0.5469
average _{neg}	-0.1034	-0.3434	-0.9206	n/a	-0.2606	-0.5273
average	0.0852	0.3477	0.9515	n/a	0.2201	0.5371
TOA	Viewing zenith angle of 47°					
maximum	2.4614	3.3907	3.8294	2.3969	2.3188	2.1293
minimum	-2.5575	-3.0237	-3.4088	-3.1383	-2.6881	-2.0364
range	5.0189	6.4144	7.2382	5.5352	5.0069	4.1657
average _{pos}	1.0259	1.2253	1.2085	0.9954	0.9454	0.7587
average _{neg}	-0.9380	-1.4061	-1.5799	-1.0014	-1.0118	-0.9284
average	0.9820	1.3157	1.3942	0.9984	0.9786	0.8436
TOA	Viewing zenith angle of 70°					
maximum	3.5087	3.4146	3.6151	2.1629	2.2301	1.8669
minimum	-3.5660	-4.0981	-4.8463	-2.7145	-3.0089	-2.7220
range	7.0747	7.5126	8.4614	4.8775	5.2390	4.5889
average _{pos}	1.4911	1.4588	1.2976	0.7187	0.7917	0.7350
average _{neg}	-1.6641	-1.7360	-1.6218	-0.9332	-0.9048	-0.8706
average	1.5776	1.5974	1.4597	0.8260	0.8483	0.8028
BOA	Viewing zenith angle of 180°					
maximum	0.0207	0.9374	2.7894	0.7146	0.9705	2.4801
minimum	-0.0401	-1.0843	-2.5039	-0.6840	-1.1961	-2.3645
range	0.0607	2.0217	5.2933	1.3986	2.1666	4.8446
average _{pos}	0.0080	0.3475	0.8804	0.2715	0.3451	0.8832
average _{neg}	-0.0127	-0.3280	-0.9598	-0.2880	-0.3691	-0.7779
average	0.0104	0.3378	0.9201	0.2798	0.3571	0.8306
BOA	Viewing zenith angle of 133°					
maximum	2.7709	1.0987	2.7912	1.1485	1.4727	3.1850
minimum	-3.0537	-0.9235	-2.4783	-1.0683	-1.1810	-3.0891
range	5.8247	2.0222	5.2695	2.2168	2.6537	6.2741
average _{pos}	1.1712	0.3276	1.0629	0.4745	0.4926	1.0835
average _{neg}	-0.9060	-0.2545	-1.0322	-0.3990	-0.4430	-1.2453
average	1.0386	0.2911	1.0476	0.4368	0.4678	1.1644
BOA	Viewing zenith angle of 110°					
maximum	2.7831	1.2889	9.4605	1.4094	2.1981	n/a
minimum	-3.0901	-2.6222	-7.7037	-1.5506	-2.3754	n/a
range	5.8733	3.9112	17.1642	2.9600	4.5734	n/a
average _{pos}	1.1601	0.6165	2.7087	0.4992	0.8352	n/a
average _{neg}	-1.1966	-0.5274	-3.3705	-0.4877	-0.8048	n/a
average	1.1784	0.5720	3.0396	0.4935	0.8200	n/a

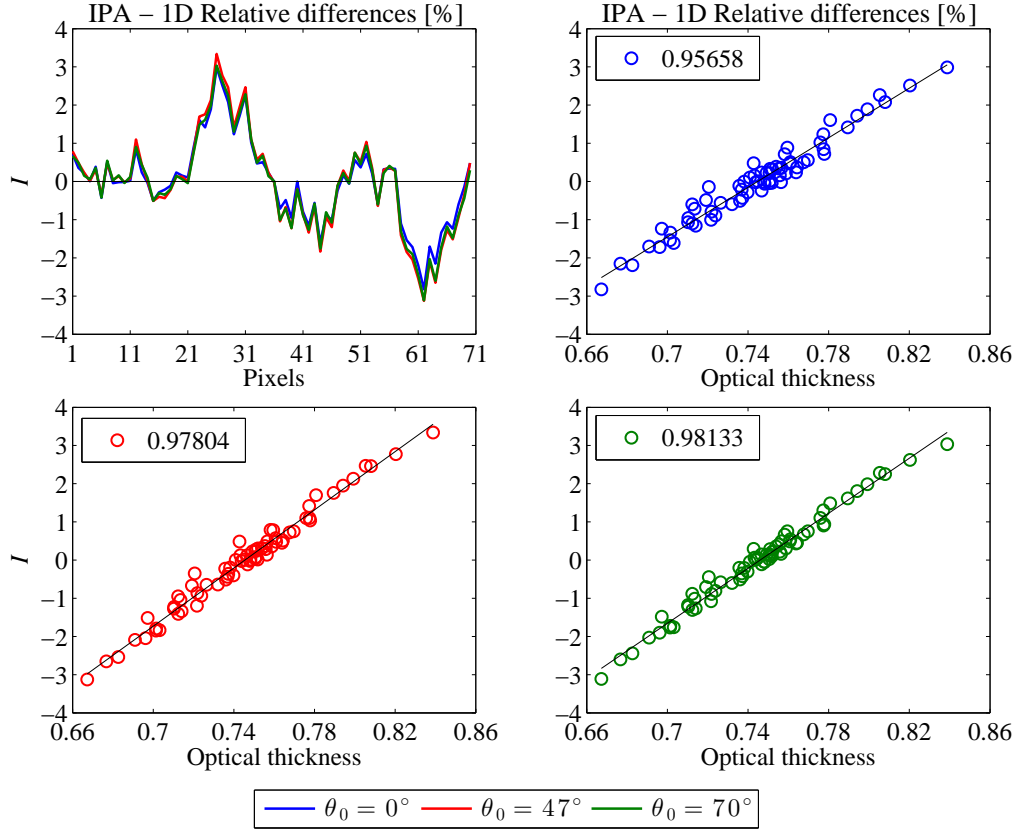


Figure 5.17: SPARTA simulated reflected radiation for the METEOR case: Relative differences in percent between the IPA and PP modes for three different solar zenith angles 0° , 47° , and 70° at a viewing zenith angle of 0° (upper left plot). Correlation plots (R^2) between the 1D bias and τ for nadir reflected field for the three sun positions considered (indicated by the different colors).

effect due to the optical thickness variability. As a result, it should be strongly dependent on the optical thickness. Toward this direction, the correlation between the 1D bias and τ has been investigated. As a demonstration, correlations are presented for the METEOR case for nadir observation (see Figure 5.17). As expected, the trendline is linear and an excellent correlation is found. Quantitatively, the fraction where the deviation of the bias is smaller than the deviation of the dependent parameter, R^2 , is 0.96, 0.98, and 0.98 for $\theta_0 = 0^\circ$, 47° , and 70° , respectively.

On the whole, such correlations are found for both cases, but are not shown here. In brief, they are more pronounced in the reflected rather than in the transmitted field, and in I as compared to Q . In most cases, for I , the R^2 is in the range of 0.83 - 0.98 for METEOR (excluding the geometry combination ($\theta_0 = 70^\circ, \theta_{\text{det}} = 70^\circ$)) and 0.5 - 0.96 for SAMUM; for Q , R^2 up to 0.99 is also found, but for different geometry combinations ($\theta_0 = 70^\circ, \theta_{\text{det}} = 70^\circ$), which may be no surprise considering how it is derived (see Eqs 3.12 and 3.18). Note here, that this strong dependence on the optical thickness was found also for the total bias (but less pronounced). However, it was not shown here owing to the assumption that the 1D bias dominates (because of the rather large horizontal pixel size).

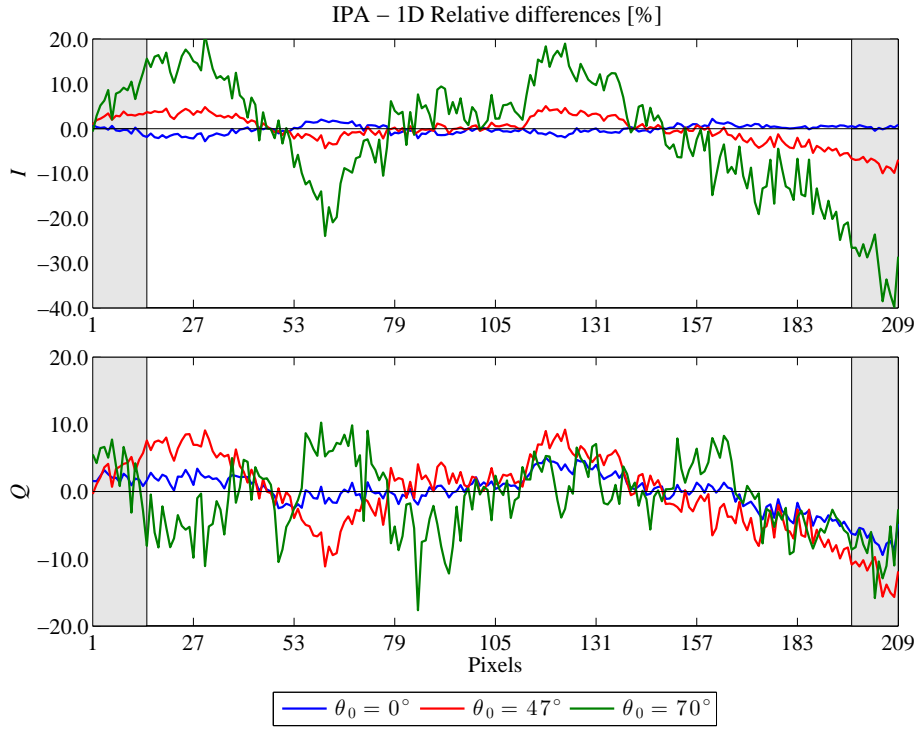


Figure 5.18: SPARTA simulated transmissivity for the SAMUM case: Relative differences in percent between the IPA and 1D modes for three solar zenith angles 0° , 47° , and 70° at a viewing zenith angle of 110° . Upper: first Stokes element. Lower: second Stokes element. Shaded areas correspond to pixels influenced by an artificial strong gradient in optical thickness.

The domain-averaged differences between the IPA and 1D are not shown since they are analogous to those found between the 2D and 1D modes (see Table 5.1). The derived statistics are tabulated for the 1D bias in Tables 5.6 and 5.7. For the diffuse upward radiation the 1D error is rather low for both measurement scenarios. Approximately within the range of $(-4.3\%, 4.2\%)$ for I , and $(-2.8\%, 3.1\%)$ for Q .

For the downward radiation, the errors linked to the neglect of horizontal optical variability are larger. Figures 5.18 and 5.19 show the 1D bias for the viewing zenith angle of 110° for both cases (for METEOR and Q results are presented for a viewing zenith angle of 133° since for 110° its values are too small to derive the relative differences), where the observed effects are most dominant. The 1D biases for the SAMUM case are: $-40 < \text{RD}_{\text{IPA}-1\text{D}} < 20.1$ for I (or $\pm 20\%$ if the shaded areas are excluded) and $-17.7 < \text{RD}_{\text{IPA}-1\text{D}} < 10.3$ for Q . Accordingly, for the METEOR case: $-14 < \text{RD}_{\text{IPA}-1\text{D}} < 9.7$ for I and $-7.2 < \text{RD}_{\text{IPA}-1\text{D}} < 4.2$ for Q .

5.2 Overall Radiative Effects

The errors in the reflected and transmitted fields for two radiative transfer assumptions (IPA and 1D) have been derived. The comparison between the full 2D inhomogeneous Saharan dust scheme and the 1D approximation introduces the total radiative effect. To explain

Table 5.6: SAMUM measurement case analysis: Maximum, minimum, range, average of positive values, average of negative values, and average of the relative difference in percent between the IPA and 1D modes for both the reflected and transmitted radiation. Abbreviation: n/a - not available.

	<i>I</i>			<i>Q</i>		
Parameter	$\theta_0 = 0^\circ$	$\theta_0 = 47^\circ$	$\theta_0 = 70^\circ$	$\theta_0 = 0^\circ$	$\theta_0 = 47^\circ$	$\theta_0 = 70^\circ$
TOA	Viewing zenith angle of 0°					
maximum	3.6985	3.8796	2.5879	n/a	2.9069	3.3738
minimum	-3.7519	-4.1818	-3.0825	n/a	-2.6698	-1.5540
range	7.4504	8.0614	5.6703	n/a	5.5768	4.9277
average _{pos}	1.2594	1.4535	0.9653	n/a	0.9240	0.8978
average _{neg}	-1.3596	-1.4473	-1.0450	n/a	-0.9207	-0.6176
average	1.3095	1.4504	1.0051	n/a	0.9224	0.7577
TOA	Viewing zenith angle of 47°					
maximum	3.7813	3.5781	1.2025	3.0856	2.5406	2.5140
minimum	-4.2229	-4.2226	-1.3057	-2.7625	-1.8519	-1.2459
range	8.0042	7.8006	2.5082	5.8480	4.3925	3.7599
average _{pos}	1.4054	1.4140	0.4035	0.9767	0.7637	0.6073
average _{neg}	-1.5028	-1.4242	-0.4273	-0.8643	-0.6737	-0.4845
average	1.4541	1.4191	0.4154	0.9205	0.7187	0.5459
TOA	Viewing zenith angle of 70°					
maximum	2.6400	1.2819	1.1208	3.3595	2.3816	1.9338
minimum	-2.7791	-1.3527	-1.3762	-1.6801	-1.4633	-0.9690
range	5.4191	2.6346	2.4970	5.0396	3.8450	2.9028
average _{pos}	1.0324	0.4260	0.3920	0.8379	0.6257	0.5321
average _{neg}	-1.0489	-0.4248	-0.4583	-0.6708	-0.4966	-0.3649
average	1.0407	0.4254	0.4252	0.7543	0.5612	0.4485
BOA	Viewing zenith angle of 180°					
maximum	2.7413	3.4079	1.4411	2.6666	2.4775	5.0307
minimum	-3.8597	-4.6746	-2.0702	-3.3318	-4.1299	-8.4744
range	6.6011	8.0825	3.5113	5.9984	6.6074	13.5051
average _{pos}	0.9732	1.4411	0.4095	0.9309	0.8023	2.0659
average _{neg}	-1.1939	-1.5540	-0.5483	-1.1113	-1.3450	-2.5264
average	1.0835	1.4975	0.4789	1.0211	1.0736	2.2961
BOA	Viewing zenith angle of 133°					
maximum	3.5904	3.8592	5.8059	2.3698	9.8606	8.4360
minimum	-4.8370	-7.0128	-10.7577	-4.7448	-14.9241	-11.9259
range	8.4275	10.8720	16.5636	7.1146	24.7847	20.3618
average _{pos}	1.5549	1.4898	2.3602	0.9073	3.6062	3.1482
average _{neg}	-1.6387	-2.4835	-3.1181	-1.3928	-4.9829	-4.1739
average	1.5968	1.9866	2.7391	1.1501	4.2945	3.6611
BOA	Viewing zenith angle of 110°					
maximum	2.2032	5.0464	20.8505	5.0350	9.2089	10.2662
minimum	-2.8305	-9.9616	-39.8112	-9.4543	-15.7094	-17.6646
range	5.0337	15.0080	60.6617	14.4893	24.9183	27.9307
average _{pos}	0.6518	2.2838	8.5316	1.7403	4.0740	3.9868
average _{neg}	-0.8660	-2.5711	-12.4503	-2.6509	-5.2122	-4.8924
average	0.7589	2.4274	10.4909	2.1956	4.6431	4.4396

Table 5.7: The same as in Table 5.6 but for the METEOR measurement case.

	<i>I</i>			<i>Q</i>		
Parameter	$\theta_0 = 0^\circ$	$\theta_0 = 47^\circ$	$\theta_0 = 70^\circ$	$\theta_0 = 0^\circ$	$\theta_0 = 47^\circ$	$\theta_0 = 70^\circ$
TOA	Viewing zenith angle of 0°					
maximum	2.9866	3.3386	3.0359	n/a	2.5925	1.3436
minimum	-2.8251	-3.1247	-3.1102	n/a	-2.4863	-1.2870
range	5.8116	6.4633	6.1460	n/a	5.0789	2.6306
average _{pos}	0.8027	0.8254	0.7804	n/a	0.8933	0.5491
average _{neg}	-0.8104	-1.1051	-1.0321	n/a	-0.8410	-0.4645
average	0.8065	0.9653	0.9063	n/a	0.8672	0.5068
TOA	Viewing zenith angle of 47°					
maximum	3.3296	4.2300	2.7995	2.5852	2.2784	1.3018
minimum	-3.2501	-4.3129	-3.2889	-2.6428	-2.4194	-1.2689
range	6.5797	8.5429	6.0883	5.2280	4.6978	2.5706
average _{pos}	0.8452	1.1291	0.8400	0.9104	0.8114	0.5391
average _{neg}	-1.0870	-1.2409	-0.8583	-0.8478	-0.7826	-0.4150
average	0.9661	1.1850	0.8491	0.8791	0.7970	0.4771
TOA	Viewing zenith angle of 70°					
maximum	3.1064	2.8838	1.5130	1.3468	1.2640	0.7922
minimum	-3.1752	-3.2613	-1.9404	-1.2206	-1.3441	-0.4903
range	6.2815	6.1450	3.4534	2.5674	2.6081	1.2825
average _{pos}	0.8172	0.8026	0.4718	0.5667	0.5404	0.2765
average _{neg}	-1.0130	-0.8964	-0.5169	-0.4728	-0.4323	-0.2290
average	0.9151	0.8495	0.4944	0.5198	0.4863	0.2527
BOA	Viewing zenith angle of 180°					
maximum	4.3547	5.6002	3.5590	4.0586	3.2997	2.5805
minimum	-6.2407	-6.6863	-4.3498	-6.1953	-2.6659	-1.7557
range	10.5954	12.2865	7.9088	10.2539	5.9657	4.3362
average _{pos}	1.6646	1.6301	1.0393	1.5987	1.2205	0.8341
average _{neg}	-2.3795	-1.8301	-1.1900	-2.2473	-1.1882	-0.6728
average	2.0220	1.7301	1.1147	1.9230	1.2044	0.7534
BOA	Viewing zenith angle of 133°					
maximum	5.7207	2.6868	2.0925	3.9481	4.2494	2.1302
minimum	-6.7441	-4.3294	-1.6052	-2.9754	-7.2116	-3.5511
range	12.4649	7.0162	3.6977	6.9235	11.4611	5.6813
average _{pos}	1.7546	0.8872	0.6830	1.4215	1.8103	0.8263
average _{neg}	-1.7982	-1.3995	-0.5945	-1.2624	-2.1378	-0.7910
average	1.7764	1.1433	0.6387	1.3420	1.9741	0.8087
BOA	Viewing zenith angle of 110°					
maximum	3.6453	3.0040	9.6138	4.7643	2.8685	n/a
minimum	-4.6111	-2.3555	-14.0125	-3.3926	-4.4158	n/a
range	8.2564	5.3594	23.6262	8.1568	7.2843	n/a
average _{pos}	1.1465	0.9988	2.8308	1.5628	1.1301	n/a
average _{neg}	-1.2325	-0.9110	-3.4713	-1.2379	-0.9933	n/a
average	1.1895	0.9549	3.1510	1.4003	1.0617	n/a

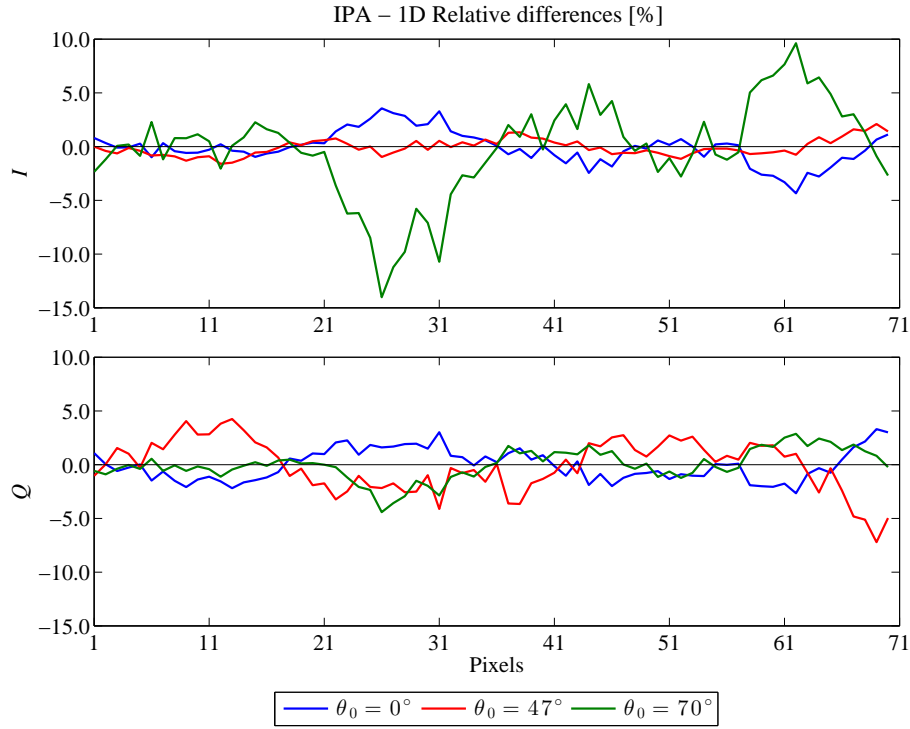


Figure 5.19: The same as in Figure ?? but for the METEOR case for a viewing zenith angle of 110° for I and 133° for Q .

the complex influence of these effects, the IPA and 1D biases were compared to the total bias, RD. In Figures 5.20 and 5.21 results are presented for nadir observations (first Stokes component only) for both LIDAR-measured fields, METEOR and SAMUM, respectively.

For the METEOR case, the total radiative effect is driven by the 1D bias. In particular, for sun overhead, there is an excellent correlation between RD (total bias) and RD_{IPA-1D} (for I), where a R^2 of 0.99 was found, meaning the horizontal photon transport is negligible. Increasing the solar zenith angle, the horizontal photon transport is increasing, and therefore, the correlation with IPA bias is increasing while the correlation with 1D bias is decreasing. However, the dominant effect is always the horizontal optical variability. This can be explained by the lower variability that is resolved by the larger horizontal pixel size (2.06 km). In the same direction are the findings for the SAMUM case. The smaller horizontal pixel size (0.96 km) as compared to the first case makes the horizontal photon transport more pronounced. For instance, for a solar zenith angle of 0° the HPT overpowers the HI. Similar behavior is found by increasing the zenith angle of observation for both test cases (reflected radiation). For the most complicated geometries, the bias inherent in the horizontal photon transport is taking the lead even for a solar zenith angle of 47° (SAMUM). On the contrary, for the METEOR case, it only occurs for very low sun (70°). The exact same pattern is followed by the second Stokes component, albeit, both effects are found a bit weaker.

Figures 5.22 and 5.23 show the transmitted field for a viewing zenith angle of 133° for METEOR and SAMUM scenarios, respectively. For the METEOR case, the results are in agreement with those obtained for the reflected field. On the other hand, the same does not

stand for the SAMUM one. For example for a solar zenith angle of 47° , there is no clear evidence of which effect is dominant (R^2 is very low for both effects). The available evidence (see Figure 5.1) seems to suggest that an artificial strong gradient is induced to the RD by the use of the periodic boundary conditions employed in SPARTA. In conclusion, increasing the horizontal pixel size results in a decrease of the IPA effect and an increase of the PP effect.

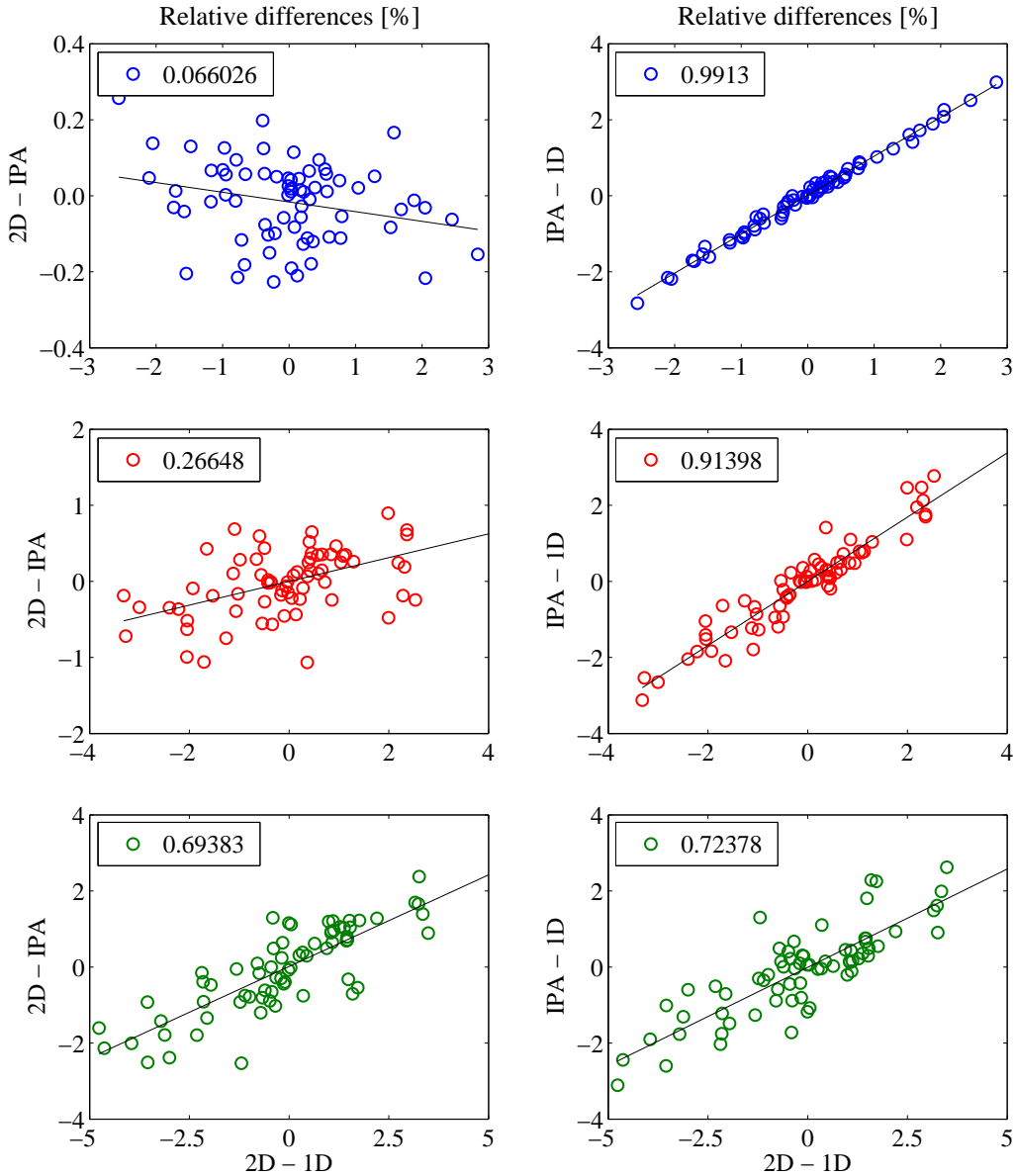


Figure 5.20: SPARTA simulated field for the METEOR case: Correlation plots (R^2) of the RD (total bias) with the IPA bias (left panels) and 1D bias (right panels) for nadir observation and three sun positions 0° (blue circles), 47° (red circles), and 70° (green circles).

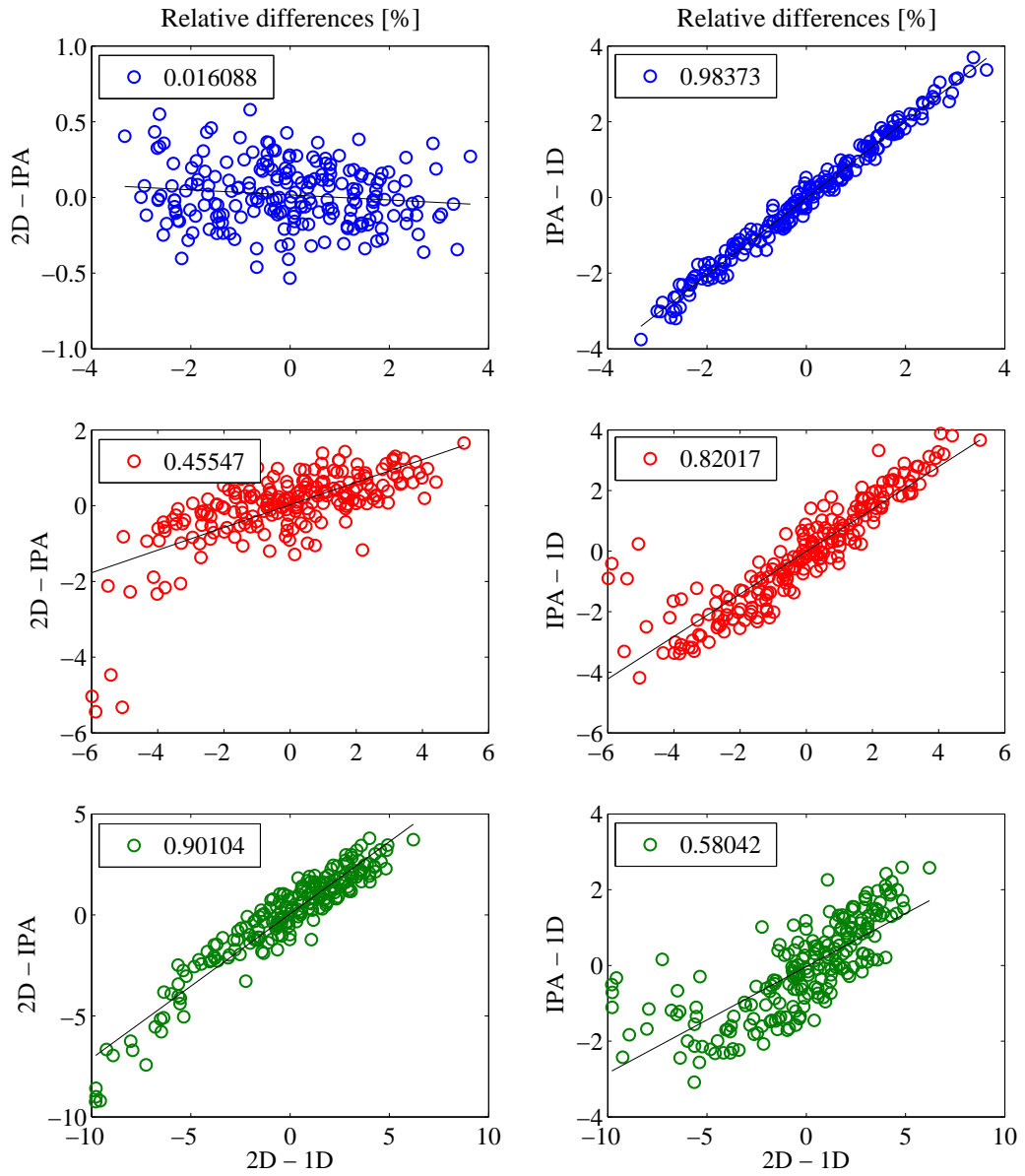


Figure 5.21: The same as in Figure 5.20 but for the SAMUM measurement case.

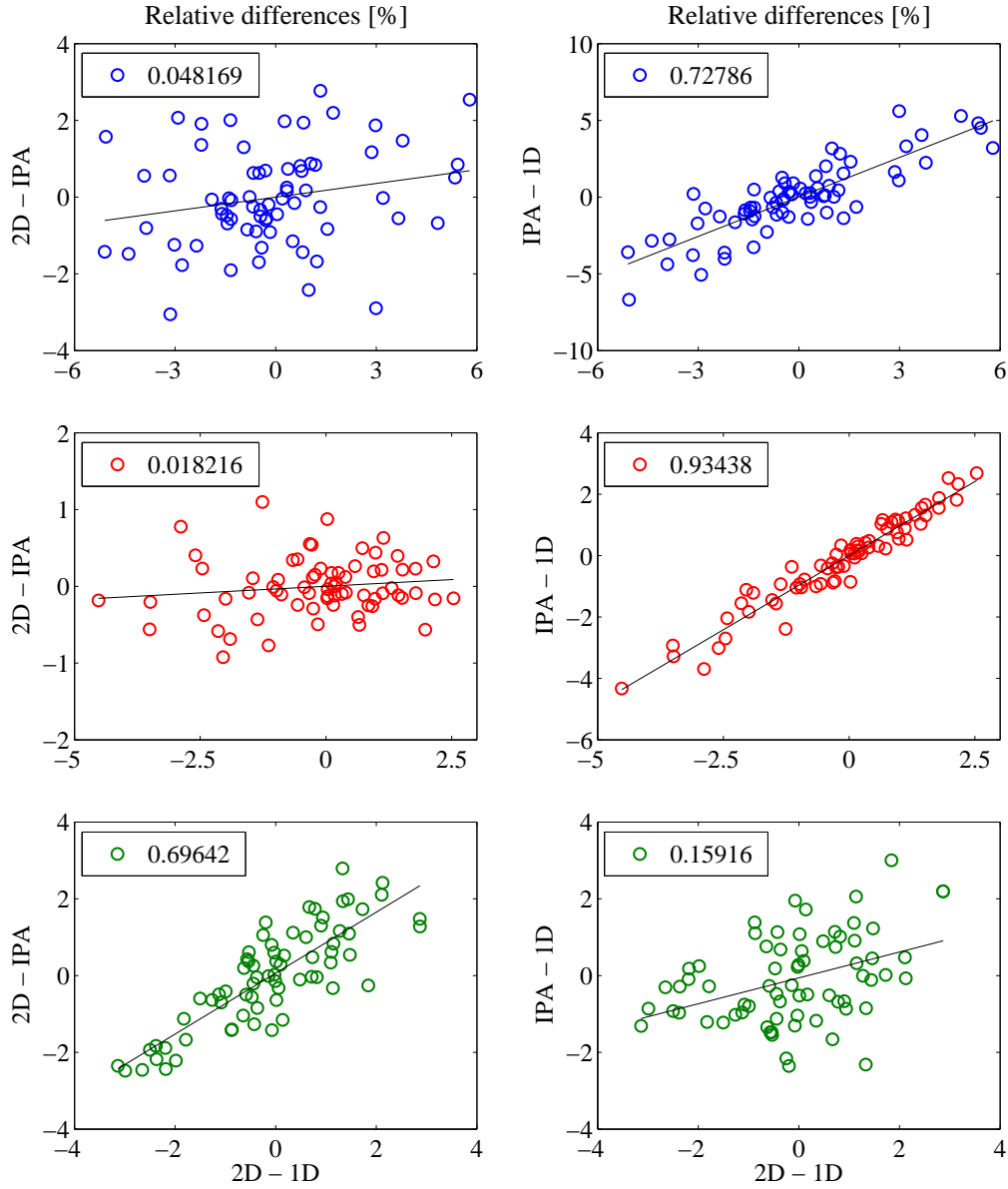


Figure 5.22: The same as in Figure 5.20 but for the transmitted field for a viewing zenith angle of 133° .

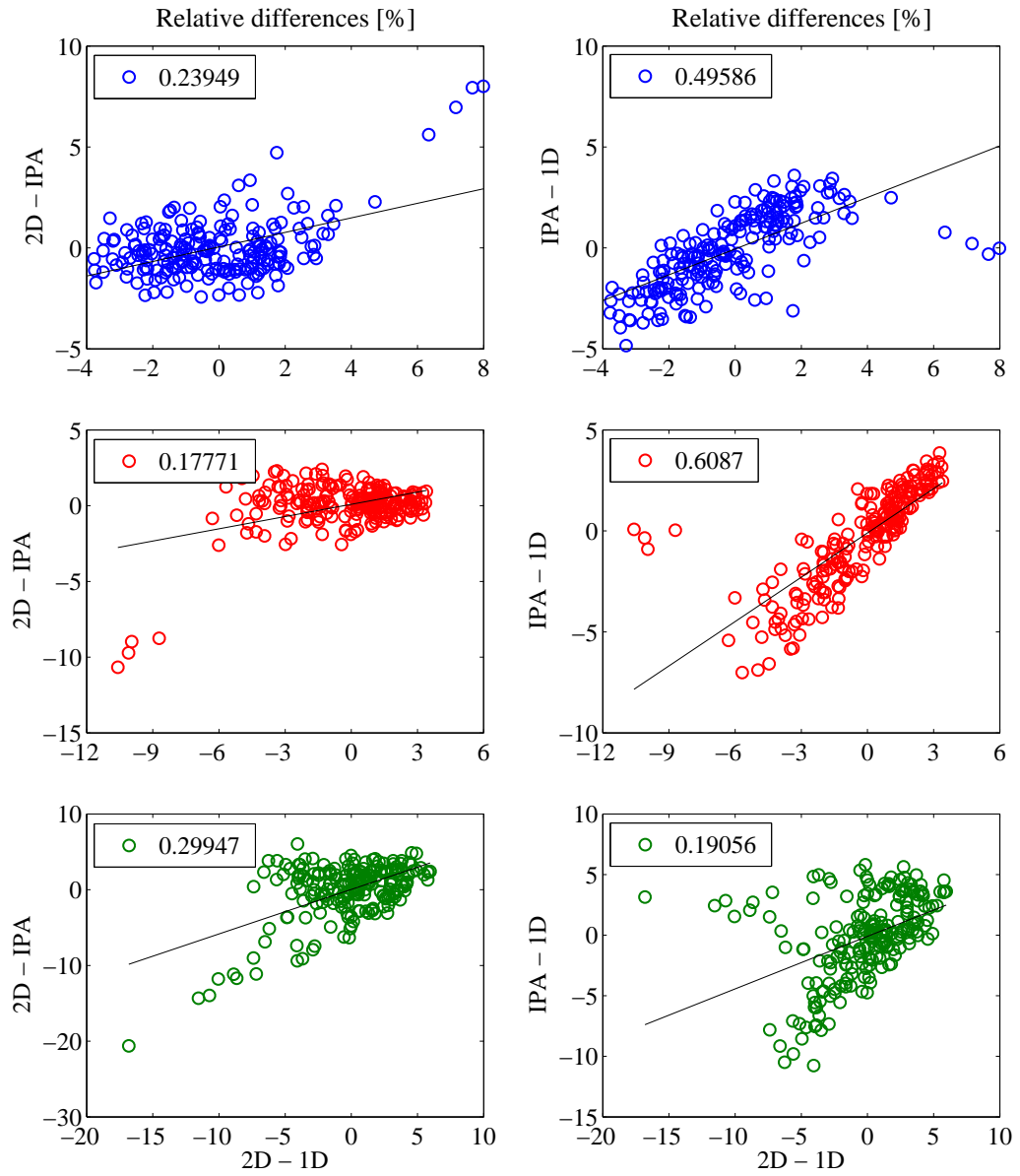


Figure 5.23: The same as in Figure 5.22 but for the SAMUM measurement case.

5.3 Errors Prompted by Neglecting Polarization in Radiance Computations

In Chapter 3 the differences between the scalar and vector radiative transfer theory have been outlined. In brief, ignoring the effects of polarization and replacing the Stokes vector $\vec{S} = (F \ Q \ U \ V)^T$ with its scalar approximation (first component only, F), and the full phase matrix ($\tilde{\mathbf{P}}$) by its first element (\tilde{P}_{11}) cause considerable errors in computing radiative transfer processes in complex scattering media.

The effect of neglecting polarization in radiance simulations have been investigated, whereby two atmospheric problems have been considered. The first one involves a homogenous Rayleigh single-layer and the second scattering problem corresponds to realistic atmospheres utilizing the two LIDAR-measured inhomogeneous Saharan dust schemes introduced in Subsection 5.1.1. Both scalar and vector calculations have been performed using SPARTA.

5.3.1 Molecular Atmosphere

To illustrate such errors, in case of a purely molecular atmosphere, a set of case studies was defined. Simulations were performed for a homogeneous plane-parallel single Rayleigh layer. Detailed information of the settings of the simulations are found in Table 5.8. The sensitivity to the optical thickness, surface albedo, and single-scattering albedo was tested.

To consider Rayleigh scattering, the analytical expression of the phase matrix Eq. (4.2) was used, and three depolarization factors were selected (0, 0.03, and 0.09). The depolarization factor describes molecular anisotropy (polarizability, Liou, 2002). While for pure Rayleigh scattering, meaning isotropic spherical particles, $\delta = 0$, for real atmospheric gases (e.g., diatomic, triatomic), and thus anisotropic molecules, δ diverges from zero. In other words, this factor corrects for molecular anisotropy in terms of polarization (Bodhaine et al., 1999). The two additional values of δ correspond to the typical value for air, namely $\delta = 0.03$, and the value for carbon dioxide ($\delta = 0.09$).

For example, Figure 5.24, depicts the vector versus scalar calculations in the reflected radiation at the TOA as a function of the viewing zenith angle for the three values of the surface albedo (0, 0.1, 0.4) considered, pertaining to an optical thickness of $\tau = 0.5$ in case

Table 5.8: Simulation settings considered in case of a pure molecular atmosphere.

Input parameters	
τ	0.1, 0.5
θ_0	0°
θ_{det}	$0^\circ, \dots, 85^\circ$ (increment 5°)
ϕ	0°
$\tilde{\omega}$	0.70, 0.90, 0.99, 1.00
α_L	0.0, 0.1, 0.4
δ	0.00, 0.03, 0.09
Altitude	TOA

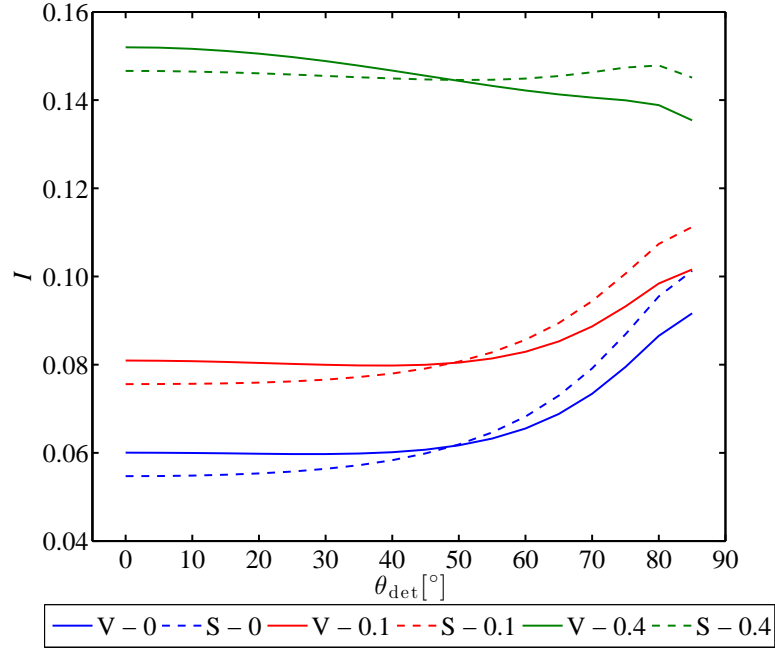


Figure 5.24: Vector (straight lines) and scalar (dashed lines) calculations in the reflected radiation at the TOA as a function of the viewing zenith angle for three surface albedo values (0, 0.1, and 0.4) pertaining to a solar zenith angle of 0° , a relative azimuth angle of 0° , optical thickness of $\tau = 0.5$, for isotropic particles ($\delta = 0$).

of pure Rayleigh scattering ($\delta = 0$). Obviously, clear differences are pinpointed over the full spectrum of the viewing directions. In order to quantify these errors, the relative differences in percent between the vector (subscript "V") and scalar (subscript "S") simulations (RD_{V-S}) have been computed according to the following equation:

$$RD_{V-S} = \frac{\text{Vector} - \text{Scalar}}{\text{Vector}} \cdot 100\% \quad (5.4)$$

Note that where RD_{V-S} are negative, the scalar scheme overestimates the radiance, where positive, it underestimates it.

In Figure 5.25, results are presented for four scenarios. All the graphs present the relative differences in percent between the vector and scalar calculations in the reflected diffuse radiation as a function of the viewing direction. Scenario 1 (left upper plot) is a test for isotropic surface reflection. The optical thickness of the pure Rayleigh atmosphere ($\delta = 0$) is set to 0.5, while molecular absorption was switched off. In Subsection 3.2.5, the effects of isotropic reflection were introduced (scattering at surface completely depolarizes incident radiation). As a result, increasing the surface albedo from zero (blue line for black non-scattering surface) to 0.4 (green line for isotropic reflection) the RD_{V-S} are decreasing. In Scenario 2, the influence of molecular anisotropy on the RD_{V-S} is observed. Simulations were conducted for a non-absorbing ($\tilde{\omega} = 0$) layer with an optical thickness of 0.5 above an ideal absorbing surface ($\alpha_L = 0$). The upper right plot shows that accounting for depolarization (from $\delta = 0 - 0.09$) corrects the scalar approximation for molecular anisotropy. The third

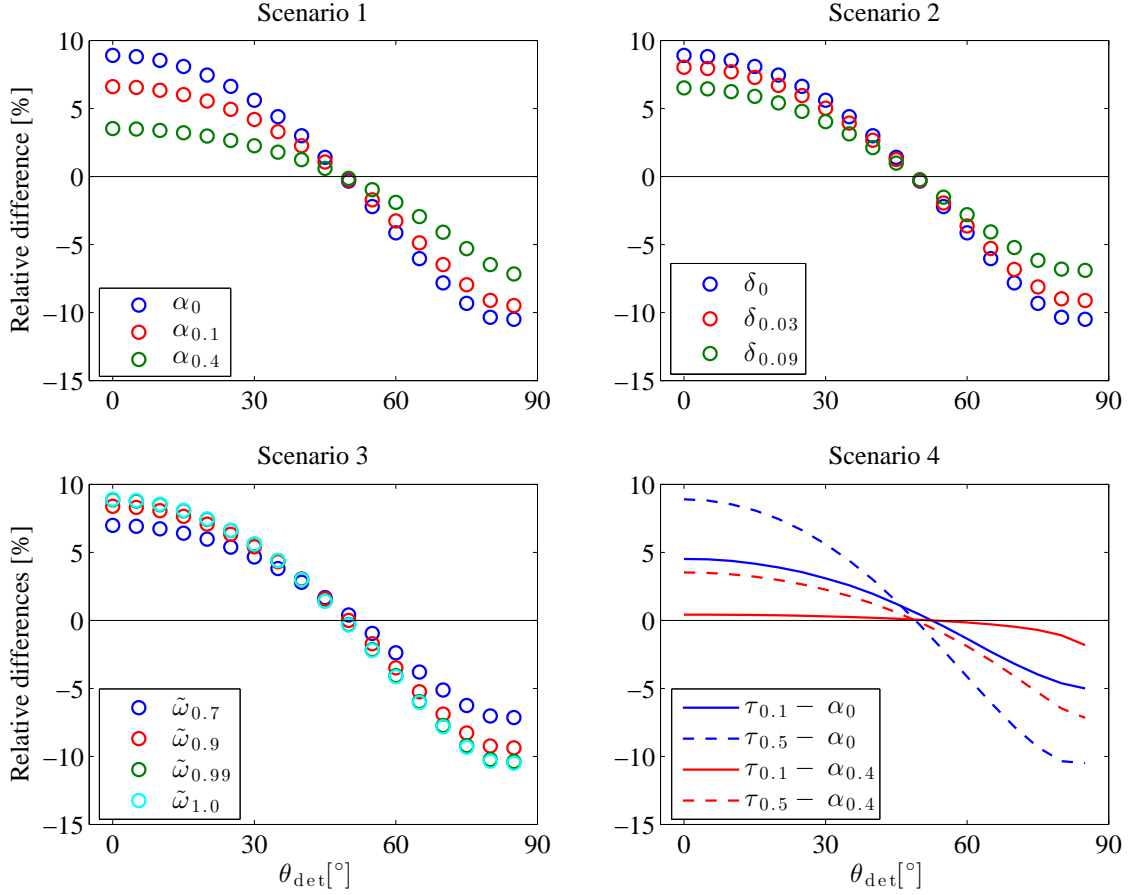


Figure 5.25: Relative differences in percent between the vector and scalar calculations in the reflected diffuse radiation as a function of the viewing direction: **Scenario 1** (left upper plot) - test for isotropic surface reflection ($\alpha_L = 0, 0.1, 0.4$), with settings ($\tau = 0.5, \delta = 0, \tilde{\omega} = 1$), **Scenario 2** (right upper plot) - test for molecular anisotropy ($\delta = 0, 0.03, 0.09$), with settings ($\tau = 0.5, \tilde{\omega} = 1, \alpha_L = 0$), **Scenario 3** (left lower plot) - test for molecular absorption ($\tilde{\omega} = 0.7, 0.9, 0.99, 1$), with settings ($\tau = 0.5, \delta = 0, \alpha_L = 0$), **Scenario 4** (right lower plot) - test for optical thickness ($\tau = 0.1, 0.5$), with settings ($\delta = 0, \alpha_L = 0$, straight lines - $\tau = 0.1$, and dashed lines - $\tau = 0.5$).

case study (Scenario 3, lower left plot) checks the impact of molecular absorption on the errors prompted by neglecting polarization in radiation simulations. A perfect Rayleigh scattering layer ($\delta = 0$) with $\tau = 0.5$ was selected, and the effects of isotropic reflection were neglected ($\alpha_L = 0$). Under these circumstances, increasing molecular absorption, or, in other words, decreasing the single-scattering albedo, the vector versus scalar differences are decreasing. Finally, Scenario 4 (lower right panel) demonstrates the RD_{V-S} dependence on τ . The straight lines correspond to $\tau=0.1$, and the dashed lines to $\tau=0.5$. Hence, it was designed on the basis of the input for which the major errors were observed, namely, for $\tilde{\omega}=1$ (no molecular absorption) and a depolarization factor of zero. Results are shown for two values of the surface albedo (0 and 0.4). It follows that the thicker the atmosphere the more pronounced are the errors. The maximum RD_{V-S} found in this study are in the range of $-5\% - 0.4\%$ for $\tau=0.1$, and $-10.5\% - 3.5\%$ for $\tau = 0.5$.

Table 5.9: Range of relative differences in percent between vector and scalar calculations for the four scenarios presented in this work.

Cases	Range of RD $v-s$
Scenario 1	−10.5 % - 3.5 %
Scenario 2	−10.5 % - 6.5 %
Scenario 3	−10.5 % - 6.9 %
Scenario 4	−5 % - 0.4% for $\tau = 0.1$ −10.5 % - 3.5 % for $\tau = 0.5$

One sees from all the panels in Figure 5.25 that the scalar assumption underestimates the simulated reflectances for viewing zenith angles up to about 48° , and it overestimates them for larger viewing zenith angles. Quantitatively, Table 5.9, lists the RD_{v-s} for the four scenarios presented here. Overall, errors in the reflected field prompted by neglecting polarization were estimated. These errors could be up to about 10.5 %, which is in agreement with former studies (Chandrasekhar, 1960; van de Hulst, 1980; Mishchenko et al., 1994; Lacis et al., 1998; Kotchenova et al., 2006). For comprehensive interpretation of the relative differences between vector and scalar calculations, the reader is referred to the work of Mishchenko et al. (1994) and Lacis et al. (1998). In brief, these errors result from lower-order scattering; except from first-order, but mainly from second-order scattering. These errors are more pronounced at scattering angles close to 90° , and right-angle rotations of the scattering plane (Mishchenko et al., 1994). Consequently, they dominate in molecular scattering owing to the special structure of the Rayleigh scattering phase matrix, meaning, considerable polarization at scattering angles close to 90° (e.g., see Figure 4.1). In this thesis, simulations were carried out for two values of τ (0.1, 0.5). Scenario 4 shows that increasing τ , the errors are increasing. This trend is known to saturate for optical thickness of about 1. For thicker layers, the increasing number of the multiple-scattering events should further diminish the errors, depending mainly on molecular absorption, and secondly on isotropic reflection.

As a conclusion, the scalar radiative transfer approach introduces errors in simulated radiances for pure Rayleigh scattering atmospheres at visible wavelengths, and thus, polarization should be utilized as a correction scheme for remote sensing applications.

5.3.2 Inhomogeneous Saharan Dust Fields

The errors induced by neglecting polarization in radiance simulations involving a purely Rayleigh atmosphere have been extensively discussed in Subsection 5.3.1, and more importantly, in Mishchenko et al. (1994) and Lacis et al. (1998). Limited investigations have been made on pure aerosol particles (Hansen, 1971b; Kotchenova et al., 2006) or mixed scenarios (aerosol + molecules) (Kotchenova et al., 2006). Hansen (1971b) reported that the corresponding vector versus scalar differences in case of spherical cloud particles (with sizes of the order or greater than the wavelength of the incident EM radiation) are up to about 1 %. Kotchenova et al. (2006) found that, for an aerosol atmosphere with polydispersed homogeneous spheres with a mean radius of about $0.15 \mu\text{m}$ (biomass burning smoke aerosol particles), the RD_{v-s} are in the range of 1.6 % - 5.3 %, depending on the wavelength, mean-

Table 5.10: Maximum relative differences in percent between vector and scalar simulations over all the viewing directions (TOA: $0^\circ, 47^\circ, 70^\circ$, and BOA: $180^\circ, 133^\circ, 110^\circ$) in case of 1D and 2D modes pertaining to solar zenith angles of $0^\circ, 47^\circ, 70^\circ$.

	SAMUM			METEOR		
TOA	$\theta_0 = 0^\circ$	$\theta_0 = 47^\circ$	$\theta_0 = 70^\circ$	$\theta_0 = 0^\circ$	$\theta_0 = 47^\circ$	$\theta_0 = 70^\circ$
1D modes	0.78	-0.49	-0.46	0.91	-0.65	-0.62
2D modes	0.81	-0.52	-0.49	0.93	-0.66	-0.64
BOA	$\theta_0 = 0^\circ$	$\theta_0 = 47^\circ$	$\theta_0 = 70^\circ$	$\theta_0 = 0^\circ$	$\theta_0 = 47^\circ$	$\theta_0 = 70^\circ$
1D modes	-0.39	-0.13	-0.41	-0.43	0.13	-0.56
2D modes	-0.41	-0.14	-0.44	-0.46	0.13	-0.58

ing that the effects are more pronounced at longer wavelengths; stronger polarization of the scattering phase function of the ensemble of smoke particles. In addition, for a mixed atmosphere (smoke particles + molecules) and two wavelengths ($\lambda = 470$ nm and 670 nm), the errors caused due to the neglect of polarization are up to about 4.3 % at 470 nm wavelength, owing to the stronger Rayleigh scattering.

Nevertheless, although the aforementioned studies reported errors up to 5 % when comparing scalar and vector schemes, the following discussion points to negligible deficiencies. In this thesis, the discussion will point to realistic 1D and 2D schemes of inhomogeneous Saharan dust fields. Towards this direction, the two measurement cases introduced in Subsection 5.1.1 have been employed. Simulations have been performed for a wavelength of 532 nm based on the settings described in Subsection 5.1.3 and results are presented for two different modes (1D and 2D) for both the reflected (TOA) and transmitted (BOA) radiation. The maximum relative differences between vector and scalar calculations are listed in Table 5.10.

In contrast to pure molecular scattering, the errors induced by neglecting polarization for realistic inhomogeneous atmospheres involving molecules, water soluble and dust particles, are insignificant. The maximum observed RD_{V-S} are less than 1 % for both measurement scenarios (SAMUM 0.81 % with averaged τ of 1.1, METEOR 0.93 % with averaged τ of 0.74). As described in the first part of this section (molecular case), the errors come from the second-order scattering. Accordingly, strongly polarized first-order scattering supplies the second-order, and consequently, the second-order supplies the third-order, and so on. The high-order scatterings linked to high optical thickness, and rather highly asymmetric scattering phase matrices of the dust particles, are the reasons of the low values of the relative differences, making the scalar assumption sufficient for remote sensing applications, depending on the use (e.g., restricted to radiance calculations; not for retrievals).

Figure 5.26 shows the scenario for which the major RD_{V-S} were found, namely for the METEOR measurement case pertaining to a solar zenith angle of 0° and detector position of ($\theta_{\text{det}} = 0^\circ, \phi_{\text{det}} = 0^\circ$).

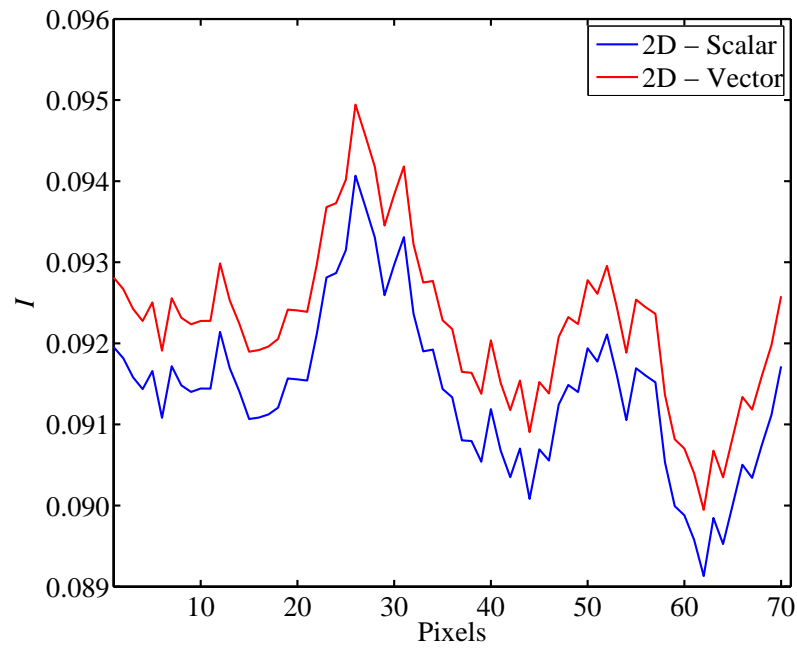


Figure 5.26: Vector (red line) and scalar (blue line) calculations in the reflected radiation at the TOA as a function of the pixel number, pertaining to a solar zenith angle of 0° and detector position of $(\theta_{\text{det}} = 0^\circ, \phi_{\text{det}} = 0^\circ)$.

6 Summary, Conclusions, and Outlook

This chapter serves as both a conceptual summary of the present work as well as providing a prospect for future work. Partially, it was published in Barlakas et al. (2016) and Emde et al. (2015).

6.1 A New Radiative Transfer Solver

To quantify polarization effects due to multiple-scattering by non-spherical particles (coarse mode dust or ice particles), a new three-dimensional (3D) vector radiative transfer model, SPARTA (Solver for Polarized Atmospheric Radiative Transfer Applications) is developed and comprehensively validated against benchmark results. Considering the limitations in availability of 3D vector models, SPARTA is going to be a freely available, user-friendly model. SPARTA is built on the scalar Monte Carlo model of the Leibniz Institute of Marine Sciences (now GEOMAR) at the UNiversity of Kiel (MC-UNIK, Macke et al. 1999) and employs the statistical forward Monte Carlo technique for efficient column-response pixel-based radiance calculations including polarization for 3D inhomogeneous cloudless and cloudy atmospheres. Thus, it is well suited for use in remote sensing applications. The major objective of this work is the application of SPARTA to scientific problems with a special emphasis on non-spherical mineral dust particles and polarization.

Free path lengths are simulated as outlined by Marchuk et al. (1980) by random number processes with attenuation described by the law of Bouguer-Beer. Scattering directions are calculated according to an importance sampling method, which seems to be the fastest approach of the different methods to the polarized radiative transfer problem (Collins et al., 1972; Marchuk et al., 1980; Emde et al., 2010). An alternative approach for polarization problems, which has been investigated during the development of SPARTA, is to employ the normalized scattered Stokes vector as the probability density function (PDF) to sample the new direction. However, this leads to a bi-variable PDF of the scattering zenith and azimuth angles introducing numerical problems (due to the trigonometric functions) and consequently to an increase in computational needs. Absorption is taken into account by decreasing the initial Stokes weight by the estimated total absorption coefficient, along the photon path, with the Bouguer-Beer Law. The surface contribution is calculated assuming isotropic reflection (Lambertian surface) or anisotropic ocean reflection as outlined in Mishchenko and Travis (1997). In order to obtain precise radiance calculations for each wavelength and to diminish the noise of simulations for highly asymmetric phase matrices the Local Estimate Method has been applied (Collins et al., 1972; Marchuk et al., 1980; Marshak and Davis, 2005). Other variance reduction methods have not been implemented. Future work will include applying

various variance reduction techniques (truncation techniques, Rozanov and Lyapustin 2010; Buras and Mayer 2011).

SPARTA has been tested for different atmospheric conditions (e.g., Rayleigh scattering, aerosol particles and randomly oriented prolate spheroids) and comprehensively compared to benchmark results (de Haan et al., 1987; Natraj et al., 2009; Kokhanovsky et al., 2010). It took part in the model intercomparison project launched by the polarization working group of the International Radiation Commission (IPRT) (Emde et al., 2015). Overall, the comparisons demonstrated that the performance of SPARTA is excellent. All deviations found in case of highly asymmetric phase matrices can be explained by the noise of the Monte Carlo technique in radiance calculations. The noisiness of the signal is a function of the number of photons. Increasing the selected number of photons diminishes the noise.

6.2 Implications from Neglecting Polarization

By means of SPARTA a sensitivity study has been carried out to quantify the errors induced by neglecting polarization in radiance simulations. Two atmospheric problems have been considered. The first scattering problem involves a homogenous Rayleigh single-layer and the second one corresponds to realistic atmospheres utilizing two LIDAR-measured inhomogeneous Saharan dust scenarios (SAMUM and METEOR). In order to quantify these errors, the relative differences in percent between the vector and scalar simulations (RD_{V-S}) have been computed.

In case of a molecular atmosphere, the sensitivity of RD_{V-S} to the optical thickness (τ), isotropic reflection (that completely depolarizes incident radiation) characterized by different surface albedos, single-scattering albedo, and the depolarization factor (that corrects for molecular anisotropy in terms of polarization) was examined. Increasing the surface albedo, the depolarization factor, and molecular absorption, the errors by ignoring polarization are decreasing. Finally, these errors are more pronounced for higher optical thicknesses. This dependency is known to saturate for optical thickness of about 1. For larger values of τ , the increasing multiple-scattering process, leads to a decrease of the bias, depending on isotropic reflection, and more importantly, on the single-scattering albedo. Overall errors in the reflected field up to about 10.5 % were estimated. This bias is caused from lower-order scattering; except from first-order, but mainly from second-order scattering. It is more pronounced for molecular scattering due to the special structure of the Rayleigh phase matrix; considerable polarization is found at scattering angles close to 90° .

For realistic inhomogeneous atmospheres, in contrast to the Rayleigh scattering case, the bias prompted by ignoring polarization in radiation simulations is negligible. The maximum observed RD_{V-S} are less than 1 % for both measurement cases. As described above, the errors come from second-order scattering. Strongly polarized first-order scattering supplies the second-order, and as a consequence, the second-order supplies the third-order, and so on. The high-order scatterings resulting from rather high τ values (1.1 for SAMUM, and 0.74 for METEOR), and highly asymmetric scattering phase matrices of the mineral dust particles results in low values of RD_{V-S} . For such cases, the scalar radiative transfer approximation

is adequate for a few remote sensing applications (e.g., limited to radiation computations; not for retrievals).

Overall, the scalar assumption may lead to significant bias in radiation computations for pure Rayleigh scattering atmospheres at visible wavelengths, and therefore, polarization should be employed to interpret remote sensing data.

6.3 Quantification of Polarization Radiative Effects

In this study, an effort has been made to quantify the radiative effects associated with 1D scalar radiative transfer simulations for two realistic LIDAR-measured inhomogeneous Saharan dust scenes. Clouds (and also dust plumes) interact with radiation depending on both their microphysical properties and spatial distribution; structure is also important (aerosol vertical profile). The objective of this application is of great importance since there is no evidence corroborating the notion that the scalar approximation is adequate to interpret the bias introduced by ignoring domain heterogeneities. Polarized radiance fields were calculated for three solar zenith angles (0° , 47° , and 70°), the same viewing directions for the reflected radiation at the TOA, and the supplementary angles (180° , 133° , and 110°) for the transmitted radiation at the BOA above a Lambertian surface with albedo $\alpha_L = 0.05$, corresponding to an ocean surface. The relative azimuth angle was set to 0° . For each measurement case, three radiative calculations were conducted at 532 nm wavelength: an 1D calculation according to the plane-parallel assumption utilizing domain-averaged optical properties (1D mode); an Independent Pixel Approximation (IPA mode) accounting horizontal inhomogeneities (HI) but omitting horizontal photon transport (HPT); and the 2D mode that takes into account the variability in only one horizontal direction (x or y). The 2D versus 1D comparison assesses the total radiative effect, the 2D versus IPA comparison renders information about the significance of the HPT, while the 1D error (IPA versus 1D) quantifies the horizontal heterogeneity effect.

2D - 1D Major Results

The differences in domain-averaged normalized radiances of reflection and transmission are insignificant between the 1D and 2D modes. However, local differences were observed since extinction depends on horizontal spatial variability. In the areas with a large gradient in optical thickness, the radiance fields of the 2D mode differ by about $\pm 20\%$ for I and Q from the fields of the 1D mode (excluding the areas with artificial strong gradient in τ). In brief, the total radiative effect is especially sensitive to the viewing direction and the gradient in optical thickness, but the sign of its two components may differ. It is more pronounced for the transmitted rather than for the reflected field and for the first Stokes component as compared to the second one. The differences between 2D and 1D are larger for the SAMUM measurement case but they are affected by an artificial gradient in optical thickness owing to the periodic boundary conditions employed in SPARTA. This can be explained by the lower gradient in optical thickness and the lower variability that is resolved by the larger horizontal pixel size of the METEOR LIDAR-measured field.

2D - IPA Major Results

The horizontal photon transport bias is larger for nadir reflection at the TOA as compared to zenith surface transmission. Increasing the solar zenith angle the HPT is increasing, and the divergence between the IPA bias found for the zenith transmitted and nadir reflected fields is decreasing. The latter trend is a bit weaker for the SAMUM case, considering the artificial gradient in optical thickness. Comparing the two measurement scenarios, the error owing to HPT is more pronounced in the SAMUM case, because of the smaller horizontal pixel size (Di Giuseppe and Tompkins, 2003), whereby the horizontal photon transport effect plays a major role for specific illumination and observation geometries. Overall, the maximum absolute IPA error is:

- SAMUM: **a.** $\theta_{\text{det}} = 47^\circ$ - (12 %, 8 %) and **b.** $\theta_{\text{det}} = 110^\circ$ - (64 %, 20 %) or (20 %, 13.6 %) if we exclude the areas with possible artificial gradient in τ .
- METEOR: **a.** $\theta_{\text{det}} = 70^\circ$ - (4.8 %, 3 %) and **b.** $\theta_{\text{det}} = 110^\circ$ - (9.4 %, n/a).

IPA - 1D Major Results

For the reflected radiation at the TOA, the 1D bias is low for both measurement cases. It is within the range of $\pm 4.3\%$ for I , and $\pm 3.1\%$ for Q . For the transmitted radiation at the BOA, the corresponding bias is larger. The 1D biases are for the SAMUM case: $-40 < \text{RD}_{\text{IPA-1D}} < 20.1$ for I (or $\pm 20\%$ if the shaded areas are excluded) and $-17.7 < \text{RD}_{\text{IPA-1D}} < 10.3$ for Q . Accordingly, for the METEOR case: $-14 < \text{RD}_{\text{IPA-1D}} < 9.7$ for I and $-7.2 < \text{RD}_{\text{IPA-1D}} < 4.2$ for Q . The one-dimensional heterogeneity effect is introduced by ignoring the domain horizontal variability. Consequently, a perfect linear correlation between the 1D error and the τ is found for both the first and second Stokes components. The correlation for Q is a bit weaker. It is more pronounced for the reflected as compared to the transmitted radiation. For example, the fraction where the deviation of the bias is smaller than the deviation of the dependent parameter, R^2 , is in the range of 0.83 - 0.98 for METEOR (excluding the geometry combination $(\theta_0 = 70^\circ, \theta_{\text{det}} = 70^\circ)$) and 0.5 - 0.96 for SAMUM for the first Stokes element; for Q , R^2 up to 0.99 were also found, but for different geometry combinations $(\theta_0 = 70^\circ, \theta_{\text{det}} = 70^\circ)$. The latter linear correlation may be used as a correction scheme of the radiative effects introduced by employing 1D radiative transfer solvers for remote sensing applications.

Overall Radiative Effects Major Results

The total radiative effect consists of two components: the horizontal photon transport and the internal horizontal heterogeneity effects. These two physical processes do not always have the same sign depending on the illumination and viewing directions. To interpret the radiative effects, the IPA and 1D biases were compared to the total bias. For the reflected radiation and the METEOR case, the total bias for the first Stokes component is driven by the 1D bias. For a solar zenith angle of 0° , there is a perfect correlation between RD (total bias) and $\text{RD}_{\text{IPA-1D}}$ ($R^2 = 0.99$), illustrating that the heterogeneity effect completely overbalances

the horizontal photon transport (negligible). Increasing the solar zenith angle, the HPT is increasing, while the HI is decreasing. Note here that for the METEOR case, the 1D bias is always the dominant effect due to the low horizontal resolution (2.06 km). For the SAMUM case, the HPT component is slightly more pronounced considering the higher horizontal resolution (0.96 km). In the same direction is the outcome for the second Stokes component; yet, both effects are found to be a bit weaker. The same holds for the transmitted field at the surface for the METEOR case. On the other hand, the SAMUM LIDAR-measured field poses some deviations driven by an artificial strong gradient introduced by the periodic boundary conditions employed in SPARTA. In conclusion, increasing the horizontal pixel size results in a decrease of the IPA effect and an increase of the 1D heterogeneity effect.

The goal of this work is to broaden such investigations by combining the 3D aspect with the vector radiative transfer scheme, pointing to a brand-new field: the quantification of the sensitivity of polarization to such physical processes.

6.4 Outlook

The strength of polarization is the capacity to be sensitive to particle shape, size and thermodynamic phase in remote sensing. Polarization effects saturate for an optical thickness of about 2 or 3, since the final polarization state results from the first few orders of scattering. Consequently, polarization measurements should be utilized to retrieve information for aerosol and cloud particles. In essence, the new 3D vector radiative transfer solver can be employed to interpret passive and active polarized remote sensing measurements. For example, SPARTA can be used to quantitatively analyze the POLDER measurements (satellite remote sensing retrieval of dust particles and cirrus clouds). By comparing the simulated and measured total and polarized reflectances, the cirrus optical properties can be derived (Labonnote et al., 2001). From a ground-based perspective, the model can be used to retrieve mineral dust properties from polarized sun photometer measurements. Polarized reflectance can be employed to discriminate between spherical water droplets (water clouds) and non-spherical ice crystals (cirrus clouds). In addition, the shape, size and orientation of non-spherical ice crystals can be inferred from polarization measurements (Liou and Takano, 2002).

In this work, results are presented for two LIDAR-based measurement cases. More 2D inhomogeneous dust LIDAR-measured fields are needed. Future work should aim at developing correction schemes that account for observable gradients of optical thickness in the dust fields. Applications may be extended to 2D inhomogeneous cirrus clouds from LIDAR measurements (Seifert et al., 2007). Moreover, further research should be conducted in order to explore the polarization radiative effects in 3D realistic mineral cloud schemes. Towards this direction, more advanced scattering phase matrices and realistic dust particle shapes shall be used.

Going even further, since polarization saturates for an optical thickness of about 2 or 3, the polarization signature may be the same for thin, thick or very thick clouds (and dust fields). This implies that polarization should be less sensitive to 3D effects. However, Cornet et al.

(2010) stated that the polarized reflectance is as sensitive as the total reflectance to 3D effects. Therefore, total and polarized reflectances from air-borne (e.g., by the Research Scanning Polarimeter) or from space-borne (e.g., POLDER) based measurements can be employed to investigate 3D radiative effects in dust fields.

SPARTA can also be used to investigate fundamental optical properties (e.g., photon path statistics to characterize cloud inhomogeneities, distribution of number of scatterings, photon densities, PDFs of spatial photon distribution).

Last but not least, the second phase of the IPRT intercomparison project (3D test cases) has started and SPARTA is going to participate.

Bibliography

- Anderson, G., Clough, S., Kneizys, F., Chetwynd, J., and Shettle, E.: AFGL Atmospheric Constituent Profiles (0–120 km), Tech. Rep. AFGL-TR-86-0110, AFGL (OPI), Hanscom AFB, MA 01736, 1986.
- Andreae, M. O.: Chapter 10 Climatic effects of changing atmospheric aerosol levels, in Future climates of the world: a modelling perspective, edited by A. Henderson-sellers, vol. 16 of *World Survey of Climatology*, pp. 347 – 398, Elsevier, [http://dx.doi.org/10.1016/S0168-6321\(06\)80033-7](http://dx.doi.org/10.1016/S0168-6321(06)80033-7), 1995.
- Ansmann, A., Petzold, A., Kandler, K., Tegen, I., Wendisch, M., Müller, D., Weinzierl, B., Müller, T., and Heintzenberg, J.: Saharan Mineral Dust Experiments SAMUM-1 and SAMUM-2: what have we learned?, *Tellus B*, 63, 403–429, doi:10.1111/j.1600-0889.2011.00555.x, 2011.
- Barlakas, V., Macke, A., Wendisch, M., and Ehrlich, A.: Implementation of polarization in a 3D Monte Carlo Radiative Transfer Model, *Wissenschaftliche Mitteilungen aus dem Institut für Meteorologie der Universität Leipzig*, 52, 1–14, iISBN: 978-3-9814401-2-6, 2014.
- Barlakas, V., Macke, A., and Wendisch, M.: SPARTA – Solver for Polarized Atmospheric Radiative Transfer Applications: Introduction and application to Saharan dust fields, *J. Quant. Spectrosc. Radiat. Transfer*, doi:10.1016/j.jqsrt.2016.02.019, in press, 2016.
- Benassi, M., Garcia, R., and Siewert, C.: A generalized spherical harmonics solution basic to the scattering of polarized light, *Zeitschrift für angewandte Mathematik und Physik ZAMP*, 36, 70–88, doi:10.1007/BF00949034, 1985.
- Benner, T. C. and Evans, K. F.: Three-dimensional solar radiative transfer in small tropical cumulus fields derived from high-resolution imagery, *J. Geophys. Res.*, 106, 14 975–14 984, doi:10.1029/2001JD900158, 2001.
- Bodhaine, B. A., Wood, N. B., Dutton, E. G., and Slusser, J. R.: On Rayleigh optical depth calculations, *J. Atmos. Oceanic Technol.*, 16, 1854–1861, doi:10.1175/1520-0426(1999)016<1854:ORODC>2.0.CO;2, 1999.
- Boesche, E., Stammes, P., Ruhtz, T., Preusker, R., and Fischer, J.: Effect of aerosol microphysical properties on polarization of skylight: sensitivity study and measurements, *Appl. Opt.*, 45, 8790–8805, doi:10.1364/AO.45.008790, 2006.
- Bristow, C. S., Hudson-Edwards, K. A., and Chappell, A.: Fertilizing the Amazon and equatorial Atlantic with West African dust, *Geophys. Res. Lett.*, 37, doi:10.1029/2010GL043486, l14807, 2010.

- Brown, A. J. and Xie, Y.: Symmetry relations revealed in Mueller matrix hemispherical maps, *J. Quant. Spectrosc. Radiat. Transfer*, 113, 644 – 651, <http://dx.doi.org/10.1016/j.jqsrt.2012.01.008>, 2012.
- Budak, V. and Korkin, S.: The spatial polarization distribution over the dome of the sky for abnormal irradiance of the atmosphere, *J. Quant. Spectrosc. Radiat. Transfer*, 109, 1347 – 1362, <http://dx.doi.org/10.1016/j.jqsrt.2008.01.014>, 2008.
- Buehler, S., Eriksson, P., Kuhn, T., von Engeln, A., and Verdes, C.: ARTS, the atmospheric radiative transfer simulator, *J. Quant. Spectrosc. Radiat. Transfer*, 91, 65 – 93, <http://dx.doi.org/10.1016/j.jqsrt.2004.05.051>, 2005.
- Buras, R. and Mayer, B.: Efficient unbiased variance reduction techniques for Monte Carlo simulations of radiative transfer in cloudy atmospheres: The solution, *J. Quant. Spectrosc. Radiat. Transfer*, 112, 434 – 447, <http://dx.doi.org/10.1016/j.jqsrt.2010.10.005>, 2011.
- Cahalan, R. F., Ridgway, W., Wiscombe, W. J., Bell, T. L., and Snider, J. B.: The albedo of fractal stratocumulus clouds, *J. Atmos. Sci.*, 51, 2434–2455, doi:10.1175/1520-0469(1994)051<2434:TAOFSC>2.0.CO;2, 1994a.
- Cahalan, R. F., Ridgway, W., Wiscombe, W. J., Gollmer, S., and Harshvardhan: Independent pixel and Monte Carlo estimates of stratocumulus albedo, *J. Atmos. Sci.*, 51, 3776–3790, doi:10.1175/1520-0469(1994)051<3776:IPAMCE>2.0.CO;2, 1994b.
- Cahalan, R. F., Oreopoulos, L., Marshak, A., Evans, K. F., Davis, A. B., Pincus, R., Yetzer, K. H., Mayer, B., Davies, R., Ackerman, T. P., Barker, H. W., Clothiaux, E. E., Ellingson, R. G., Garay, M. J., Kassianov, E., Kinne, S., Macke, A., O'Hirok, W., Partain, P. T., Prigarin, S. M., Rublev, A. N., Stephens, G. L., Szczap, F., Takara, E. E., Várnai, T., Wen, G., and Zhuravleva, T. B.: The I3RC: Bringing together the most advanced radiative transfer tools for cloudy atmospheres, *Bull. Am. Meteorol. Soc.*, 86, 1275–1293, doi:10.1175/BAMS-86-9-1275, 2005.
- Cairns, B., Russell, E. E., and Travis, L. D.: Research scanning polarimeter: calibration and ground-based measurements, in *Proc. SPIE*, vol. 3754, pp. 186–196, doi:10.1117/12.366329, 1999.
- Cairns, B., Russell, E. E., LaVeigne, J. D., and Tennant, P. M. W.: Research scanning polarimeter and airborne usage for remote sensing of aerosols, in *Proc. SPIE*, vol. 5158, pp. 33–44, doi:10.1117/12.518320, 2003.
- Cantrell, W. and Heymsfield, A.: Production of ice in tropospheric clouds: A review, *Bull. Am. Meteorol. Soc.*, 86, 795–807, doi:10.1175/BAMS-86-6-795, 2005.
- Cashwell, E. D. and Everett, C. J.: A practical manual on the Monte Carlo method for random walk problems, Pergamon, New York, <http://trove.nla.gov.au/work/6138332>, 1959.

- Chadwick, O. A., Derry, L. A., Vitousek, P. M., Huebert, B. J., and Hedin, L. O.: Changing sources of nutrients during four million years of ecosystem development, *Nature*, 397, 491–497, <http://dx.doi.org/10.1038/17276>, 1999.
- Chandrasekhar, S.: *Radiative Transfer*, Dover Books on Intermediate and Advanced Mathematics, Dover Publications, ISBN: 9780486605906, 1960.
- Chouza, F., Reitebuch, O., Groß, S., Rahm, S., Freudenthaler, V., Toledano, C., and Weinzierl, B.: Retrieval of aerosol backscatter and extinction from airborne coherent Doppler wind lidar measurements, *Atmos. Meas. Tech. Discuss.*, 8, 1935–1986, doi:10.5194/amtd-8-1935-2015, 2015.
- Chowdhary, J., Cairns, B., Mishchenko, M. I., and Travis, L. D.: Constraining aerosol single scattering albedos from multiangle multispectral photo-polarimetric observations over the ocean, in *Proc. SPIE*, vol. 5571, pp. 127–139, doi:10.1117/12.565705, 2004.
- Collins, D. G., Blättner, W. G., Wells, M. B., and Horak, H. G.: Backward Monte Carlo calculations of the polarization characteristics of the radiation emerging from spherical-shell atmospheres, *Appl. Opt.*, 11, 2684–2696, doi:10.1364/AO.11.002684, 1972.
- Cornet, C., C-Labonnote, L., and Szczap, F.: Three-dimensional polarized Monte Carlo atmospheric radiative transfer model (3DMCPOL): 3D effects on polarized visible reflectances of a cirrus cloud, *J. Quant. Spectrosc. Radiat. Transfer*, 111, 174 – 186, <http://dx.doi.org/10.1016/j.jqsrt.2009.06.013>, 2010.
- Coulson, K. L., Dave, J. V., and Sekera, Z.: *Tables related to radiation emerging from a planetary atmosphere with Rayleigh scattering*, University of California Press, Berkeley, <http://catalog.hathitrust.org/Record/001485933>, 1960.
- Cox, C. and Munk, W.: Measurement of the roughness of the sea surface from photographs of the sun’s glitter, *J. Opt. Soc. Am.*, 44, 838–850, doi:10.1364/JOSA.44.000838, 1954.
- Davis, A., Marshak, A., Cahalan, R., and Wiscombe, W.: The Landsat scale break in stratocumulus as a three-dimensional radiative transfer effect: Implications for cloud remote sensing, *J. Atmos. Sci.*, 54, 241–260, doi:10.1175/1520-0469(1997)054<0241:TLBSIS>2.0.CO;2, 1997.
- Davison, B. and Sykes, J. B.: *Neutron Transport Theory*, vol. First, Oxford University Press, London, 1957.
- de Haan, J. F., Bosma, P. B., and Hovenier, J. W.: The adding method for multiple scattering calculations of polarized light, *Astron. Astr.*, 183, 371–391, <http://adsabs.harvard.edu/abs/1987A%26A...183..371D>, 1987.
- de Rooij, W. A. and van der Stap, C. C. A. H.: Expansion of Mie scattering matrices in generalized spherical functions, *Astron. Astr.*, 131, 237–248, 1984.
- Deirmendjian, D.: *Electromagnetic Scattering on Spherical Polydispersions*, American Elsevier Pub. Co., Inc., New York, 1969.

- DeMott, P. J., Prenni, A. J., Liu, X., Kreidenweis, S. M., Petters, M. D., Twohy, C. H., Richardson, M. S., Eidhammer, T., and Rogers, D. C.: Predicting global atmospheric ice nuclei distributions and their impacts on climate, *Proceedings of the National Academy of Sciences*, 107, 11 217–11 222, doi:10.1073/pnas.0910818107, 2010.
- Deschamps, P.-Y., Breon, F.-M., Leroy, M., Podaire, A., Bricaud, A., Buriez, J.-C., and Seze, G.: The POLDER mission: instrument characteristics and scientific objectives, *IEEE Trans. Geosci. Rem. Sens.*, 32, 598–615, doi:10.1109/36.297978, 1994.
- Di Giuseppe, F. and Tompkins, A. M.: Effect of spatial organisation on solar radiative transfer in three-dimensional idealized stratocumulus cloud fields, *J. Atmos. Sci.*, 60, 1774–1794, doi:10.1175/1520-0469(2003)060<1774:E0S00S>2.0.CO;2, 2003.
- Diner, D. J., Xu, F., Garay, M. J., Martonchik, J. V., Rheingans, B. E., Geier, S., Davis, A., Hancock, B. R., Jovanovic, V. M., Bull, M. A., Capraro, K., Chipman, R. A., and McClain, S. C.: The Airborne Multiangle SpectroPolarimetric Imager (AirMSPI): a new tool for aerosol and cloud remote sensing, *Atmos. Meas. Tech. Discuss.*, 6, 1717–1769, doi:10.5194/amtd-6-1717-2013, 2013.
- Doicu, A., Efremenko, D., and Trautmann, T.: A multi-dimensional vector spherical harmonics discrete ordinate method for atmospheric radiative transfer, *J. Quant. Spectrosc. Radiat. Transfer*, 118, 121 – 131, <http://dx.doi.org/10.1016/j.jqsrt.2012.12.009>, 2013.
- Duan, M., Min, Q., and Lü, D.: A polarized Radiative Transfer model based on successive order of scattering, *Adv. Atmos. Sci.*, 27, 891–900, doi:10.1007/s00376-009-9049-8, 2010.
- Emde, C., Buras, R., Mayer, B., and M., B.: The impact of aerosols on polarized sky radiance: model development, validation, and applications, *Atmos. Chem. Phys.*, 10, 383–396, doi:10.5194/acp-10-383-2010, 2010.
- Emde, C., Barlakas, V., Cornet, C., Evans, F., Korkin, S., Ota, Y., Labonnote, L. C., Lyapustin, A., Macke, A., Mayer, B., and Wendisch, M.: IPRT polarized radiative transfer model intercomparison project – Phase A, *J. Quant. Spectrosc. Radiat. Transfer*, 164, 8 – 36, <http://dx.doi.org/10.1016/j.jqsrt.2015.05.007>, 2015.
- Evans, K. and Stephens, G.: A new polarized atmospheric radiative transfer model, *J. Quant. Spectrosc. Radiat. Transfer*, 46, 413 – 423, [http://dx.doi.org/10.1016/0022-4073\(91\)90043-P](http://dx.doi.org/10.1016/0022-4073(91)90043-P), 1991.
- Evans, K. F.: The spherical harmonics discrete ordinate method for three-dimensional atmospheric radiative transfer, *J. Atmos. Sci.*, 55, 429–446, doi:10.1175/1520-0469(1998)055<0429:TSHDOM>2.0.CO;2, 1998.
- Fauchez, T., Cornet, C., Szczap, F., Dubuisson, P., and Rosambert, T.: Impact of cirrus clouds heterogeneities on top-of-atmosphere thermal infrared radiation, *Atmos. Chem. Phys.*, 14, 5599–5615, doi:10.5194/acp-14-5599-2014, 2014.

- Garcia, R. and Siewert, C.: A generalized spherical harmonics solution for radiative transfer models that include polarization effects, *J. Quant. Spectrosc. Radiat. Transfer*, 36, 401 – 423, [http://dx.doi.org/10.1016/0022-4073\(86\)90097-X](http://dx.doi.org/10.1016/0022-4073(86)90097-X), 1986.
- Garcia, R. and Siewert, C.: The FN method for radiative transfer models that include polarization effects, *J. Quant. Spectrosc. Radiat. Transfer*, 41, 117 – 145, [http://dx.doi.org/10.1016/0022-4073\(89\)90133-7](http://dx.doi.org/10.1016/0022-4073(89)90133-7), 1989.
- Gasteiger, J., Groß, S., Freudenthaler, V., and Wiegner, M.: Volcanic ash from Iceland over Munich: mass concentration retrieved from ground-based remote sensing measurements, *Atmos. Chem. Phys.*, 11, 2209–2223, doi:10.5194/acp-11-2209-2011, 2011.
- Ginoux, P., Prospero, J. M., Gill, T. E., Hsu, N. C., and Zhao, M.: Global-scale attribution of anthropogenic and natural dust sources and their emission rates based on MODIS Deep Blue aerosol products, *Rev. Geophys.*, 50, doi:10.1029/2012RG000388, 2012.
- Hansen, J. E.: Multiple scattering of polarized light in planetary atmospheres. Part I. The doubling method, *J. Atmos. Sci.*, 28, 120–125, doi:10.1175/1520-0469(1971)028<0120:MSOPLI>2.0.CO;2, 1971a.
- Hansen, J. E.: Multiple scattering of polarized light in planetary atmospheres. Part II. Sunlight reflected by terrestrial water clouds, *J. Atmos. Sci.*, 28, 1400–1426, doi:10.1175/1520-0469(1971)028<1400:MSOPLI>2.0.CO;2, 1971b.
- Hansen, J. E. and Travis, L. D.: Light scattering in planetary atmospheres, *Space Sci. Rev.*, 16, 527–610, doi:10.1007/BF00168069, 1974.
- Haywood, J. and Boucher, O.: Estimates of the direct and indirect radiative forcing due to tropospheric aerosols: A review, *Rev. Geophys.*, 38, 513–543, doi:10.1029/1999RG000078, 2000.
- Heintzenberg, J.: The SAMUM-1 experiment over Southern Morocco: overview and introduction, *Tellus B*, 61, 2–11, doi:10.1111/j.1600-0889.2008.00403.x, 2009.
- Hess, M., Koepke, P., and Schult, I.: Optical Properties of Aerosols and Clouds: The Software Package OPAC, *Bull. Am. Meteorol. Soc.*, 79, 831–844, doi:10.1175/1520-0477(1998)079<0831:OPOAAC>2.0.CO;2, 1998.
- Hovenier, J. W., van der Mee, C., and Domke, H.: *Transfer of Polarized Light in Planetary Atmospheres*, Kluwer Academic Publishers, Dordrecht, Netherlands, 2004.
- Hutchins, D. A. and Bruland, K. W.: Iron-limited diatom growth and Si:N uptake ratios in a coastal upwelling regime, *Nature*, 393, 561–564, <http://dx.doi.org/10.1038/31203>, 1998.
- IPCC: *Climate Change 2013: The Physical Science Basis*, Cambridge University Press, www.climatechange2013.org, 2013.

- Kandler, K., Schütz, L., Deutscher, C., Ebert, M., Hofmann, H., Jäckel, S., Jaenicke, R., Knippertz, P., Lieke, K., Massling, A., Petzold, A., Schladitz, A., Weinzierl, B., Wiedensohler, A., Zorn, S., and Weinbruch, S.: Size distribution, mass concentration, chemical and mineralogical composition and derived optical parameters of the boundary layer aerosol at Tinfou, Morocco, during SAMUM 2006, *Tellus B*, 61, 32–50, doi:10.1111/j.1600-0889.2008.00385.x, 2009.
- Kandler, K., Lieke, K., Benker, N., Emmel, C., Küpper, M., Müller-Ebert, D., Ebert, M., Scheuven, D., Schladitz, A., Schütz, L., and Weinbruch, S.: Electron microscopy of particles collected at Praia, Cape Verde, during the Saharan Mineral Dust Experiment: particle chemistry, shape, mixing state and complex refractive index, *Tellus B*, 63, 475–496, doi:10.1111/j.1600-0889.2011.00550.x, 2011.
- Kanitz, T., Engelmann, R., Heinold, B., Baars, H., Skupin, A., and Ansmann, A.: Tracking the Saharan Air Layer with shipborne lidar across the tropical Atlantic, *Geophys. Res. Lett.*, 41, 1044–1050, doi:10.1002/2013GL058780, 2014.
- Kattawar, G. W. and Plass, G. N.: Electromagnetic scattering from absorbing spheres, *Appl. Opt.*, 6, 1377–1382, doi:10.1364/AO.6.001377, 1967.
- Kaufman, Y. J., Tanre, D., and Boucher, O.: A satellite view of aerosols in the climate system, *Nature*, 419, 215–223, <http://dx.doi.org/10.1038/nature01091>, 2002.
- Kokhanovsky, A. A., Budak, V. P., Cornet, C., Duan, M., Emde, C., Katsev, I. L., Klyukov, D. A., Korkin, S. V., C-Labonnote, L., Mayer, B., Min, Q., Nakajima, T., Ota, Y., Prikhach, A. S., Rozanov, V. V., Yokota, T., and Zege, E. P.: Benchmark results in vector atmospheric radiative transfer, *J. Quant. Spectrosc. Radiat. Transfer*, 111, 1931 – 1946, <http://dx.doi.org/10.1016/j.jqsrt.2010.03.005>, 2010.
- Korkin, S. V., Lyapustin, A. I., and Rozanov, V. V.: APC: A new code for Atmospheric Polarization Computations, *J. Quant. Spectrosc. Radiat. Transfer*, 127, 1 – 11, <http://dx.doi.org/10.1016/j.jqsrt.2013.06.019>, 2013.
- Kotchenova, S. Y., Vermote, E. F., Matarrese, R., and Klemm, F. J. J.: Validation of a vector version of the 6S radiative transfer code for atmospheric correction of satellite data. Part I: Path radiance, *Appl. Opt.*, 45, 6762–6774, doi:10.1364/AO.45.006762, 2006.
- Labonnote, L., Brogniez, G., Buriez, J.-C., Doutriaux-Boucher, M., Gayet, J.-F., and Macke, A.: Polarized light scattering by inhomogeneous hexagonal monocrystals: Validation with ADEOS-POLDER measurements, *J. Geophys. Res.*, 106, 12 139–12 155, 2001.
- Lacis, A. A., Chowdhary, J., Mishchenko, M. I., and Cairns, B.: Modeling errors in diffuse-sky radiation: Vector vs scalar treatment, *Geophys. Res. Lett.*, 25, 135–138, doi:10.1029/97GL03613, 1998.
- Lenoble, J.: Application de la méthode des harmoniques spheriques au cas de la diffusion anisotrope, *C.R. Acad. Sci.*, 252, 2087–2089, 1961.

- Levin, Z., Ganor, E., and Gladstein, V.: The effects of desert particles coated with sulfate on rain formation in the Eastern Mediterranean, *J. Appl. Meteorol.*, 35, 1511–1523, doi:10.1175/1520-0450(1996)035<1511:TEODPC>2.0.CO;2, 1996.
- Li, L., Li, Z., Li, K., Blarel, L., and Wendisch, M.: A method to calculate Stokes parameters and angle of polarization of skylight from polarized CIMEL sun/sky radiometers, *J. Quant. Spectrosc. Radiat. Transfer*, 149, 334 – 346, <http://dx.doi.org/10.1016/j.jqsrt.2014.09.003>, 2014.
- Li, Z., Goloub, P., Dubovik, O., Blarel, L., Zhang, W., Podvin, T., Sinyuk, A., Sorokin, M., Chen, H., Holben, B., Tanré, D., Canini, M., and Buis, J.-P.: Improvements for ground-based remote sensing of atmospheric aerosol properties by additional polarimetric measurements, *J. Quant. Spectrosc. Radiat. Transfer*, 110, 1954 – 1961, <http://dx.doi.org/10.1016/j.jqsrt.2009.04.009>, 2009.
- Liou, K.-N.: Influence of cirrus clouds on weather and climate processes: A global perspective, *Mon. Wea. Rev.*, 114, 1167–1199, doi:10.1175/1520-0493(1986)114<1167:IOCCOW>2.0.CO;2, 1986.
- Liou, K. N.: An Introduction to Atmospheric Radiation, Academic Press, iSBN: 9780124514515, 2002.
- Liou, K. N. and Takano, Y.: Interpretation of cirrus cloud polarization measurements from radiative transfer theory, *Geophys. Res. Lett.*, 29, 27–1–27–4, doi:10.1029/2001GL014613, 2002.
- Macke, A., Mishchenko, M., Carlson, B., and Muinonen, K.: Scattering of light by large spherical, spheroidal, and circular cylindrical scatterers: Geometrical optics approximation versus T-matrix method, in *IRS 96: Current problems in atmospheric radiation*, edited by W. Smith and K. Stamnes, pp. 822–825, A. Deepak Publ., Hampton, <http://oceanrep.geomar.de/891/>, 1997.
- Macke, A., Mitchell, D. L., and V., B. L.: Monte Carlo radiative transfer calculations for inhomogeneous mixed phase clouds, *Phys. Chem. Earth*, 24, 237–241, [http://dx.doi.org/10.1016/S1464-1909\(98\)00044-6](http://dx.doi.org/10.1016/S1464-1909(98)00044-6), 1999.
- Marchuk, G. I., Mikhailov, G. A., and A., N. M.: The Monte Carlo Methods in Atmospheric Optics, Springer-Verlag, New York, 1980.
- Marshak, A. and Davis, A.: 3D Radiative Transfer in Cloudy Atmospheres, Springer Berlin Heidelberg, http://dx.doi.org/10.1007/3-540-28519-9_4, 2005.
- Marshak, A., Davis, A., Wiscombe, W., Ridgway, W., and Cahalan, R.: Biases in short-wave column absorption in the presence of fractal clouds, *J. Climate*, 11, 431–446, doi:10.1175/1520-0442(1998)011<0431:BISCAI>2.0.CO;2, 1998.
- Mayer, B.: Radiative transfer in the cloudy atmosphere, *Eur. Phys. J. Conferences*, 1, 75–99, 2009.

- Mayer, B. and Kylling, A.: Technical note: The *libRadtran* software package for radiative transfer calculations - description and examples of use, *Atmos. Chem. Phys.*, 5, 1855–1877, 2005.
- Metropolis, N. and Ulam, S.: The Monte Carlo method, *J. Amer. Statistical Assoc.*, 44, 335–341, 1949.
- Mie, G.: Beiträge zur Optik trüber Medien, speziell kolloidaler Metallösungen, *Annalen der Physik*, Vierte Folge, 25, 377–445, 1908.
- Min, Q. and Duan, M.: A successive order of scattering model for solving vector radiative transfer in the atmosphere, *J. Quant. Spectrosc. Radiat. Transfer*, 87, 243 – 259, <http://dx.doi.org/10.1016/j.jqsrt.2003.12.019>, 2004.
- Mishchenko, M. I.: Reflection of polarized light by plane-parallel slabs containing randomly-oriented, nonspherical particles, *J. Quant. Spectrosc. Radiat. Transfer*, 46, 171 – 181, [http://dx.doi.org/10.1016/0022-4073\(91\)90022-I](http://dx.doi.org/10.1016/0022-4073(91)90022-I), 1991.
- Mishchenko, M. I.: Gustav Mie and the fundamental concept of electromagnetic scattering by particles: A perspective, *J. Quant. Spectrosc. Radiat. Transfer*, 110, 1210 – 1222, <http://dx.doi.org/10.1016/j.jqsrt.2009.02.002>, 2009.
- Mishchenko, M. I. and Travis, L. D.: Satellite retrieval of aerosol properties over the ocean using polarization as well as intensity of reflected sunlight, *J. Geophys. Res.*, 102, 16 989–17 013, doi:10.1029/96JD02425, 1997.
- Mishchenko, M. I., Lacis, A. A., and Travis, L. D.: Errors induced by the neglect of polarization in radiance calculations for rayleigh-scattering atmospheres, *J. Quant. Spectrosc. Radiat. Transfer*, 51, 491 – 510, [http://dx.doi.org/10.1016/0022-4073\(94\)90149-X](http://dx.doi.org/10.1016/0022-4073(94)90149-X), 1994.
- Mishchenko, M. I., Travis, L. D., and Lacis, A. A.: *Scattering, Absorption, and Emission of Light by Small Particles*, Cambridge University Press, ISBN: 9780521782524, 2002.
- Natraj, V., Li, K.-F., and Yung, Y. L.: Rayleigh scattering in planetary atmospheres: Corrected tables through accurate computation of X and Y functions, *Astrophys. J.*, 691, 1909–2009, <http://stacks.iop.org/0004-637X/691/i=2/a=1909>, 2009.
- Ota, Y., Higurashi, A., Nakajima, T., and Yokota, T.: Matrix formulations of radiative transfer including the polarization effect in a coupled atmosphere–ocean system, *J. Quant. Spectrosc. Radiat. Transfer*, 111, 878 – 894, <http://dx.doi.org/10.1016/j.jqsrt.2009.11.021>, 2010.
- Otto, S., Bierwirth, E., Weinzierl, B., Kandler, K., Esselborn, M., Tesche, M., Schladitz, A., Wendisch, M., and Trautmann, T.: Solar radiative effects of a Saharan dust plume observed during SAMUM assuming spheroidal model particles, *Tellus B*, 61, 270–296, doi:10.1111/j.1600-0889.2008.00389.x, 2009.

- Phillips, V. T. J., DeMott, P. J., and Andronache, C.: An empirical parameterization of heterogeneous ice nucleation for multiple chemical species of aerosol, *J. Atmos. Sci.*, 65, 2757–2783, doi:10.1175/2007JAS2546.1, 2008.
- Pierluissi, J. H. and Peng, G.-S.: New molecular transmission band models for LOWTRAN, *Opt. Eng.*, 24, 243 541–243 541–, doi:10.1117/12.7973523, 1985.
- Ricchiazzi, P., Yang, S., Gautier, C., and Sowle, D.: SBDART: A research and teaching software tool for plane-parallel radiative transfer in the Earth’s atmosphere, *Bull. Amer. Meteorol. Soc.*, 79, 2101–2114, doi:10.1175/1520-0477(1998)079<2101:SARATS>2.0.CO;2, 1998.
- Rozanov, A., Rozanov, V., Buchwitz, M., Kokhanovsky, A., and Burrows, J.: SCI-ATRAN 2.0 - A new radiative transfer model for geophysical applications in the 175-2400 nm spectral region RID G-1510-2011, *Adv. Space Res.*, 36, 1015 – 1019, <http://dx.doi.org/10.1016/j.asr.2005.03.012>, 2005.
- Rozanov, V., Rozanov, A., Kokhanovsky, A., and Burrows, J.: Radiative transfer through terrestrial atmosphere and ocean: Software package SCIATRAN, *J. Quant. Spectrosc. Radiat. Transfer*, 133, 13 – 71, <http://dx.doi.org/10.1016/j.jqsrt.2013.07.004>, 2014.
- Rozanov, V. V. and Kokhanovsky, A. A.: The solution of the vector radiative transfer equation using the discrete ordinates technique: Selected applications, *Atm. Res.*, 79, 241 – 265, <http://dx.doi.org/10.1016/j.atmosres.2005.06.006>, 2006.
- Rozanov, V. V. and Lyapustin, A. I.: Similarity of radiative transfer equation: Error analysis of phase function truncation techniques, *J. Quant. Spectrosc. Radiat. Transfer*, 111, 1964–1979, 2010.
- Scheirer, R. and Macke, A.: On the accuracy of the independent column approximation in calculating the downward fluxes in the UVA, UVB, and PAR spectral ranges, *J. Geophys. Res.*, 106, 14 301–14 312, doi:10.1029/2001JD900130, 2001.
- Scheirer, R. and Macke, A.: Cloud inhomogeneity and broadband solar fluxes, *J. Geophys. Res.*, 108, doi:10.1029/2002JD003321, 4599, 2003.
- Schulz, F., Stammes, K., and Weng, F.: VDISORT: An improved and generalized discrete ordinate method for polarized (vector) radiative transfer, *J. Quant. Spectrosc. Radiat. Transfer*, 61, 105 – 122, [http://dx.doi.org/10.1016/S0022-4073\(97\)00215-X](http://dx.doi.org/10.1016/S0022-4073(97)00215-X), 1999.
- Schuster, A.: Radiation through a foggy atmosphere, *Astrophys. J.*, 21, 1–22, doi:10.1086/141186, 1905.
- Schwarzschild, K.: Ueber das Gleichgewicht der Sonnenatmosphäre, *Nachr. Ges. Wiss. Göttingen, Math.-Phys. Kl.*, 1906, 41–53, <http://eudml.org/doc/58631>, 1906.
- Seifert, P., Ansmann, A., Müller, D., Wandinger, U., Althausen, D., Heymsfield, A. J., Massie, S. T., and Schmitt, C.: Cirrus optical properties observed with lidar, radiosonde, and satellite over the tropical Indian Ocean during the aerosol-polluted northeast and clean

- maritime southwest monsoon, *J. Geophys. Res. Atmos.*, 112, doi:10.1029/2006JD008352, 2007.
- Seinfeld, J. H. and Pandis, S. N.: *Atmospheric Chemistry and Physics: From Air Pollution to Climate Change*, John Wiley & Sons, Inc., New York, ISBN: 9780471178156, 1998.
- Stammes, P., de Haan, J. F., and Hovenier, J. W.: The polarized internal radiation field of a planetary atmosphere, *Astron. Astrophys.*, 225, 239–259, 1989.
- Stokes, G. G.: On the Composition and Resolution of Streams of Polarized Light from Different Sources, *Proceedings of the Cambridge Philosophical Society : Mathematical and physical sciences*, Cambridge Philosophical Society, <http://books.google.de/books?id=41VFGwAACAAJ>, 1852.
- Stokes, G. G.: On the intensity of the light reflected from or transmitted through a pile of plates, *Proc. R. Soc. London*, 11, 545–556, doi:10.1098/rspl.1860.0119, 1860.
- Tegen, I.: Modeling the mineral dust aerosol cycle in the climate system, *Quat. Sci. Rev.*, 22, 1821 – 1834, [http://dx.doi.org/10.1016/S0277-3791\(03\)00163-X](http://dx.doi.org/10.1016/S0277-3791(03)00163-X), 2003.
- Teller, A., Xue, L., and Levin, Z.: The effects of mineral dust particles, aerosol regeneration and ice nucleation parameterizations on clouds and precipitation, *Atmos. Chem. Phys.*, 12, 9303–9320, doi:10.5194/acp-12-9303-2012, 2012.
- Tesche, M., Gross, S., Ansmann, A., Müller, D., Althausen, D., Freudenthaler, V., and Esselborn, M.: Profiling of Saharan dust and biomass-burning smoke with multiwavelength polarization Raman lidar at Cape Verde, *Tellus B*, 63, 649–676, <http://www.tellusb.net/index.php/tellusb/article/view/16360>, 2011.
- Torge, A., Macke, A., Heinold, B., and Wauer, J.: Solar radiative transfer simulations in Saharan dust plumes: particle shapes and 3-D effect, *Tellus B*, 63, 770–780, doi:10.1111/j.1600-0889.2011.00560.x, 2011.
- Tsang, L. and Li, Q.: *Microwave Remote Sensing Theory*, John Wiley & Sons, Inc., doi:10.1002/047134608X.W3615, ISBN: 9780471346081, 2001.
- Twohy, C. H., Kreidenweis, S. M., Eidhammer, T., Browell, E. V., Heymsfield, A. J., Bansemer, A. R., Anderson, B. E., Chen, G., Ismail, S., DeMott, P. J., and Van Den Heever, S. C.: Saharan dust particles nucleate droplets in eastern Atlantic clouds, *Geophys. Res. Lett.*, 36, doi:10.1029/2008GL035846, l01807, 2009.
- van de Hulst, H. C.: *Multiple light scattering. Tables, formulas and applications*, vol. 1, Academic Press, ISBN: 978-0-12-710701-1, 1980.
- van de Hulst, H. C.: *Light Scattering by Small Particles*, Dover Publications, Mineola, NY, ISBN: 9780486642284, 1981.
- Várnai, T. and Davies, R.: Effects of cloud heterogeneities on shortwave radiation: comparison of cloud-top variability and internal heterogeneity, *J. Atmos. Sci.*, 56, 4206–4224, doi:10.1175/1520-0469(1999)056<4206:E0CHOS>2.0.CO;2, 1999.

- Wauben, W. M. F. and Hovenier, J. W.: Polarized radiation of an atmosphere containing randomly-oriented spheroids, *J. Quant. Spectrosc. Radiat. Transfer*, 47, 491 – 504, [http://dx.doi.org/10.1016/0022-4073\(92\)90108-G](http://dx.doi.org/10.1016/0022-4073(92)90108-G), 1992.
- Wauer, J., Schmidt, K., Rother, T., Ernst, T., and Hess, M.: Two software tools for plane-wave scattering on nonspherical particles in the German Aerospace Center’s virtual laboratory, *Appl. Opt.*, 43, 6371–6379, doi:10.1364/AO.43.006371, 2004.
- Wendisch, M. and Yang, P.: *Theory of Atmospheric Radiative Transfer - A Comprehensive Introduction*, Wiley-VCH Verlag GmbH & Co. KGaA, Weinheim, Germany, iSBN: 978-3-527-40836-8, 2012.
- Weng, F.: A multi-layer discrete-ordinate method for vector radiative transfer in a vertically-inhomogeneous, emitting and scattering atmosphere—I. Theory, *J. Quant. Spectrosc. Radiat. Transfer*, 47, 19 – 33, [http://dx.doi.org/10.1016/0022-4073\(92\)90076-G](http://dx.doi.org/10.1016/0022-4073(92)90076-G), 1992a.
- Weng, F.: A multi-layer discrete-ordinate method for vector radiative transfer in a vertically-inhomogeneous, emitting and scattering atmosphere—II. Application, *J. Quant. Spectrosc. Radiat. Transfer*, 47, 35 – 42, [http://dx.doi.org/10.1016/0022-4073\(92\)90077-H](http://dx.doi.org/10.1016/0022-4073(92)90077-H), 1992b.
- Wick, G.: Über ebene Diffusionsprobleme, *Zeitschrift für Physik*, 121, 702–718, doi:10.1007/BF01339167, 1943.
- Wiscombe, W.: Improved Mie scattering algorithms, *Appl. Opt.*, 19, 1505–1509, 1980.
- Yang, P., Feng, Q., Hong, G., Kattawar, G. W., Wiscombe, W. J., Mishchenko, M. I., Dubovik, O., Laszlo, I., and Sokolik, I. N.: Modeling of the scattering and radiative properties of nonspherical dust-like aerosols, *J. Aerosol Sci.*, 38, 995 – 1014, <http://dx.doi.org/10.1016/j.jaerosci.2007.07.001>, 2007.
- Zdunkowski, W., Trautmann, T., and Bott, A.: *Radiation in the Atmosphere - A Course in Theoretical Meteorology*, Cambridge University Press, New York, iSBN: 9781139464604, 2007.
- Zhang, H., McFarquhar, G. M., Saleeby, S. M., and Cotton, W. R.: Impacts of Saharan dust as CCN on the evolution of an idealized tropical cyclone, *Geophys. Res. Lett.*, 34, doi:10.1029/2007GL029876, 114812, 2007.

List of Symbols

α_L	-	Surface albedo
β_{abs}	m^{-1}	Spectral volumetric absorption coefficient
$\beta_{\text{abs}}^{\text{tot}}$	m^{-1}	Total volumetric absorption coefficient
β_{ext}	m^{-1}	Spectral volumetric extinction coefficient
$\beta_{\text{ext}}^{\text{tot}}$	m^{-1}	Total volumetric extinction coefficient
β_{sca}	m^{-1}	Spectral volumetric scattering coefficient
$\beta_{\text{sca}}^{\text{tot}}$	m^{-1}	Total volumetric scattering coefficient
δ	-	Depolarization factor
ϵ	$\text{A s V}^{-1} \text{m}^{-1}$	Electric permeability
ζ	rad or $^\circ$	Phase of the electric field vector
η	rad or $^\circ$	Rotation angles
θ	rad or $^\circ$	Atmospheric zenith angle
θ_0	rad or $^\circ$	Solar zenith angle
θ_{det}	rad or $^\circ$	Zenith angle, viewing (detector) direction
θ_{inc}	rad or $^\circ$	Zenith angle, incident direction
θ_{refl}	rad or $^\circ$	Zenith angle, reflection direction
θ_{sca}	rad or $^\circ$	Zenith angle, scattering direction
ϑ	rad or $^\circ$	Scattering zenith angle
κ	$\text{V s A}^{-1} \text{m}^{-1}$	Magnetic permittivity
λ	m	Wavelength
μ	-	Cosine of the zenith angle
ρ_λ	-	Spectral albedo
τ	-	Cloud optical thickness
τ_{cum}	-	Cumulated optical thickness
τ_{rand}	-	Randomly chosen optical thickness
ϕ	rad or $^\circ$	Atmospheric azimuth angle
ϕ_0	rad or $^\circ$	Solar azimuth angle
ϕ_{det}	rad or $^\circ$	Azimuth angle, viewing (detector) direction
ϕ_{inc}	rad or $^\circ$	Azimuth angle, incident direction
ϕ_{refl}	rad or $^\circ$	Azimuth angle, reflection direction
ϕ_{sca}	rad or $^\circ$	Azimuth angle, scattering direction
φ	rad or $^\circ$	Scattering azimuth angle
ξ	-	Random number
$\tilde{\omega}$	-	Single-scattering albedo
$\tilde{\omega}^{\text{tot}}$	-	Total single-scattering albedo
ω_c	$\text{s}^{-1} = \text{Hz}$	Circular frequency

d^2A	m^2	Infinitesimal area element
d^2A_{\perp}	m^2	Infinitesimal area element perpendicular to \hat{k}
Θ_j ($j = 1, 2$)	rad or $^{\circ}$	Incident and refracted angles with respect to the surface normal
Φ_{λ}	$\text{J s}^{-1} \text{nm}^{-1}$	Spectral radiant energy flux
Φ_{abs}	$\text{J s}^{-1} \text{nm}^{-1}$	Radiant energy flux absorbed by an individual particle
Φ_{sca}	$\text{J s}^{-1} \text{nm}^{-1}$	Radiant energy flux scattered by an individual particle
X, Y	-	Solutions of the two nonlinear integral equations of radiative transfer equation
$d^2\Omega$	sr	Infinitesimal solid angle
b	-	Hemispheric backscatter ratio
c	m s^{-1}	Velocity of light in vacuum
$\hat{e}_1, \hat{e}_2, \hat{e}_3$	-	Euklidic base vectors
g	-	Asymmetry parameter
h	J s	Planck's constant
\hat{k}	-	Direction of propagation
\hat{k}_{inc}	-	Incident direction
$\hat{k}_{\text{inc},0}$	-	Initial incident direction
\hat{k}_{sca}	-	Scattering direction
\hat{k}_{refl}	-	Reflection direction
k	m^{-1}	Wavenumber
k_{B}	J deg^{-1}	Boltzmann constant
l_{back}	m	Backward step
\hat{n}	-	Surface orientation of d^2A
\hat{n}_{\perp}	-	Surface orientation of d^2A_{\perp}
\tilde{n}	-	Complex index of refraction
n_j	m^{-3}	Particle number density
n_{re}	-	Real part of \tilde{n}
r	m	Radius of aerosol particle
s^2	m s^{-1}	Mean square surface slope of waves
t	s	Time
w	m s^{-1}	Near-surface wind velocity
x, y, z	-	Axes of Cartesian coordinate system (z vertical altitude above ground)
z_{base}	m	Medium base, altitude
z_{top}	m	Medium top, altitude
IA	m	Complex amplitude scattering matrix
A_{ij} ($i, j = 1, 2$)	m	Complex scattering amplitudes
B_{λ}	$\text{W m}^{-2} \text{sr}^{-1} \mu\text{m}^{-1}$	Spectral Planck function
BRDF	-	Bidirectional reflection distribution function
C_{abs}	m^2	Absorption cross section
$\langle C_{\text{abs}} \rangle$	m^2	Average absorption cross section per particle

C_{ext}	m^2	Extinction cross section
$\langle C_{\text{ext}} \rangle$	m^2	Average extinction cross section per particle
C_{sca}	m^2	Scattering cross section
$\langle C_{\text{sca}} \rangle$	m^2	Average scattering cross section per particle
D	m	Diameter of cloud particle
$\vec{\mathbf{E}}$	V m^{-1}	Complex electric field vector
$\vec{\mathbf{E}}_0$	V m^{-1}	Complex electric amplitude vector
E_{rad}	J	Radiant energy
ERF	W m^{-2}	Effective radiative forcing
$\langle \vec{\mathbf{F}} \rangle$	W m^{-2}	Poynting vector
F_0	$\text{W m}^{-2} \text{nm}^{-1}$	Extraterrestrial irradiance
F_λ	$\text{W m}^{-2} \text{nm}^{-1}$	Spectral irradiance
F_λ^\downarrow	$\text{W m}^{-2} \text{nm}^{-1}$	Downward spectral irradiance
F_λ^\uparrow	$\text{W m}^{-2} \text{nm}^{-1}$	Upward spectral irradiance
F_{inc}	$\text{W m}^{-2} \text{nm}^{-1}$	Incident irradiance
$\vec{\mathbf{H}}$	A m^{-1}	Complex magnetic field vector
I_λ	$\text{W m}^{-2} \text{nm}^{-1} \text{sr}^{-1}$	Spectral radiance
\mathbf{M}	-	Mueller matrix
\mathbf{M}_{refl}	-	Matrix based on Fresnel formulas
M	-	Number of scattering events
$M_{ij} (i, j = 1, 2)$	-	Mueller matrix elements
N	-	Number of particles
N_{ph}	-	Number of particles photons
\mathbf{P}	m^2	Scattering phase matrix
$\tilde{\mathbf{P}}^{\text{tot}}$	m^2	Total normalized scattering phase matrix
$\tilde{\mathbf{P}}$	-	Normalized scattering phase matrix
$\langle \mathbf{P} \rangle$	m^2	Average scattering phase matrix
\mathcal{P}	sr	Phase function
P	-	Degree of polarization
$P_{ij} (i, j = 1, 2)$	m^2	Scattering phase matrix elements
P_{cir}	-	Degree of circular polarization
P_{lin}	-	Degree of linear polarization
Q	W m^{-2}	Parallel minus perpendicular linear polarized irradiance
\mathbf{R}	-	Rotation matrix
\mathbf{IR}_L	-	Lambertian (isotropic) reflection matrix
$\mathbf{IR}_{\text{ocean}}$	-	Ocean reflection matrix
RD	%	Relative differences between the 2D and 1D modes
RD _{2D-IPA}	%	Relative differences between the 2D and IPA modes
RD _{IPA-1D}	%	Relative differences between the IPA and 1D modes
RD _{V-S}	%	Relative differences between the vector and scalar modes
RF	W m^{-2}	Radiative forcing
$\vec{\mathbf{S}}$	W m^{-2}	Stokes vector

$\vec{\mathbf{S}}_{\text{inc}}$	W m^{-2}	Incident Stokes vector
$\vec{\mathbf{S}}_{\text{sca}}$	W m^{-2}	Scattered Stokes vector
S	-	Bidirectional shadowing function
T	K	Absolute temperature
U	W m^{-2}	Linear polarized irradiance under 45°
V	W m^{-2}	Circularly polarized irradiance
W	-	The exponential term of W describes the Gaussian distribution of the surface slope
\mathbf{Z}	m^2	Transformation phase matrix
$\tilde{\mathbf{Z}}$	-	Normalized transformation phase matrix
$\langle \mathbf{Z} \rangle$	m^2	Ensemble average transformation phase matrix
$\langle \mathbf{Z}_j \rangle$	m^2	Ensemble average transformation phase matrix for one particle

List of Abbreviations

1D	One-dimensional
2D	Two-dimensional
3D	Three-dimensional
3DMCPOL	Three-dimensional polarized Monte Carlo atmospheric radiative transfer model
6SV1	Second Simulation of a Satellite Signal in the Solar Spectrum, Vector, version 1
ADEOS I	Advanced Earth Observing Satellite 1
A-DM	Adding-Doubling Method
ARTS	Atmospheric Radiative Transfer Simulator
BOA	Bottom Of Atmosphere
BRDF	Bidirectional Reflection Distribution Function
CCN	Cloud Condensation Nuclei
CPU	Central Processing Unit
DAK	Doubling-Adding KNMI (Koninklijk Nederlands Meteorologisch Instituut)
DFG	Deutsche Forschungsgemeinschaft
DLR	Deutsches Zentrum für Luft- und Raumfahrt
DOM	Discrete Ordinate Method
EM	ElectroMagnetic
ERF	Effective Radiative Forcing
erfc	Complementary error function
GCMs	General Circulation Models
GEOS-5	Goddard Earth Observing System Model, Version 5
HI	Horizontal Inhomogeneity
HPT	Horizontal Photon Transport
I3RC	Intercomparison of 3-D Radiation Codes
IN	Ice Nuclei
IPA	Independent Pixel Approximation
IPCC	Intergovernmental Panel on Climate Change
IPOL	Intensity and POLarization
IPRT	International Polarized Radiative Transfer
IRC	International Radiation Commission
LEM	Local Estimate Method
LIDAR	LIght Detection And Ranging
LMU	Ludwig-Maximilians-Universität München

LOWTRAN	LOW altitude atmospheric TRANsmission
MBL	Marine Boundary Layer
MCM	Monte Carlo Method
MC-UNIK	Monte Carlo model of the Leibniz Institute of Marine Sciences (now GEOMAR) at the UNiversity of Kiel (GEOMAR - Helmholtz Centre for Ocean Research Kiel)
MIESCHKA	Program for calculating the scattering properties of axisymmetric particles in a fixed orientation
MSOS	Method of Successive Order of Scattering
MSPI	Multiage SpectroPolarimetric Imager
MVDOM	Modified Vectorial Discrete Ordinates Method
MYSTIC	Monte-Carlo code for the phYSically correct Tracing of photons In Cloudy atmospheres
n/a	Not available
OPAC	Optical Properties of Aerosols and Clouds
PDF	Probability Density Function
POLDER	POLarization and Directionality of the Earth's Reflectances
PolRadTran	Polarized Radiative Transfer
PP	Plane-Parallel
Pstar	Polarized radiance System for Transfer of Atmospheric Radiation
RD	Relative Differences between the 2D and 1D modes
RD _{2D-IPA}	Relative Differences between the 2D and IPA modes
RD _{IPA-1D}	Relative Differences between the IPA and 1D modes
RD _{V-S}	Relative Differences between the vector and scalar modes
RF	Radiative Forcing
RPS	Research Scanning Polarimeter
SALTRACE	Saharan Aerosol Long-range Transport and Aerosol-Cloud-Interaction Experiment
SAMUM	SAharian Mineral dUst experiMent
SBDART	Santa Barbara DISORT Atmospheric Radiative Transfer
SCIATRAN	radiative transfer model for SCIAMACHY (SCanning Imaging Absorption SpectroMeter for Atmospheric CHartographY)
SHM	Spherical Harmonics Method
SOSVRT	Successive Order of Scattering Vector Radiative Transfer model
SPARTA	Solver for Polarized Atmospheric Radiative Transfer Applications
SSA	Single-Scattering Albedo
T-matrix	Program for calculating scattering properties of spherical particles
TOA	Top Of Atmosphere
TROPOS	Leibniz Institute for Tropospheric Research
VDISORT	Vector DIScrete Ordinate Radiative Transfer model

List of Figures

1.1	Portrait of global aerosols yielded by GEOS-5.	2
1.2	RF of climate change during the period 1750-2011 shown by emitted atmospheric components.	3
1.3	Retrieved dust properties obtained from two AERONET inversion algorithms.	5
2.1	Illustration of the definition of radiances.	9
2.2	Electromagnetic wave illustration.	11
2.3	Illustration of scattering of an EM wave by an object.	14
2.4	Transfer of diffuse Stokes vector of the EM wave in the atmosphere.	20
2.5	A schematic representation of the adding-doubling procedure.	22
3.1	2D representation of the scheme of the photon path within the 3D domain of the Monte Carlo radiative transfer model.	28
3.2	Illustration of photon tracing within a regular array of cloud boxes.	30
3.3	Geometric configuration for the transformation of the Stokes vector from the incident meridian plane to the scattering meridian plane.	31
3.4	The geometry of anisotropic scattering.	32
3.5	2D representation of the scheme of the Local Estimate Method.	36
4.1	Scattering phase matrix elements for the aerosol case and for two different molecular scattering cases.	40
4.2	Comparison between SPARTA and the tabulated values by Natraj et al. (2009) for a single Rayleigh layer above Lambertian surfaces. Optically thin atmosphere ($\tau = 0.02$), $\mu_0 = 0.92$, and $\phi = 90^\circ$	41
4.3	Comparison between SPARTA and the tabulated values by Natraj et al. (2009) for a single Rayleigh layer above Lambertian surfaces, for $\tau = 0.1$, $\mu_0 = 0.8$, $\phi = 90^\circ$, and $\alpha_L = 0, 0.25, 0.8$ at TOA.	42
4.4	The same as in Figure 4.3, but for the Stokes vector at the BOA.	43
4.5	Comparison between SPARTA and the tabulated values by Natraj et al. (2009) for a single Rayleigh layer above Lambertian surfaces, for $\tau = 0.5$, $\mu_0 = 0.8$, and $\phi = 90^\circ$ at TOA.	44
4.6	The same as in Figure 4.5, but for the Stokes vector at the BOA.	45
4.7	Comparison between SPARTA and the tabulated values by Natraj et al. (2009) for a single Rayleigh layer above Lambertian surfaces, for $\tau = 0.5$, $\mu_0 = 1$, and $\phi = 0^\circ$ at TOA.	46
4.8	The same as in Figure 4.7, but for the Stokes vector at the BOA.	48
4.9	Scattering phase matrix elements for the aerosol and cloud cases.	50

4.10	Comparison between SPARTA and SCIATRAN for a single aerosol layer above a black surface.	51
4.11	The same as in Figure 4.10, but for a cloud layer.	52
4.12	Phase matrix elements for the spheroidal aerosol particles, water cloud droplets, and molecular scattering.	55
4.13	Comparison between SPARTA and MYSTIC for spheroidal aerosol particles.	56
4.14	Comparison between SPARTA and MYSTIC for Rayleigh scattering above an ocean surface.	58
4.15	Comparison between SPARTA and MYSTIC for Rayleigh scattering and absorption for a standard atmosphere.	59
4.16	Comparison between SPARTA and MYSTIC for an aerosol profile of spheroidal particles and a standard atmosphere.	61
4.17	Comparison between SPARTA and MYSTIC for a standard atmosphere with a cloud layer above an ocean surface - TOA	62
4.18	The same as in Figure 4.17, but for the Stokes vector at TOA.	63
5.1	Height - time display of LIDAR measurements during the SAMUM-2 field experiment.	66
5.2	Height - time display of LIDAR measurements during the METEOR cruise.	66
5.3	Optical thickness at 532 nm for the SAMUM and METEOR measurement cases.	67
5.4	Scattering and absorption coefficient profiles at 532 nm for the Rayleigh atmosphere.	68
5.5	Scattering phase matrix elements for non-spherical mineral dust particles.	69
5.6	Total radiative effects including polarization for the SAMUM measurement case at a viewing zenith angle of 0° (TOA).	71
5.7	The same as in Figure 5.6 but for a viewing zenith angle of 47°	72
5.8	The same as in Figure 5.6 but for the METEOR measurement case.	75
5.9	The same as in Figure 5.8 but for a viewing zenith angle of 47°	75
5.10	Total radiative effects including polarization for the SAMUM measurement case at a viewing zenith angle of 180° (BOA).	76
5.11	The same as in Figure 5.10 but for a viewing zenith angle of 110°	77
5.12	The same as in Figure 5.10 but for METEOR measurement case.	78
5.13	The same as in Figure 5.12 but for a viewing zenith angle of 110°	78
5.14	Comparison of 2D and IPA modes for sun overhead in case of nadir reflectivity (I) and zenith transmissivity (Q) for the METEOR measurement case.	80
5.15	Horizontal photon transport effect including polarization for the SAMUM measurement case at a viewing zenith angle of 0°	81
5.16	The same as in Figure 5.15 but for the METEOR case for a viewing zenith angle of 180°	82
5.17	1D heterogeneity effect including polarization for the METEOR measurement case at a viewing zenith angle of 0° (upper left plot). Correlation plots between the 1D effect and τ	85
5.18	1D heterogeneity effect including polarization for the SAMUM measurement case at a viewing zenith angle of 110° (BOA).	86

5.19	The same as in Figure ?? but for the METEOR case for a viewing zenith angle of 110° for I and 133° for Q	89
5.20	Correlation plots of the total bias with the IPA bias (left panels) and 1D bias (right panels) for nadir observation for the METEOR measurement case. . . .	90
5.21	The same as in Figure 5.20 but for the SAMUM measurement case.	91
5.22	The same as in Figure 5.20 but for the transmitted field for a viewing zenith angle of 133°	92
5.23	The same as in Figure 5.22 but for the SAMUM measurement case.	93
5.24	Vector and scalar calculations in the reflected radiation as a function of the viewing zenith angle for a single Rayleigh scattering layer.	95
5.25	Errors prompted by ignoring polarization in radiance simulations for a pure Rayleigh atmosphere.	96
5.26	Vector and scalar calculations in the reflected radiation as a function of the pixel number for a realistic inhomogenous atmosphere.	99

List of Tables

2.1	Overview on the most commonly used vector radiative transfer models. . . .	25
3.1	SPARTA efficiency.	37
4.1	Test cases for comparison between SPARTA and the tabulated values by Natraj et al. (2009) for pure molecular scattering.	39
4.2	Comparison between SPARTA and the benchmark results by de Haan et al. (1987) for a homogeneous layer of water-haze droplets in the reflected diffuse radiation for a cosine of the solar zenith angle of 0.5.	47
4.3	As in Table 4.2 but the cosine of the solar zenith angle is 0.1.	47
4.4	Comparison between SPARTA and the benchmark results by de Haan et al. (1987) for an inhomogeneous atmosphere of molecules and water-haze droplets in the reflected diffuse radiation for a cosine of the solar zenith angle of 0.5.	47
4.5	As in Table 4.4 but the cosine of the solar zenith angle is 0.1.	48
4.6	Comparison between SPARTA and SCIATRAN for an aerosol layer and a cloud layer, for both the reflected (TOA) and transmitted (BOA) radiation.	50
4.7	Comparison between SPARTA and MYSTIC for the single-layer scenarios of the IPRT project.	54
4.8	Comparison between SPARTA and MYSTIC for the multi-layer scenarios of the IPRT project.	54
5.1	Domain-averaged differences in percent between the 2D and 1D modes for both the reflected (TOA) and transmitted (BOA) radiation.	70
5.2	Total radiative effects including polarization - analysis for the SAMUM measurement case.	73
5.3	The same as in Table 5.2 but for the METEOR measurement case.	74
5.4	Horizontal photon transport effect including polarization - analysis for the SAMUM measurement case.	83
5.5	The same as in Table 5.4 but for the METEOR measurement case.	84
5.6	1D heterogeneity effect including polarization - analysis for the SAMUM measurement case.	87
5.7	The same as in Table 5.6 but for the METEOR measurement case.	88
5.8	Simulation settings considered in case of a pure molecular atmosphere.	94
5.9	Range of relative differences in percent between vector and scalar calculations in case of a pure molecular atmosphere.	97
5.10	Maximum relative differences in percent between vector and scalar calculations in case of realistic 1D and 2D inhomogeneous Saharan dust fields.	98

Acknowledgements

This project is part of the Leipzig Graduate School on Clouds, Aerosols and Radiation (LGS–CAR) and is funded by the Leibniz Association and the Leibniz–Institute for Tropospheric Research.

First and foremost, I would like to extend my sincere gratitude to my supervisors, Andreas Macke and Manfred Wendisch. I am deeply grateful to Andreas Macke who has been a mentor and a valuable supporter throughout the development of SPARTA. Additionally, I would like to thank Manfred Wendisch for his continuous support and all his instructive advices during this research.

I am grateful to Holger Baars for providing the height–time lidar profiles. I would like to thank Claudia Emde, Céline Cornet, and Tim Deutschmann for their support during the validation of SPARTA. Furthermore, I would like to express my thanks to Michael Mishchenko for providing the code to compute the ocean reflectance matrix.

I would like to thank André Ehrlich, Evelyn Jäkel, Tim Carlsen, Michael Schäfer, Marlen Brückner, and Fanny Finger for very motivating feedback and discussions related to my work; especially, Tim Carlsen and Michael Schäfer for the enjoyable atmosphere in the office.

Many colleagues and friends made this research a most memorable time. Among them Emmanouil Veroutis, Özge Can, Henner Bieligk, Daniel Merk, Ferdinand Stolz, and Sabrina Horn. They supported me during my stay in Germany and made me feel like home. I would also like to thank my friends Nikos, Giorgos, and Dimitris.

Last but not least, I am heartily thankful to my family for their patience, encouragement, and continuous support throughout all the years. Thank you for always believing in me.

Curriculum vitae

Name	Vasileios Barlakas
Date of birth	8 April 1986
Place of birth	Thessaloniki, Greece
Citizenship	Greek
Current address	Tarostr. 12 04103 Leipzig, Germany Email: mparlakasvas (at) yahoo.gr

Education

09/1992 – 06/1998	6th Primary School of Thessaloniki, Greece
09/1998 – 06/2001	28th Gymnasium of Thessaloniki, Greece
09/2001 – 06/2004	5th High School of Thessaloniki, Greece
09/2004 – 07/2009	Physics at the Aristotle University of Thessaloniki, Greece Degree: Undergraduate
09/2009 – 10/2011	Environmental Physics at the Aristotle University of Thessaloniki, Greece Degree: Postgraduate
07/2012 – present	PhD student at the University of Leipzig in cooperation with Leibniz–Institute for Tropospheric Research in the framework of the Leipzig Graduate School on Clouds, Aerosols and Radiation, Germany

Employments

07/2012 – 06/2015	Scientific employee at University of Leipzig, Germany
07/2015 – present	Scientific employee at Leibniz–Institute for Tropospheric Research Leipzig, Germany